ADVANCES IN ANALYTICAL FEATURES OF ELECTROCHEMICAL METHODS FOR THE ANALYSIS OF COMPLICATED REAL SAMPLES,
2nd Edition

EDITED BY: Masoud Fouladgar, Hassan Karimi-maleh and Fatih Sen
PUBLISHED IN: Frontiers in Chemistry

frontiers Research Topics

ISSN 1664-8714
ISBN 978-2-8325-5373-2
DOI 10.3389/978-2-8325-5373-2

About Frontiers

Frontiers is more than just an open-access publisher of scholarly articles: it is a pioneering approach to the world of academia, radically improving the way scholarly research is managed. The grand vision of Frontiers is a world where all people have an equal opportunity to seek, share and generate knowledge. Frontiers provides immediate and permanent online open access to all its publications, but this alone is not enough to realize our grand goals.

Frontiers Journal Series

The Frontiers Journal Series is a multi-tier and interdisciplinary set of open-access, online journals, promising a paradigm shift from the current review, selection and dissemination processes in academic publishing. All Frontiers journals are driven by researchers for researchers; therefore, they constitute a service to the scholarly community. At the same time, the Frontiers Journal Series operates on a revolutionary invention, the tiered publishing system, initially addressing specific communities of scholars, and gradually climbing up to broader public understanding, thus serving the interests of the lay society, too.

Dedication to Quality

Each Frontiers article is a landmark of the highest quality, thanks to genuinely collaborative interactions between authors and review editors, who include some of the world's best academicians. Research must be certified by peers before entering a stream of knowledge that may eventually reach the public - and shape society; therefore, Frontiers only applies the most rigorous and unbiased reviews.
Frontiers revolutionizes research publishing by freely delivering the most outstanding research, evaluated with no bias from both the academic and social point of view. By applying the most advanced information technologies, Frontiers is catapulting scholarly publishing into a new generation.

What are Frontiers Research Topics?

Frontiers Research Topics are very popular trademarks of the Frontiers Journals Series: they are collections of at least ten articles, all centered on a particular subject. With their unique mix of varied contributions from Original Research to Review Articles, Frontiers Research Topics unify the most influential researchers, the latest key findings and historical advances in a hot research area! Find out more on how to host your own Frontiers Research Topic or contribute to one as an author by contacting the Frontiers Editorial Office: frontiersin.org/about/contact

ADVANCES IN ANALYTICAL FEATURES OF ELECTROCHEMICAL METHODS FOR THE ANALYSIS OF COMPLICATED REAL SAMPLES, 2nd Edition

Topic Editors:
Masoud Fouladgar, Islamic Azad University, Iran
Hassan Karimi-maleh, University of Electronic Science and Technology of China, China
Fatih Sen, Dumlupinar University, Turkey

Publisher's note: This is a 2nd edition due to an article retraction.

Citation: Fouladgar, M., Karimi-maleh, H., Sen, F., eds. (2024). Advances in Analytical Features of Electrochemical Methods for the Analysis of Complicated Real Samples, 2nd Edition. Lausanne: Frontiers Media SA. doi: 10.3389/978-2-8325-5373-2

Table of Contents

frontiers in Chemistry

EDITORIAL
published: 17 March 2021
doi: 10.3389/fchem.2021.648920

Editorial: Advances in Analytical Features of Electrochemical Methods for the Analysis of Complicated Real Samples

Masoud Fouladgar[1]*, *Hassan Karimi-maleh*[2] *and Fatih Sen*[3]

[1]*Department of Biochemistry, Falavarjan Branch, Islamic Azad University, Isfahan, Iran,* [2]*Department of Chemical Engineering, Quchan University of Technology, Quchan, Iran,* [3]*Sen Research Group, Biochemistry Department, Faculty of Arts and Science, Dumlupinar University, Evliya Çelebi Campus, Kütahya, Turkey*

Keywords: electrochemical methods, real sample, complicated matrices, sensors, selectivity

Editorial on the Research Topic

Advances in Analytical Features of Electrochemical Methods for the Analysis of Complicated Real Samples

The aim of this topic was presentation of several features of electrochemical methods for analysis of real samples.

In the last few decades, with the technical progress of electrochemical devices, much attention has been paid to electrochemical methods for analysis of different species. However, like other analytical methods, there has been the challenge of analyzing real samples with complex matrices and several interferences.

Several techniques have been presented to improve selectivity and other figures of merit. Most of them are based on modification of electrodes and creating selective electoactive sites on the surface of electrodes (Fouladgar, 2016). In addition, the modifiers may have electrocatalytic effect on the redox of analyte.

On the other hand, application of nanomaterials has become popular because of increasing the active surface area of electrodes and consequently increasing sensitivity (Negahban et al., 2017).

Papers in this research topic, present various aspects of new methods and techniques, which have been applied for analysis of complicated samples.

As mentioned above, nanomaterials are widely used for modification of electrodes. Metal oxides are among the nanomaterials that used for this purpose. They are applied single or combination with other nanomaterials (Fouladgar and Mohammadzadeh, 2014). Naghian et al. have exhibited that using nanostructures including CdO and magnetic Fe_3O_4 nanoparticles can improve kinetics of the electron transfer process on the electrode. They applied this effect to determine an antiviral drug in urine, plasma and tablet. Moreover, different inherent redox potential of species or different interaction of species with electrode modifier can make simultaneous measurement possible. Accordingly, Pan et al. have reported an electrochemical method for simultaneous determination of Ascorbic acid, dopamine and uric acid in pharmaceutical samples. To reduce utilizing chemical reagents, Jing et al. have used *Plectranthus amboinicus* leaf extract for biosynthesis of gold nanoparticles. They determined nicotine in tobacco products by modifying glassy carbon with these nanoparticles.

OPEN ACCESS

Edited and reviewed by:
Nosang Vincent Myung, University of Notre Dame, Notre Dame, IN, United States

***Correspondence:**
Masoud Fouladgar
Fouladgar@iaufala.ac.ir

Specialty section:
This article was submitted to Electrochemistry, a section of the journal Frontiers in Chemistry

Received: *02 January 2021*
Accepted: *11 February 2021*
Published: *17 March 2021*

Citation:
Fouladgar M, Karimi-maleh H and Sen F (2021) Editorial: Advances in Analytical Features of Electrochemical Methods for the Analysis of Complicated Real Samples. Front. Chem. 9:648920. doi: 10.3389/fchem.2021.648920

Feng et al. presented an electrochemical method for determination of ursolic acid in a fruit extract (*Ligustrum lucidum*) which has many biological effects. Deposited composite of boron nitride nanosheets and Pt nanoparticles on the surface of glassy carbon, exhibits catalytic activity toward ursolic acid oxidation.

In addition to the analytical aspects of a sensor, biocompatibility of the sensor is important for analysis of clinical samples. Naderi Asrami et al. have prepared a biocompatible electrode containing glucose oxidase enzyme, which was covalently immobilized on a multi-layer thin film electrode. This electrode can be used to direct determination of glucose in blood serum.

Hou et al. presented another aspect of electrochemical methods based on changing piezoelectric properties of quartz crystal by deposition of analyte on it. They immobilized antibodies against B. bifidum on an Au chip and used it as an immunosensor. This kind of sensor has both sensitivity of quartz crystal and specification of immune response between antigen and antibody. Shen et al. have described application of signal amplification technique for creating an immunosensor to determine alpha-fetoprotein in serum samples. They used an immune complex consisting of alpha-fetoprotein antibody and horseradish peroxidase for immune response. In addition, the catalytic effect of a nanocomposite containing graphene oxide, methylene blue and gold nanoparticles has been applied for fabrication of this immunosensor.

One area in which application of electrochemical methods has received much attention is analysis of pharmacological and biological samples. Electrochemistry has presented simple, fast and sensitive methods to analyze these samples. Alizadeh et al. have used effects of modifying electrodes with different nanomaterials and ionic liquid.

Increasing conductivity of carbon paste subsequently increases the redox current and also increases sensitivity of the method. This technique has provided methods for determination of drugs in pharmaceutical samples (Alizadeh et al.).

Remote sensing is important for monitoring chemical species in the environment. Kim et al. have proposed a wireless sensing system for real time measuring chloride ion. They have succeeded in reducing electrolyte leakage by modifying the structure of the electrode.

Finally, the effect of species on the profile of electrochemical oscillation systems has been used for identification chemical compounds. Yan et al. have been shown that recording the oscillation profile of an oscillation reaction in the presence of different herbal medicine can be used as a fingerprint for identification of them.

AUTHOR CONTRIBUTIONS

MF drafted the manuscript. All co-authors contributed to review the manuscript.

ACKNOWLEDGMENTS

We want to thank all the authors and reviewers for their valuable contributions to this research topic, and we hope that this collection of articles will be helpful for researchers and students.

REFERENCES

Fouladgar, M. (2016). Application of ZnO nanoparticle/ion liquid modified carbon paste electrode for determination of isoproterenol in pharmaceutical and biological samples. *J. Electrochem. Soc.* 163, B38–B42. doi:10.1149/2.0611603jes

Fouladgar, M., and Mohammadzadeh, S. (2014). Determination of methimazole on a multiwall carbon nanotube titanium dioxide nanoparticle paste electrode. *Anal. Lett.* 47, 763–777. doi:10.1080/00032719.2013.855782

Negahban, S., Fouladgar, M., and Amiri, G. (2017). Improve the performance of carbon paste electrodes for determination of dobutamine using MnZnFe2O4 nanoparticles and ionic liquid. *J. Taiwan Inst. Chem. Eng.* 78, 51–55. doi:10.1016/j.jtice.2017.05.032

Conflict of Interest: The authors declare that the research was conducted in the absence of any commercial or financial relationships that could be construed as a potential conflict of interest.

frontiers in Chemistry

ORIGINAL RESEARCH
published: 27 May 2020
doi: 10.3389/fchem.2020.00444

Determination of Ursolic Acid in Extracts From *Ligustri lucidum* Fruit Using an Electrochemical Method

Yingpu Feng[1,2†], *Zheng Wei*[3†] *and Junping Zhang*[3*]

[1] Centre of Cerebrovascular, Zhengzhou University People's Hospital, Zhengzhou, China, [2] Centre of Cerebrovascular, Henan Provincial People's Hospital, Zhengzhou, China, [3] Department of Traditional Chinese Medicine, Henan Academy Institute of Traditional Chinese Medicine, Zhengzhou, China

In this work, we reported a facile wet chemical method for depositing Pt nanoparticles on the surface of boron nitride nanosheets (BNNS-Pt NPs). The deposited nanocomposite was applied for glassy carbon electrode surface modification. The modified electrode was then used for detecting ursolic acid (UA). The results indicate that the BNNS-Pt NPs exhibited excellent electrocatalytic activity toward UA oxidation compared with that of the bare glassy carbon electrode (GCE) and Pt NPs/GCE. The UA oxidation currents is linearly related its concentration from 1 to 1,200 pM. The limit of detection can be calculated to be 0.5 pM. In addition, the UA sensor was also successfully used for the determination of UA in *Ligustri lucidum* fruit samples.

Keywords: electrochemical sensor, Pt nanoparticles, voltammetry, nanocomposite, boron nitride nanosheets, *Ligustri lucidum*, ursolic acid, biosensor

OPEN ACCESS

Edited by:
Hassan Karimi-Maleh,
University of Electronic Science and Technology of China, China

Reviewed by:
Mehdi Baghayeri,
Hakim Sabzevari University, Iran
Yasin Orooji,
Nanjing Forestry University, China
Fatih Sen,
Dumlupinar University, Turkey

***Correspondence:**
Junping Zhang
zhangjunping888@163.com

[†]These authors have contributed equally to this work

Specialty section:
This article was submitted to Electrochemistry, a section of the journal Frontiers in Chemistry

Received: *30 March 2020*
Accepted: *28 April 2020*
Published: *27 May 2020*

Citation:
Feng Y, Wei Z and Zhang J (2020) Determination of Ursolic Acid in Extracts From Ligustri lucidum Fruit Using an Electrochemical Method. Front. Chem. 8:444. doi: 10.3389/fchem.2020.00444

INTRODUCTION

Privet fruit is the ripe fruit of the *Ligustrum lucidum* Ait plant (Hu et al., 2014). This fruit has the function of nourishing the liver and kidneys and improving eyesight according to the study of traditional Chinese medicine (Gao et al., 2015a). The benefits of privet fruit are gradual, but their long-term use can be effective. Modern clinical applications also include the treatment of optic neuritis, leukocyte reduction, chronic hepatitis, hyperlipidemia, coronary heart disease, hypertension, children's poisoning, hearing loss, neurasthenia, facial paralysis, and hair loss (Gao et al., 2007; Pang et al., 2015). A study found that *L. lucidum* fruit contains a high quantity of ursolic acid (UA). UA is a pentacyclic triterpenoid identified in many herbs. UA has many biological effects, such as acting as a sedative, having anti-inflammatory, antibacterial, anti-diabetes, and anti-ulcer effects, and reducing blood sugar (Li et al., 2019). UA is also widely used as a raw material for medicine and cosmetics because of its antioxidant function. The clinical uses of UA demonstrate significantly decreased serum aminotransferase and alanine aminotransferase, alleviated jaundice, increased appetite, suppressed fibrosis and recovered liver function, with the advantages of fast and stable effects and short treatment course (Hussain et al., 2017).

Ursolic acid (5∼20 mg/kg) can treat rat liver toxicity (Saraswat et al., 2000; Saraswati et al., 2013). Pretreatment with UA can significantly improve the survival rate of rat hepatocytes and can provide anti-cholestasis effects (Chai et al., 2015). Both the flow and the contents of bile increased accordingly. According to the mechanism of CC1, the mechanism of UA in the treatment of damaged hepatocytes may be similar to that of the isomers of oleanolic acid, which is to protect and stabilize the biofilm system of the liver cell membrane and organelles (Yan et al., 2010). The change was evident, and active transport functions returned to normal. The distribution of mobile ions and water inside and outside the cells recover consequently, which restores the regeneration

function and promotes the repair of hepatic centrilobular necrosis of the liver cells (Alam et al., 2018). The study found that UA plays an important role in the treatment of viral hepatitis whether it is used alone or with other drugs in preparation for the treatment of viral hepatitis. Compared with oleanolic acid (Liu, 1995), 102 cases of acute hepatitis A and B were treated with UA with a dose of 102 and 60 mg/d; the average time of treatment was 21 days, and the cure rate was 89.3%. The curative effect of 100 cases treated with oleanolic acid (68%, $P < 0.01$) was better than that of the control group with the same treatment time. Clinical trials prove that UA shows a significant and rapid reduction in alanine transaminase, elimination of jaundice and recovery of liver function. After 3 weeks of treatment, the negative rate of 21 cases of HBeAg-positive patients was 61.9%. The negative rate of 21 cases of HBsAg positive patients was 42.8%, indicating that it also has a certain therapeutic effect on hepatitis B. In addition, Ramos-Hryb also confirmed that UA not only has the effect of treating viral hepatitis but also acts as an antidepressant; it contains UA perilla extract as a treatment for depression (Ramos-Hryb et al., 2017). UA causes almost no adverse reactions (Gharibi et al., 2018). Compared with western medicine, the antidepressant spectrum is narrow, while the toxicity and side effects are very minor (Machado et al., 2012). UA has the obvious advantages of decreasing recurrence and suicidal tendencies after drug use. The capsule made from the extract of *Ligustrum lucidum* leaves mainly composed of UA is primarily used for primary hyperlipidemia (Yuliang et al., 2015). Therefore, the development of a reliable method for UA determination is very important in clinical and pharmacological fields (Seo et al., 2018; Burhan et al., 2020; Demirkan et al., 2020).

Thus far, several methods have been developed for the determination of UA, including micellar electrokinetic capillary chromatography (Zhang et al., 2005), HPLC (Li et al., 2019), LC-MS (Novotny et al., 2003), capillary zone electrophoresis (Gao et al., 2015b) and UV spectroscopy (Pironi et al., 2018). These methods all require complicated sample preparation procedures and a sophisticated operation. An electrochemical method may be considered as an alternative for UA detection because of the high sensitivity, fast response and low detection limit (Karimi-Maleh et al., 2019a,b; Shamsadin-Azad et al., 2019; Tahernejad-Javazmi et al., 2019; Karimi-Maleh and Arotiba, 2020). However, electrochemical sensors have often been restricted by the high redox overpotential of target molecules. Therefore, electrode surface modification has been widely used for improving the sensing performance by triggering an electrocatalytic reaction (Baghayeri et al., 2014, 2018a,b; Orooji et al., 2019). A studyreported that BNNS can be used as a loading platform catalyst deposition and consequently applied as an excellent modifier for electrochemical sensing (Nam et al., 2018). In addition, BNNS showed superior dispersibility than graphene in aqueous conditions, which allows further construction (Azamat et al., 2015; Rajski et al., 2020).

In this study, we report a facial strategy for the *in situ* growth of Pt nanoparticles on BNNS without using additional reductants. The resulting BNNS-Pt nanocomposite has been modified on a glassy carbon electrode (GCE) for the electrocatalytic determination of UA. Meanwhile, the proposed approach has been successfully used for determining UA content in the *Ligustri lucidum* fruit extract.

EXPERIMENTS

The exfoliation of BN was performed according to the literature and contains two steps (Fu et al., 2017). In the first stage, NaOH (2.8434 g) and KOH (2.1566 g) were ground finely, and then BN powder (1 g) was added. The mixture was further ground into a homogeneous form and transferred to a 100 mL Teflon-lined stainless-steel autoclave. The autoclave was heated to 180°C, and the temperature was maintained for 2 h in an oven and then naturally cooled to room temperature. In the secondary stage, the solid product collected from the autoclave was dispersed in 300 mL of water. The dispersion was sonicated for 1 h using a sonic tip (90% of 600 W using 5 s on 2 s off pulsation). After a filtration process to remove hydroxide, the BN slurry was dispersed into 300 mL using 10 min of bath sonication before centrifugation. The BN dispersion was centrifuged at 2,000 rpm for 30 min to remove the aggregated material and thick flakes. The supernatant was collected as BNNS.

The BNNS-Pt NP composite was prepared by growing Pt NPs *in situ* on BNNS. Briefly, 0.2 mL of 2% H_2PtCl_6 was added into 25 mL BNNS (0.2 mg/mL). After the pH was adjusted to 10 using 0.1 M NaOH, the solution was stirred for 24 h at room temperature. After centrifugation and washing twice with water, the resulting BNNS-Pt NP composite was obtained and re-dispersed in 10 mL water for further use.

Scanning electron microscopy (SEM, QUANTA FEG250) was used for morphology characterization. XRD characterization was carried out with a BRUKER D8–Advance XRD system with Cu Kα radiation. All the electrochemical sensing and characterizations were conducted using a CHI 832 electrochemical workstation. All the experiments were performed at room temperature.

A glassy carbon electrode (GCE) was polished by 0.05 μm alumina dispersion and cleaned by water and ethanol. Then, 4 μL of catalyst dispersion (0.2 mg/mL) was dropped onto the GCE surface and dried naturally. The anti-interference study was carried out by square wave voltammetry (SWV) in the presence of UA and interference species. Triplicate measurements were recorded and the average values of current changes were calculated. Peanut shells and *Ligustri lucidum* (fruit) were purchased from a local traditional Chinese medical center. For the real sample preparation, the dried *Ligustri lucidum* (fruit) was grounded and then dispersed into 50 mL methanol with vigorous stirring for 12 h. Then, the dispersion was filtered through a 0.45 μm filter paper and diluted to 50 mL by PBS.

RESULTS AND DISCUSSION

Figure 1A shows the SEM image of the synthesized BNNS-Pt NPs. It can be seen that the Pt NPs can be clearly differentiated from the BNNS surface by the contrast. The XRD patterns of the BNNS and BNNS-Pt NP composites are shown in **Figure 1B**. The characteristic peaks at 26.8°, 41.7°, 44.2°, 50.3°, 55.2°, 71.4°,

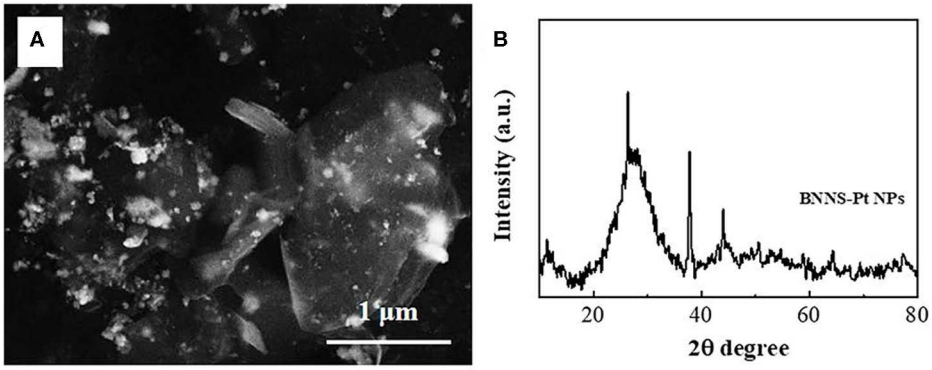

FIGURE 1 | (A) SEM image and **(B)** XRD spectrum of BNNS-Pt NPs.

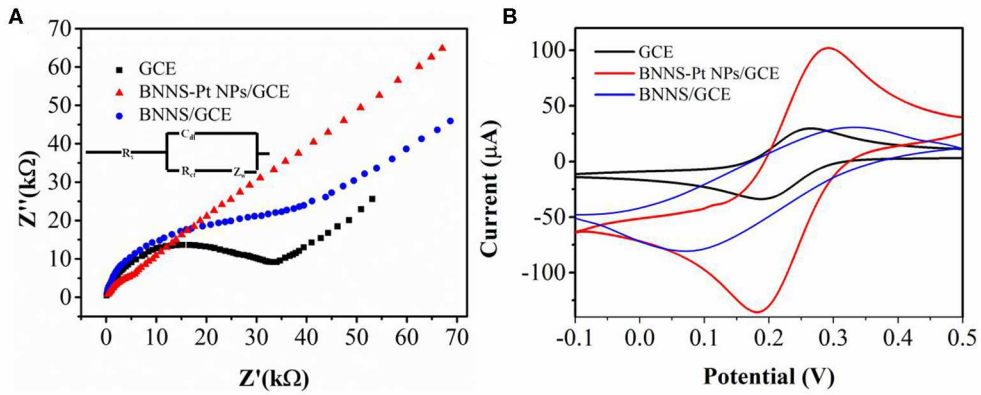

FIGURE 2 | (A) Electrochemical impedance spectra and **(B)** CV profiles of bare GCE, BNNS/GCE, and BNNS-Pt NP/GCE in 0.1 M KCl containing 5 mM $[Fe(CN)_6]^{3-/4-}$.

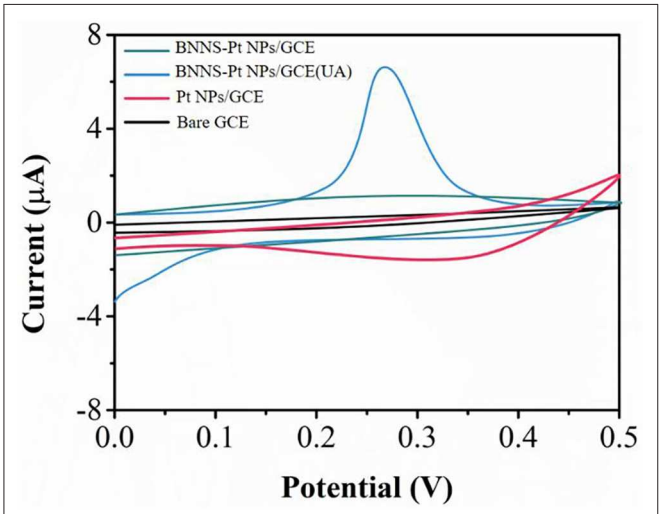

FIGURE 3 | CV profiles of bare GCE, Pt NPs/GCE and BNNS-Pt NPs/GCE in 0.1 M PBS (pH 7.0) in the presence and the absence of 0.2 μM UA.

and 76.1° can be assigned to the (002), (100), (101), (102), (004), (104), and (110) planes of the hexagonal phase of BN (JCPDS 34-0421) (Lim et al., 2013), respectively. The additional peaks at 38.5°, 44.7°, 64.4, and 77.6 in the XRD pattern of the BNNS-Pt NP composite are attributed to the (111), (200), (220), and (331) crystal face of face-centered cubic (fcc) Pt (JCPDS 65-2870) (Wang et al., 2014). The average size of the Pt NPs can be calculated to be 21 nm.

The electrochemical properties of bare GCE and modified GCE were investigated using 5 mM $[Fe(CN)_6]^{3-/4-}$ in 0.1 M KCl by electrochemical impedance spectroscopy (EIS). As shown in **Figure 2A**, the EIS spectrum of BNNS/GCE shows a much larger semicircle than that of bare GCE due to the low electron transfer rate, indicating that BNNS hindered interfacial electron transfer. In contrast, BNNS-Pt NP/GCE shows much smaller semicircles, suggesting that the surface modification promotes the electron transfer rate on the GCE surface.

Cyclic voltammetry was used to further study the electrochemical properties of various electrodes (**Figure 2B**). A clear change was noticed in the voltammograms before and

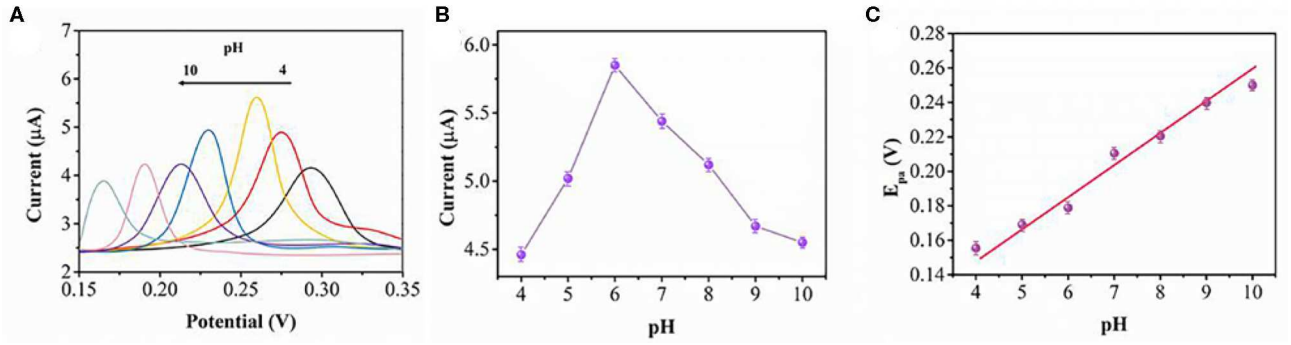

FIGURE 4 | (A) SWV scans of BNNS-Pt NPs/GCE toward 0.2 μM UA at different pH values from 4.0 to 10.0. **(B)** The relationship of pH value and peak current. **(C)** Plot of pH vs. peak potential.

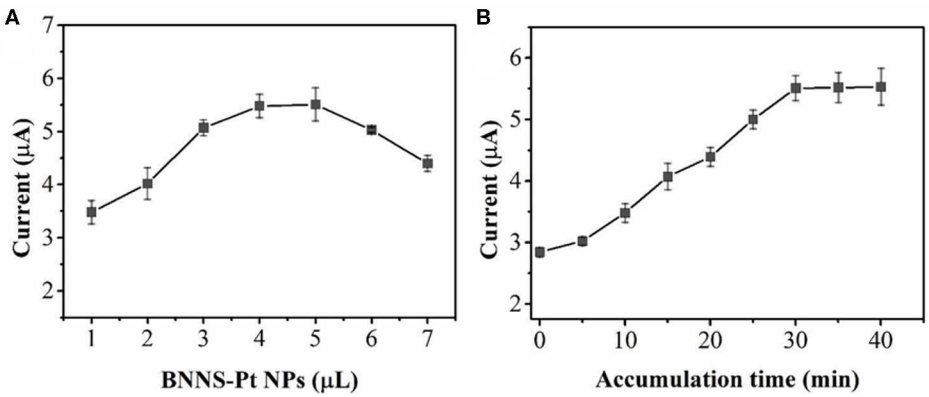

FIGURE 5 | Effect of **(A)** the BNNS-Pt NPs content and **(B)** accumulation time toward 0.2 μM UA detection.

after catalyst modification. The electrochemical profiles of $[Fe(CN)_6]^{3-/4-}$ redox is largely suppressed with a larger peak to peak splitting, indicating that the insulation of the BNNS lowers the electron transfer rate, which agrees with the EIS result (Fu et al., 2018b). On the other hand, a clear improvement of the current intensity is noticed after the loading of Pt NPs. In addition, BNNS-Pt NPs/GCE displays an even higher response than Pt NPs/GCE, indicating that the loading of Pt NPs on BNNS surface can provide more electrocatalytic sites by exposing individual Pt NPs to the $[Fe(CN)_6]^{3-/4-}$ without agglomeration.

We tested the sensing performance of the proposed electrochemical sensor toward UA using ABS (pH4.5), PBS (pH 7.0), and Tris (pH9.5). The PBS showed the best performance. Therefore, we selected the PBS in this work. **Figure 3** shows CV curves of 0.1 μM UA recorded at bare GCE and modified GCE in 0.1 M PBS. The UA shows no redox peaks at either GCE or BNNS/GCE. In contrast, BNNS-Pt NPs/GCE shows an oxidation peak due to the electrocatalytic activity of the Pt NPs. The Pt NPs may be applied as an excellent electrocatalyst for lowering the overpotential to overcome the interference compounds (Morsbach et al., 2014). In addition, the UA oxidation current at the BNNS-Pt NPs/GCE is larger than that of the Pt NPs/GCE, indicating the BNNS is an excellent substrate for Pt NP deposition. It can exhibit advanced electrocatalytic performance than chemically synthesized Pt NPs. The CV curve of BNNS-Pt NPs/GCE without UA was recorded as well. No obvious peak was noticed during the scan, suggesting the oxidation peak observed previously was caused by UA oxidation.

The effect of pH on the oxidation of 0.2 μM UA is shown in **Figure 4A**. The pH value of the PBS was changed by adding 0.1 M HCl or 0.1 M NaOH. We investigated UA oxidation in the pH range between 4.0 and 10.0 in PBS using SWV. **Figure 4B** shows the relationship between the oxidation current and pH conditions. The peak current increases when the pH increases. After pH 6, the peak current decreases with a further increase of pH. Therefore, pH 6 has been chosen for the optimum pH condition for UA detection. As shown in **Figure 4C**, the oxidation peak potential shifts along with the pH value. A linear expression can be deduced as: $E_{pa}(V)=(-0.0211)\ pH+0.0802$ ($R = 0.997$). The number of electrons (n) in the overall reaction can be calculated as 2 for a totally irreversible diffusion-controlled process.

The effect of the amount of BNNS-Pt NPs on the UA oxidation has been optimized. As shown in **Figure 5A**, the oxidation peak current increases along with the BNNS-Pt NP loading increase from 1 to 5 μL. Further increases in the BNNS-Pt NPs will

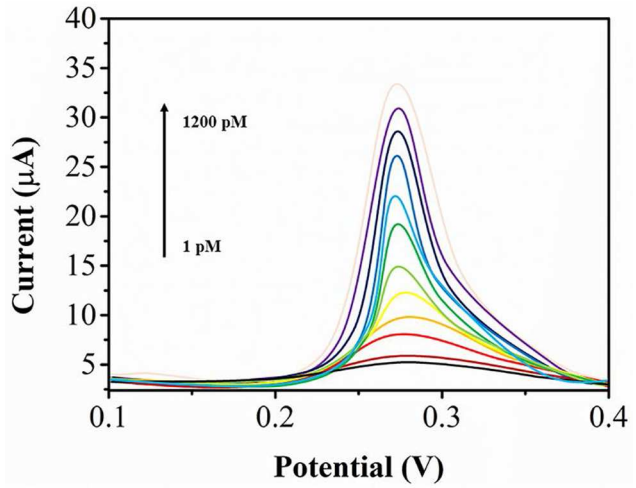

FIGURE 6 | SWV profiles of UA at BNNS-Pt NPs/GCE from a to k: 1, 5, 20, 50, 100, 200, 300, 400, 500, 700, 900, 1,200 pM.

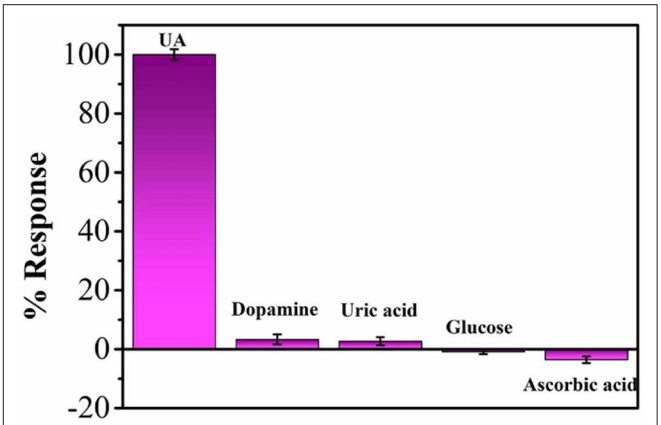

FIGURE 7 | Percentage response of BNNS-Pt NPs/GCE for various interferences with respect to UA.

result in a lower current response due to the thicker modification layer and will consequently lower the electron transfer efficiency. Therefore, 5 μL of the BNNS-Pt NP dispersion was applied as electrode modifier. The accumulation process was further optimized for UA oxidation. As seen from **Figure 5B**, the peak response increases significantly from 0 to 30 min. Then, the peak currents remain steady with the further increase of accumulation time. Therefore, 30 min was chosen before sensing.

Under the optimum conditions, SWV was used for UA analysis. **Figure 6** shows the SWV profiles of UA at BNNS-Pt NPs/GCE. The UA oxidation currents is linearly related its concentration from 1 to 1200 pM. The equations can be expressed as I_{pa} (μA) = 0.24221 c (nM) + 2.4454. The LOD can be calculated to be 0.5 pM (S/N=3).

The reproducibility of the proposed electrochemical sensor was investigated by the detection of 0.2 μM UA with eight individual detections. A RSD of 4.1% was recorded, indicating that the BNNS-Pt NP dispersion exhibits good reproducibility compared with previous BNNS based works (Fu et al., 2016, 2018a). The stability of the sensor was investigated by ten successive detections of 0.2 μM UA. The current remained at more than 85% after ten scans. The proposed electrochemical sensor could maintain more than 95% performance after 1 month storage.

The anti-interference performance was investigated as well. The results show that 50-fold higher concentrations of common cations (Ca^{2+}, Na^{+}, K^{+}, Zn^{2+}) and anions (NO_3^-, Cl^-, SO_4^{2-}) show no changes of sensing. Ten-fold higher concentrations common species of dopamine, uric acid, glucose and ascorbic acid also show no changes of sensing (**Figure 7**). Therefore, the proposed BNNS-Pt NPs/GCE shows excellent selectivity for UA oxidation.

In this work, *Ligustri lucidum* fruit samples were used. The standard addition process was used and the results are showed in **Table 1**. The average UA concentration is found to be 0.397 μM in *Ligustri lucidum* fruit. An HPLC (Agilent 1100) method was also conducted for comparison.

TABLE 1 | Detection of UA in *Ligustri lucidum* fruit and the recovery results.

Sample	Found (μM)	HPLC (μMs)	Added (μM)	Found (μM)	Recovery (%)	RSD (%)
1	0.399	0.387	0.5	0.885	98.44	3.12
2	0.413	0.405	0.5	0.901	98.69	2.65
3	0.427	0.425	0.5	0.922	99.46	3.22
4	0.350	0.352	0.5	0.841	99.94	4.05

CONCLUSIONS

Deposition of Pt NPs on a BNNS surface can be used for UA electro-oxidation. The BNNS-Pt NPs nanocomposite exhibited electrocatalytic activity toward UA oxidation. Loading of Pt NPs on BNNS surface can provide more electrocatalytic sites by exposing individual Pt NPs to the analyte without agglomeration. The proposed UA sensing platform showed a linear detected from 1 to 1,200 pM, with a low LOD of 0.5 pM. In addition, the sensing platform has been successfully used for determining UA content in *Ligustri lucidum* fruit.

DATA AVAILABILITY STATEMENT

The raw data supporting the conclusions of this article will be made available by the authors, without undue reservation.

AUTHOR CONTRIBUTIONS

YF and JZ conducted the main experiments and wrote the paper. ZW did the material characterization and proofreading.

FUNDING

This research work was financially supported by National Natural Science Foundation of China (No. 81873290), Henan TCM Foundation (2018ZYZD14&2019ZYBJ28), the scientific and technological project of Henan Province in China (No. 182102311164) and China Postdoctoral Science Foundation (No. 2019T120626).

REFERENCES

Alam, P., Al-Yousef, H. M., Siddiqui, N. A., Alhowiriny, T. A., Alqasoumi, S. I., Amina, M., et al. (2018). Anticancer activity and concurrent analysis of ursolic acid, β-sitosterol and lupeol in three different Hibiscus species (aerial parts) by validated HPTLC method. *Saudi Pharm. J.* 26, 1060–1067. doi: 10.1016/j.jsps.2018.05.015

Azamat, J., Sattary, B. S., Khataee, A., and Joo, S. W. (2015). Removal of a hazardous heavy metal from aqueous solution using functionalized graphene and boron nitride nanosheets: insights from simulations. *J. Mol. Graph. Model.* 61, 13–20. doi: 10.1016/j.jmgm.2015.06.012

Baghayeri, M., Amiri, A., Alizadeh, Z., Veisi, H., and Hasheminejad, E. (2018a). Non-enzymatic voltammetric glucose sensor made of ternary NiO/Fe3O4-SH/para-amino hippuric acid nanocomposite. *J. Electroanal. Chem.* 810, 69–77. doi: 10.1016/j.jelechem.2018.01.007

Baghayeri, M., Amiri, A., Maleki, B., Alizadeh, Z., and Reiser, O. (2018b). A simple approach for simultaneous detection of cadmium(II) and lead(II) based on glutathione coated magnetic nanoparticles as a highly selective electrochemical probe. *Sens. Actuators B Chem.* 273, 1442–1450. doi: 10.1016/j.snb.2018.07.063

Baghayeri, M., Maleki, B., and Zarghani, R. (2014). Voltammetric behavior of tiopronin on carbon paste electrode modified with nanocrystalline Fe50Ni50 alloys. *Mater. Sci. Eng. C* 44, 175–182. doi: 10.1016/j.msec.2014.08.023

Burhan, H., Ay, H., Kuyuldar, E., and Sen, F. (2020). Monodisperse Pt-Co/GO anodes with varying Pt: Co ratios as highly active and stable electrocatalysts for methanol electrooxidation reaction. *Sci. Rep.* 10:6114. doi: 10.1038/s41598-020-63247-6

Chai, J., Du, X., Chen, S., Feng, X., Cheng, Y., Zhang, L., et al. (2015). Oral administration of oleanolic acid, isolated from *Swertia mussotii* Franch, attenuates liver injury, inflammation, and cholestasis in bile duct-ligated rats. *Int. J. Clin. Exp. Med.* 8, 1691–1702. doi: 10.1155/2015/948376

Demirkan, B., Bozkurt, S., Cellat, K., Arikan, K., Yilmaz, M., Savk, A., et al. (2020). Palladium supported on polypyrrole/reduced graphene oxide nanoparticles for simultaneous biosensing application of ascorbic acid, dopamine, and uric acid. *Sci. Rep.* 10:2946. doi: 10.1038/s41598-020-59935-y

Fu, L., Chen, G., Jiang, N., Yu, J., Lin, C.-T., and Yu, A. (2016). *In situ* growth of metal nanoparticles on boron nitride nanosheets as highly efficient catalysts. *J. Mater. Chem. A* 4, 19107–19115. doi: 10.1039/C6TA06409D

Fu, L., Liu, Z., Huang, Y., Lai, G., Zhang, H., Su, W., et al. (2018a). Square wave voltammetric quantitative determination of flavonoid luteolin in peanut hulls and Perilla based on Au NPs loaded boron nitride nanosheets. *J. Electroanal. Chem.* 817, 128–133. doi: 10.1016/j.jelechem.2018.04.009

Fu, L., Wang, A., Lai, G., Su, W., Malherbe, F., Yu, J., et al. (2018b). Defects regulating of graphene ink for electrochemical determination of ascorbic acid, dopamine and uric acid. *Talanta* 180, 248–253. doi: 10.1016/j.talanta.2017.12.058

Fu, L., Wang, T., Yu, J., Dai, W., Sun, H., Liu, Z., et al. (2017). An ultrathin high-performance heat spreader fabricated with hydroxylated boron nitride nanosheets. *2D Mater.* 4:025047. doi: 10.1088/2053-1583/aa636e

Gao, D., Li, Q., Li, Y., Liu, Z., Liu, Z., Fan, Y., et al. (2007). Antidiabetic potential of oleanolic acid from *Ligustrum lucidum* Ait. *Can. J. Physiol. Pharmacol.* 85, 1076–1083. doi: 10.1139/Y07-098

Gao, L., Li, C., Wang, Z., Liu, X., You, Y., Wei, H., et al. (2015a). Ligustri lucidi fructus as a traditional Chinese medicine: a review of its phytochemistry and pharmacology. *Nat. Prod. Res.* 29, 493–510. doi: 10.1080/14786419.2014.954114

Gao, R., Wang, L., Yang, Y., Ni, J., Zhao, L., Dong, S., et al. (2015b). Simultaneous determination of oleanolic acid, ursolic acid, quercetin and apigenin in *Swertia mussotii* Franch by capillary zone electrophoresis with running buffer modifier. *Biomed. Chromatogr.* 29, 402–409. doi: 10.1002/bmc.3290

Gharibi, S., Bakhtiari, N., Elham-Moslemee-Jalalvand, and Bakhtiari, F. (2018). Ursolic acid mediates hepatic protection through enhancing of anti-aging biomarkers. *Curr. Aging Sci.* 11, 16–23. doi: 10.2174/1874609810666170531103140

Hu, B., Du, Q., Deng, S., An, H.-M., Pan, C.-F., Shen, K., et al. (2014). *Ligustrum lucidum* Ait. fruit extract induces apoptosis and cell senescence in human hepatocellular carcinoma cells through upregulation of p21. *Oncol. Rep.* 32, 1037–1042. doi: 10.3892/or.2014.3312

Hussain, H., Green, I. R., Ali, I., Khan, I. A., Ali, Z., Al-Sadi, A. M., et al. (2017). Ursolic acid derivatives for pharmaceutical use: a patent review (2012-2016). *Expert Opin. Ther. Pat.* 27, 1061–1072. doi: 10.1080/13543776.2017.1344219

Karimi-Maleh, H., and Arotiba, O. A. (2020). Simultaneous determination of cholesterol, ascorbic acid and uric acid as three essential biological compounds at a carbon paste electrode modified with copper oxide decorated reduced graphene oxide nanocomposite and ionic liquid. *J. Colloid Interface Sci.* 560, 208–212. doi: 10.1016/j.jcis.2019.10.007

Karimi-Maleh, H., Fakude, C. T., Mabuba, N., Peleyeju, G. M., and Arotiba, O. A. (2019a). The determination of 2-phenylphenol in the presence of 4-chlorophenol using nano-Fe_3O_4/ionic liquid paste electrode as an electrochemical sensor. *J. Colloid Interface Sci.* 554, 603–610. doi: 10.1016/j.jcis.2019.07.047

Karimi-Maleh, H., Karimi, F., Alizadeh, M., and Sanati, A. L. (2019b). Electrochemical sensors, a bright future in the fabrication of portable kits in analytical systems. *Chem. Rec.* doi: 10.1002/tcr.201900092. [Epub ahead of print].

Li, P., Liu, A., Li, Y., Yuan, B., Xiao, W., Liu, Z., et al. (2019). Development and validation of an analytical method based on HPLC-ELSD for the simultaneous determination of rosmarinic acid, carnosol, carnosic acid, oleanolic acid and ursolic acid in rosemary. *Molecules* 24:323. doi: 10.3390/molecules24020323

Lim, H. S., Oh, J. W., Kim, S. Y., Yoo, M.-J., Park, S.-D., and Lee, W. S. (2013). Anisotropically alignable magnetic boron nitride platelets decorated with iron oxide nanoparticles. *Chem. Mater.* 25, 3315–3319. doi: 10.1021/cm401488a

Liu, J. (1995). Pharmacology of oleanolic acid and ursolic acid. *J. Ethnopharmacol.* 49, 57–68. doi: 10.1016/0378-8741(95)90032-2

Machado, D. G., Neis, V. B., Balen, G. O., Colla, A., Cunha, M. P., Dalmarco, J. B., et al. (2012). Antidepressant-like effect of ursolic acid isolated from *Rosmarinus officinalis* L. in mice: evidence for the involvement of the dopaminergic system. *Pharmacol. Biochem. Behav.* 103, 204–211. doi: 10.1016/j.pbb.2012.08.016

Morsbach, E., Brauns, E., Kowalik, T., Lang, W., Kunz, S., and Bäumer, M. (2014). Ligand-stabilized Pt nanoparticles (NPs) as novel materials for catalytic gas sensing: influence of the ligand on important catalytic properties. *Phys. Chem. Chem. Phys.* 16, 21243–21251. doi: 10.1039/C4CP02993C

Nam, S., Chang, K., Lee, W., Kim, M. J., Hwang, J. Y., and Choi, H. (2018). Structural effect of two-dimensional BNNS on grain growth suppressing behaviors in Al-matrix nanocomposites. *Sci. Rep.* 8, 1–12. doi: 10.1038/s41598-018-20150-5

Novotny, L., Abdel-Hamid, M. E., Hamza, H., Masterova, I., and Grancai, D. (2003). Development of LC-MS method for determination of ursolic acid: application to the analysis of ursolic acid in staphylea holocarpa hemsl. *J. Pharm. Biomed. Anal.* 31, 961–968. doi: 10.1016/S0731-7085(02)00706-9

Orooji, Y., Alizadeh, A., ad, Ghasali, E., Derakhshandeh, M. R., Alizadeh, M., Asl, M. S., et al. (2019). Co-reinforcing of mullite-TiN-CNT composites with ZrB2 and TiB2 compounds. *Ceram. Int.* 45, 20844–20854. doi: 10.1016/j.ceramint.2019.07.072

Pang, Z., Zhi-yan, Z., Wang, W., Ma, Y., Feng-ju, N., Zhang, X., et al. (2015). The advances in research on the pharmacological effects of fructus ligustri lucidi. *BioMed Res. Int.* 2015:281873. doi: 10.1155/2015/281873

Pironi, A. M., de Araújo, P. R., Fernandes, M. A., Salgado, H. R. N., and Chorilli, M. (2018). Characteristics, biological properties and analytical methods of ursolic acid: a review. *Crit. Rev. Anal. Chem.* 48, 86–93. doi: 10.1080/10408347.2017.1390425

Rajski, Ł., Beraza, I., Gómez Ramos, M. J., Ferrer, C., and Fernández-Alba, A. R. (2020). Evaluation of segmented non-target data acquisition (SWATH/vDIA) in a QToF and QOrbitrap for pesticide residue analysis. *Anal. Methods* 12, 2027–2038. doi: 10.1039/D0AY00290A

Ramos-Hryb, A. B., Cunha, M. P., Pazini, F. L., Lieberknecht, V., Prediger, R. D., Kaster, M. P., et al. (2017). Ursolic acid affords antidepressant-like effects in mice through the activation of PKA, PKC, CAMK-II and MEK1/2. *Pharmacol. Rep*. 69, 1240–1246. doi: 10.1016/j.pharep.2017.05.009

Saraswat, B., Visen, P. K., and Agarwal, D. (2000). Ursolic acid isolated from Eucalyptus tereticornis protects against ethanol toxicity in isolated rat hepatocytes. *Phytother. Res*. 14, 163–166. doi: 10.1002/(SICI)1099-1573(200005)14:3<163::AID-PTR588>3.0.CO;2-D

Saraswati, S., Agrawal, S. S., and Alhaider, A. A. (2013). Ursolic acid inhibits tumor angiogenesis and induces apoptosis through mitochondrial-dependent pathway in *Ehrlich ascites* carcinoma tumor. *Chem. Biol. Interact*. 206, 153–165. doi: 10.1016/j.cbi.2013.09.004

Seo, D. Y., Lee, S. R., Heo, J.-W., No, M.-H., Rhee, B. D., Ko, K. S., et al. (2018). Ursolic acid in health and disease. *Korean J. Physiol. Pharmacol*. 22, 235–248. doi: 10.4196/kjpp.2018.22.3.235

Shamsadin-Azad, Z., Taher, M. A., Cheraghi, S., and Karimi-Maleh, H. (2019). A nanostructure voltammetric platform amplified with ionic liquid for determination of tert-butylhydroxyanisole in the presence kojic acid. *J. Food Meas. Charact*. 13, 1781–1787. doi: 10.1007/s11694-019-00096-6

Tahernejad-Javazmi, F., Shabani-Nooshabadi, M., and Karimi-Maleh, H. (2019). 3D reduced graphene oxide/FeNi3-ionic liquid nanocomposite modified sensor; an electrical synergic effect for development of tert-butylhydroquinone and folic acid sensor. *Compos. Part B Eng*. 172, 666–670. doi: 10.1016/j.compositesb.2019.05.065

Wang, T., Jin, B., Jiao, Z., Lu, G., Ye, J., and Bi, Y. (2014). Photo-directed growth of Au nanowires on ZnO arrays for enhancing photoelectrochemical performances. *J. Mater. Chem. A* 2, 15553–15559. doi: 10.1039/C4TA02960G

Yan, S., Huang, C., Wu, S., and Yin, M. (2010). Oleanolic acid and ursolic acid induce apoptosis in four human liver cancer cell lines. *Toxicol. In Vitro* 24, 842–848. doi: 10.1016/j.tiv.2009.12.008

Yuliang, W., Zejian, W., Hanlin, S., Ming, Y., and Kexuan, T. (2015). The hypolipidemic effect of artesunate and ursolic acid in rats. *Pak. J. Pharm. Sci*. 28:77.

Zhang, G., Qi, Y., Lou, Z., Liu, C., Wu, X., and Chai, Y. (2005). Determination of oleanolic acid and ursolic acid in cornel by cyclodextrin-modified micellar electrokinetic chromatography. *Biomed. Chromatogr*. 19, 529–532. doi: 10.1002/bmc.475

Conflict of Interest: The authors declare that the research was conducted in the absence of any commercial or financial relationships that could be construed as a potential conflict of interest.

frontiers in Chemistry

ORIGINAL RESEARCH
published: 07 July 2020
doi: 10.3389/fchem.2020.00548

Rapid Detection of *Bifidobacterium bifidum* in Feces Sample by Highly Sensitive Quartz Crystal Microbalance Immunosensor

*Kaijian Hou[1†], Pingsen Zhao[2†], Yongru Chen[3†], Guiping Li[4], Yu Lin[5], Danjie Chen[6], Dan Zhu[1], Zezhen Wu[1], Danchun Lian[7], Xiaojun Huang[7] and Jilin Li[7]**

[1] Department of Endocrine and Metabolic Diseases, Longhu Hospital, The First Affiliated Hospital of Shantou University Medical College, Shantou, China, [2] Department of Laboratory Medicine, Yuebei People's Hospital, Shantou University Medical College, Shaoguan, China, [3] Department of Emergency Intensive Care Unit (EICU), The First Affiliated Hospital of Shantou University Medical College, Shantou, China, [4] Department of Endocrine and Metabolic Diseases, The Third People's Hospital of Huizhou, Huizhou, China, [5] Department of Endocrinology, Jieyang People's Hospital, Jieyang, China, [6] Department of Endocrinology, Puning People's Hospital, Puning, China, [7] Department of Cardiology, The Second Affiliated Hospital of Shantou University Medical College, Shantou, China

OPEN ACCESS

Edited by:
Hassan Karimi-Maleh,
University of Electronic Science and Technology of China, China

Reviewed by:
Somaye Cheraghi,
Shahid Bahonar University of Kerman, Iran
Vahid Arabali,
Islamic Azad University Sari Branch, Iran

***Correspondence:**
Jilin Li
stlijilin@aliyun.com

[†]These authors have contributed equally to this work

Specialty section:
This article was submitted to Analytical Chemistry, a section of the journal Frontiers in Chemistry

Received: 28 April 2020
Accepted: 27 May 2020
Published: 07 July 2020

Citation:
Hou K, Zhao P, Chen Y, Li G, Lin Y, Chen D, Zhu D, Wu Z, Lian D, Huang X and Li J (2020) Rapid Detection of Bifidobacterium bifidum in Feces Sample by Highly Sensitive Quartz Crystal Microbalance Immunosensor. Front. Chem. 8:548. doi: 10.3389/fchem.2020.00548

In this work, a quartz crystal microbalance (QCM) sensor has been fabricated using immunoassay for sensitive determination of *Bifidobacterium bifidum*. Au nanoparticle has been used for amplifying sandwich assays. The proposed immunosensor exhibited a linear detection range between 10^3 and 10^5 CFU/mL with a limit of detection of 2.1 × 10^2 CFU/mL. The proposed immunosensor exhibited good selectivity for *B. bifidum* sensing with low cross reactivity for other foodborne pathogens such as *Lactobacillus acidophilus*, *Listeria monocytogenes*, and *Escherichia coli*. In addition, the proposed immunosensor has been successfully used for *B. bifidum* detection in feces samples and food samples. The frequency decreases of 12, 17, and 10 Hz were observed from the milk samples consisting of the mixtures of *L. acidophilus*, *L. monocytogenes*, and *E. coli*. The frequency decreases of 8, 15, and 7 Hz were observed from the feces samples consisting of the mixtures of *L. acidophilus*, *L. monocytogenes*, and *E. coli*.

Keywords: quartz crystal microbalance sensor, *Bifidobacterium bifidum*, immunosensor, Au nanoparticle, feces sample

INTRODUCTION

Under normal circumstances, the intestinal microorganisms in the human body form a relatively balanced state. Once the balance is damaged, it will lead to the imbalance of intestinal flora (Horie et al., 2017; Xue et al., 2018). Some intestinal microorganisms, such as *Clostridium perfringens*, overproduce in the intestinal tract and produce harmful substances such as ammonia, amines, hydrogen sulfide, manure, indole, nitrite, and bacterial toxins, which will further affect the health of the body (Ashida et al., 2018; Duranti et al., 2019). *Bifidobacterium bifidum* is an important intestinal beneficial microorganism. *B. bifidum*, as a physiological beneficial bacterium, has many important physiological functions for human health, such as biological barrier, anti-tumor, immune enhancement, improvement of gastrointestinal function, and anti-aging (Wang et al., 2016; Mauras et al., 2018; Din et al., 2020). *B. bifidum* can inhibit the growth of harmful bacteria, resist the infection of pathogenic bacteria, and synthesize vitamins needed by human body. It can promote

the absorption of minerals, produce organic acids such as acetic acid, propionic acid, butyric acid, and lactic acid to stimulate intestinal peristalsis and promote defecation. It can prevent constipation, purify the intestinal environment, decompose carcinogens, stimulate the human immune system, and improve the disease resistance (Gomi et al., 2018; Bondue et al., 2019; Speciale et al., 2019). It is of crucial importance to identify *B. bifidum* either in food and excreta. Although the normal microbiological isolation methods have been widely used for identifying bacterial strains, they are time-consuming (Yang et al., 2017; Cheng et al., 2018; Faraki et al., 2020). Therefore, the development of a fast method for *B. bifidum* identification is very essential for sample scanning.

The biosensor first immobilizes the bioactive components (enzyme, antibody, tissue, cell) on the transducer. When the target analyte is recognized by the immobilized bioactive components, the biochemical reaction can be immediately converted into a quantifiable electrical signal through the transducer (Fu et al., 2015; Huertas et al., 2019; Alamgholiloo et al., 2020; Fouladgar et al., 2020; Karimi-Maleh et al., 2020). Since the rise of biosensor in the late 1960s, after nearly half a century of development, biosensor has become a comprehensive and interdisciplinary field, which is used in food safety testing, environmental testing, and clinical diagnosis. QCM is a new type of micro mass sensor based on quartz crystal resonance, which was developed in 1960s. According to the piezoelectric effect of quartz crystal, the resonance frequency of quartz crystal will change with the mass of adsorbed material, and they are in a positive proportion (Bearzotti et al., 2017; Speller et al., 2017; Wang A. et al., 2017; Ayankojo et al., 2018). QCM immunosensor is a specific biosensor combining the high sensitivity of quartz crystal and the high specificity of immune response (Bearzotti et al., 2017; Speller et al., 2017; Wang L. et al., 2017; Ayankojo et al., 2018; Zhang et al., 2018). At present, QCM immunosensor has been widely used in clinical testing, food hygiene, environmental testing, as well as other fields of chemical analysis, and biological analysis. The detection of bacteria by QCM is a new and attractive Research Topic in electronic informatics and medicine (Muckley et al., 2016; Tai et al., 2016; Chen et al., 2018; Ding et al., 2018; Lal and Tiwari, 2018; Temel et al., 2019).

In this work, a QCM immunosensor has been developed for sensitive determination of *B. bifidum*. Monoclonal and polyclonal antibody have been used with the signal amplifying based on the Au nanoparticle. The proposed immunosensor exhibited a wide linear detection range with a low detection of limit. The sensitivity was enhanced when the antibody-conjugated Au nanoparticle. We believe the proposed assay was validated by cross reactivity investigation using *Lactobacillus acidophilus*, *Listeria monocytogenes* and *Escherichia coli*.

MATERIALS AND METHODS

Reagents, Bacterial Strains, and Instruments

Polyclonal antibody and mouse monoclonal antibody against *B. bifidum* were purchased from San Ying Biotechnology Co., Ltd (Wuhan, China). Mouse IgG, 11-mercaptoundecanoic acid (11-MUDA), bovine serum albumin (BSA), and ethanolamine hydrochloride were purchased from Linc-Bio Science Co., Ltd (Shanghai, China). Au colloidal (AuNPs) with 20 nm was purchased from Shenzhen Nano Tech Co., Ltd (Shenzhen, China). All other common regents were supplied by Sinopharm Chemical Reagent Co., Ltd (Shanghai, China) and used without further purification. A QCA922 quartz crystal analyzer (Princeton, USA) has been used for sensing with an Au coated chips. *Bifidobacterium bifidum* (*B. bifidum*), *L. acidophilus*, *L. monocytogenes*, and *E. coli* strains were purchased from American Type Culture Collection (ATCC, Manassas, VA). MRS (de Man, Rogosa, and Sharpe) and Bifidus Selective Medium (BSM) were used as growth media.

Sensor Chip Preparation

Piranha solution has been used for removing any impurities on the QCM Au chip. Then, the Au chip was immersed into 20 mM thiol (11-MUDA, prepared using ethanol) overnight for fabricating carboxy-terminated thiol layer on the Au surface. After rinse by ethanol and water, the Au chip was used for baseline correction under 10 mM PBS (pH 7.4). A mixture solution of EDC (0.4 M)-NHS (0.1 M) at ratio of 1:1 was then used for sensor activation. Then, different concentrations of polyclonal or mouse monoclonal antibodies against *B. bifidum* were immobilized on the Au chip. Then, capture and control were carried out by injected either polyclonal or mouse monoclonal antibodies and mouse IgG antibody. Then, BSA (50 μg/mL) and ethanolamine (1 M) were used for blocking and capping the sensors.

Detection of *B. bifidum*

Direct detection of *B. bifidum* was carried out by the injection of different concentrations of *B. bifidum* cells suspension prepared in PBS over above-mentioned polyclonal, mouse monoclonal, and mouse IgG antibodies fabricated sensor. The detection was carried out by comparing either *B. bifidum* captured polyclonal or mouse monoclonal antibodies with the control group.

The sandwich assay with antibody-AuNPs conjugation was prepared according to previous methods with some modifications (Uludag and Tothill, 2012). Typically, 0.1 mL of polyclonal or mouse monoclonal antibodies was added into 0.5 mL of AuNPs suspension with 2 h slow stirring. Then, 0.1 mL of BSA (10%) was introduced to the mixture with 2 h slow stirring. A centrifugation process was carried out to remove the excess of BSA and AuNPs. The detection process of using antibody-AuNPs conjugation was similar to the direct detection except the polyclonal and mouse monoclonal antibodies were replaced by the polyclonal-AuNPs and mouse monoclonal-AuNPs antibodies. Non-linear regression with four parameter logistic equations has been used for construing the calibration curves (Karpinski, 1990).

Selectivity Test

L. acidophilus, *L. monocytogenes*, and *E. coli* have been used for evaluating the specificity of the assay to *B. bifidum*. The selectivity test only carried out using antibody-AuNPs conjugation. The detection process of

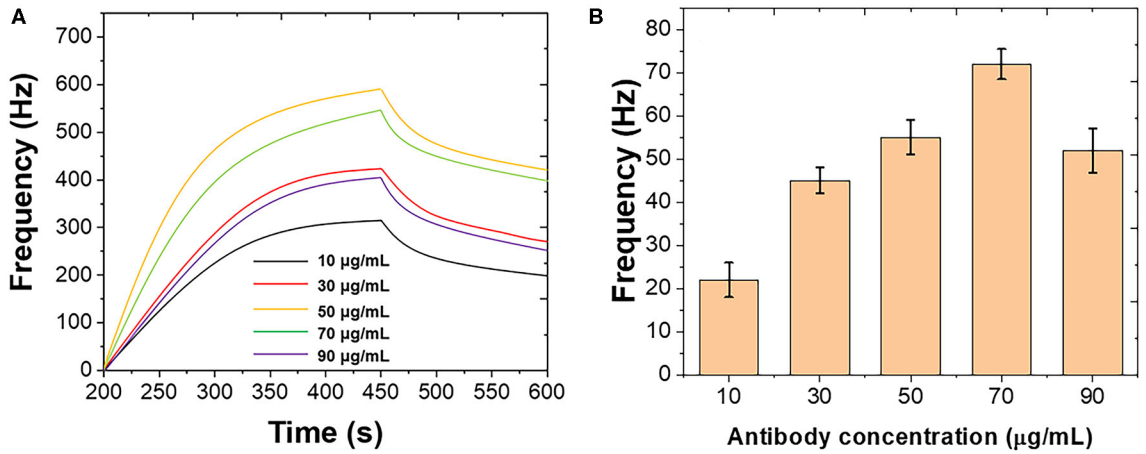

FIGURE 1 | (A) Frequencies recorded at QCM when different concentrations of polyclonal antibody immobilized on the Au chip surface. **(B)** Frequencies performance of QCM after introduction of *B. bifidum* after the immobilization of different concentrations of polyclonal antibody.

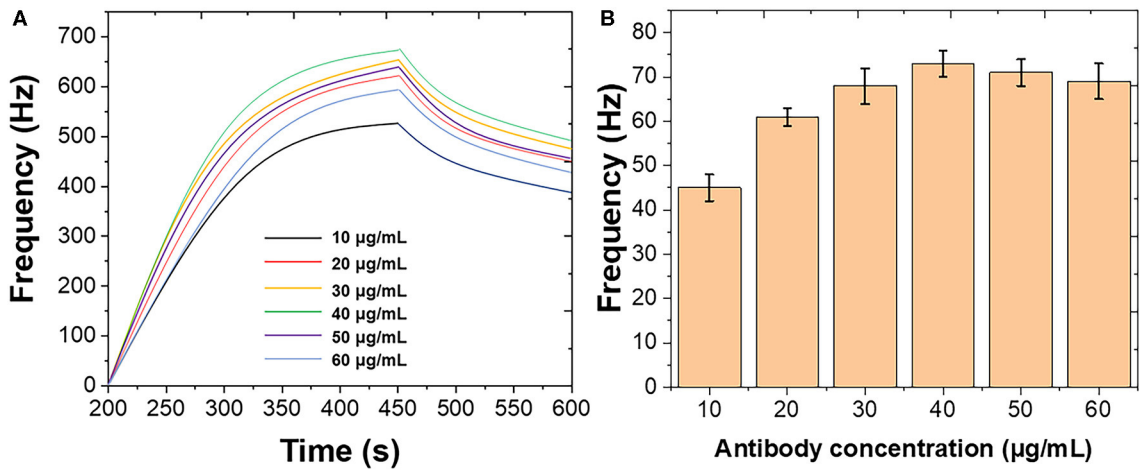

FIGURE 2 | (A) Frequencies recorded at QCM when different concentrations of mouse monoclonal antibody immobilized on the Au chip surface. **(B)** Frequencies performance of QCM after introduction of *B. bifidum* after the immobilization of different concentrations of mouse monoclonal antibody.

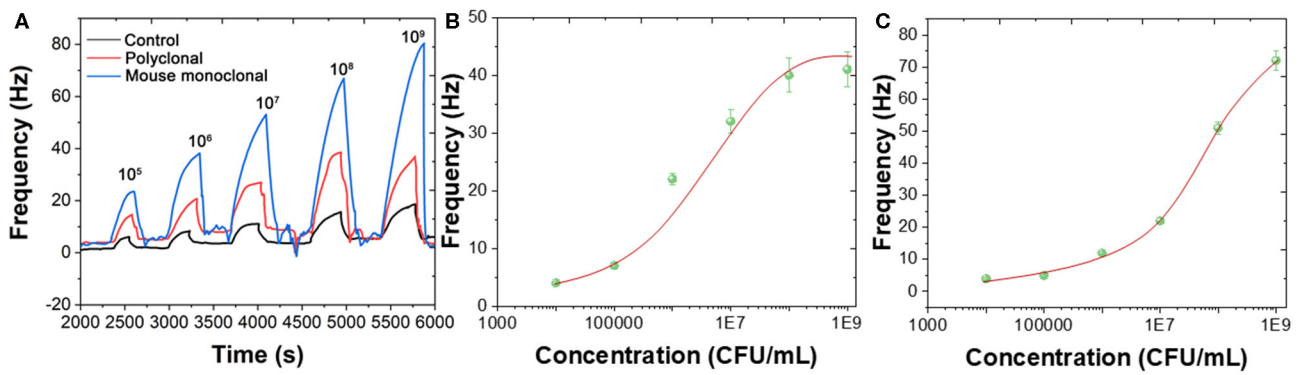

FIGURE 3 | (A) Frequencies recorded at QCM when different concentrations of *B. bifidum* introduced using polyclonal antibody immobilized sensor, mouse monoclonal antibody immobilized sensor, and mouse IgG antibody immobilized sensor. Plots of Frequency vs. concentrations of *B. bifidum* using **(B)** polyclonal antibody immobilized sensor and **(C)** mouse monoclonal antibody immobilized sensor.

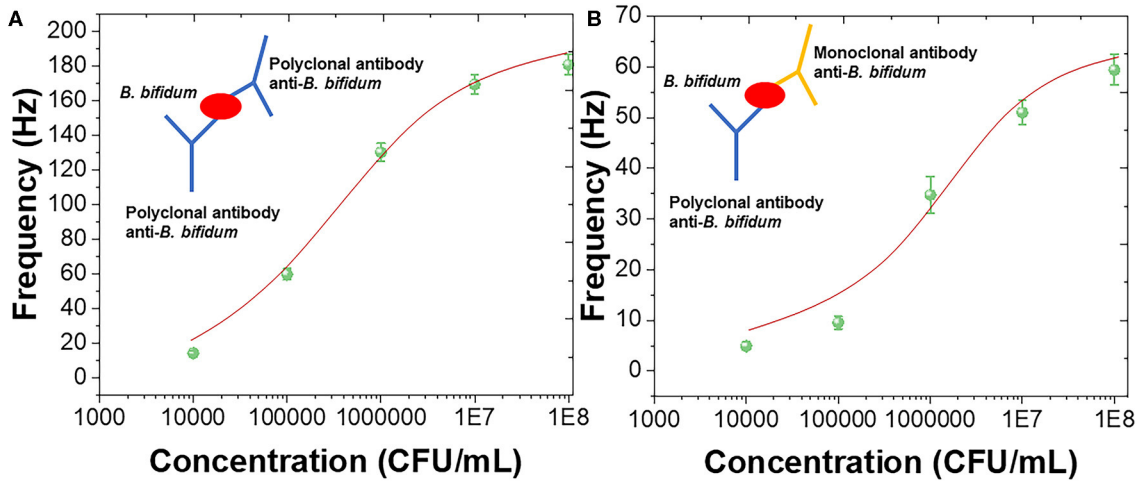

FIGURE 4 | Frequency vs. concentrations of *B. bifidum* using **(A)** polyclonal antibody and **(B)** mouse monoclonal antibody as the detection antibodies.

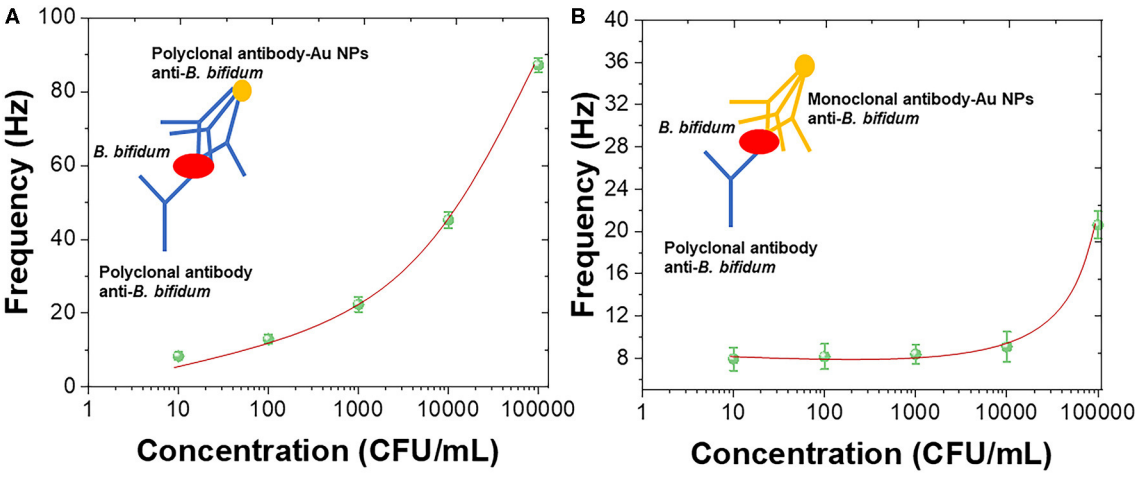

FIGURE 5 | Frequency vs. concentrations of *B. bifidum* using **(A)** polyclonal antibody-AuNPs conjugation and **(B)** mouse monoclonal antibody-AuNPs conjugation as the detection layers.

was similar to the above-mentioned protocol except replaced *B. bifidum* by *L. acidophilus*, *L. monocytogenes*, and *E. coli*.

Real Sample Preparation

The sensing of *B. bifidum* in milk and feces were investigated. Fresh milk was purchased form local supermarket. Feces samples were provided by The First Affiliated Hospital of Shantou University Medical College. For the sensing of *B. bifidum*, 1 g of real sample was dispersed using 50 mL PBS and transferred into a filtering stomacher bag. Then, 0.5 mL of the *B. bifidum* suspension was inoculated into both real samples at 37°C for 2 h. All liquid samples after preparation were directly used for sensing purpose.

RESULTS AND DISCUSSION

Figure 1 shows the optimization of the immobilization of polyclonal antibody on the Au chip surface. Different concentrations of polyclonal antibody were introduced using the standard *B. bifidum*. As shown in **Figure 1A**, the frequency was initially increased when the polyclonal antibody increased from 10 to 50 μg/mL. Then, the frequency decreased when the further increase of the polyclonal antibody. **Figure 1B** shows the binding response of *B. bifidum* at these concentrations of polyclonal antibody used. It can be seen that the best response was achieved when the concentration of polyclonal antibody at 50 μg/mL. Therefore, 50 μg/mL of polyclonal antibody has been selected in this study.

Figure 2 shows the optimization of the immobilization of mouse monoclonal antibody on the Au chip surface. Different

TABLE 1 | Sensing performance of the proposed QCM sensor with other reports.

Analyte	Linear detection range	Limit of detection	References
S. paratyphi	10^2-10^5 CFU/mL	1.7×10^2 CFU/mL	Fung and Wong, 2001
E. coli O157:H7	0–1 log CFU/mL	–	Guo et al., 2012
α-Amylase	–	1 μg/mL	Della Ventura et al., 2017
H5N1 avian influenza virus	2^{-4}-2^4 HAUs/50 μL	2^{-4} HAU/50 μL	Wang L. et al., 2017
Albumin	35–55 mg/mL	0.234 mg/mL	Pohanka, 2018a
S. aureus	–	5.18×10^8 CFU/mL	Pohanka, 2020
B. bifidum	10^3-10^5 CFU/mL	2.1×10^2 CFU/mL	This work

concentrations of mouse monoclonal antibody were introduced using the standard *B. bifidum*. As shown in **Figure 2A**, the frequency was initially increased when the mouse monoclonal antibody increased from 10 to 40 μg/mL. Then, the frequency decreased when the further increase of the mouse monoclonal antibody. **Figure 2B** shows the binding response of *B. bifidum* at these concentrations of mouse monoclonal antibody used. It can be seen that the best response was achieved when the concentration of mouse monoclonal antibody at 50 μg/mL. Therefore, 50 μg/mL of mouse monoclonal antibody has been selected in this study. Both studies suggested a high concentration of antibodies could result in a high steric hindrance, which lower the sensitivity of the sensor. Similar results were obtained for *Campylobacter jejuni* and *Vibrio harveyi* as well (Buchatip et al., 2010; Masdor et al., 2016).

B. bifidum can be directed detected using both polyclonal and mouse monoclonal antibodies immobilized Au chips. **Figure 3** shows the frequency changes when different concentrations of *B. bifidum* introduced in the QCM system in the presence of polyclonal antibody immobilized sensor, mouse monoclonal antibody immobilized sensor, and mouse IgG antibody immobilized sensor. As shown in **Figures 3B,C**, sigmoidal relationship between frequency change signals and concentrations of *B. bifidum* were obtained for both polyclonal antibody immobilized sensor and mouse monoclonal antibody immobilized sensor. The linear portions of the concentrations of *B. bifidum* between 10^5-10^7 and 10^6-10^8 CFU/mL were obtained for polyclonal antibody immobilized sensor and mouse monoclonal antibody immobilized sensor, respectively. The limit of detection (LOD) of polyclonal antibody immobilized sensor and mouse monoclonal antibody immobilized sensor can be calculated to be 3.0×10^5 and 3.0×10^6 CFU/mL, respectively. Since the polyclonal antibody immobilized sensor exhibited a lower LOD, it has been further used for construction of sandwich assay.

The sandwich assay has been constructed using polyclonal antibody against *B. bifidum*. The sandwich assay could improve sensitivity as well as prevented the false negative results (Amani et al., 2018). **Figure 4A** shows the sensing performance of using polyclonal antibody as the capture and detection antibody with schematic diagram. **Figure 4B** shows the sensing performance of using polyclonal antibody as the capture and mouse monoclonal antibody as the detection antibody with schematic diagram. It can be seen that both sandwich assay exhibited sigmoidal relationship between frequency and concentrations of *B. bifidum*. Linear portions of the concentrations of *B. bifidum* between 10^4-10^8 and 10^5-10^8 CFU/mL were observed using polyclonal antibody and mouse monoclonal antibody as the detection antibodies, respectively. The LOD of using polyclonal antibody and mouse monoclonal antibody as the detection antibodies can be calculated to be 2.0×10^4 and 3.3×10^5 CFU/mL, respectively. These results indicated that the sandwich assay could increase the sensitivity of the QCM sensor (Cervera-Chiner et al., 2018; Makhneva et al., 2018; Pohanka, 2020).

In order to further enhance the sensitivity of the QCM immunosensor, Au nanoparticles were introduced for forming the antibody-AuNPs conjugation (Zheng et al., 2015; Wang L. et al., 2017; Fu et al., 2020; Xu et al., 2020). **Figure 5A** shows the sensing performance of using polyclonal antibody-AuNPs conjugation as detection layer with schematic diagram. **Figure 5B** shows the sensing performance of using mouse monoclonal antibody-AuNPs conjugation as detection layer with schematic diagram. A linear portions of the concentrations of *B. bifidum* between 10^3 and 10^5 CFU/mL was observed using polyclonal antibody-AuNPs conjugation as detection layer. The LOD of using mouse monoclonal antibody-AuNPs conjugation can be calculated to be 2.1×10^2 CFU/mL. No clear linear portions of the concentrations of *B. bifidum* can be observed using mouse monoclonal antibody-AuNPs conjugation as detection layer. The results recorded in this study are very competitive with previous reports (Fung and Wong, 2001; Guo et al., 2012; Skládal, 2016; Della Ventura et al., 2017; Wang R. et al., 2017; Gao et al., 2018; Pohanka, 2018a,b, 2019). **Table 1** showed the sensing performance comparison.

The selectivity of the proposed QCM immunosensor has been tested by *L. acidophilus*, *L. monocytogenes*, and *E. coli*. As shown in **Figure 6**, <10% of cross reactivities were observed by *L. acidophilus*, *L. monocytogenes*, and *E. coli*, suggesting the proposed QCM immunosensor exhibited an excellent selectivity toward *B. bifidum*.

The applicability of the novel QCM immunosensor to determine *B. bifidum* in milk and feces were also carried out. For the detection of *B. bifidum* in real samples, the QCM sensor was firstly calibrated by the measurement in the absence of *B. bifidum*. As shown in **Figure 7**, frequency change of 3 and 7 Hz were recorded from the milk sample and feces sample

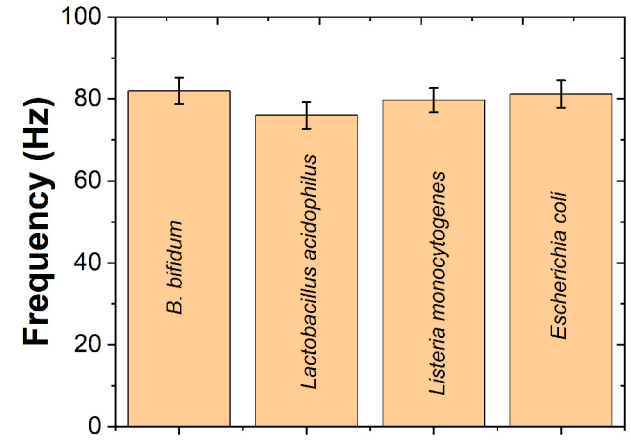

FIGURE 6 | Selectivity performance of the proposed QCM immunosensor toward *B. bifidum* sensing compared with that of the *Lactobacillus acidophilus*, *Listeria monocytogenes* and *Escherichia coli*.

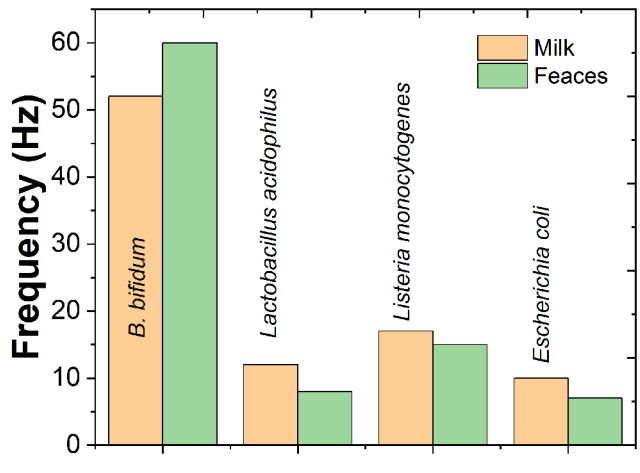

FIGURE 7 | Specific detection of 10^4 CFU/mL of *B. bifidum*, *Lactobacillus acidophilus*, *Listeria monocytogenes* and *Escherichia coli* inoculated on milk and feces samples.

containing 10^4 CFU/mL of *B. bifidum*, respectively. These results suggested the proposed QCM immunosensor could be used for real sample test. In addition, the frequency decreases of 12, 17, and 10 Hz were observed from the milk samples consisting of the mixtures of *L. acidophilus*, *L. monocytogenes*, and *E. coli*. The frequency decreases of 8, 15, and 7 Hz were observed from the feces samples consisting of the mixtures of *L. acidophilus*, *L. monocytogenes*, and *E. coli*. The results indicate that the QCM system developed in the present study is practical for the simultaneous enrichment and detection of viable *B. bifidum* in real samples.

CONCLUSION

In this work, an advanced piezoelectric biosensor-QCM system was proposed. In order to further enhance the sensitivity of the QCM immunosensor, Au nanoparticles were introduced for forming the antibody-AuNPs conjugation. A linear portions of the concentrations of *B. bifidum* between 10^3 and 10^5 CFU/mL was observed using polyclonal antibody-AuNPs conjugation as detection layer. The LOD of using mouse monoclonal antibody-AuNPs conjugation can be calculated to be 2.1×10^2 CFU/mL. The selectivity of the proposed QCM immunosensor has been tested by *L. acidophilus*, *L. monocytogenes*, and *E. coli*. The applicability of the novel QCM immunosensor to determine *B. bifidum* in milk and feces were tested. The frequency decreases of 12, 17, and 10 Hz were observed from the milk samples consisting of the mixtures of *L. acidophilus*, *L. monocytogenes*, and *E. coli*. The frequency decreases of 8, 15, and 7 Hz were observed from the feces samples consisting of the mixtures of *L. acidophilus*, *L. monocytogenes*, and *E. coli*.

DATA AVAILABILITY STATEMENT

The raw data supporting the conclusions of this article will be made available by the authors, without undue reservation.

ETHICS STATEMENT

Ethical review and approval was not required for the study on human participants in accordance with the local legislation and institutional requirements. Written informed consent from the participants was not required to participate in this study in accordance with the national legislation and the institutional requirements.

AUTHOR CONTRIBUTIONS

KH, YC, and JL contributed conception and design of the study. GL, YL, and DC conducted QCM experiments. DZ and ZW performed the statistical analysis. DL and XH did the characterizations. KH and YC wrote the manuscript. All authors contributed to the article and approved the submitted version.

REFERENCES

Alamgholiloo, H., Rostamnia, S., Hassankhani, A., Liu, X., Eftekhari, A., Hasanzadeh, A., et al. (2020). Formation and stabilization of colloidal ultra-small palladium nanoparticles on diamine-modified Cr-MIL-101: synergic boost to hydrogen production from formic acid. *J. Colloid Interface Sci.* 567, 126–135. doi: 10.1016/j.jcis.2020.01.087

Amani, J., Maleki, M., Khoshroo, A., Sobhani-Nasab, A., and Rahimi-Nasrabadi, M. (2018). An electrochemical immunosensor based on poly p-phenylenediamine and graphene nanocomposite for detection of neuron-specific enolase via electrochemically amplified detection. *Anal. Biochem.* 548, 53–59. doi: 10.1016/j.ab.2018.02.024

Ashida, H., Tanigawa, K., Kiyohara, M., Katoh, T., Katayama, T., and Yamamoto, K. (2018). Bifunctional properties and characterization of a novel sialidase with

esterase activity from *Bifidobacterium bifidum*. *Biosci. Biotechnol. Biochem.* 82, 2030–2039. doi: 10.1080/09168451.2018.1497944

Ayankojo, A. G., Reut, J., Boroznjak, R., Öpik, A., and Syritski, V. (2018). Molecularly imprinted poly (meta-phenylenediamine) based QCM sensor for detecting Amoxicillin. *Sens. Actuators B Chem.* 258, 766–774. doi: 10.1016/j.snb.2017.11.194

Bearzotti, A., Macagnano, A., Papa, P., Venditti, I., and Zampetti, E. (2017). A study of a QCM sensor based on pentacene for the detection of BTX vapors in air. *Sens. Actuators B Chem.* 240, 1160–1164. doi: 10.1016/j.snb.2016.09.097

Bondue, P., Crèvecoeur, S., Brose, F., Daube, G., Seghaye, M.-C., Griffiths, M. W., et al. (2019). Corrigendum: cell-free spent media obtained from *bifidobacterium bifidum* and Bifidobacterium crudilactis grown in media supplemented with 3′-Sialyllactose modulate virulence gene expression in *Escherichia coli* O157: H7 and *Salmonella Typhimurium*. *Front. Microbiol.* 10:2490. doi: 10.3389/fmicb.2019.02490

Buchatip, S., Ananthanawat, C., Sithigorngul, P., Sangvanich, P., Rengpipat, S., and Hoven, V. P. (2010). Detection of the shrimp pathogenic bacteria, Vibrio harveyi, by a quartz crystal microbalance-specific antibody based sensor. *Sens. Actuators B Chem.* 145, 259–264. doi: 10.1016/j.snb.2009.12.003

Cervera-Chiner, L., Juan-Borrás, M., March, C., Arnau, A., Escriche, I., Montoya, Á., et al. (2018). High fundamental frequency quartz crystal microbalance (HFF-QCM) immunosensor for pesticide detection in honey. *Food Control* 92, 1–6. doi: 10.1016/j.foodcont.2018.04.026

Chen, W., Deng, F., Xu, M., Wang, J., Wei, Z., and Wang, Y. (2018). GO/Cu2O nanocomposite based QCM gas sensor for trimethylamine detection under low concentrations. *Sens. Actuators B Chem.* 273, 498–504. doi: 10.1016/j.snb.2018.06.062

Cheng, R., Yao, J., Wan, Q., Guo, J., Pu, F., Shi, L., et al. (2018). Oral administration of *Bifidobacterium bifidum* TMC3115 to neonatal mice may alleviate IgE-mediated allergic risk in adulthood. *Benef. Microbes* 9, 815–828. doi: 10.3920/BM2018.0005

Della Ventura, B., Sakač, N., Funari, R., and Velotta, R. (2017). Flexible immunosensor for the detection of salivary α-amylase in body fluids. *Talanta* 174, 52–58. doi: 10.1016/j.talanta.2017.05.075

Din, A. U., Hassan, A., Zhu, Y., Zhang, K., Wang, Y., Li, T., et al. (2020). Inhibitory effect of *Bifidobacterium bifidum* ATCC 29521 on colitis and its mechanism. *J. Nutr. Biochem.* 79:108353. doi: 10.1016/j.jnutbio.2020.108353

Ding, X., Chen, X., Chen, X., Zhao, X., and Li, N. (2018). A QCM humidity sensor based on fullerene/graphene oxide nanocomposites with high quality factor. *Sens. Actuators B Chem.* 266, 534–542. doi: 10.1016/j.snb.2018.03.143

Duranti, S., Lugli, G. A., Milani, C., James, K., Mancabelli, L., Turroni, F., et al. (2019). *Bifidobacterium bifidum* and the infant gut microbiota: an intriguing case of microbe-host co-evolution. *Environ. Microbiol.* 21, 3683–3695. doi: 10.1111/1462-2920.14705

Faraki, A., Noori, N., Gandomi, H., Banuree, S. A. H., and Rahmani, F. (2020). Effect of Auricularia auricula aqueous extract on survival of *Lactobacillus acidophilus* La-5 and *Bifidobacterium bifidum* Bb-12 and on sensorial and functional properties of synbiotic yogurt. *Food Sci. Nutr.* 8, 1254–1263. doi: 10.1002/fsn3.1414

Fouladgar, M., Karimi-Maleh, H., Opoku, F., and Govender, P. P. (2020). Electrochemical anticancer drug sensor for determination of raloxifene in the presence of tamoxifen using graphene-CuO-polypyrrole nanocomposite structure modified pencil graphite electrode: theoretical and experimental investigation. *J. Mol. Liq.* 311:113314. doi: 10.1016/j.molliq.2020.113314

Fu, L., Yu, S., Thompson, L., and Yu, A. (2015). Development of a novel nitrite electrochemical sensor by stepwise in situ formation of palladium and reduced graphene oxide nanocomposites. *RSC Adv.* 5, 40111–40116. doi: 10.1039/C5RA02661J

Fu, L., Zheng, Y., Zhang, P., Zhang, H., Xu, Y., Zhou, J., et al. (2020). Development of an electrochemical biosensor for phylogenetic analysis of Amaryllidaceae based on the enhanced electrochemical fingerprint recorded from plant tissue. *Biosens. Bioelectron.* 159:112212. doi: 10.1016/j.bios.2020.112212

Fung, Y., and Wong, Y. (2001). Self-assembled monolayers as the coating in a quartz piezoelectric crystal immunosensor to detect Salmonella in aqueous solution. *Anal. Chem.* 73, 5302–5309. doi: 10.1021/ac010655y

Gao, K., Cui, S., and Liu, S. (2018). Development of an electrochemical quartz crystal microbalance-based immunosensor for C-reactive protein determination. *Int. J. Electrochem. Sci.* 13, 812–821. doi: 10.20964/2018.01.49

Gomi, A., Yamaji, K., Watanabe, O., Yoshioka, M., Miyazaki, K., Iwama, Y., et al. (2018). *Bifidobacterium bifidum* YIT 10347 fermented milk exerts beneficial effects on gastrointestinal discomfort and symptoms in healthy adults: a double-blind, randomized, placebo-controlled study. *J. Dairy Sci.* 101, 4830–4841. doi: 10.3168/jds.2017-13803

Guo, X., Lin, C.-S., Chen, S.-H., Ye, R., and Wu, V. C. (2012). A piezoelectric immunosensor for specific capture and enrichment of viable pathogens by quartz crystal microbalance sensor, followed by detection with antibody-functionalized gold nanoparticles. *Biosens. Bioelectron.* 38, 177–183. doi: 10.1016/j.bios.2012.05.024

Horie, M., Miura, T., Hirakata, S., Hosoyama, A., Sugino, S., Umeno, A., et al. (2017). Comparative analysis of the intestinal flora in type 2 diabetes and nondiabetic mice. *Exp. Anim.* 66, 405–416. doi: 10.1538/expanim.17-0021

Huertas, C. S., Calvo Lozano, O., Mitchell, A., and Lechuga, L. M. (2019). Advanced evanescent-wave optical biosensors for the detection of nucleic acids: an analytic perspective. *Front. Chem.* 7:724. doi: 10.3389/fchem.2019.00724

Karimi-Maleh, H., Karimi, F., Alizadeh, M., and Sanati, A. L. (2020). Electrochemical sensors, a bright future in the fabrication of portable kits in analytical systems. *Chem. Rec.* doi: 10.1002/tcr.201900092. [Epub ahead of print].

Karpinski, K. (1990). Optimality assessment in the enzyme-linked immunosorbent assay (ELISA). *Biometrics* 46, 381–390. doi: 10.2307/2531443

Lal, G., and Tiwari, D. (2018). Investigation of nanoclay doped polymeric composites on piezoelectric Quartz Crystal Microbalance (QCM) sensor. *Sens. Actuators B Chem.* 262, 64–69. doi: 10.1016/j.snb.2018.01.200

Makhneva, E., Farka, Z., Skládal, P., and Zajíčková, L. (2018). Cyclopropylamine plasma polymer surfaces for label-free SPR and QCM immunosensing of Salmonella. *Sens. Actuators B Chem.* 276, 447–455. doi: 10.1016/j.snb.2018.08.055

Masdor, N. A., Altintas, Z., and Tothill, I. E. (2016). Sensitive detection of Campylobacter jejuni using nanoparticles enhanced QCM sensor. *Biosens. Bioelectron.* 78, 328–336. doi: 10.1016/j.bios.2015.11.033

Mauras, A., Chain, F., Faucheux, A., Ruffié, P., Gontier, S., Ryffel, B., et al. (2018). A new Bifidobacteria expression system (BEST) to produce and deliver interleukin-10 in *Bifidobacterium bifidum*. *Front. Microbiol.* 9:3075. doi: 10.3389/fmicb.2018.03075

Muckley, E. S., Lynch, J., Kumar, R., Sumpter, B., and Ivanov, I. N. (2016). PEDOT: PSS/QCM-based multimodal humidity and pressure sensor. *Sens. Actuators B Chem.* 236, 91–98. doi: 10.1016/j.snb.2016.05.054

Pohanka, M. (2018a). Piezoelectric immunosensor for the determination of immunoglobulin G. *Int. J. Electrochem. Sci.* 13, 8784–8791. doi: 10.20964/2018.09.01

Pohanka, M. (2018b). The determination of human albumin by a quartz crystal microbalance immunosensor. *Int. J. Electrochem. Sci.* 13, 8471–8480. doi: 10.20964/2018.09.14

Pohanka, M. (2019). Piezoelectric immunosensor for the determination of c-reactive protein. *Int. J. Electrochem. Sci.* 14, 8470–8478. doi: 10.20964/2019.09.02

Pohanka, M. (2020). QCM immunosensor for the determination of *Staphylococcus aureus* antigen. *Chem. Pap.* 74, 451–458. doi: 10.1007/s11696-019-00889-5

Skládal, P. (2016). Piezoelectric biosensors. *TrAC Trends Anal. Chem.* 79, 127–133. doi: 10.1016/j.trac.2015.12.009

Speciale, I., Verma, R., Di Lorenzo, F., Molinaro, A., Im, S.-H., and de Castro, C. (2019). *Bifidobacterium bifidum* presents on the cell surface a complex mixture of glucans and galactans with different immunological properties. *Carbohydr. Polym.* 218, 269–278. doi: 10.1016/j.carbpol.2019.05.006

Speller, N. C., Siraj, N., McCarter, K. S., Vaughan, S., and Warner, I. M. (2017). QCM virtual sensor array: vapor identification and molecular weight approximation. *Sens. Actuators B Chem.* 246, 952–960. doi: 10.1016/j.snb.2017.02.042

Tai, H., Zhen, Y., Liu, C., Ye, Z., Xie, G., Du, X., et al. (2016). Facile development of high performance QCM humidity sensor based on protonated polyethylenimine-graphene oxide nanocomposite thin film. *Sens. Actuators B Chem.* 230, 501–509. doi: 10.1016/j.snb.2016.01.105

Temel, F., Erdemir, S., Ozcelik, E., Tabakci, B., and Tabakci, M. (2019). Rapid and real-time detection of arginine enantiomers by QCM sensor having a Calix [4] arene receptor bearing asymmetric centers. *Talanta* 204, 172–181. doi: 10.1016/j.talanta.2019.05.093

Uludag, Y., and Tothill, I. E. (2012). Cancer biomarker detection in serum samples using surface plasmon resonance and quartz crystal microbalance sensors with nanoparticle signal amplification. *Anal. Chem.* 84, 5898–5904. doi: 10.1021/ac300278p

Wang, A., Wang, C., Fu, L., Wong-Ng, W., and Lan, Y. (2017). Recent advances of graphitic carbon nitride-based structures and applications in catalyst, sensing, imaging, and LEDs. *Nano-Micro Lett.* 9:47. doi: 10.1007/s40820-017-0148-2

Wang, G.-H., Chen, C.-Y., Lin, C.-P., Huang, C.-L., Lin, C., Cheng, C.-Y., et al. (2016). Tyrosinase inhibitory and antioxidant activities of three *Bifidobacterium bifidum*-fermented herb extracts. *Ind. Crops Prod.* 89, 376–382. doi: 10.1016/j.indcrop.2016.05.037

Wang, L., Wang, Z., Xiang, Q., Chen, Y., Duan, Z., and Xu, J. (2017). High performance formaldehyde detection based on a novel copper (II) complex functionalized QCM gas sensor. *Sens. Actuators B Chem.* 248, 820–828. doi: 10.1016/j.snb.2016.12.015

Wang, R., Wang, L., Callaway, Z. T., Lu, H., Huang, T. J., and Li, Y. (2017). A nanowell-based QCM aptasensor for rapid and sensitive detection of avian influenza virus. *Sens. Actuators B Chem.* 240, 934–940. doi: 10.1016/j.snb.2016.09.067

Xu, Y., Lu, Y., Zhang, P., Wang, Y., Zheng, Y., Fu, L., et al. (2020). Infrageneric phylogenetics investigation of Chimonanthus based on electroactive compound profiles. *Bioelectrochemistry* 133:107455. doi: 10.1016/j.bioelechem.2020.107455

Xue, M., Ji, X., Liang, H., Liu, Y., Wang, B., Sun, L., et al. (2018). The effect of fucoidan on intestinal flora and intestinal barrier function in rats with breast cancer. *Food Funct.* 9, 1214–1223. doi: 10.1039/C7FO01677H

Yang, D., Wu, X., Yu, X., He, L., Shah, N. P., and Xu, F. (2017). Mutual growth-promoting effect between *Bifidobacterium bifidum* WBBI03 and *Listeria monocytogenes* CMCC 54001. *J. Dairy Sci.* 100, 3448–3462. doi: 10.3168/jds.2016-11804

Zhang, D., Wang, D., Zong, X., Dong, G., and Zhang, Y. (2018). High-performance QCM humidity sensor based on graphene oxide/tin oxide/polyaniline ternary nanocomposite prepared by in-situ oxidative polymerization method. *Sens. Actuators B Chem.* 262, 531–541. doi: 10.1016/j.snb.2018.02.012

Zheng, Y., Fu, L., Han, F., Wang, A., Cai, W., Yu, J., et al. (2015). Green biosynthesis and characterization of zinc oxide nanoparticles using Corymbia citriodora leaf extract and their photocatalytic activity. *Green Chem. Lett. Rev.* 8, 59–63. doi: 10.1080/17518253.2015.1075069

Conflict of Interest: The authors declare that the research was conducted in the absence of any commercial or financial relationships that could be construed as a potential conflict of interest.

frontiers in Chemistry

ORIGINAL RESEARCH
published: 15 July 2020
doi: 10.3389/fchem.2020.00503

Glucose Oxidase/Nano-ZnO/Thin Film Deposit FTO as an Innovative Clinical Transducer: A Sensitive Glucose Biosensor

Padideh Naderi Asrami[1], *Parviz Aberoomand Azar*[1]*, *Mohammad Saber Tehrani*[1] and *Sayed Ahmad Mozaffari*[2]

[1] Department of Chemistry, Science and Research Branch, Islamic Azad University, Tehran, Iran, [2] Thin Layer and Nanotechnology Laboratory, Institute of Chemical Technology, Iranian Research Organization for Science and Technology (IROST), Tehran, Iran

In the present research, a new biocompatible electrode is proposed as a rapid and direct glucose biosensing technique that improves on the deficiencies of fast clinical devices in laboratory investigations. Nano-ZnO (nanostructured zinc oxide) was sputtered by reactive direct current magnetron sputtering system on a precovered fluorinated tin oxide (FTO) conductive layer. Spin-coated polyvinyl alcohol (PVA) at optimized instrumental deposition conditions was applied to prepare the effective medium for glucose oxidase enzyme (GOx) covalent immobilization through cyanuric chloride (GOx/nano-ZnO/PVA/FTO). The electrochemical behavior of glucose on the fabricated GOx/nano-ZnO/PVA/FTO biosensor was investigated by *I-V* techniques. In addition, field emission scanning electron microscopy and electrochemical impedance spectroscopy were applied to assess the morphology of the modified electrode surface. The *I-V* results indicated good sensitivity for glucose detection (0.041 mA per mM) within 0.2–20 mM and the limit of detection was 2.0 μM. We believe that such biodevices have good potential for tracing a number of biocompounds in biological fluids along with excellent accuracy, selectivity, and precise analysis. The fast response time of the fabricated GOx/nano-ZnO/PVA/FTO biosensor (less than 3 s) could allow most types of real-time analysis.

Keywords: covalent GOx immobilization, direct current magnetron sputtering, disposable glucose biosensor, medicinal chemistry, clinical chemistry

OPEN ACCESS

Edited by:
Hassan Karimi-Maleh, University of Electronic Science and Technology of China, China

Reviewed by:
Vahid Arabali, Islamic Azad University Sari Branch, Iran
Mehdi Baghayeri, Hakim Sabzevari University, Iran
Yasin Orooji, Nanjing Forestry University, China

***Correspondence:**
Parviz Aberoomand Azar
parvizaberoomand@gmail.com

Specialty section:
This article was submitted to Electrochemistry, a section of the journal Frontiers in Chemistry

Received: *07 April 2020*
Accepted: *15 May 2020*
Published: *15 July 2020*

Citation:
Naderi Asrami P, Aberoomand Azar P, Saber Tehrani M and Mozaffari SA (2020) Glucose Oxidase/Nano-ZnO/Thin Film Deposit FTO as an Innovative Clinical Transducer: A Sensitive Glucose Biosensor. Front. Chem. 8:503. doi: 10.3389/fchem.2020.00503

INTRODUCTION

During recent decades, the determination of blood glucose level has become essential and routine because of the rapid increase in the incidence of diabetes mellitus and associated diseases. Hypoglycemia (low blood glucose level) and hyperglycemia (high blood glucose level) seriously affect the daily life of patients with diabetes (Gavin, 2007; Shabnam et al., 2017; Jedrzak et al., 2018a,b; Salek-Maghsoudi et al., 2018).

Diabetes, which is characterized by persistent hyperglycemia in clinical medicine, is one of the most important causes of death and amputation, affecting over 100 million people worldwide (Rivas et al., 2007; Zhu et al., 2016; Anderson et al., 2017). Some routine clinical laboratory checks for

glucose levels, which have become an integral part of diabetes care, suffer from several limitations in accuracy, such as strip manufacturing variation, strip storage, and aging. In addition, the accuracy might be affected by environmental factors, such as temperature and altitude, and human factors, such as improper hand washing, altered hematocrit, and naturally occurring interfering substances. Last but not least, exogenous interfering substances may cause errors in the systematic measurement of blood glucose. Consequently, diabetes research centers, clinical laboratories, and medical equipment manufacturers all around the world are working toward the development and design of advanced and domestic glucose-checking devices with improved accuracy (Baghayeri, 2015; Baghayeri et al., 2017, 2020). Plenty of methods have therefore been proposed to monitor blood glucose concentration (Mozaffari et al., 2014; Rahmanian and Mozaffari, 2015; Rahmanian et al., 2015).

Among the most successful and reliable diagnostic devices are the glucose electrochemical biosensors that determine the glucose blood level based on glucose oxidase (GOx) using amperometric, impedimetric, conductometric, and potentiometric techniques. Thus, both a steady platform for enzyme immobilization and electroanalytical characterization of the fabricated sensor can guarantee the accuracy of the glucose level investigation (Miwa et al., 1994; Morikawa et al., 2002; Li et al., 2008; Wang et al., 2008; Bollella et al., 2017). There are many medical research reports on enzymatic glucose measurements based on the best-nanostructured metal oxide textures and composites (Karimi-Maleh et al., 2019c). Some nanostructured metal oxides such as zinc oxide (ZnO) have been studied in recent years owing to their strong ability to facilitate electron transfer between the electrode and the surface active site (Aini et al., 2015; Baghizadeh et al., 2015; Gallay et al., 2016; Zhao et al., 2016; Chung et al., 2017; Israr-Qadir et al., 2017; Moghaddam, 2017; Zhou et al., 2017; Karimi-Maleh et al., 2019a,c; Miraki et al., 2019; Shamsadin-Azad et al., 2019; Karimi-Maleh and Arotiba, 2020). The application of nanomaterials, especially nanoparticles, in various industries and technologies, and especially in the design of electrochemical sensors, has been well-studied (Rayati and Malekmohammadi, 2016; Dehhaghi et al., 2019; Hassandoost et al., 2019; Hosseini et al., 2019; Karimi-Maleh et al., 2019b, 2020a,b,c; Malekmohammadi et al., 2019). The direct current (DC) magnetron sputtering system is the main strategy for the production of nanostructured ZnO because of its strong capacity created by various materials for fabrication of thin films of metals, alloys, and compounds with thicknesses up to 5 p.m.

The advantages of deposition by DC magnetron sputtering system have been documented in many research papers; for example, its high purity; high adhesion film production; proper coverage by high deposition rates; deposition of any metals, alloys, or compounds; suitable porosity; and preparation of considerable volume-to-surface ratios have been intensely discussed in the literature (Panzner et al., 1985).

In this study, we develop a powerful glucose biosensor using a covalent immobilization strategy of GOx on a ZnO–polyvinyl alcohol (PVA) composite film (through cyanuric chloride) that enhances enzyme stability and the biological activity of the biomolecule. The PVA was initially deposited on fluorinated tin oxide (FTO) by a spin-coating technique (PVA/FTO), followed by DC magnetron sputtering to fabricate a nano-ZnO/PVA/FTO electrode.

The spin coating technique employed for PVA deposition is a procedure used for homogeneous thin film preparation on smooth substrates. Compared with other preparation methods, the spin coating method for the deposition of films has some significant advantages, e.g., low cost of materials and simplicity of technological runs and equipment. In this work, PVA with hydroxyl functional groups exposed on the sensor surface and many other benefits such as water-soluble organic additive activity and an electrostatic repulsive layer for anionic interference was applied to achieve ZnO/PVA nanostructures that can be used as excellent reactive sites for GOx immobilization via covalent linking.

To the best of our knowledge, for the first time, glucose determination was carried out by a unique voltammetric method using a GOx/nano-ZnO/PVA/FTO biosensor, which demonstrated a powerful ability for real sample analysis with a low detection limit (2.0 μM).

EXPERIMENTAL

Chemicals

The FTO (resistivity = 15 Ω cm^{-2}) was purchased from Dyesol Company and used for fabrication of the working electrode. The FTO was washed with deionized (DI; resistivity = 18 MΩ) water, a detergent solution, and ethanol in an ultrasonic bath. PVA (MW 88 000–97 000) was purchased from Alfa Aesar Company. D(+)-Glucose was purchased from Merck Company. GOx (G6125-10KU from *Aspergillus niger*, type II, 15 000–25 000 units g^{-1}) was purchased from Sigma-Aldrich. K_2HPO_4 and KH_2PO_4 were purchased from Sigma-Aldrich Co. and used for the preparation of phosphate-buffered saline (PBS; 7.4). A 100-unit solution of GOx in PBS (0.1 M, pH 7.4) was prepared as the stock solution of enzyme and kept at 4°C. A low-concentration glucose solution was freshly prepared for each measurement.

Apparatus

In this work, a Mettler Toledo TGA 850 instrument was used for thermogravimetric analysis (TGA). Surface analysis of the fabricated sensor after the coating process was carried out by means of field emission scanning electron microscopy (FE-SEM) (TESCAN, Czech Republic). A spectrophotometer (Lambda 25 UV-Vis; PerkinElmer, USA) was used for evaluation of the absorbance factor. A DC magnetron sputtering system (The Nanostructured Coatings Co., Tehran, Iran) was used to fabricate nano-ZnO thin films with a 99.999% pure ZnO target under different experimental conditions. A 302N Autolab PGSTAT (Eco Chemie, The Netherlands) machine was used for all electrochemical assessments. GOx/nano-ZnO/PVA/FTO (A = 1 cm^2), saturated calomel electrode (SCE), and Pt electrode were used as the working, reference, and counter electrodes, respectively. A 10 mV peak-to-peak AC amplitude was selected for electrochemical impedance spectroscopy (EIS) assessment

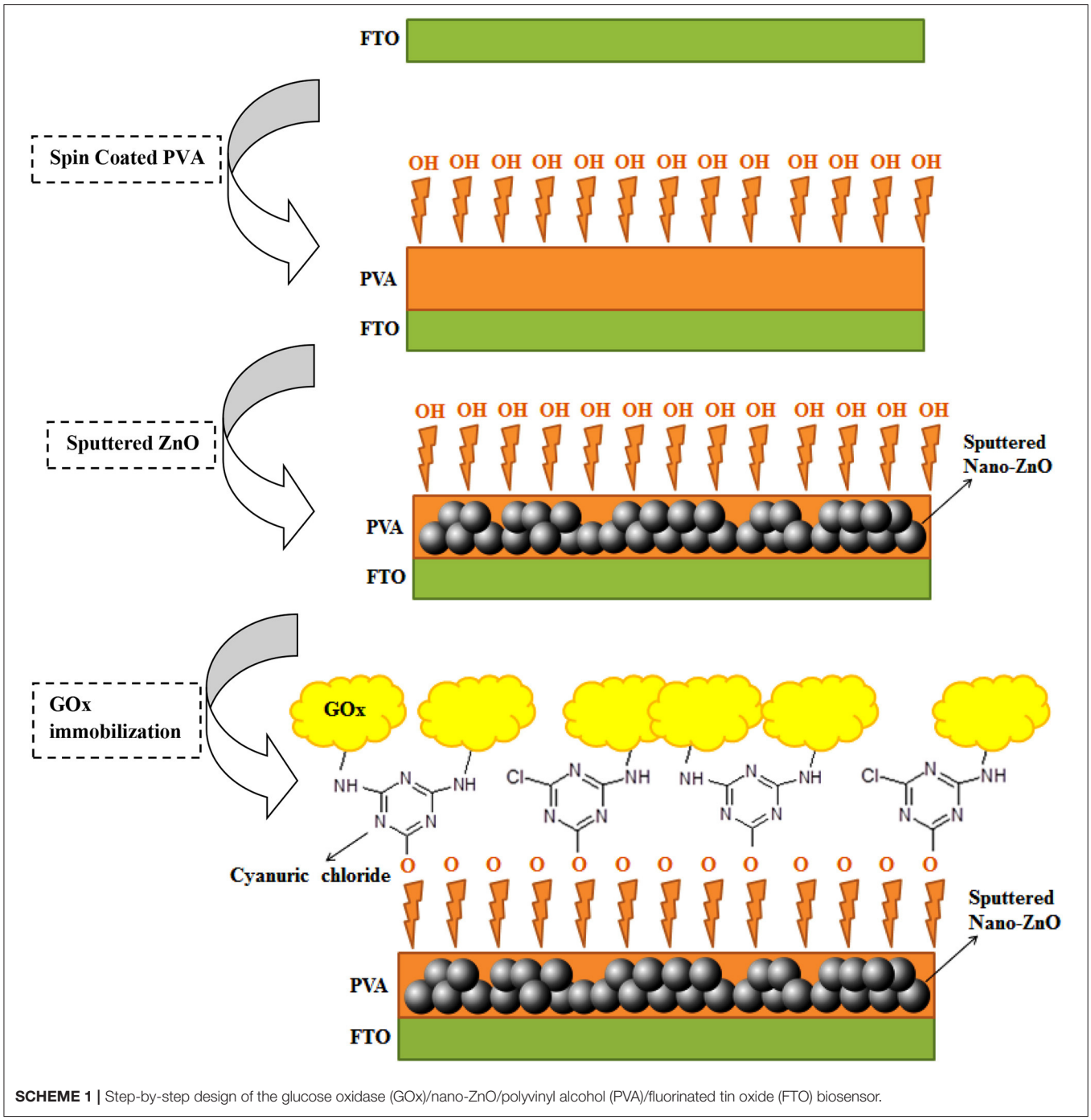

SCHEME 1 | Step-by-step design of the glucose oxidase (GOx)/nano-ZnO/polyvinyl alcohol (PVA)/fluorinated tin oxide (FTO) biosensor.

with scanning frequencies ranging from 100 kHz to 10 MHz using the Zview/Zplot software (Macdonald et al., 1982).

RESULTS AND DISCUSSION

Fabrication of the GOx/nano-ZnO/PVA/FTO Electrode

The surface modification and engineering of the GOx/nano-ZnO/PVA/FTO electrode is shown in **Scheme 1**. The step-by-step surface engineering process will be discussed in more detail below. The current–voltage *(I-V)* results confirm successful modification of FTO by GOx and the nano-ZnO/PVA composite.

Fabrication of PVA/FTO by Spin Coating

Because of its high electron density, affording further electrical conductivity to the ZnO film transducer and water solubility, PVA was selected as the substrate for fabrication of the biosensor. First, we optimized the spin coating parameters, such as spinning speed, spinning duration, solution volume, and PVA content, for the electrical resistivity. The resistivity of a PVA/FTO surface

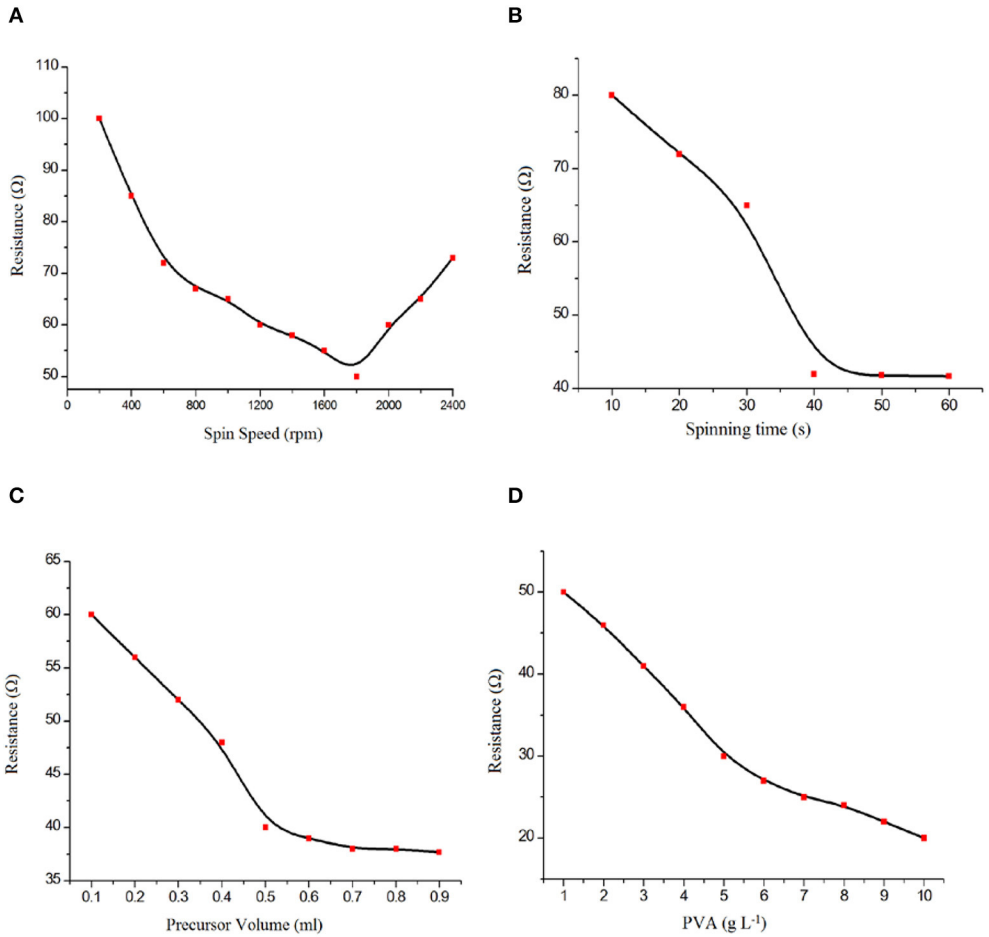

FIGURE 1 | Effect of **(A)** spin speed, **(B)** spinning time, **(C)** precursor volume, and **(D)** polyvinyl alcohol (PVA) content on PVA/fluorinated tin oxide (FTO) characteristics.

fabricated by the spin coating technique was measured by using a four-point collinear probe in the air. Four sets of deposition parameters—spinning speed (200–2,400 rpm), spinning duration (10–60 s), solution volume (0.1–0.9 mL), and precursor PVA content (1–10 g L^{-1})—were investigated in order to obtain a uniform and suitable thin film. In each set of samples, only one of the parameters mentioned above was varied while the other parameters were kept constant. Spinning speed has been shown to have substantial effects on many physical properties, such as film thickness and mechanical properties. The spin coating conditions were chosen to be optimal for PVA thin film formation with the best electrical resistivity in this work.

Figure 1A shows the relation between the PVA thin film electrical resistivity and the spinning speed (200–2,400 rpm). Increasing the spinning speed to 1,750 rpm results in a decrease in the electrical resistivity of the thin film. Decreasing the film thickness by decreasing the spinning speed to 1,750 rpm results in a uniform PVA structure while increasing the spinning speed to 2,500 rpm results in a non-uniform PVA thin film because of the high centrifugal force. The result shows a non-linear relationship between the spinning speed and electrical resistivity of the thin film. A spinning speed of 1,750 rpm was selected as the optimum spinning speed.

Figure 1B shows that the electrical resistivity is improved by an increase in spinning duration from 10 to 40 s, while there was no noticeable change after 40 s. During the first few seconds of the spin coating process, a small portion of the substrate is covered by PVA as an electrically conductive layer. After 40 s, the spinning duration did not have any significant effect on the electrode resistance. Therefore, the optimum spinning time was selected as 40 s.

Figure 1C shows that the resistivity is decreased with an increase in the volume of the deposition solution from 0.1 to 0.7 mL, while there was no noticeable change after 0.9 mL. Thus, 0.7 mL was selected as the optimum volume of the solution for economic reasons.

The precursor PVA content is an effective parameter in the spin coating process. The PVA content not only results in a thin film with lower electrical resistivity but also prepares suitable –OH groups in the substrate for GOx covalent immobilization. By increasing the amount of PVA content in the precursor, a lower electrical resistivity of the thin film has been observed

(**Figure 1D**). Furthermore, the precursor PVA content has a significant effect on GOx immobilization, so a precursor concentration of 10 g L^{-1} was selected.

In summary, 1,750 rpm (spinning speed), 40 s (spinning duration), 0.7 mL (the volume of solution), and 10 g L^{-1} (PVA content) were selected as the optimum conditions for the spin coating procedure.

Fabrication of nano-ZnO/PVA/FTO

The nano-ZnO was deposited on the surface of a PVA/FTO electrode using reactive DC magnetron sputtering under an Ar: O_2 gas atmosphere while the resistivity was measured by a four-point collinear probe in the air. The Zn cathode plate was bombarded by Ar^+ ions generated in the glow discharge plasma placed in front of the Zn target in the evacuated sputtering chamber. A specific amount of O_2 gas is used for metal-oxide fabrication in a reactive sputtering process.

The deposited ZnO thin film was prepared by chemical reaction of Zn atoms from the target surface and O_2 reactive gas during reactive sputtering. The metal–metal oxide composition of the nano-ZnO film can be determined by control of the pressure of Ar and O_2 gases (Kelly and Arnell, 2000; Baghriche et al., 2012; Bijad et al., 2013; Yao and Lu, 2013; Mozaffari et al., 2014).

The optimum conditions in the synthesis procedure were obtained by varying the sputtering experiment conditions, such as the sputtering power (100–400 W); deposition time (1–25 min); distance between the target and substrate (4–10 cm); mixed gas pressure (total gas pressure from 1×10^{-3} to 1×10^{-2} Torr); and Ar: O_2 gas flow ratio (1:1–8:1 sccm/min) in order to obtain a very uniform ZnO thin film.

According to the data reported in **Figure 2A**, the DC sputtering power showed strong effects on the fabrication of the ZnO thin film. Therefore, optimization of the sputtering conditions to form nano-ZnO thin films with the lowest electrical resistivity is necessary.

As can be observed, increasing or reducing the DC sputtering power affects the amount of nano-ZnO sputtered atoms from the target to the substrate. Hence, a lower DC sputtering power leads to a lower amount of Zn sputtered atoms and increases the chance of ZnO formation, which results in higher electrical resistivity of the thin film. However, a higher DC sputtering power of up to 250 watts produced higher amounts of non-reacted Zn sputtered atoms. Additionally, oxygen deficiency in the deposited film increases and leads to lower electrical resistivity. The probable reality behind these comments could be that the PVA thin film is degraded by high-energy particle bombardment due to the excessive DC sputtering power supply, which resulted in a non-uniform thin film.

The deposition time was selected as the effective factor for obtaining a uniform nano-ZnO thin film. Lower electrical resistivity of the thin film is observed by increasing the time of deposition from 1 to 10 min (**Figure 2B**). With the increase in deposition time and improvement in the thickness of the thin film, we observed low thin film resistivities that are useful for this type of sensor.

The effect of distance between the target and substrate in the range 4–7 cm on the electrical resistivity of the nano-ZnO thin film is shown in **Figure 2C**. Because of the lower amount of nano-ZnO particles deposited, we detected an improvement in electrical resistivity of the film by increasing the distance between the target and the substrate from 4 to 7 cm. Also, thin film defection by highly energized Ar^+ occurred. As shown in **Figure 2C**, a distance of 7 cm between the target and the substrate was selected as the best condition in this study.

The porosity and physical homogeneity of the ZnO thin film is directly affected by the total gas pressure during plasma formation (**Figure 2D**). This factor can be affected by the deposition rate, which therefore also helps to create a more homogeneous thin film. In this case, a total gas pressure in the range of 1×10^{-3} to 1×10^{-2} Torr was tested and, according to the results obtained, 1×10^{-3} Torr was selected as the optimum condition for total gas pressure.

The Ar: O_2 gas flow ratio was selected as another factor affecting the preparation of a ZnO thin film with lower electrical resistivity in a reactive DC magnetron sputtering system. By decreasing the oxygen ratio in the gas flow, we detected a lower electrical resistivity of the thin film that is useful for the fabrication of GOx/nano-ZnO/PVA/FTO (**Figure 2E**). This term clarified the important role of the oxygen gas flow ratio in Zn: ZnO phase formation in thin film preparation.

According to the obtained results, 250 W (sputtering power), 10 min (deposition time), 7 cm (distance between target and substrate), 4×10^{-3} Torr (total pressure), and 8: 1 (Ar: O_2 gas flow ratio) were selected as the optimum conditions for the preparation of a uniform ZnO thin film.

Fabrication of GOx/nano-ZnO/PVA/FTO Biosensor

The bonding status of the biomolecule to the transducer matrix is one of the significant factors in biosensor fabrication. One serious problem is the leaching of the biomolecule out of the surface during the preparation process.

Therefore, a new design based on the reaction between cyanuric chloride as the anchor molecule and PVA as the source of free –OH groups was used. This design helps GOx to be covalently attached to the anchor by its $–NH_2$ groups (**Scheme 1**). The nano-ZnO/PVA/FTO electrode was dipped into cyanuric chloride ethanolic solution (100 g L^{-1}) for 2 h with stirring. After this step, the amplified sensor was put into 0.1 M PBS (pH 7.4) containing 100 units of GOx for 4.0 h with stirring. Step-by-step fabricated biosensor monitoring was achieved by EIS and cyclic voltammetry (CV) techniques. The *I-V* technique was also applied to the fabricated glucose biosensor (Ansari et al., 2008; Mahadeva and Kim, 2011; Rahmanian and Mozaffari, 2015).

Morphological Characterization of GOx/nano-ZnO/PVA/FTO

The surface morphology of ZnO/PVA/FTO and also the size distribution histogram of ZnO nanoparticles was investigated by FE-SEM. The results are presented in **Figures 3A–C**. The results confirm a good and uniform distribution of ZnO/PVA as a film

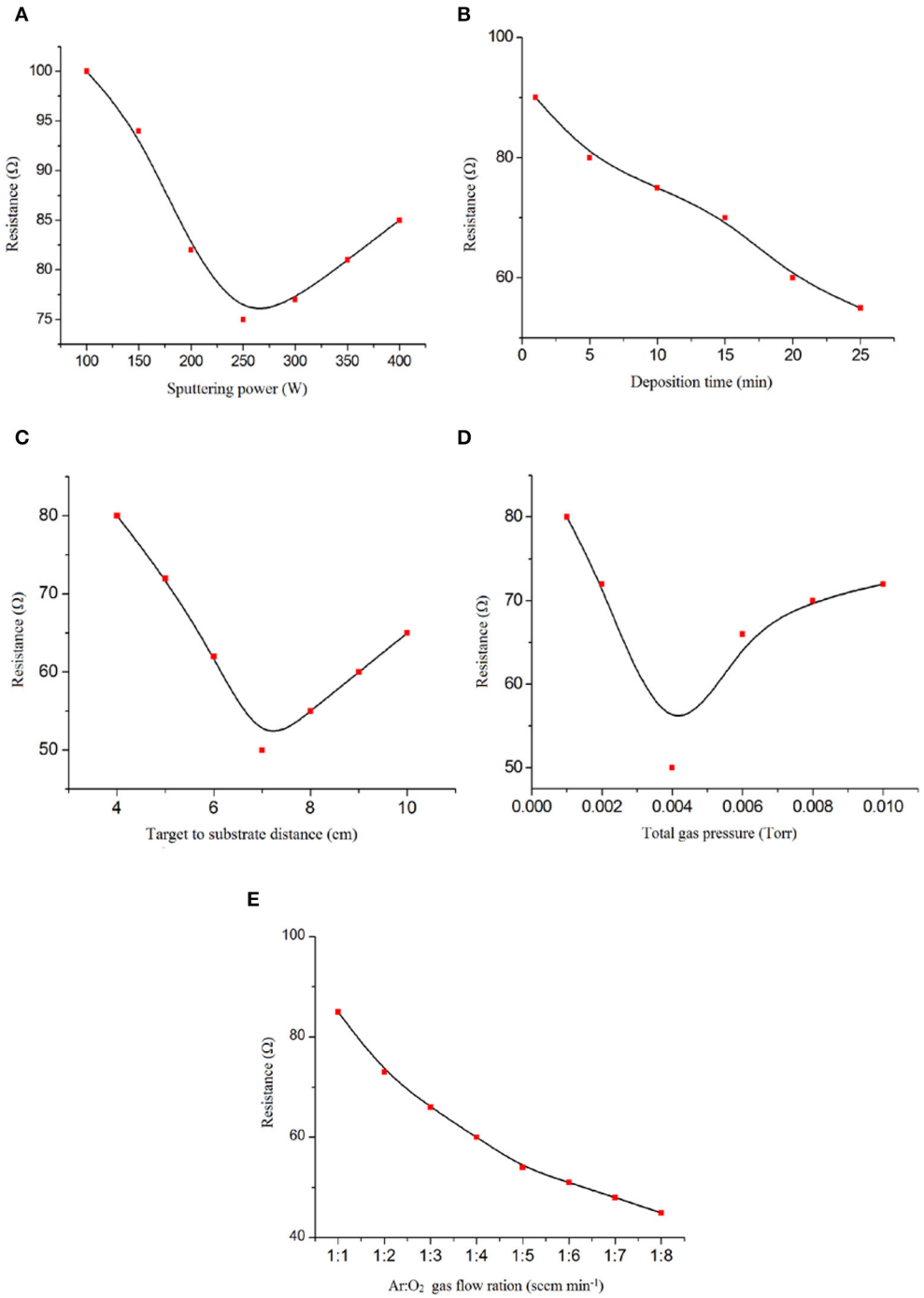

FIGURE 2 | Effect of **(A)** DC magnetron sputtering power, **(B)** deposition time, **(C)** target-to-substrate distance, **(D)** total gas pressure, and **(E)** Ar: O_2 gas ratio on nano-ZnO/polyvinyl alcohol (PVA)/fluorinated tin oxide (FTO) characteristics.

on the surface of FTO that can play a significant role in covalent enzyme immobilization.

The optical transmission (ultraviolet) spectrum of the nano-ZnO/PVA composite film was recorded and the result is presented in **Figure 4A**. As can be seen in **Figure 4A**, there is a sharp absorption band at a wavelength above 317 nm that confirms the optical quality and low concentration of defects of the nano-ZnO/PVA thin film. Additionally, the TGA technique was applied for mass loss assessment of the thin film as a function of temperature at 5°C min^{-1} and under an N_2 atmosphere for thermal stability determination of the nano-ZnO/PVA. The ZnO/PVA mass loss curve shows the low thermal stability of the

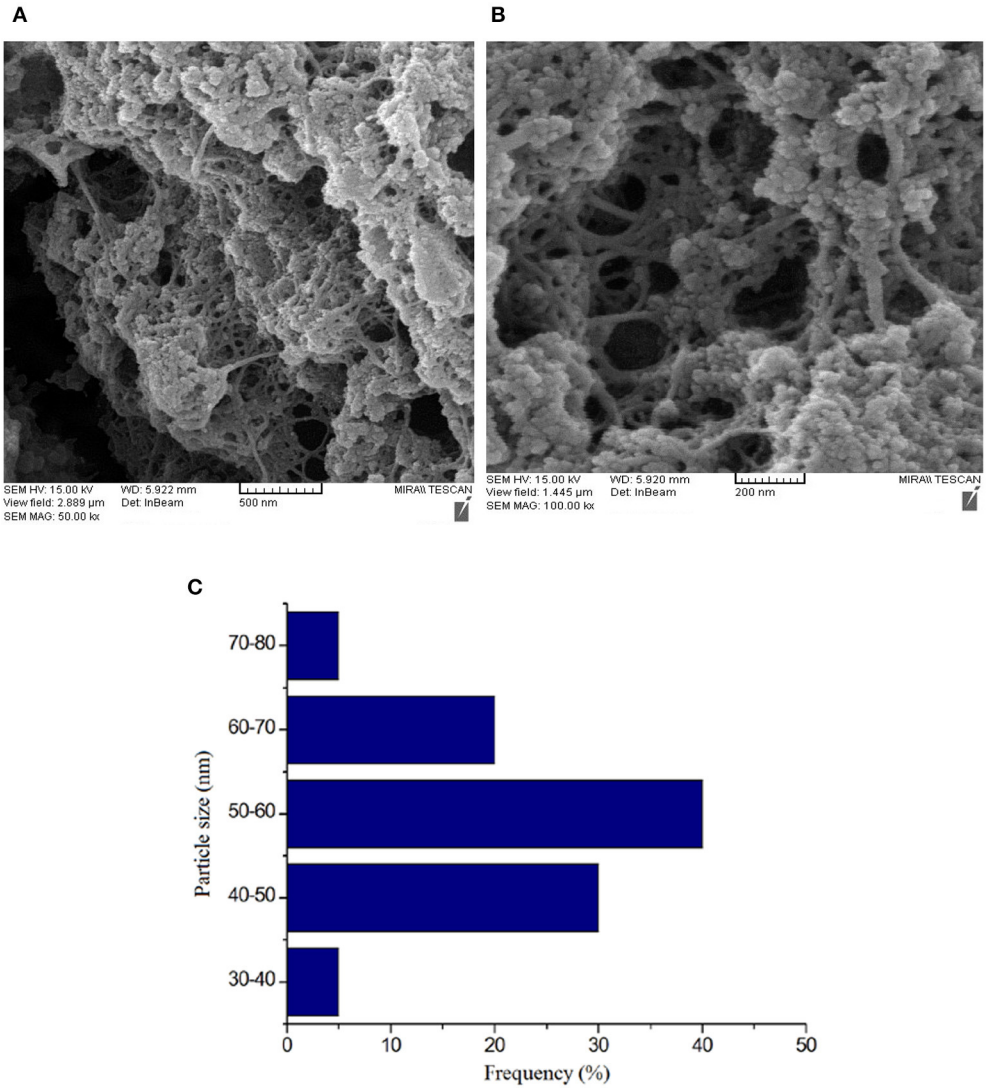

FIGURE 3 | Field emission scanning electron microscopy images of **(A,B)** the nano-ZnO/polyvinyl alcohol (PVA)/fluorinated tin oxide (FTO) at different magnifications and **(C)** its size distribution histogram. The particle size abundance was 50–60 nm.

polymer, as a property common to polymers with low molecular weight. The ZnO/PVA curve exhibits two degradation stages. The first one at 327°C is related to the elimination of the amorphous parts of the PVA polymer while the second one, at 380°C, corresponds to the degradation of the crystalline parts with higher thermal stability (**Figure 4B**). Ultimately, the white ZnO powder remained after TGA analysis.

Electrochemical Characterization of GOx/nano-ZnO/PVA/FTO

We used the EIS method in the presence of a redox probe ($[Fe(CN)_6]^{3-/4-}$) as a powerful technique to study the interfacial changes at the surface of the FTO during the modification process (Jamali et al., 2014; Mozaffari et al., 2015a,b; Tahernejad-Javazmi et al., 2018, 2019; Khodadadi et al., 2019). Using the semicircle diameter of a Nyquist plot of the modification process in a solution containing the redox probe $[Fe(CN)_6]^{3-/4-}$, we can study the change in the charge transfer resistance (R_{ct}) and examine the effect of conductive mediators at the surface of the electrodes (Mozaffari et al., 2009, 2010; Ensafi and Karimi-Maleh, 2010; Karimi-Maleh et al., 2016; Shojaei et al., 2016; Asrami et al., 2017; Shamsadin-Azad et al., 2019). **Figure 5A** shows Nyquist plots of a solution containing 5.0 mM $[Fe(CN)_6]^{3-/4-}$ with 1.0 M KNO_3 at the surface of different modified electrodes. We detected an R_{ct} value of 0.9 kΩ for an FTO bare electrode, which confirms that the highest conductivity of this electrode is due to its inherent electrode properties. FTO exhibits a low electrical resistivity owing to the high carrier concentration (N_d) caused by the oxygen vacancies and the fluorine doping. The maximum R_{ct} value (9.2 kΩ) is obtained on GOx/nano-ZnO/PVA/FTO (final modified structure). The progressively increasing interfacial resistance

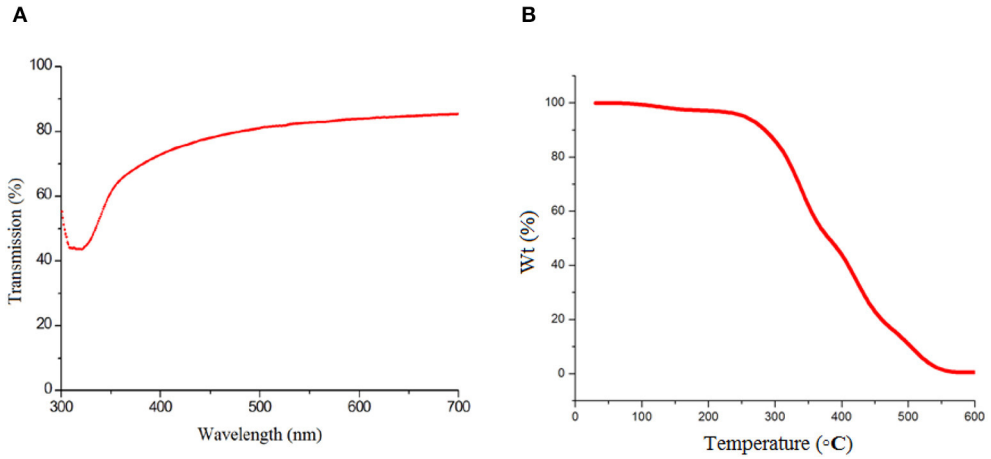

FIGURE 4 | (A) Typical optical transmission spectra recorded for nano-ZnO/polyvinyl alcohol (PVA)/fluorinated tin oxide (FTO) and **(B)** thermogravimetric analysis of nano-ZnO/PVA/FTO.

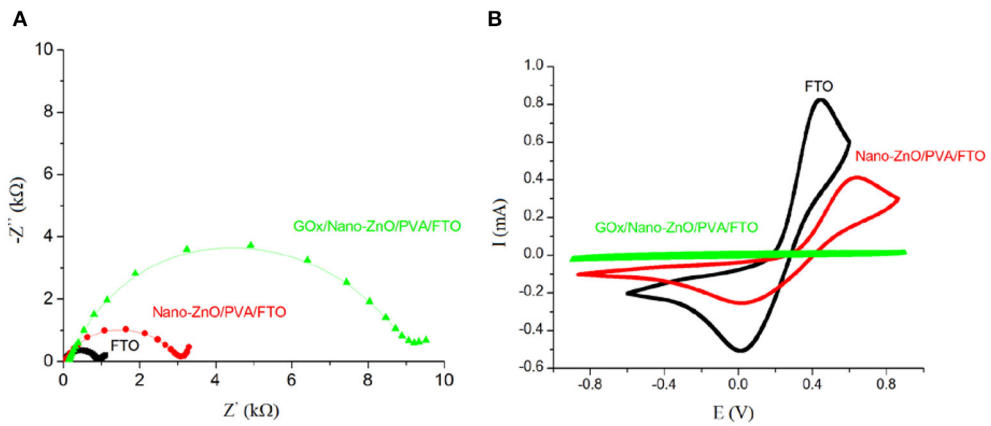

FIGURE 5 | (A) Nyquist plots of a solution containing 5 mM $[Fe(CN)_6]^{3-/4-}$ at the surface of fluorinated tin oxide (FTO), nano-ZnO/polyvinyl alcohol (PVA)/FTO, and glucose oxidase (GOx)/nano-ZnO/PVA/FTO. **(B)** Cyclic voltammograms (scan rate of 0.1 V s^{-1}) of a solution containing 5 mM $[Fe(CN)_6]^{3-/4-}$ at the surface of FTO, nano-ZnO/PVA/FTO, and GOx/nano-ZnO/PVA/FTO. (Z′ is the real Warburg impedance and Z″ is the imaginary Warburg impedance).

during the surface modification is attributed to the lower electrical resistivity of the newly generated layer on FTO because of the GOx insulating characterization. Moreover, the CV study of the layer-by-layer assembly of GOx/nano-ZnO/PVA/FTO in glucose-free PBS containing 5.0 mM $[Fe(CN)_6]^{3-/4-}$ is shown in **Figure 5B**. The magnitude of the anodic peak current for the GOx/nano-ZnO/PVA/FTO electrode (0.03 mA) being lower than that for the bare FTO electrode (0.82 mA) reveals the insulating characteristics of GOx. The outcome data from CV and EIS in the modification process confirm each other.

Electrochemical Characterization of the GOx/nano-ZnO/PVA/FTO Biosensor in the Presence of Glucose

The electrochemical behavior of the layer-by-layer assembly of the biosensor was verified in the presence of 5.0 mM glucose and 1.0 M KNO_3. **Figure 6A** shows the recorded levels relative to the EIS investigation in the presence of glucose to determine the R_{ct} value of the interfacial properties of the GOx/nano-ZnO/PVA/FTO. For reliable impedimetric studies with unchanging conditions, we selected an open circuit potential (OCP) −0.1 V system. The other reason for choosing a −0.1 V DC potential is related to R_{ct}, which is the kinetic component of the resistance determined by EIS. Therefore, to obtain a kinetic-controlled interfacial process, the DC potential was selected to match the kinetic region of the voltammogram in **Figure 6B**.

The R_{ct} value in the presence of glucose for the nano-ZnO/PVA/FTO (9.71 kΩ) is lower than that for the FTO electrode (28.80 kΩ), which is due to a small direct glucose reaction with FTO. A further reduction in the R_{ct} value (1.61 kΩ) was observed after immobilization of GOx onto the nano-ZnO/PVA/FTO matrix owing to rapid glucose oxidation by the GOx, which can represent the faster, predictable, and reproducible response of GOx/nano-ZnO/PVA/FTO compared with the slower, unpredictable, and non-reproducible response

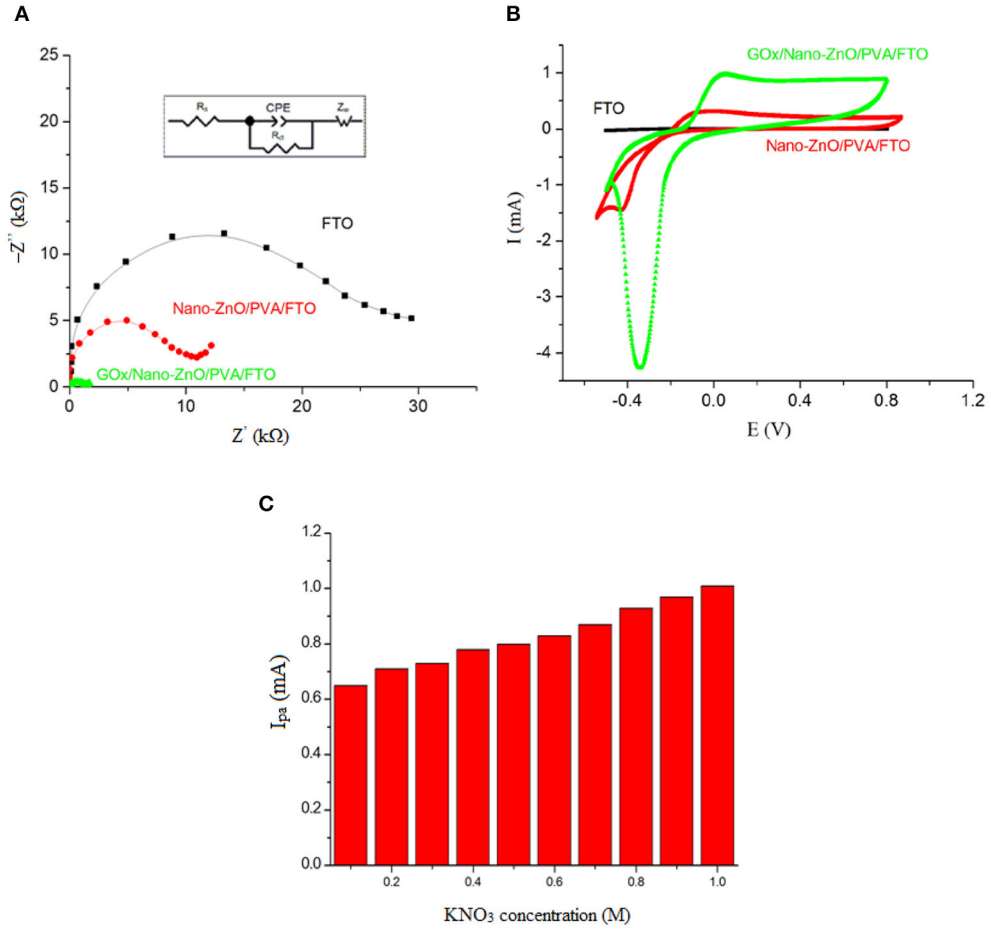

FIGURE 6 | (A) The Nyquist plots (−Z″ vs. Z′), and **(B)** Cyclic voltammograms at the scan rate of 0.1 V s−1 obtained in PBS (pH 7.4) containing 5 mM glucose in the absence of [Fe(CN)6]3−/4− probe, and **(C)** The influence of KNO3 salt concentration, as a supporting electrolyte, on the cyclic voltammogram electrochemical response of 5 mM of glucose on GOx/Nano-ZnO/PVA/FTO biosensor. The inset in **(A)** shows equivalent circuit. (Zw: Warburg impedance, Ipa: anodic peak current, Rs: solution resistance, Rct: charge transfer resistance).

of ZnO. The EIS analysis was carried out by means of a modified Randles equivalent circuit, where the constant phase element (CPE) is in series with the Warburg impedance (Z_w), in parallel with the R_{ct}, and in series with the solution resistance (R_s) (**Figure 6A**, inset). Cyclic voltammetric studies of the layer-by-layer assembly of GOx/nano-ZnO/PVA/FTO in PBS containing 5.0 mM glucose are shown in **Figure 6B**. The CV results support the EIS findings, where the cathodic peak current refers to the $O_2 + 2e^- \rightarrow 2O^-$ reaction accompanied by the $H_2O_2 \rightarrow O_2 + 2H^+ + 2e^-$ reaction for the anodic peak current. The mechanism is explained in detail below.

According to the Henry and Peter microscopic model, sensors researchers described the changing electrical conductance of a semiconducting film sensor in a solution containing toxic gases (Guilbault and Lubrano, 1973; Windischmann and Mark, 1979; Ansari et al., 2008). According to the microscopic model, in the first step, the atmospheric oxygen molecules could be adsorbed at surface sites by physical bonding. According to this reaction, atmospheric oxygen molecules convert to the ion form and are then adsorbed at the surface of the system as O^-_{ads}. The resulting equation is:

$$O_2 + 2e^- \rightarrow 2O^- \quad (1)$$

Equation (1) leads to a decrease in the conductance of the transducer, as indicated by an increase in the potential barrier at the grain boundaries, upon exposing GOx immobilized to glucose, the reaction between GOx and glucose can be described according to the below equations:

$$\text{Glucose} + O_2 \rightarrow \text{gluconolactone} + H_2O_2 \quad (2)$$

$$H_2O_2 \rightarrow O_2 + 2H^+ + 2e^- \quad (3)$$

This results in the production of D-gluconate with an H^+ ion, which reacts with O^-_{ads} and thereby releases the trapped electron to the conduction band of ZnO, as indicated by the decrease in the potential barrier at the grain boundary. Further, when reducing molecules (R: H_2O_2) react with preadsorbed negatively

charged oxygen adsorbates, the trapped electrons are returned to the conduction band of the material. The energy released during the decomposition of adsorbed molecules would be sufficient for the electrons to jump up into the conduction band in such a way that it increases the conductivity of the biosensor based on the following reaction:

$$R + O^- \rightarrow RO + e^- \quad (4)$$

However, some valuable proposed photoelectric mechanisms is interesting for researchers and can prepare a vast view in the semiconductors researches (Liang et al., 2017).

Effect of Salt Concentration and pH of Solution

Because of the maximum activity of GOx enzyme at pH 7.4, this pH value was selected as the optimum value for glucose oxidation in the present study. It must be noted that the survival of the enzyme's natural structure is necessary to improve the detection limit and sensitivity for glucose detection. PVA possesses a negative charge surface, which repels the negatively charge GOx [with low isoelectric point (IEP) 4.5] at physiological pH (pH = 7.4), so covalent GOx immobilization to the substrate was required.

Using supporting electrolytes in an electrochemical process is necessary to eliminate the transport of electroactive species by ion migration in an electric field and to increase the conductivity of the solution. The selection of a suitable supporting electrolyte with special properties such as electrochemical stability; solubility; interaction with the reaction intermediate; and some preparation difficulties is very important in a voltammetric investigation. Different types of water-based buffers were used as inorganic supporting electrolytes. In this case, the test solutions, such as $KClO_4$, $NaNO_3$, KCl, KNO_3, and KI, were also used to examine the effects of the supporting electrolytes at different concentrations (concentration changed between 0.0 and 1.0 M) on the voltammogram signals of 5.0 mM glucose. The outcomes showed that the sensor sensitivity and the oxidation signal of glucose were enhanced by increasing the concentration of the salt to 1.0 M KNO_3 as a supporting electrolyte (**Figure 6C**) and this supporting electrolyte was selected as the best condition for the following steps.

The Working Curve for Ohmic Behavior Measurements

The catalytic activity of the GOx/nano-ZnO/PVA/FTO was determined under the following conditions: a DC current cell and a gold wire (5 cm length, Φ 0.3 mm) as an electrode and the GOx/nano-ZnO/PVA/FTO as a working electrode were used in a potential range of 0.0–1.0 V. At higher voltages, it is possible to oxidize water as a solvent. In water electrolysis, the oxygen will bubble at the anode.

As can be seen in **Figure 7A**, different concentrations of glucose solutions, such as 0.2–20 mM, were prepared in 50 mL of PBS electrolyte at 25°C. The effect of increasing the glucose concentration is specified in the *I-V* curve (**Figure 7A**).

The increase in the slope of the *I-V* curve ($\Delta I/\Delta V$) indicates successful enzyme immobilization. The proposed equation for sensitivity determination is: sensitivity = $(\Delta I/\Delta V)_x$ – $(\Delta I/\Delta V)_0/(\Delta I/\Delta V)_0$, where $(\Delta I/\Delta V)_0$ is the *I-V* curve's slope at a glucose concentration of "0.0" mM and $(\Delta I/\Delta V)_x$ is the slope of the *I-V* curve at a glucose concentration of "*x*" mM, where *x* = 0.2–20 mM of glucose.

The volume of 50 mL of electrolyte was chosen in all of the electrochemical measurements. Since the amount of glucose with respect to PBS changes with increasing molar concentration, this effect would be reflected in the $\Delta I/\Delta V$ of the *I-V* curves, as presented in **Figure 7A**. Enhancement in the sample current is noticeable, i.e., the film conductivity increases. This enhancement is attributed to the catalytic reaction of GOx and glucose:

$$\text{Glucose} + O_2 \rightarrow \text{gluconolactone} + H_2O_2$$

The sensitivity ($\Delta I/\Delta V$) increases promptly with the increase in glucose concentration because of the increase in the hydrolysis of glucose. The resistance of GOx/nano-ZnO/PVA/FTO decreases in the presence of glucose. Obviously, H_2O_2 increases with the increase in glucose, and more and more trapped electrons are returned to the conduction band of the biosensor, which explains the increase in sensitivity of the sensor (partially) linearly (ohmic behavior) with glucose concentration. The high activity of GOx/nano-ZnO/PVA/FTO is due to the high surface area of the thin film.

The *I-V* investigation confirms a reversible system and supports the catalytic activity of GOx at the surface of GOx/nano-ZnO/PVA/FTO. The linear dynamic range investigation results for the determination of glucose using a GOx/nano-ZnO/PVA/FTO biosensor are shown in **Figure 7B**. *I-V* responses in **Figure 7B** shows a working curve in a linear scale [log i (mA) = −7.137 (±0.005) + 0.041 (±0.001) × [glucose] (mM); R^2 = 0.998] in a concentration range of 0.2–20 mM of glucose in E = 0.5 V. The GOx/nano-ZnO/PVA/FTO biosensor exhibits a detection limit of 2.0 μM for glucose and a sensitivity of 0.041 mA per mM with a linear range of 0.2–20 mM.

In addition, the impedimetric signal of nano-ZnO/PVA/FTO vs. the reducing (R) molecule (H_2O_2, in the absence of glucose) concentration was recorded as new evidence to validate our proposed biosensing mechanism. According to the data (were not shown), there was a significant decrease in the R_{ct} value after the addition of H_2O_2 from 0.001 to 0.021 M. This phenomenon is due to the reaction between the reducing species and the preadsorbed negatively charged oxygen adsorbates (Equation 3). This reaction results in trapped electrons being returned to the conduction band of ZnO, and as a result a decrease in R_{ct} is observed. The obtained results in the impedimetric investigation in the presence of H_2O_2 species support the proposed mechanism.

Analytical Characteristics

The ZnO thin film (IEP ∼9.5; pH = 7.4) possesses a positive charge surface that repulses positive metal ions; as a result, quantitative analysis in the presence of metal ions

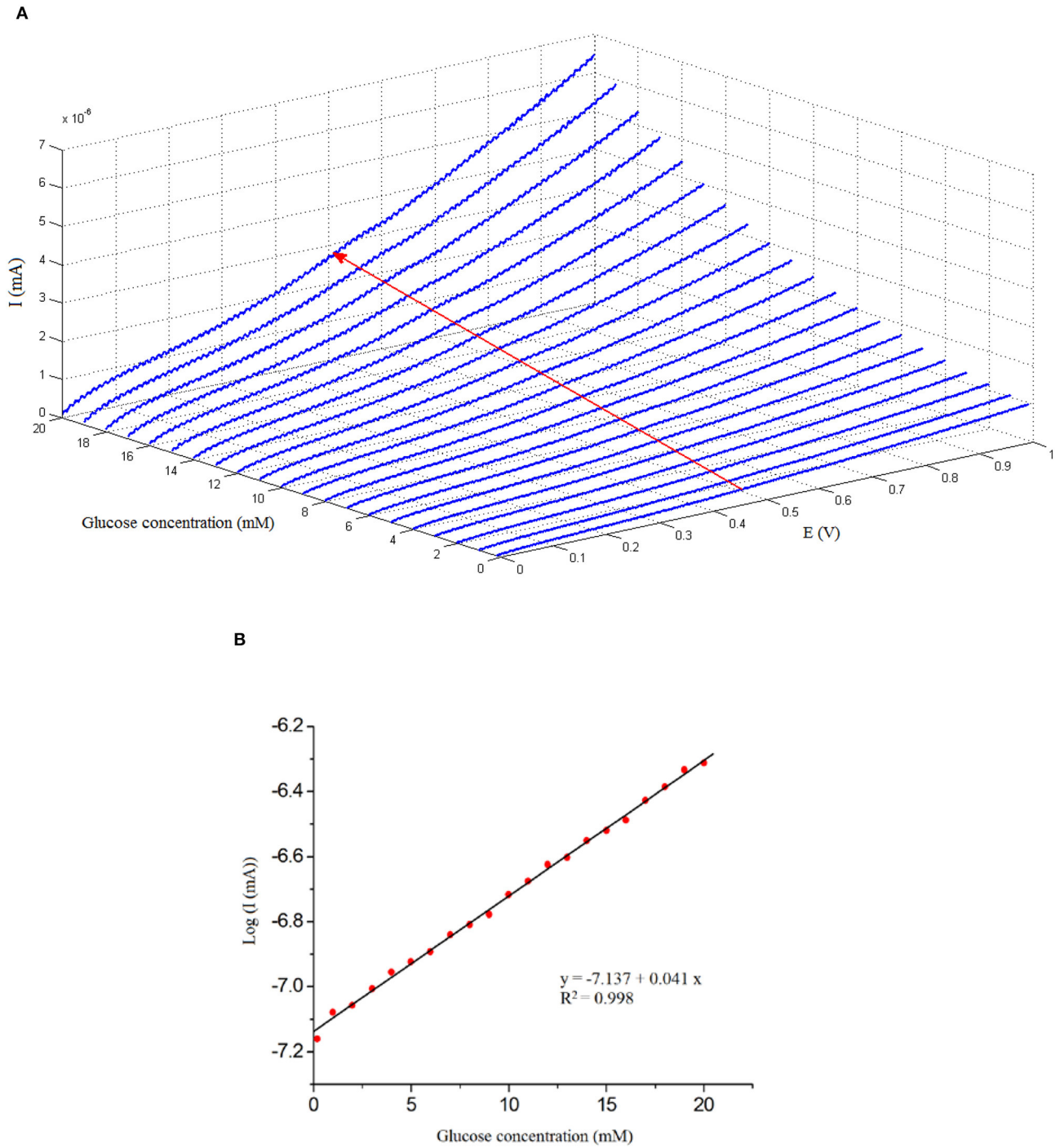

FIGURE 7 | (A) Current–voltage (*I-V*) plots obtained on the GOx/nano-ZnO/polyvinyl alcohol (PVA)/fluorinated tin oxide (FTO) biosensor in the presence of different concentrations of glucose: 0.2–20 mM with a rate of 0.1 V/s. **(B)** Variation of *I-V* plots current as a function of glucose concentration, at $E = 0.5$ V, which represents the calibration curve ($y = -7.137 + 0.041x$, $R^2 = 0.998$).

(including Zn^{2+}, Mn^{2+}, Ca^{2+}, Ag^{+}, Cu^{2+}, Al^{3+}, Mg^{2+}, and Pb^{2+}) was possible. Furthermore, the selectivity of GOx/nano-ZnO/PVA/FTO toward the determination of glucose (5 mM) was investigated by an electrochemical technique by adding the usual concentration of interfering substances that are present in human serum such as uric acid (0.1 mM) and ascorbic acid

TABLE 1 | Measurement of the level of glucose in blood serum.

Method	Sample number				
	1	2	3	4	5
Determination by Spectrophotometry (mM)	4.42	5.25	4.10	3.24	6.10
Determination by GOx/Nano-ZnO/PVA/FTO biosensor (mM)	4.43	5.27	4.09	3.24	6.09
R.S.D.[a] ($n = 5$) (%)	1.50	1.10	1.2	1.55	1.00

R.S.D.[a] Relative Standard Deviation.

TABLE 2 | Analytical characteristics GOx/Nano-ZnO/PVA/FTO biosensor compared with the other reported ZnO base glucose biosensors.

Electrode matrix	D.L (nM/μM)	Sensitivity	D.R (μM/mM)	RT (Sec)	Detection method	Ref.
ZnO nanorods/Au hybrid	10 nM	48.0 μA/mM	0.1–33.0 μM	–	Amperometric/Enzymatic	Wei et al., 2010
ZnO nanorods	0.089 mM	1 mA/mM cm^{-2}	1.27–16.62 mM	–	Amperometric/Enzymatic	Mandal et al., 2016
Zinc oxide nanorods	0.22 μM	10.911 mA/mM cm^{-2} 17 μA/mM cm^{-2}	1.5–7 mM	3	Amperometric/Enzymatic	Marie et al., 2015
Zinc oxide nanwire	–		0.03–1.52 mM	–	Amperometric/Enzymatic	Gallay et al., 2016
GOx/Nano-ZnO/PVA/FTO	2.0 μM	0.041 mA/mM	0.2–20 mM	3	I –V technique/Enzymatic	This work

DR, Detection Range; DL, Detection Limit; RT, Response Time.

(0.1 mM). The obtained *I-V* data show a maximum interference of 1.5% in the presence of all of the interfering substances, which confirms the selectivity of GOx/nano-ZnO/PVA/FTO as a glucose biosensor.

Numerous assays have been conducted on blood serum to examine the ability of the GOx/nano-ZnO/PVA/FTO biosensor to determine glucose levels in real-life samples using a calibration curve. The results obtained by the proposed method were checked with a spectrophotometric method by a local clinical laboratory (**Table 1**). The results presented in **Table 1** show clearly the ability of the GOx/nano-ZnO/PVA/FTO biosensor to act as a novel and powerful tool for determination of glucose in real-life samples.

The sensor was studied by recording the CV anodic peak currents in the presence of 5.0 mM glucose and 1.0 M KNO_3 after continuous scanning for 500 cycles, which showed that the electrode retained 96.5% of the initial current response and proved the stability of the biosensor in buffer solution (The data were not shown).

Additionally, 10 modified electrodes were utilized for parallel determinations of 5.0 mM glucose and the relative standard deviation (RSD) was determined as 1.21%, indicating that the electrode had good reproducibility for the precision study. We detected an RSD value of 1.65% for determination of 5.0 mM glucose using the same 10 GOx/nano-ZnO/PVA/FTO electrodes fabricated with the same procedure. This RSD value confirmed the good repeatability for GOx/nano-ZnO/PVA/FTO as a novel glucose biosensor. The response time of GOx/nano-ZnO/PVA/FTO was checked as an important analytical factor and results showed a fast response time (less than 3 s) for GOx/nano-ZnO/PVA/FTO in the determination of glucose, confirming the rapid rate of diffusion of the analyte into the enzyme surface and rapid reaction between the analyte and the enzyme. Furthermore, the stability of the GOx/nano-ZnO/PVA/FTO biosensor was checked by comparing the oxidation signal of glucose at different time periods. Three GOx/nano-ZnO/PVA/FTO biosensors lost about 0.0, 2.0, and 3.0% of their original activity (for a fixed glucose concentration of 5.0 mM), after storage times of 1, 30, and 60 days, respectively. **Table 2** compares the analytical characteristics of the GOx/nano-ZnO/PVA/FTO biosensor with other reported glucose biosensors. The biosensor in the present work clearly shows better analytical factors, such as the detection limit and response time, than previously reported sensors (Wei et al., 2010; Marie et al., 2015; Gallay et al., 2016; Mandal et al., 2016; Asrami et al., 2018; Nguyen et al., 2019; Sabu et al., 2019). This advantage is relative to covalent enzyme immobilization in our fabricated biosensor. This covalent enzyme immobilization is the main consideration in creating good K_m and V_m factors in an enzymatic biosensor that help to improve biosensor activity.

CONCLUSIONS

A novel applied GOx/nano-ZnO/PVA/FTO was reported to have high sensitivity and to be a powerful enzymatic biosensor in the measurement of glucose in human blood serum. The nano-material used in the design of GOx/nano-ZnO/PVA/FTO created a greater surface area for loading of enzyme that may improve the activity of the fabricated biosensor for determination of glucose. Because of strong enzyme–substrate covalent bonding we concluded that our fabricated biosensor had faster detection kinetics and reduced diffusion resistance in the measurement of glucose. The results obtained at the surface of the GOx/nano-ZnO/PVA/FTO showed a fast response time (less than 3 s) and a limit of detection of 2.0 μM with a sensitivity of 0.041 mA per mM for determination of glucose under optimum conditions. The GOx/nano-ZnO/PVA/FTO showed good selectivity with high sensitivity for determination of glucose in real-life samples

such as human blood serum. The manufacturing process of the proposed biosensor is the future project of our research team.

DATA AVAILABILITY STATEMENT

The raw data supporting the conclusions of this article will be made available by the authors, without undue reservation.

ETHICS STATEMENT

No potentially identifiable human images or data is presented in this study.

AUTHOR CONTRIBUTIONS

All authors listed have made a substantial, direct and intellectual contribution to the work, and approved it for publication.

ACKNOWLEDGMENTS

We acknowledge the support of Dr. Sayed Ahmad Mozaffari and his thin layer and nanotechnology working group especially Dr. Reza Rahmanian in the Iranian Research Organization Science and Technology, Iran Nanotechnology Initiative Council (INIC), and Nanostructured Coating Co. for this research.

REFERENCES

Aini, B. N., Siddiquee, S., Ampon, K., Rodrigues, K. F., and Suryani, S. (2015). Development of glucose biosensor based on ZnO nanoparticles film and glucose oxidase-immobilized eggshell membrane. *Sens. Biosens. Res.* 4, 46–56. doi: 10.1016/j.sbsr.2015.03.004

Anderson, K., Poulter, B., Dudgeon, J., Li, S.-E., and Ma, X. (2017). A highly sensitive nonenzymatic glucose biosensor based on the regulatory effect of glucose on electrochemical behaviors of colloidal silver nanoparticles on MoS2. *Sensors* 17:1807. doi: 10.3390/s17081807

Ansari, S., Ansari, Z., Wahab, R., Kim, Y.-S., Khang, G., and Shin, H.-S. (2008). Glucose sensor based on nano-baskets of tin oxide templated in porous alumina by plasma enhanced CVD. *Biosens. Bioelectron.* 23, 1838–1842. doi: 10.1016/j.bios.2008.02.022

Asrami, P. N., Mozaffari, S. A., Tehrani, M. S., and Azar, P. A. (2018). A novel impedimetric glucose biosensor based on immobilized glucose oxidase on a CuO-Chitosan nanobiocomposite modified FTO electrode. *Int. J. Biol. Macromol.* 118, 649–660. doi: 10.1016/j.ijbiomac.2018.05.228

Asrami, P. N., Tehrani, M. S., Azar, P. A., and Mozaffari, S. A. (2017). Impedimetric glucose biosensor based on nanostructure nickel oxide transducer fabricated by reactive RF magnetron sputtering system. *J. Electroanal. Chem.* 801, 258–266. doi: 10.1016/j.jelechem.2017.07.052

Baghayeri, M. (2015). Glucose sensing by a glassy carbon electrode modified with glucose oxidase and a magnetic polymeric nanocomposite. *RSC Adv.* 5, 18267–18274. doi: 10.1039/C4RA15888A

Baghayeri, M., Nodehi, M., Amiri, A., Amirzadeh, N., Behazin, R., and Iqbal, M. Z. (2020). Electrode designed with a nanocomposite film of CuO Honeycombs/Ag nanoparticles electrogenerated on a magnetic platform as an amperometric glucose sensor. *Anal. Chim. Acta.* doi: 10.1016/j.aca.2020.03.039

Baghayeri, M., Veisi, H., and Ghanei-Motlagh, M. (2017). Amperometric glucose biosensor based on immobilization of glucose oxidase on a magnetic glassy carbon electrode modified with a novel magnetic nanocomposite. *Sensors Actuators B Chem.* 249, 321–330. doi: 10.1016/j.snb.2017.04.100

Baghizadeh, A., Karimi-Maleh, H., Khoshnama, Z., Hassankhani, A., and Abbasghorbani, M. (2015). A voltammetric sensor for simultaneous determination of vitamin C and vitamin B 6 in food samples using ZrO_2 nanoparticle/ionic liquids carbon paste electrode. *Food Anal. Methods* 8, 549–557. doi: 10.1007/s12161-014-9926-3

Baghriche, O., Ruales, C., Sanjines, R., Pulgarin, C., Zertal, A., Stolitchnov, I., et al. (2012). Ag-surfaces sputtered by DC and pulsed DC-magnetron sputtering effective in bacterial inactivation: testing and characterization. *Surf. Coat. Technol.* 206, 2410–2416. doi: 10.1016/j.surfcoat.2011.10.041

Bijad, M., Karimi-Maleh, H., and Khalilzadeh, M. A. (2013). Application of ZnO/CNTs nanocomposite ionic liquid paste electrode as a sensitive voltammetric sensor for determination of ascorbic acid in food samples. *Food Anal. Methods* 6, 1639–1647. doi: 10.1007/s12161-013-9585-9

Bollella, P., Gorton, L., Ludwig, R., and Antiochia, R. (2017). A third generation glucose biosensor based on cellobiose dehydrogenase immobilized on a glassy carbon electrode decorated with electrodeposited gold nanoparticles: characterization and application in human saliva. *Sensors* 17:1912. doi: 10.3390/s17081912

Chung, R.-J., Wang, A.-N., Liao, Q.-L., and Chuang, K.-Y. (2017). Non-enzymatic glucose sensor composed of carbon-coated nano-zinc oxide. *Nanomaterials* 7:36. doi: 10.3390/nano7020036

Dehhaghi, M., Tabatabaei, M., Aghbashlo, M., Panahi, H. K. S., and Nizami, A.-S. (2019). A state-of-the-art review on the application of nanomaterials for enhancing biogas production. *J. Environ. Manage.* 251:109597. doi: 10.1016/j.jenvman.2019.109597

Ensafi, A. A., and Karimi-Maleh, H. (2010). Modified multiwall carbon nanotubes paste electrode as a sensor for simultaneous determination of 6-thioguanine and folic acid using ferrocenedicarboxylic acid as a mediator. *J. Electroanal. Chem.* 640, 75–83. doi: 10.1016/j.jelechem.2010.01.010

Gallay, P., Tosi, E., Madrid, R., Tirado, M., and Comedi, D. (2016). Glucose biosensor based on functionalized ZnO nanowire/graphite films dispersed on a Pt electrode. *Nanotechnology* 27:425501. doi: 10.1088/0957-4484/27/42/425501

Gavin, J. (2007). The importance of monitoring blood glucose US. *Endocr. Dis.* 1:1–3. doi: 10.17925/USE.2007.00.2.42

Guilbault, G., and Lubrano, G. (1973). An enzyme electrode for the amperometric determination of glucose. *Anal. Chim. Acta* 64, 439–455. doi: 10.1016/S0003-2670(01)82476-4

Hassandoost, R., Pouran, S. R., Khataee, A., Orooji, Y., and Joo, S. W. (2019). Hierarchically structured ternary heterojunctions based on Ce^{3+}/Ce^{4+} modified Fe_3O_4 nanoparticles anchored onto graphene oxide sheets as magnetic visible-light-active photocatalysts for decontamination of oxytetracycline. *J. Hazard. Mater.* 376, 200–211. doi: 10.1016/j.jhazmat.2019.05.035

Hosseini, E., Rajaei, A., Tabatabaei, M., Mohsenifar, A., and Jahanbin, K. (2019). Preparation of pickering flaxseed oil-in-water emulsion stabilized by chitosan-myristic acid nanogels and investigation of its oxidative stability in presence of clove essential oil as antioxidant. *Food Biophys.* 15, 216–228. doi: 10.1007/s11483-019-09612-z

Israr-Qadir, M., Jamil-Rana, S., Nur, O., and Willander, M. (2017). Zinc oxide-based self-powered potentiometric chemical sensors for biomolecules and metal ions. *Sensors* 17:1645. doi: 10.3390/s17071645

Jamali, T., Karimi-Maleh, H., and Khalilzadeh, M. A. (2014). A novel nanosensor based on Pt:Co nanoalloy ionic liquid carbon paste electrode for voltammetric determination of vitamin B9 in food samples. *LWT Food Sci. Technol.* 57, 679–685. doi: 10.1016/j.lwt.2014.01.023

Jedrzak, A., Rebiś, T., Klapiszewski, Ł., Zdarta, J., Milczarek, G., and Jesionowski, T. (2018a). Carbon paste electrode based on functional GOx/silica-lignin system to prepare an amperometric glucose biosensor. *Sensors Actuators B Chem.* 256, 176–185. doi: 10.1016/j.snb.2017.10.079

Jedrzak, A., Rebiś, T., Nowicki, M., Synoradzki, K., Mrówczynski, R., and Jesionowski, T. (2018b). Polydopamine grafted on an advanced Fe_3O_4/lignin hybrid material and its evaluation in biosensing. *Appl. Surf. Sci.* 455, 455–464. doi: 10.1016/j.apsusc.2018.05.155

Karimi-Maleh, H., and Arotiba, O. A. (2020). Simultaneous determination of cholesterol, ascorbic acid and uric acid as three essential biological compounds at a carbon paste electrode modified with copper oxide decorated reduced

graphene oxide nanocomposite and ionic liquid. *J. Colloid Interface Sci.* 560, 208–212. doi: 10.1016/j.jcis.2019.10.007

Karimi-Maleh, H., Cellat, K., Arikan, K., Savk, A., and Karimi, F., Sen F (2020a). Palladium–Nickel nanoparticles decorated on Functionalized-MWCNT for high precision non-enzymatic glucose sensing. *Mat. Chem. Phys.* 250:123042. doi: 10.1016/j.matchemphys.2020.123042

Karimi-Maleh, H., Fakude, C. T., Mabuba, N., Peleyeju, G. M., and Arotiba, O. A. (2019a). The determination of 2-phenylphenol in the presence of 4-chlorophenol using nano-Fe_3O_4/ionic liquid paste electrode as an electrochemical sensor. *J. Colloid Interface Sci.* 554, 603–610. doi: 10.1016/j.jcis.2019.07.047

Karimi-Maleh, H., Karimi, F., Alizadeh, M., and Sanati, A. L. (2020c). Electrochemical sensors, a bright future in the fabrication of portable kits in analytical systems. *Chem. Rec.* 20, 1–12. doi: 10.1002/tcr.201900092

Karimi-Maleh, H., Karimi, F., Malekmohammadi, S., Zakariae, N., Esmaeili, R., Rostamnia, S., et al. (2020b). An amplified voltammetric sensor based on platinum nanoparticle/polyoxometalate/two-dimensional hexagonal boron nitride nanosheets composite and ionic liquid for determination of *N*-hydroxysuccinimide in water samples. *J. Mol. Liquids* 310:113185. doi: 10.1016/j.molliq.2020.113185

Karimi-Maleh, H., Shafieizadeh, M., Taher, M. A., Opoku, F., Kiarii, E. M., Govender, P. P., et al. (2019b). The role of magnetite/graphene oxide nanocomposite as a high-efficiency adsorbent for removal of phenazopyridine residues from water samples, an experimental/theoretical investigation. *J. Mol. Liquids* 298:112040. doi: 10.1016/j.molliq.2019.112040

Karimi-Maleh, H., Sheikhshoaie, M., Sheikhshoaie, I., Ranjbar, M., Alizadeh, J., Maxakato, N. W., et al. (2019c). A novel electrochemical epinine sensor using amplified CuO nanoparticles and an-hexyl-3-methylimidazolium hexafluorophosphate electrode. *New J. Chem.* 43, 2362–2367. doi: 10.1039/C8NJ05581E

Karimi-Maleh, H., Shojaei, A. F., Tabatabaeian, K., Karimi, F., Shakeri, S., and Moradi, R. (2016). Simultaneous determination of 6-mercaptopruine, 6-thioguanine and dasatinib as three important anticancer drugs using nanostructure voltammetric sensor employing Pt/MWCNTs and 1-butyl-3-methylimidazolium hexafluoro phosphate. *Biosens. Bioelectron.* 86, 879–884. doi: 10.1016/j.bios.2016.07.086

Kelly, P. J., and Arnell, R. D. (2000). Magnetron sputtering: a review of recent developments and applications. *Vacuum* 56, 159–172. doi: 10.1016/S0042-207X(99)00189-X

Khodadadi, A., Faghih-Mirzaei, E., Karimi-Maleh, H., Abbaspourrad, A., Agarwal, S., and Gupta, V. K. (2019). A new epirubicin biosensor based on amplifying DNA interactions with polypyrrole and nitrogen-doped reduced graphene: experimental and docking theoretical investigations. *Sensors Actuators B Chem.* 284, 568–574. doi: 10.1016/j.snb.2018.12.164

Li, C., Liu, Y., Li, L., Du, Z., Xu, S., Zhang, M., et al. (2008). A novel amperometric biosensor based on NiO hollow nanospheres for biosensing glucose. *Talanta* 77, 455–459. doi: 10.1016/j.talanta.2008.06.048

Liang, Q., Jin, J., Zhang, M., Liu, C., Xu, S., Yao, C., et al. (2017). Construction of mesoporous carbon nitride/binary metal sulfide heterojunction photocatalysts for enhanced degradation of pollution under visible light. *Appl. Catal. B Environ.* 218, 545–554. doi: 10.1016/j.apcatb.2017.07.003

Macdonald, J. R., Schoonman, J., and Lehnen, A. (1982). Applicability and power of complex nonlinear least squares for the analysis of impedance and admittance data. *J. Electroanal. Chem. Interfac. Electrochem.* 131, 77–95. doi: 10.1016/0022-0728(82)87062-9

Mahadeva, S. K., and Kim, J. (2011). Conductometric glucose biosensor made with cellulose and tin oxide hybrid nanocomposite. *Sensors Actuators B Chem.* 157, 177–182. doi: 10.1016/j.snb.2011.03.046

Malekmohammadi, S., Hadadzadeh, H., Rezakhani, S., and Amirghofran, Z. (2019). Design and synthesis of gatekeeper coated dendritic silica/titania mesoporous nanoparticles with sustained and controlled drug release properties for targeted synergetic chemo-sonodynamic therapy. *ACS Biomater. Sci. Eng.* 5, 4405–4415. doi: 10.1021/acsbiomaterials.9b00237

Mandal, S., Marie, M., and Manasreh, O. (2016). Fabrication of an electrochemical sensor for glucose detection using ZnO nanorods. *MRS Adv.* 1, 861–867. doi: 10.1557/adv.2016.149

Marie, M., Mandal, S., and Manasreh, O. (2015). An electrochemical glucose sensor based on zinc oxide nanorods. *Sensors* 15, 18714–18723. doi: 10.3390/s150818714

Miraki, M., Karimi-Maleh, H., Taher, M. A., Cheraghi, S., Karimi, F., Agarwal, S., et al. (2019). Voltammetric amplified platform based on ionic liquid/NiO nanocomposite for determination of benserazide and levodopa. *J. Mol. Liquids* 278, 672–676. doi: 10.1016/j.molliq.2019.01.081

Miwa, Y., Nishizawa, M., Matsue, T., and Uchida, I. (1994). A conductometric glucose sensor based on a twin-microband electrode coated with a polyaniline thin film. *Bull. Chem. Soc. Jpn.* 67, 2864–2866. doi: 10.1246/bcsj.67.2864

Moghaddam, A. B. (2017). Electrodeposited nanoscale zinc oxide particles: facilitating the electron transfer of immobilised protein and biosensing. *Micro Nano Lett.* 12, 425–429. doi: 10.1049/mnl.2016.0563

Morikawa, M.a, Kimizuka, N., Yoshihara, M., and Endo, T. (2002). New colorimetric detection of glucose by means of electron-accepting indicators: ligand substitution of [Fe (acac) 3– n (phen) n] n+ complexes triggered by electron transfer from glucose oxidase. *Chem. A Eur. J.* 8, 5580–55843. doi: 10.1002/1521-3765(20021216)8:24<5580::AID-CHEM5580>3.0.CO;2-V

Mozaffari, S. A., Chang, T., and Park, S.-M. (2009). Diffusional electrochemistry of cytochrome c on mixed captopril/3-mercapto-1-propanol self-assembled monolayer modified gold electrodes. *J. Phys. Chem. C* 113, 12434–12442. doi: 10.1021/jp9027645

Mozaffari, S. A., Chang, T., and Park, S.-M. (2010). Self-assembled monolayer as a pre-concentrating receptor for selective serotonin sensing. *Biosens. Bioelectron.* 26, 74–79. doi: 10.1016/j.bios.2010.05.015

Mozaffari, S. A., Rahmanian, R., Abedi, M., and Amoli, H. S. (2014). Urea impedimetric biosensor based on reactive RF magnetron sputtered zinc oxide nanoporous transducer. *Electrochim. Acta* 146, 538–547. doi: 10.1016/j.electacta.2014.08.105

Mozaffari, S. A., Ranjbar, M., Kouhestanian, E., Amoli, H. S., and Armanmehr, M. (2015a). An investigation on the effect of electrodeposited nanostructured ZnO on the electron transfer process efficiency of TiO_2 based DSSC. *Mater. Sci. Semicond. Process.* 40, 285–292. doi: 10.1016/j.mssp.2015.06.081

Mozaffari, S. A., Saeidi, M., and Rahmanian, R. (2015b). Photoelectric characterization of fabricated dye-sensitized solar cell using dye extracted from red Siahkooti fruit as natural sensitizer. *Spectrochim. Acta Part A Mol. Biomol. Spectrosc.* 142, 226–231. doi: 10.1016/j.saa.2015.02.003

Nguyen, H. H., Lee, S. H., Lee, U. J., Fermin, C. D., and Kim, M. (2019). Immobilized enzymes in biosensor applications. *Materials* 12:121. doi: 10.3390/ma12010121

Panzner, G., Egert, B., and Schmidt, H. P. (1985). The stability of CuO and Cu_2O surfaces during argon sputtering studied by XPS and AES. *Surf. Sci.* 151, 400–408. doi: 10.1016/0039-6028(85)90383-8

Rahmanian, R., and Mozaffari, S. A. (2015). Electrochemical fabrication of ZnO-polyvinyl alcohol nanostructured hybrid film for application to urea biosensor. *Sensors Actuators B Chem.* 207, 772–781. doi: 10.1016/j.snb.2014.10.129

Rahmanian, R., Mozaffari, S. A., and Abedi, M. (2015). Disposable urea biosensor based on nanoporous ZnO film fabricated from omissible polymeric substrate. *Mater. Sci. Eng. C* 57, 387–396. doi: 10.1016/j.msec.2015.08.004

Rayati, S., and Malekmohammadi, S. (2016). Catalytic activity of multi-wall carbon nanotube supported manganese (III) porphyrin: an efficient, selective and reusable catalyst for oxidation of alkenes and alkanes with urea–hydrogen peroxide. *J. Exp. Nanosci.* 11, 872–883. doi: 10.1080/17458080.2016.1179802

Rivas, G. A., Rubianes, M. D., Rodríguez, M. C., Ferreyra, N. F., Luque, G. L., Pedano, M. L., et al. (2007). Carbon nanotubes for electrochemical biosensing. *Talanta* 74, 291–307. doi: 10.1016/j.talanta.2007.10.013

Sabu, C., Henna, T., Raphey, V., Nivitha, K., and Pramod, K. (2019). Advanced biosensors for glucose and insulin. *Biosens. Bioelectron.* 141:111201. doi: 10.1016/j.bios.2019.03.034

Salek-Maghsoudi, A., Vakhshiteh, F., Torabi, R., Hassani, S., Ganjali, M. R., Norouzi, P., et al. (2018). Recent advances in biosensor technology in assessment of early diabetes biomarkers. *Biosens. Bioelectron.* 99, 122–135. doi: 10.1016/j.bios.2017.07.047

Shabnam, L., Faisal, S. N., Roy, A. K., Haque, E., Minett, A. I., and Gomes, V. G. (2017). Doped graphene/Cu nanocomposite: a high sensitivity non-enzymatic glucose sensor for food. *Food Chem.* 221, 751–759. doi: 10.1016/j.foodchem.2016.11.107

Shamsadin-Azad, Z., Taher, M. A., Cheraghi, S., and Karimi-Maleh, H. (2019). A nanostructure voltammetric platform amplified with ionic liquid for determination of tert-butylhydroxyanisole in the presence kojic acid. *J. Food Meas. Character.* 13, 1781–1787. doi: 10.1007/s11694-019-00096-6

Shojaei, A. F., Tabatabaeian, K., Shakeri, S., and Karimi, F. (2016). A novel 5-fluorouracile anticancer drug sensor based on $ZnFe_2O_4$ magnetic nanoparticles ionic liquids carbon paste electrode. *Sensors Actuators B Chem.* 230, 607–614. doi: 10.1016/j.snb.2016.02.082

Tahernejad-Javazmi, F., Shabani-Nooshabadi, M., and Karimi-Maleh, H. (2018). Analysis of glutathione in the presence of acetaminophen and tyrosine via an amplified electrode with MgO/SWCNTs as a sensor in the hemolyzed erythrocyte. *Talanta* 176, 208–213. doi: 10.1016/j.talanta.2017.08.027

Tahernejad-Javazmi, F., Shabani-Nooshabadi, M., and Karimi-Maleh, H. (2019). 3D reduced graphene oxide/$FeNi_3$-ionic liquid nanocomposite modified sensor; an electrical synergic effect for development of tert-butylhydroquinone and folic acid sensor. *Compos. Part B Eng.* 172, 666–670. doi: 10.1016/j.compositesb.2019.05.065

Wang, Y., Xu, H., Zhang, J., and Li, G. (2008). Electrochemical sensors for clinic analysis. *Sensors* 8, 2043–2081. doi: 10.3390/s8042043

Wei, Y., Li, Y., Liu, X., Xian, Y., Shi, G., and Jin, L. (2010). ZnO nanorods/Au hybrid nanocomposites for glucose biosensor. *Biosens. Bioelectron.* 26, 275–278. doi: 10.1016/j.bios.2010.06.006

Windischmann, H., and Mark, P. (1979). A model for the operation of a thin-film SnO x conductance-modulation carbon monoxide sensor. *J. Electrochem. Soc.* 126:627. doi: 10.1149/1.2129098

Yao, L. R., and Lu, F. H. (2013). Low vacuum deposition of aluminum nitride thin films by sputtering. *Int. J. Appl. Ceram. Technol.* 10, 51–59. doi: 10.1111/j.1744-7402.2012.02790.x

Zhao, Y., Li, W., Pan, L., Zhai, D., Wang, Y., Li, L., et al. (2016). ZnO-nanorods/graphene heterostructure: a direct electron transfer glucose biosensor. *Sci. Rep.* 6:32327. doi: 10.1038/srep32327

Zhou, F., Jing, W., Liu, P., Han, D., Jiang, Z., and Wei, Z. (2017). Doping Ag in ZnO nanorods to improve the performance of related enzymatic glucose. *Sensors* 17:2214. doi: 10.3390/s17102214

Zhu, H., Li, L., Zhou, W., Shao, Z., and Chen, X. (2016). Advances in non-enzymatic glucose sensors based on metal oxides. *J. Mater. Chem. B* 4, 7333–7349. doi: 10.1039/C6TB02037B

Conflict of Interest: The authors declare that the research was conducted in the absence of any commercial or financial relationships that could be construed as a potential conflict of interest.

frontiers in Chemistry

ORIGINAL RESEARCH
published: 10 September 2020
doi: 10.3389/fchem.2020.00689

Electrochemical Oxidation and Determination of Antiviral Drug Acyclovir by Modified Carbon Paste Electrode With Magnetic CdO Nanoparticles

Ebrahim Naghian[1,2,3], *Elnaz Marzi Khosrowshahi*[4], *Esmail Sohouli*[5], *Hamid Reza Pazoki-Toroudi*[6], *Ali Sobhani-Nasab*[7,8], *Mehdi Rahimi-Nasrabadi*[1,2]* and *Farhad Ahmadi*[6,9]*

[1] Chemical Injuries Research Center, Systems Biology and Poisonings Institute, Baqiyatallah University of Medical Sciences, Tehran, Iran, [2] Faculty of Pharmacy, Baqiyatallah University of Medical Sciences, Tehran, Iran, [3] Department of Chemistry, South Tehran Branch Islamic Azad University, Tehran, Iran, [4] Faculty of Pharmacy, Tabriz University of Medical Sciences, Tabriz, Iran, [5] Young Researchers and Elites Club, Science and Research Branch, Islamic Azad University, Tehran, Iran, [6] Physiology Research Center, Iran University of Medical Sciences, Tehran, Iran, [7] Social Determinants of Health (SDH) Research Center, Kashan University of Medical Sciences, Kashan, Iran, [8] Core Research Lab, Kashan University of Medical Sciences, Kashan, Iran, [9] Department of Medicinal Chemistry, School of Pharmacy-International Campus, Iran University of Medical Sciences, Tehran, Iran

With the development of nanomaterials in electrochemical sensors, the use of nanostructures to modify the electrode surface has been shown to improve the kinetics of the electron transfer process. In this study, a sensor was developed for the electrochemical determination of Acyclovir (ACV) based on the modified carbon paste electrode (CPE) by CdO/Fe_3O_4. The magnetic CdO nanoparticles characterization was studied by energy-dispersive X-ray spectroscopy (EDS) and X-ray diffraction (XRD). To study of the modified CPE surface morphology, scanning electron microscopy (SEM) was used. At the optimal conditions, a noteworthy enhancement in the electrochemical behavior of ACV was observed at the surface of the modified CPE compared to the unmodified CPE. A detection limit of 300 nM and a linear range of 1–100 μM were obtained for the quantitative monitoring of ACV at the modified CPE surface using differential pulse voltammetry (DPV) in phosphate buffer. The RSD% (relative standard deviation) of the electrode response was <4.3% indicating the development of a high precision method. Also, satisfactory results were obtained in the determination of ACV with the modified electrode in tablet, blood serum, and urine samples with a satisfactory relative recovery (RR%) in the range of 94.0–104.4%.

Keywords: acyclovir, antiviral drug, carbon paste electrode, electrochemical sensor, magnetic cadmium oxide, nanoparticle

OPEN ACCESS

Edited by:
Hassan Karimi-Maleh, University of Electronic Science and Technology of China, China

Reviewed by:
Alexandru Mihai Grumezescu, Politehnica University of Bucharest, Romania
Fatemeh Karimi, Ton Duc Thang University, Vietnam
Somaye Cheraghi, Shahid Bahonar University of Kerman, Iran
Vahid Arabali, Islamic Azad University Sari Branch, Iran

***Correspondence:**
Mehdi Rahimi-Nasrabadi
rahiminasrabadi@gmail.com
Farhad Ahmadi
farhadljhnf@yahoo.com

Specialty section:
This article was submitted to Analytical Chemistry, a section of the journal Frontiers in Chemistry

Received: *21 May 2020*
Accepted: *02 July 2020*
Published: *10 September 2020*

Citation:
Naghian E, Marzi Khosrowshahi E, Sohouli E, Pazoki-Toroudi HR, Sobhani-Nasab A, Rahimi-Nasrabadi M and Ahmadi F (2020) Electrochemical Oxidation and Determination of Antiviral Drug Acyclovir by Modified Carbon Paste Electrode With Magnetic CdO Nanoparticles. Front. Chem. 8:689. doi: 10.3389/fchem.2020.00689

INTRODUCTION

Herpes simplex is a type of skin infection caused by the herpes hominies virus (Braun-Falco et al., 1991) and is commonly known as herpes blister. There are two different types of herpes simplex virus types 1 and 2 of the herpes virus family that infect humans. The immune system removes the virus from the skin, but the virus hides itself in the nerves and may reappear in the future.

2-amino-9-[(2-hydroxyethoxy) methyl]-6,9-dihydro-3H-purin-6-one or acyclovir (ACV) is one of the effective drugs for reduces of this virus (Piret and Boivin, 2017). ACV is an antiviral drug with significant activity. It plays a significant role in the treatment of the virus illnesses and is very distinctive in helping the body to fight infection effectively and provide the necessary immunity. ACV does not completely cure herpes disease, but it certainly works to reduce the symptoms and spread herpes infection (Kłysik et al., 2020; Luyt et al., 2020). ACV is widely used in the therapy of herpes zoster infections, herpes simplex, herpetic encephalitis, primary genital herpes, and varicella-zoster virus infections in immunosuppressed patients. It is also helpful in inhibiting HSV infections in renal allograft receptors (Tenser and Tenser, 2019) and its anti-hepatitis B virus activity has been demonstrated (Huang et al., 2011). ACV may lead to neurotoxicity (coma, hallucinations, lethargy, tremors, and seizures) and nephrotoxicity (crystallization of ACV within renal tubules, transient, and enhancement of serum creatinine) (Fleischer and Johnson, 2010). As ACV is structurally similar to endogenous substances and because of its high solubility in water, it is very difficult to isolate and measure it in biological fluids. Therefore, its analysis in human serum is complicated and requires high selective analytical methods. With notice of these facts, the quantitative monitoring of ACV in biological fluids and other real samples appears very important. Several analytical methods have been developed for the analysis of ACV including near-infrared spectroscopy (Yu and Xiang, 2008), fluorimetric and photometric methods (Macka et al., 1993), radioimmunoassay (RIA) (Tadepalli and Quinn, 1996), and LC (liquid chromatography) (Tzanavaras and Themelis, 2007; Mulabagal et al., 2020). The mentioned methods are commonly needed expensive equipment, more time and tedious processes. For example, LC methods need to optimize the chromatographic conditions and samples preparation or RIA method hands the radioactive wastes. Although, electrochemical methods including differential pulse voltammetry (DPV), cyclic voltammetry (CV), square wave voltammetry, amperometry, electro-chemiluminescence, and polarography (Wang et al., 2006, 2013; Heli et al., 2010; Shetti et al., 2012, 2017; Karim-Nezhad et al., 2018) provide advantages such as simplicity, high sensitivity, low cost, fast response, and more environmentally friendly techniques (Adib et al., 2016; Rahimi-Nasrabadi et al., 2017; Amani et al., 2018a,b; Khoshroo et al., 2018, 2019; Naghian et al., 2020; Sanatkar et al., 2020; Sohouli et al., 2020a,b). Metal oxide nanoparticles have been extensively developed in the past decades. Among the metal oxide nanoparticles, cadmium oxide nanoparticles (CdONPs) are attractive because of wide non-toxicity, high isoelectric point and large surface area. So, CdNPs is a promising candidate for support material in the construction of the biosensors (Jing and Bowser, 2011; Fouladgar, 2018; Malekmohammadi et al., 2018; Kumar H.C. et al., 2019; Maduraiveeran et al., 2019; Mitra et al., 2019). metal nanoparticles modified electrodes show rapid redox activity toward the compounds with slow electron kinetics at bare electrodes, resolve overlapped peaks of analytes with close oxidation potentials and reveal good peak to peak separations (Baig et al., 2019; Sajid and Baig, 2019; Sinha et al., 2019). Metal ferrite or magnetic compounds have long been considered owing to its unique properties such as chemical and thermal stability, lower toxicity relative to other metals and cost-effectiveness. The most special and important property of metal ferrite for electrochemical applications is its good conductivity which originates from charge hopping of carriers between cations occupying the octahedral site (Beitollai et al., 2019; Khorshed et al., 2019; Kumar S. et al., 2019; Pastucha et al., 2019).

In this paper, a novel magnetic cadmium oxide CdO/Fe_3O_4 modifier was used to modify a carbon paste electrode (CPE). The electrocatalytic activity of the modified CPE was investigated for the detection and analysis of ACV using DPV. The interaction between cadmium ion and ACV enhances the accumulation of the drug on the surface of the modified electrode and increasing the sensitivity of the measurement. After optimization of the experimental parameters, the modified electrode was used for analyses of the low level of ACV in real samples including biological fluid (plasma and urine) and tablet.

EXPERIMENTAL

Instrumentation

Voltammetric measurements were performed using a three-electrode system consisting of the Ag/AgCl electrode as the reference electrode (Azar Electrode Co., Iran), the platinum wire as the auxiliary electrode (Azar Electrode Co., Iran) and a modified CPE as the working electrode. A μ-Autolab type III/FRA2 potentiostat/galvanostat with NOVA software was used for impedance measurements. To determine the structure and morphology of synthesized magnetic nanoparticles, FESEM images were obtained the SIGMA VP field emission scanning electron microscope coupled with EDS analysis and FEI NOVA NanoSEM450 instrument. X-ray diffraction (XRD) patterns were recorded by a Philips-X'pertpro, diffractometer containing Ni-filtered Cu K*a* radiation. The Metrohm pH meter (Model 691) was used to adjust the solutions' pH. The voltammograms were recorded via the PSTrace software and all data analysis were performed using Excel software.

Chemicals and Reagents

All chemicals were prepared in high purity analytical grade from Merck Company (Germany). ACV standard powder was obtained from the Rouz Darou Company. The Stock solutions of ACV were prepared by dissolving the appropriate amounts in a suitable volume of water before analysis. Other standard solutions were obtained by diluting the stock solutions with phosphate buffer solution.

Synthesis of Fe_3O_4 Nanoparticles

The Fe_3O_4 magnetic nanoparticles were synthesis by a reaction between 0.02 mol of iron (II) chloride and 0.03 mol of iron (III) chloride. These salts were dissolved in a 40 mL of degassed HCl (0.4 M) solution and then 375 mL of degassed ammonia solution (25%) was added to the above solution during 45 min drop by drop under sonication. After that, the black precipitate (Fe_3O_4 nanoparticles) was formed. Finally, the separated products were

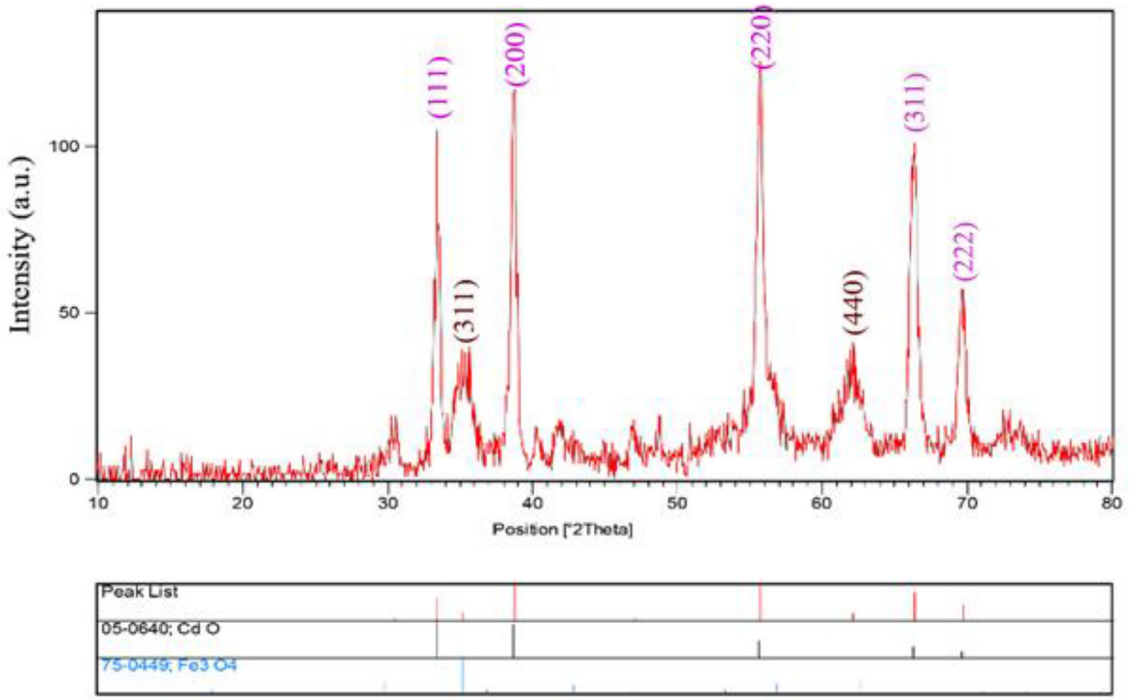

FIGURE 1 | The XRD pattern of CdO/Fe_3O_4.

washed with ethanol and deionized water and dried in an oven at 70°C (Enayat, 2018).

Synthesis of CdO/Fe_3O_4 Nanoparticles

The synthesized Fe_3O_4 nanoparticles were dispersed in 50 mL of deionized water. The dispersion was stirred softly for 10 min to become homogenous. One millimole of cadmium nitrate warm solution (70°C) and Fe_3O_4 dispersion were added to 50 mL of NaOH with a concentration of 2.5 mol L^{-1} under stirring conditions for 15 min. Finally, the CdO/Fe_3O_4 precipitation was rinsed with distilled water and after drying, it was calcined at 450°C for 70 min (Vosoughifar, 2018).

Preparation of Modified Carbon Paste Electrode With Magnetic Nanoparticles

0.14 g of graphite, 0.01 g of magnetic nanoparticles and some oil were mixed to achieve a uniform paste. The resulting paste was then put into a plastic tube (id = 2 mm). The electrical transmission was made using a copper wire. The surface of the electrode was polished on a paper sheet to be perfectly uniform. The unmodified CPE was obtained from a mixture of 0.15 g of graphite and oil with no modifier similar to the mentioned procedure.

Tablet, Urine, and Plasma Samples Pretreatment

To prepare tablet sample (ROUZ DAROU Co.), 10 tablets (each containing 200 mg of ACV) were weighed and uniformly powdered. The 225 mg of the obtained powder was dissolved in 100 mL of 0.1 M phosphate buffer (pH = 4). The resulting solution was diluted 500-folds and stirred for 10 min to dissolve completely and finally it was filtered before use. Urine and plasma samples were stored in the refrigerator after collection. Then 5 ml of the solutions were centrifuged for 5 min at 5,000 rpm (to remove suspended particles. These particles sometimes contaminate the surface by absorbing on the electrode and reduce its efficiency). The dilution with phosphate buffer (pH = 4) was done at a ratio of 0.1 to reduce the matrix effect. The ACV content of samples was measured using the standard addition method.

RESULTS AND DISCUSSION

EDS and XRD Analysis of As-Synthesized Magnetic CdO

The XRD patterns of CdO/Fe_3O_4 nanostructures have been presented in **Figure 1**. As our results advice, CdO/Fe_3O_4 nanostructure has high purity and two phases. The first phase is the Fe_3O_4 sample shows a series of diffraction peaks at the position of 35.45° [(311) line], 43.08° [(400) line], 57.16° [(511) line], and 62.72° [(440) line] that is in good agreement with the standard JCPDS file of Fe_3O_4 Cubic phase (space group Fd-3m, JCPDS No. 75-0449) and CdO shows a series of diffraction peaks at the position of 33.35° [(111) line], 38.78° [(200) line], 55.52° [(220) line], 65.92° [(311) line], and 69.33° [(222) line] which is in good agreement with the standard JCPDS with the crystal structure of tetragonal (JCPDS 75-0592) with a space group of Fd-3m, respectively (Vosoughifar,

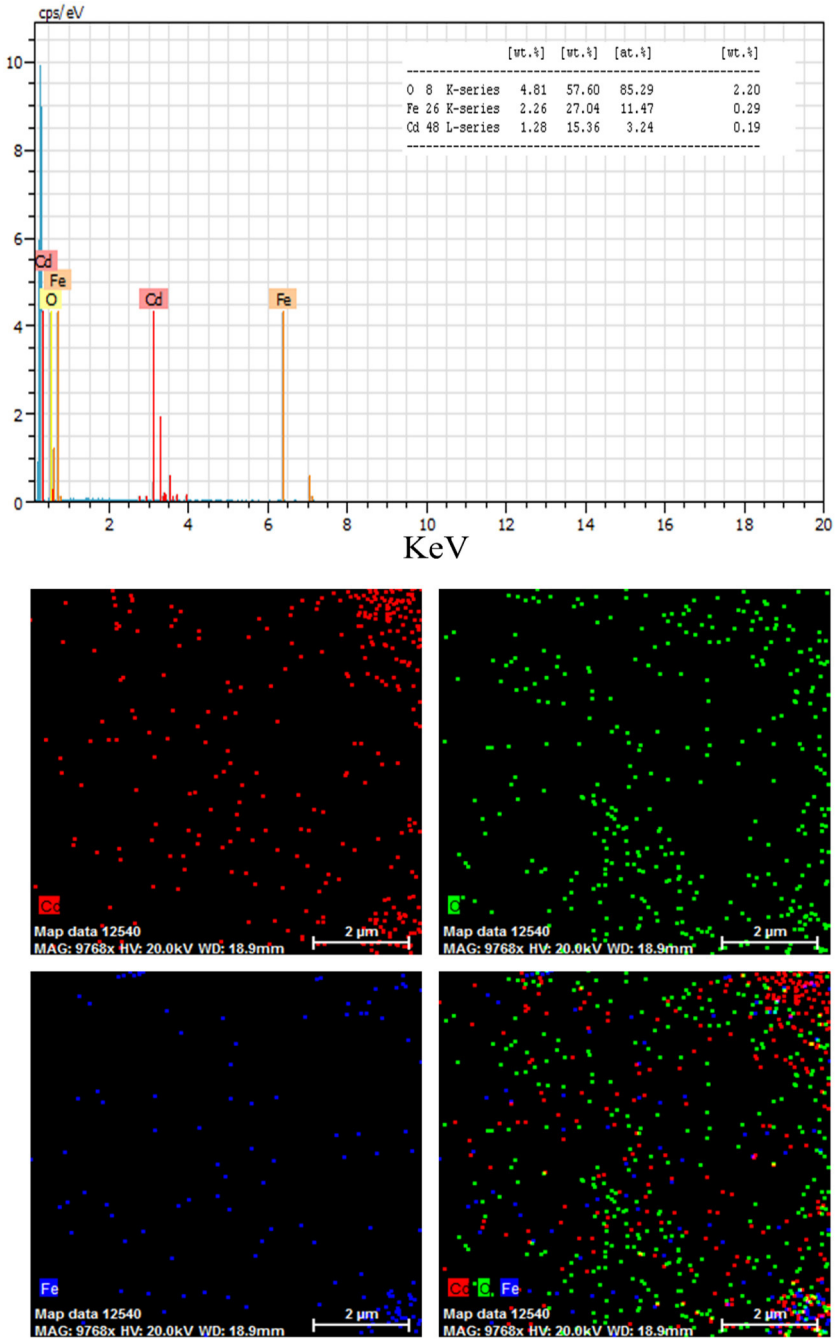

FIGURE 2 | The results of EDS analysis for CdO/Fe_3O_4 nanoparticles.

2018). Crystalline sizes of nanoparticles are calculated from Scherer equation:

$$Dc = K\lambda/\beta Cos\theta$$

where K is the shape factor, λ is the X-ray wavelength (Cu Kα radiation, equals to 0.154 nm), β is the width of the observed diffraction peak at its half maximum intensity, which takes a value of about 0.9 and θ is the angle between the incident beam and the sample surface. The CdO/Fe_3O_4 nanoparticles sizes were about 23 nm. The EDS analysis approves the presence of Cd, Fe and oxygen elements with no impurity (**Figure 2**).

Optimization of the Percentage of Magnetic Nanoparticles

To achieve the high-performance CPE, a suitable ratio between oil and graphite is needed (9–10%). Higher and lower percentages

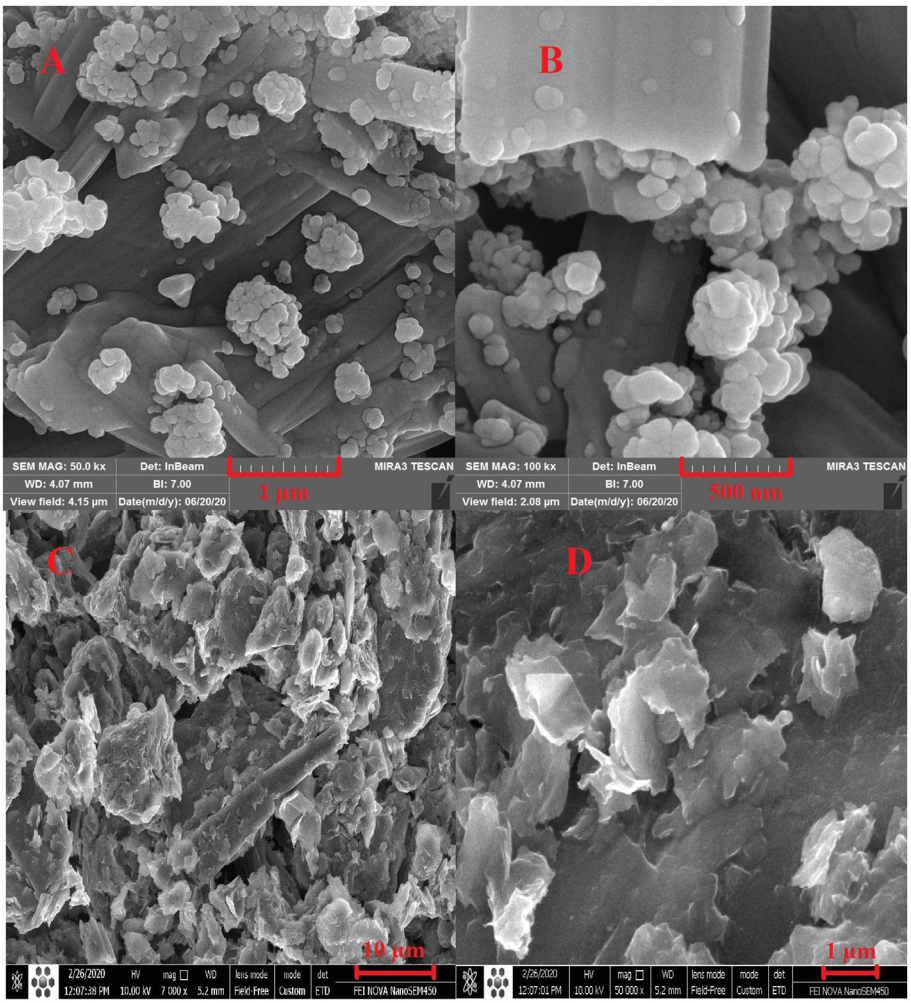

FIGURE 3 | The SEM images of magnetic CdO nanoparticles **(A,B)** and carbon paste with magnetic CdO **(C,D)**.

are not suitable because the high amounts of oil obtain a flowing liquid and increase the surface hydrophobicity. In lower oil percentages, the electrode absorbs water and falls apart. However, the percentage of nanoparticles should be optimized due to the effect on sensor sensitivity and signal amplification. For this purpose, CPE with different weight ratios of magnetic CdO: graphite (3, 5, 7, and 10%) were prepared and its efficiency for measuring 30 µA of ACV was evaluated. The results showed that from 3 to 10 incremental trends are observed in the signal, but after 7% this trend continues with a lower slope, so for optimal consumption of nanoparticles, this value was used as the optimal percentage in the structure of the electrode.

Working Electrode Surface Area and Microscopic Imaging

The SEM technique was used to illustrate the morphology of magnetic nanoparticles after being embedded in the carbon paste matrix. **Figure 3** shows that the CPE plate morphology becomes cavernous by adding nanoparticles and the surface area increases significantly. The enhancement of magnetic nanoparticles provides a more porous structure for the CPE and increases the active surface area of the electrode in contact with the electrolyte and the electroactive species.

The effective surface area of the electrode (A, cm^2) was calculated from obtained CV data of 5 mM $K_3[Fe(CN)_6]$ with a diffusion coefficient (D, $Cm^2\ s^{-1}$) of 7.5×10^{-6}. It was calculated from the Randles-Sevcik equation (Bard and Faulkner, 2001):

$$I_{pa} = 2.69\times10^5 n^{3/2} A C_0 D^{1/2}\ v^{1/2}$$

where n is the number of transferred electrons in the oxidation and reduction process of ferrocyanide, C is the concentration of ferrocyanide (5×10^{-9} mol cm^{-3}) and v is the scan rate. The value of CdO/Fe_3O_4/CPE surface area (0.31 cm^2) is greater than the unmodified CPE (0.14 cm^2) which can be lead to exist of more electrochemical reaction sites.

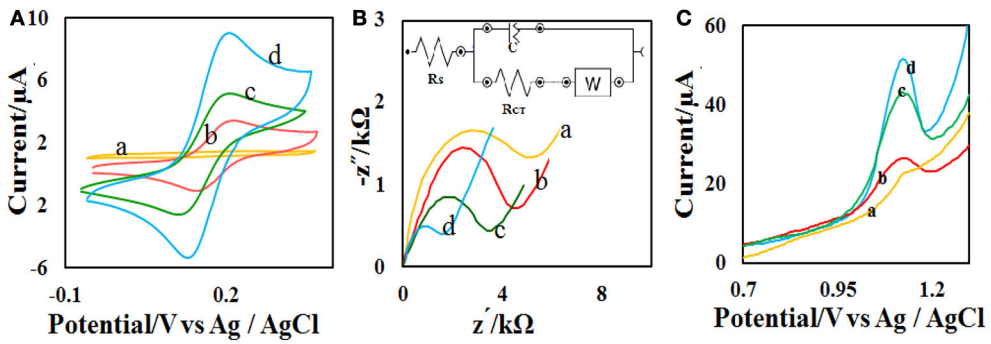

FIGURE 4 | (A) CVs and **(B)** Nyquist plots of the different modified electrodes in 0.1 M PB containing 5.0 mM $[Fe(CN)_6]^{-3/-4}$ at (a) bare, (b) CdO NP/CPE, (c) Fe_3O_4 NP/CPE, and (d) CdO/Fe_3O_4 NP/CPE in the scan rate of 50 mV s^{-1} **(C)** The recorded DPVs of the (a) bare, (b) CdO NP/CPE, (c) Fe_3O_4 NP/CPE, and (d) CdO/Fe_3O_4 NP/CPE in presence of 50 μM ACV.

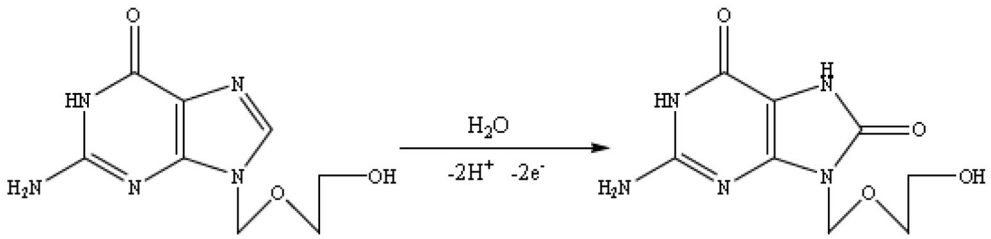

FIGURE 5 | The ACV oxidation mechanism.

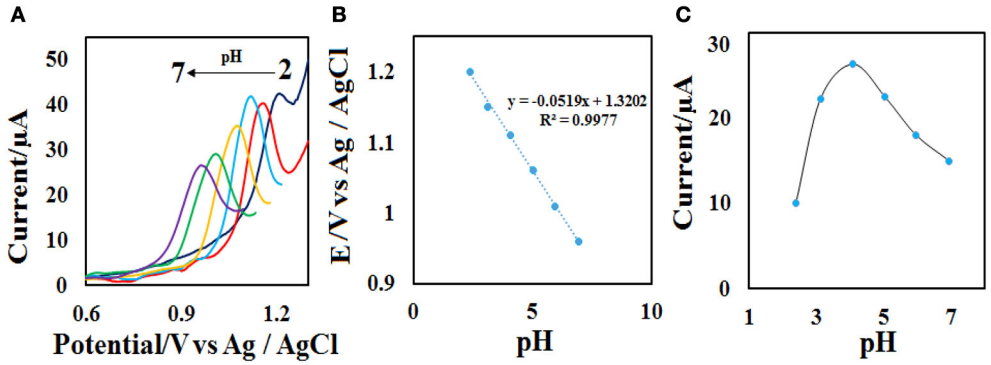

FIGURE 6 | (A) DPVs of the CdO/Fe_3O_4/CPE at various pH values (2, 3, 4, 5, 6, and 7). **(B)** Plots of the E_p vs. pH value and **(C)** I_p vs. pH value in the presence of 50 μM ACV.

Electro-Oxidation Behavior of the Redox Probe and ACV on the Modified CPE

The CV technique was employed to evaluate the performance of the prepared electrodes. For this purpose, electrochemical measurements were done in the mixture of Fe^{2+}/Fe^{3+} aqueous solution (5 mM, molar ratio 1:1) containing 0.1 M potassium chloride in the potential range of −0.3 to 0.7 V (**Figure 4A**). At the CPE surface, the oxidation and reduction peaks of Fe^{2+}/Fe^{3+} are very weak. However, when the electrode was modified with CdO/Fe_3O_4 an oxidation-reduction peak for Fe^{2+}/Fe^{3+} solution showed a difference between the peaks of 80 mV indicating that this electrode has better capability rather than the unmodified electrode.

EIS (electrochemical impedance spectroscopy) was used to measure the surface resistance of different electrodes. The purpose of this section is to examine changes in the rate of electron transfer at different electrode surfaces. **Figure 4B** presents the Nyquist plots in the presence of Fe^{2+}/Fe^{3+} aqueous solution (5 mM) and 0.1 M potassium chloride solution. Semicircular diameter indicates electron transfer resistance (R_{ct}) of the redox probe reaction. The R_{ct} parameter in this technique indicates the reaction kinetics at the electrode surfaces. The value of R_{ct} for CPE (5 kΩ) bigger than the modified CPE (1.2 Ω).

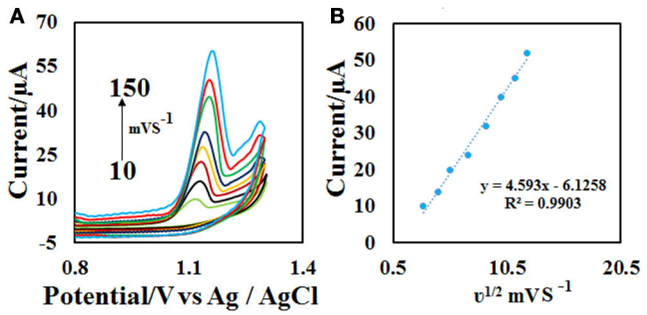

FIGURE 7 | (A) CVs on the CdO/Fe_3O_4/CPE in 0.1 M phosphate buffer (pH = 4.0) containing 50 μM ACV solution at different scan rates (10–150 mVs^{-1}) and **(B)** the plot of **(B)** I_p vs. $\upsilon^{1/2}$.

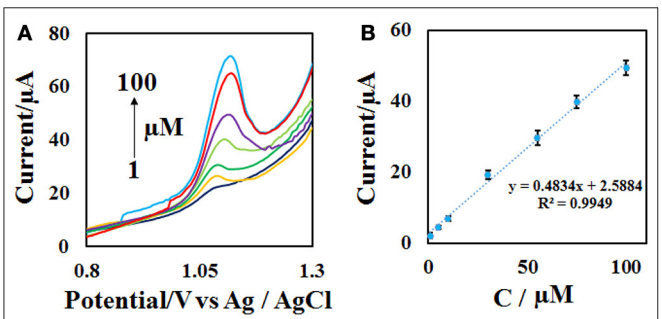

FIGURE 8 | (A) DPVs of the CdO/Fe_3O_4/CPE in the presence of 1–100 μM ACV in 0.1 M phosphate buffer (pH = 4) and the scan rate of 50 mV s^{-1} and **(B)** the calibration curve.

TABLE 1 | Comparison of the method with other electrochemical methods.

Modifier/electrode	Linear range (μM)	LOD (μM)	References
GCE/MWCNT/ZnO	0.009–1	0.006	Karim-Nezhad et al., 2018
CPE/Nnao clay	0.05–1	0.0002	Shetti et al., 2017
GCE/MWCNT-DHP[a]	0.79–130	0.16	Wang et al., 2006
GCE/C60	0.8–6	0.15	Shetti et al., 2012
CPE/PVP[b]	0.01–75	0.03	Wang et al., 2013
CPE/CuNPs	27–521	2.6	Heli et al., 2010
CdO/Fe_3O_4/CPE	1–100	0.3	This work

[a] *Dihexadecyl hydrogen phosphate.*
[b] *Polyvinylpyrrolidone.*

This behavior is due to the accelerate of the probe redox electron transfer at the CdO/Fe_3O_4/CPE surface.

The electro-oxidation behavior of the analyte on the CdO/Fe_3O_4/CPE surface was examined by the DPV method (**Figure 4C**). Comparison of the recorded DPVs of the bare, CdO/CPE, Fe_3O_4/CPE, and CdO/Fe_3O_4/CPE in presence of 50 μM ACV shows that the oxidation of ACV on the CdO/Fe_3O_4/CPE surface has a higher current and lower potential.

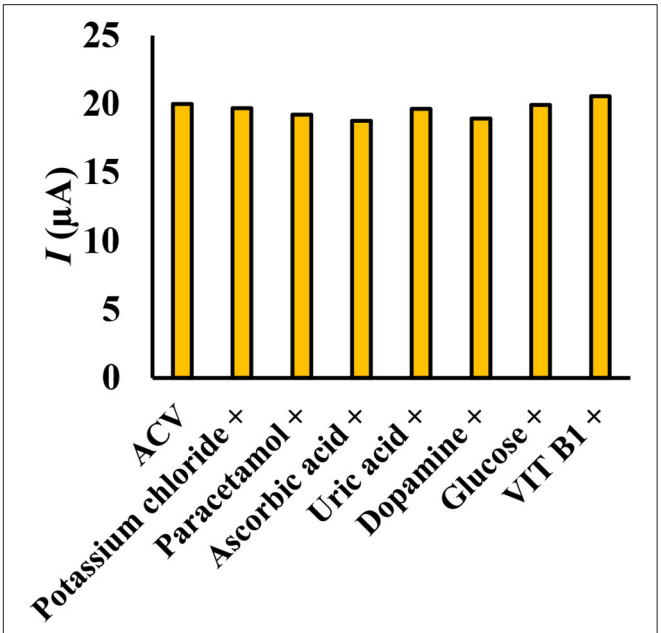

FIGURE 9 | Simultaneous determination of ACV in the presence of some interfering species (ratio >100), the experimental conditions: 0.1 M phosphate buffer, pH = 4, scan rate = 50 mVs^{-1}, ACV concentration = 30 μM.

TABLE 2 | Determination of ACV content in real samples with relative recovery.

Sample	Added (μM)	Found (μM)	RR (%)	RSD (%), $n = 5$
Tablet (200 mg)	0	20.2	100.1	2.3
	5	24.7	98.8	1.9
	10	30.2	100.6	1.9
	20	40.1	100.2	2.1
Urine	0	0	Not detected	–
	10.0	9.4	94.0	1.9
	15.0	15.1	100.6	2.3
	30.0	31.1	103.4	1.7
Plasma	0	0	Not detected	–
	25.0	26.1	104.4	1.5
	35.0	34.4	98.3	2.1
	50.0	50.0	100.1	2.1

Effect of Electrolyte pH and Reaction Mechanism

The effect of solution pH on the ACV oxidation peak in the pH ranges from 2 to 7 was investigated in the presence of phosphate buffer as a supporting electrolyte. The oxidation potential of ACV changed with increasing pH. This indicates that the proton is involved in oxidative reactions. The oxidation potential of ACV is shifted to negative values by changing pH. According to the structure of ACV, the electrochemical oxidation process of ACV participates is equal protons and electrons (**Figure 5**).

This mechanism is also confirmed by electrochemical methods presented in the previous work (Shetti et al., 2017). So the pH is important for the determination of ACV and its maximum oxidation current at developed sensor was obtained in pH = 4 that used for further studies (**Figure 6**).

Effect of Scan Rate

The effect of scan rate on the electrochemical properties of the CdO/Fe_3O_4/CPE was investigated by the recording of the related voltammogram at different scan rates from 10.0 to 150.0 mV s^{-1} in the 0.1 M phosphate buffer containing 50 μM ACV. As seen in **Figure 7A**, with the increase of scan rates the oxidation peak current increases and the E_p value, slightly increases. The relationship between the oxidation peak currents (I_p) vs. the square root of the scan rate ($\upsilon^{1/2}$) was obtained to be linear in the range of 10.0–150.0 mV s^{-1} under the corresponding equations including $I_{pa} = 4.593\ \upsilon^{1/2} - 6.1258$ (**Figure 7B**). These results emphasize a diffusion-controlled oxidation process at the CdO/Fe_3O_4/CPE surface.

Analytical Variation and Comparison of the Proposed Method With Other Electrosensors

To achieve the working range of the developed sensor, the DPV of different concentrations of ACV (**Figure 8A**) were obtained at the optimal condition (0.1 M phosphate buffer with pH = 4.0 and the scan rate = 50 mV s^{-1}) with 3 replicates. The plotting of current vs. concentration shows that the linear range of the method is in the range of 1–100 μM with a detection limit of 0.3 μM (**Figure 8B**). Other analytical performance parameters including repeatability and stability were investigated according to follow.

To investigate the repeatability of the modified electrode response, the ACV related voltammograms were plotted 5 times at three different concentrations and the RSD (relative standard deviation) of the electrode response was calculated. RSD values of the electrode response were <4.3%. The stability of the modified CPE was checked with the recording of ACV voltammograms once a week consecutively for 8 weeks. The results indicate that the desired CdO/Fe_3O_4/CPE surface has long-term stability and in the eighth week, only a 5% signal decrease was observed compared with the first week.

In a comparison of the developed method with the other proposed methods for the measurement of ACV (**Table 1**) appears some advantages of this method. The used electrode is economical in comparing of glassy carbon electrode (GCE) or dispersed nanoparticles modifiers. Other analysis parameters such as the detection limit and the linear range are comparable and in some cases better than the presented methods.

Interfering Effect

To measure ACV in different matrices, it is necessary to investigate the effect of species that can oxidize or reduce on the electrode surface. The effect of different substances on the potential interaction of ACV determination at optimum conditions was studied. Interfering substances were selected from the group of substances present in biological and pharmaceutical fluids. The nuisance threshold was determined as the maximum species with an error of <5% in the determination of ACV. The results (**Figure 9**) showed that the presence of glucose, ascorbic acid, dopamine, uric acid, paracetamol, acetaminophen, vitamin B1, and potassium chloride did not affect the sensor selectivity. It should be noted that these species do not have any overlapped peak in the same peak potential of ACV.

Real Sample Analysis

To investigate the application of the modified electrode in the electrochemical determination of ACV, tablet, urine and plasma samples were selected. **Table 2** shows the results of this analysis. The results confirm the high performance of the modified electrode for measuring ACV in real samples. Each sample was spiked with three levels of ACV in the calibration range and the amount of ACV was obtained from the standard addition method. To achieve the relative recovery (RR) of the method, the ratio of ACV analytical signal in phosphate buffer and real samples was calculated. The recovery results (94.0–104.4%) indicate good accuracy for the presented method in real samples.

CONCLUSIONS

The electrochemical behavior of ACV was investigated on an electrochemical sensor modified with magnetic CdO nanoparticles. The electrochemical response was a diffusion control process. High sensitivity and low detection limit (300 nM), as well as easy preparation and easy surface recovery of the modified electrode, are the main advantages of this sensor. The proposed sensor as an effective electrochemical sensor was used to the ACV determination by DPV technique in biological fluids.

DATA AVAILABILITY STATEMENT

The raw data supporting the conclusions of this article will be made available by the authors, without undue reservation.

ETHICS STATEMENT

The studies involving human participants were reviewed and approved by ethics committee of Iran University of Medical Sciences. Written informed consent from the participants was not required to participate in this study in accordance with the national legislation and the institutional requirements.

AUTHOR CONTRIBUTIONS

All authors listed have made a substantial, direct and intellectual contribution to the work, and approved it for publication.

ACKNOWLEDGMENTS

The authors gratefully acknowledge the financial support of this work by Iran University of Medical Sciences with Grant No. 15507. Also, this proposal has the ethic code of IR.IUMS.REC.1398.665.

REFERENCES

Adib, K., Rahimi-Nasrabadi, M., Rezvani, Z., Pourmortazavi, S. M., Ahmadi, F., Naderi, H. R., et al. (2016). Facile chemical synthesis of cobalt tungstates nanoparticles as high performance supercapacitor. *J. Mater. Sci. Mater. Electron.* 27, 4541–4550. doi: 10.1007/s10854-016-4329-4

Amani, J., Khoshroo, A., and Rahimi-Nasrabadi, M. (2018a). Electrochemical immunosensor for the breast cancer marker CA 15–3 based on the catalytic activity of a CuS/reduced graphene oxide nanocomposite towards the electrooxidation of catechol. *Microchim. Acta* 185, 79. doi: 10.1007/s00604-017-2532-5

Amani, J., Maleki, M., Khoshroo, A., Sobhani-Nasab, A., and Rahimi-Nasrabadi, M. (2018b). An electrochemical immunosensor based on poly p-phenylenediamine and graphene nanocomposite for detection of neuron-specific enolase via electrochemically amplified detection. *Analyt. Biochem.* 548, 53–59. doi: 10.1016/j.ab.2018.02.024

Baig, N., Sajid, M., and Saleh, T. A. (2019). Recent trends in nanomaterial-modified electrodes for electroanalytical applications. *TrAC Trends Analyt. Chem.* 111, 47–61. doi: 10.1016/j.trac.2018.11.044

Bard, A. J., and Faulkner, L. R. (2001). *Electrochemical Methods: Fundamentals and Applications*, Vol. 2. New York, NY: John Wiley & Sons, 482.

Beitollai, H., Mohammadi, S. Z., and Tajik, S. (2019). Electrochemical behavior of morphine at the surface of magnetic core shell manganese ferrite nanoparticles modified screen printed electrode and its determination in real samples. *Int. J. Nano Dimens.* 10, 304–312.

Braun-Falco, O., Plewig, G., Wolff, H. H., and Winkelmann, R. K. (eds.). (1991). "Erythematous and erythematosquamous skin diseases," in *Dermatology* (Berlin; Heidelberg: Springer), 403–466. doi: 10.1007/978-3-662-00181-3_14

Enayat, M. J. (2018). Fabrication of $Fe_3O_4/CaCO_3/CuWO_4$ heterostructures for enhanced photocatalytic activities for the degradation of organic dyes. *J. Mater. Sci. Mater. Electron.* 29, 19435–42. doi: 10.1007/s10854-018-0072-3

Fleischer, R., and Johnson, M. (2010). Acyclovir nephrotoxicity: a case report highlighting the importance of prevention, detection, and treatment of acyclovir-induced nephropathy. *Case Rep. Med.* 2010:602783. doi: 10.1155/2010/602783

Fouladgar, M. (2018). CuO-CNT nanocomposite/ionic liquid modified sensor as new breast anticancer approach for determination of doxorubicin and 5-fluorouracil drugs. *J. Electrochem. Soc.* 165:B559. doi: 10.1149/2.1001811jes

Heli, H., Zarghan, M., Jabbari, A., Parsaei, A., and Moosavi-Movahedi, A. (2010). Electrocatalytic oxidation of the antiviral drug acyclovir on a copper nanoparticles-modified carbon paste electrode. *J. Solid State Electrochem.* 14, 787–795. doi: 10.1007/s10008-009-0846-x

Huang, S.-T., Du, Y.-Z., Yuan, H., Zhang, X.-G., Miao, J., Cui, F.-D., et al. (2011). Synthesis and anti-hepatitis B virus activity of acyclovir conjugated stearic acid-g-chitosan oligosaccharide micelle. *Carbohydrate Polym.* 83, 1715–1722. doi: 10.1016/j.carbpol.2010.10.032

Jing, M., and Bowser, M. T. (2011). Methods for measuring aptamer-protein equilibria: a review. *Analyt. Chim. Acta* 686, 9–18. doi: 10.1016/j.aca.2010.10.032

Karim-Nezhad, G., Sarkary, A., Khorablou, Z., and Dorraji, P. S. (2018). Synergistic effect of ZnO nanoparticles and carbon nanotube and polymeric film on electrochemical oxidation of acyclovir. *Iran J Pharm. Res.* 17, 52–62.

Khorshed, A. A., Khairy, M., Elsafty, S. A., and Banks, C. E. (2019). Disposable screen-printed electrodes modified with uniform iron oxide nanocubes for the simple electrochemical determination of meclizine, an antihistamine drug. *Analyt. Methods* 11, 282–287. doi: 10.1039/C8AY02405G

Khoshroo, A., Hosseinzadeh, L., Sobhani-Nasab, A., Rahimi-Nasrabadi, M., and Ahmadi, F. (2019). Silver nanofibers/ionic liquid nanocomposite based electrochemical sensor for detection of clonazepam via electrochemically amplified detection. *Microchem. J.* 145, 1185–1190. doi: 10.1016/j.microc.2018.12.049

Khoshroo, A., Hosseinzadeh, L., Sobhani-Nasab, A., Rahimi-Nasrabadi, M., and Ehrlich, H. (2018). Development of electrochemical sensor for sensitive determination of oxazepam based on silver-platinum core–shell nanoparticles supported on graphene. *J. Electroanalyt. Chem.* 823, 61–66. doi: 10.1016/j.jelechem.2018.05.030

Kłysik, K., Pietraszek, A., Karewicz, A., and Nowakowska, M. (2020). Acyclovir in the treatment of herpes viruses–a review. *Curr. Med. Chem.* 25:4118–4137. doi: 10.2174/0929867325666180309105519

Kumar, H. C., Shilpa, R., and Ananda, S. (2019). Synthesis of cadmium oxide nanoparticles by electrochemical method: its photodegradative effects on carboxylic acids and antibacterial behaviours. *J. Nanosci. Technol.* 5, 840–5. doi: 10.30799/jnst.278.19050505

Kumar, S., Umar, M., Saifi, A., Kumar, S., Augustine, S., Srivastava, S., et al. (2019). Electrochemical paper based cancer biosensor using iron oxide nanoparticles decorated PEDOT: PSS. *Analyt. Chim. Acta* 1056, 135–45. doi: 10.1016/j.aca.2018.12.053

Luyt, C.-E., Forel, J.-M., Hajage, D., Jaber, S., Cayot-Constantin, S., Rimmelé, T., et al. (2020). Acyclovir for mechanically ventilated patients with herpes simplex virus oropharyngeal reactivation: a randomized clinical trial. *JAMA Int. Med.* 180, 263–272. doi: 10.1001/jamainternmed.2019.5713

Macka, M., Borak, J., Semenkova, L., Popl, M., and Mikeš, V. (1993). Determination of acyclovir in blood serum and plasma by micellar liquid chromatography with fluorimetric detection. *J. Liquid Chromatogr. Related Technol.* 16, 2359–2386. doi: 10.1080/10826079308020992

Maduraiveeran, G., Sasidharan, M., and Jin, W. (2019). Earth-abundant transition metal and metal oxide nanomaterials: synthesis and electrochemical applications. *Progr. Mater. Sci.* 106:100574. doi: 10.1016/j.pmatsci.2019.100574

Malekmohammadi, S., Hadadzadeh, H., Farrokhpour, H., and Amirghofran, Z. (2018). Immobilization of gold nanoparticles on folate-conjugated dendritic mesoporous silica-coated reduced graphene oxide nanosheets: a new nanoplatform for curcumin pH-controlled and targeted delivery. *Soft Matter* 14, 2400–2410. doi: 10.1039/C7SM02248D

Mitra, S., Purkait, T., Pramanik, K., Maiti, T. K., and Dey, R. S. (2019). Three-dimensional graphene for electrochemical detection of Cadmium in Klebsiella michiganensis to study the influence of Cadmium uptake in rice plant. *Mater. Sci. Eng. C* 103:109802. doi: 10.1016/j.msec.2019.109802

Mulabagal, V., Annaji, M., Kurapati, S., Dash, R. P., Srinivas, N. R., Tiwari, A. K., et al. (2020). Stability-indicating HPLC method for acyclovir and lidocaine in topical formulations. *Biomed. Chromatogr.* 34:e4751. doi: 10.1002/bmc.4751

Naghian, E., Khosrowshahi, E. M., Sohouli, E., Ahmadi, F., Rahimi-Nasrabadi, M., and Safarifard, V. (2020). A new electrochemical sensor for the detection of fentanyl lethal drug by a screen-printed carbon electrode modified with the open-ended channels of Zn (ii)-MOF. *N. J. Chem.* 44, 9271–9277. doi: 10.1039/D0NJ01322F

Pastucha, M., Farka, Z., Lacina, K., Mikušová, Z., and Skládal, P. (2019). Magnetic nanoparticles for smart electrochemical immunoassays: a review on recent developments. *Microchim. Acta* 186:312. doi: 10.1007/s00604-019-3410-0

Piret, J., and Boivin, G. (2017). "Herpesvirus resistance to antiviral drugs," in *Antimicrobial Drug Resistance*, ed D. Mayers, J. Sobel, M. Ouellette, K. Kaye, and D. Marchaim (Cham: Springer), 1185–1211. doi: 10.1007/978-3-319-47266-9_24

Rahimi-Nasrabadi, M., Pourmohamadian, V., Karimi, M. S., Naderi, H. R., Karimi, M. A., Didehban, K., et al. (2017). Assessment of supercapacitive performance of europium tungstate nanoparticles prepared via hydrothermal method. *J. Mater. Sci. Mater. Electron.* 28, 12391–12398. doi: 10.1007/s10854-017-7059-3

Sajid, M., and Baig, N. (2019). Chemically modified electrodes for electrochemical detection of dopamine: challenges and opportunities. *TrAC Trends Analyt. Chem.* 118, 368–385. doi: 10.1016/j.trac.2019.05.042

Sanatkar, T. H., Khorshidi, A., Sohouli, E., and Janczak, J. (2020). Synthesis, crystal structure, and characterization of two Cu (II) and Ni (II) complexes of a tetradentate N_2O_2 Schiff base ligand and their application in fabrication of a hydrazine electrochemical sensor. *Inorg. Chim. Acta* 506:119537. doi: 10.1016/j.ica.2020.119537

Shetti, N. P., Malode, S. J., and Nandibewoor, S. T. (2012). Electrochemical behavior of an antiviral drug acyclovir at fullerene-C60-modified glassy carbon electrode. *Bioelectrochemistry* 88, 76–83. doi: 10.1016/j.bioelechem.2012.06.004

Shetti, N. P., Nayak, D. S., Malode, S. J., and Kulkarni R. M. (2017). Nano molar detection of acyclovir, an antiviral drug at nanoclay modified carbon paste electrode. *Sens. Bio Sens. Res.* 14, 39–46. doi: 10.1016/j.sbsr.2017.04.004

Sinha, A., Chen, J., and Jain, R. (2019). "Functionalized graphenemetal nanoparticles nanohybrids as electrochemical sensors," in *Graphene*

Functionalization Strategies, eds A. Khan, M. Jawaid, B. Neppolian, and A. Asiri (Singapore: Springer), 49–62. doi: 10.1007/978-981-32-9057-0_2

Sohouli, E., Keihan, A. H., Shahdost-fard, F., Naghian, E., Plonska-Brzezinska, M. E., Rahimi-Nasrabadi, M. et al. (2020a). A glassy carbon electrode modified with carbon nanoonions for electrochemical determination of fentanyl. *Mater. Sci. Eng. C* 110:110684. doi: 10.1016/j.msec.2020.110684

Sohouli, E., Shahdost-Fard, F., Rahimi-Nasrabadi, M., Plonska-Brzezinska, M. E., and Ahmadi, F. (2020b). Introducing a novel nanocomposite consisting of nitrogen-doped carbon nano-onions and gold nanoparticles for the electrochemical sensor to measure acetaminophen. *J. Electr. Chem.* 871:114309. doi: 10.1016/j.jelechem.2020.114309

Tadepalli, S. M., and Quinn, R. P. (1996). Scintillation proximity radioimmunoassay for the measurement of acyclovir. *J. Pharmac. Biomed. Anal.* 15, 157–163. doi: 10.1016/0731-7085(96)01835-3

Tenser, R. B., and Tenser, R. B. (2019). Acyclovir resistant HSV in immunocompromised patients. *Neurology*.

Tzanavaras, P. D., and Themelis, D. G. (2007). High-throughput HPLC assay of acyclovir and its major impurity guanine using a monolithic column and a flow gradient approach. *J. Pharm. Biomed. Anal.* 43, 1526–1530. doi: 10.1016/j.jpba.2006.11.002

Vosoughifar, A. (2018). Synthesis of $NiWO_4$ nanostructure and $NiWO_4$/CdO nanocomposites as an effective photocatalyst for enhanced degradation and removal of organic contaminant. *J. Mater. Sci.* 29, 4862–4868. doi: 10.1007/s10854-017-8442-9

Wang, F., Chen, L., Chen, X., and Hu, S. (2006). Studies on electrochemical behaviors of acyclovir and its voltammetric determination with nano-structured film electrode. *Anal. Chim. Acta* 576, 17–22. doi: 10.1016/j.aca.2005.12.023

Wang, P., Gan, T., Zhang, J., Luo, J., and Zhang, S. (2013). Polyvinylpyrrolidone-enhanced electrochemical oxidation and detection of acyclovir. *J. Mol. Liquids* 177, 129–132. doi: 10.1016/j.molliq.2012.11.009

Yu, L., and Xiang, B. (2008). Quantitative determination of acyclovir in plasma by near infrared spectroscopy. *Microchem. J.* 90, 63–66. doi: 10.1016/j.microc.2008.03.006

Conflict of Interest: The authors declare that the research was conducted in the absence of any commercial or financial relationships that could be construed as a potential conflict of interest.

frontiers in Chemistry

ORIGINAL RESEARCH
published: 11 September 2020
doi: 10.3389/fchem.2020.00748

Development of Electrochemical Oscillation Method for Identification of *Prunus persica*, *Prunus davidiana*, and *Prunus armeniaca* Nuts

Shuai Yan[1†], *Yinzi Yue*[1†], *Lianlin Su*[2], *Min Hao*[3], *Xiaopeng Wang*[1*] *and Ting Zuo*[4*]

[1] *Suzhou TCM Hospital Affiliated to Nanjing University of Chinese Medicine, Suzhou, China,* [2] *School of Pharmacy, Nanjing University of Chinese Medicine, Nanjing, China,* [3] *School of Pharmacy, Zhejiang Chinese Medicine University, Hangzhou, China,* [4] *School of Pharmacy, Henan University of Chinese Medicine, Zhengzhou, China*

In this work, an electrochemical oscillation system has been developed using the Belousov–Zhabotinsky reaction. The effect of the combination of each reagent, reaction temperature, and stirring speed on the induction period, oscillating period, and oscillating life were optimized. The nuts of *Prunus persica*, *Prunus davidiana,* and *Prunus armeniaca* have been widely used for medical purposes. The proposed electrochemical oscillation system was then used for the identification of *P. persica*, *P. davidiana,* and *P. armeniaca*. Three nuts exhibited very different electrochemical oscillation profiles. The dendrogram was divided into three main principal infrageneric clades. Each cluster only contains one species, suggesting that no outlier was observed in this study. Based on the discussed results, we proposed a simple method for herbal medicine identification.

Keywords: electrochemical oscillation, Belousov–Zhabotinsky, plant identification, herbal medicine, *Prunus* spp.

OPEN ACCESS

Edited by:
Hassan Karimi-maleh, University of Electronic Science and Technology of China, China

Reviewed by:
Li Fu, Hangzhou Dianzi University, China
Vahid Arabali, Islamic Azad University Sari Branch, Iran

***Correspondence:**
Xiaopeng Wang
wxpeng2004@163.com
Ting Zuo
381165010@qq.com

[†] *These authors have contributed equally to this work*

Specialty section:
This article was submitted to Electrochemistry, a section of the journal Frontiers in Chemistry

Received: *25 June 2020*
Accepted: *20 July 2020*
Published: *11 September 2020*

Citation:
Yan S, Yue Y, Su L, Hao M, Wang X and Zuo T (2020) Development of Electrochemical Oscillation Method for Identification of Prunus persica, Prunus davidiana, and Prunus armeniaca Nuts. Front. Chem. 8:748. doi: 10.3389/fchem.2020.00748

INTRODUCTION

The fingerprint of traditional herbal medicine refers to the map of common peaks that can mark the characteristics of the traditional herbal medicine after proper pretreatment with a certain analysis method (Xie et al., 2006; Zhu et al., 2016; Wang et al., 2017). It is the visual characterization of the physical and chemical information of the traditional herbal medicine (Donno et al., 2016; Deconinck et al., 2017; Afshar et al., 2020; Fu et al., 2020; Karimi-Maleh et al., 2020a,c; Li et al., 2020; Tavana et al., 2020). The fingerprint of traditional herbal medicine has two characteristics: (1) Through the characteristics of the fingerprint, it can identify the authenticity or origin of the sample. (2) The area or ratio of the main characteristic peaks on the fingerprint can effectively control the quality of traditional herbal medicine.

At present, the common fingerprints of traditional herbal medicine are thin layer chromatography fingerprint (Szeremeta et al., 2017; Sibug-Torres et al., 2019a,b), high-performance liquid chromatography fingerprint (Li et al., 2016; Xue et al., 2017; Esteki et al., 2019), gas chromatography fingerprint (Aliakbarzadeh et al., 2016; Shekari et al., 2018; Huang et al., 2019), high-performance capillary electrophoresis fingerprint (Hou et al., 2019; Sun et al., 2019), high-speed countercurrent chromatography fingerprint (Gan et al., 2016; Wang et al., 2020), ultraviolet fingerprint, infrared fingerprint (Custers et al., 2017; Dai et al., 2019), nuclear magnetic resonance fingerprint (Sun et al., 2018; Flores et al., 2020), mass spectrometry fingerprint (Yang and Deng, 2016; Kharbach et al., 2020), X-ray diffraction fingerprint (Chen et al., 2017; Devi et al., 2017), immunoassay fingerprint

(Cui et al., 2019), and DNA fingerprint (Pawar et al., 2017; Selvakumari et al., 2017). These methods can be used for in-depth research on traditional herbal medicine, but proper pretreatment of traditional herbal medicine is required. The pretreatment process will cause the loss of ingredients, so the existing fingerprint is actually only a collection of information on the chemical composition of some herbal medicines, not a complete reflection of the chemical composition of herbal medicines. Therefore, it is a primary task to explore a direct operation method of fingerprints that can be applied to the cluster characterization of traditional herbal medicine chemical components in various phases and dosage forms without pretreatment operations such as separation and purification. The discovery of non-linear chemical phenomena has opened the study of complex systems. Due to the good reproducibility of the oscillating response, its application research is becoming more and more extensive, which provides a new idea and method for solving this problem.

At present, the Belousov–Zhabotinsky (B-Z) oscillation reaction is most widely used in analysis and detection, followed by the copper ion oscillation system (Alfifi et al., 2016; Luiz Fernando Oliveira Maia et al., 2019; Nawabi et al., 2019; Ullah et al., 2019). There are also Bray–Liebhafsky oscillation reaction, Briggs–Rauscher oscillation reaction, peroxidase–oxidase biochemical oscillator (peroxidase–oxidase oscillation system), and liquid membrane oscillator (Mukouyama et al., 2016; Bai et al., 2017; Peng et al., 2017; Chan and Dow, 2019; Ding et al., 2019). The basis for applying chemical oscillation reaction to analysis and detection is that the substance to be tested can interfere with the oscillation reaction. Different chemical oscillation reactions have different characteristics, and the shape of the potential–time (E-t) curve and various characteristic information parameters are also different (Miyazaki et al., 2016; Zhou et al., 2020). Herbal medicines of different types or origins and sources contain different chemical components and content. When the herbal medicine is added to the chemical oscillation system, the interference to the induction phase and the oscillation phase may be different from the effects of various substances in the oscillation system, causing different changes. By comparing the different changes of the E-t curve after adding different herbal medicines to the chemical oscillation system, not only the corresponding E-t curve is completely different from the curve of the blank system under the same experimental conditions, but more importantly, it reflects the chemical composition characteristics of different herbal medicine (Jin and Shen, 2017; Mohtashami et al., 2018). The fingerprint can be used to analyze the chemical composition of herbal medicine as a whole and to identify or qualitatively analyze herbal medicine. Electrochemistry has been widely used for sensing purpose in pharmaceutic fields (Fu et al., 2019; Fouladgar et al., 2020; Karimi-Maleh et al., 2020b; Mohanraj et al., 2020; Xu et al., 2020; Ying et al., 2020; Zabihpour et al., 2020). In this work, we proposed an electrochemical oscillation system based on B-Z reaction. The effect of a combination of each reagent, reaction temperature, and stirring speed on the induction period, oscillating period, and oscillating life were optimized. The nuts of *Prunus persica*, *Prunus davidiana,* and *Prunus armeniaca* have been selected as samples.

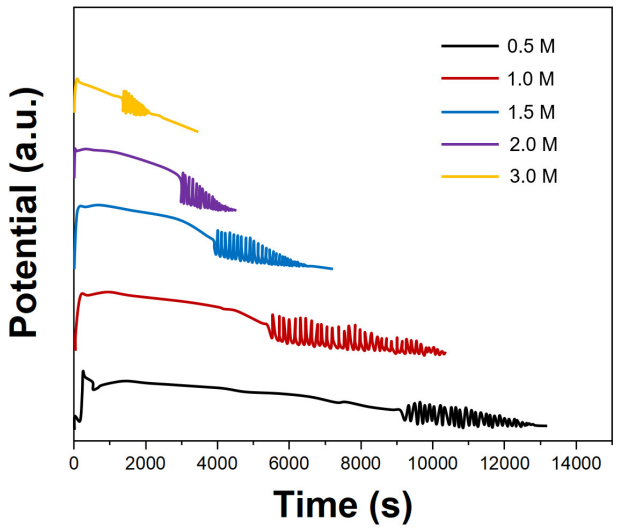

FIGURE 1 | Oscillating profiles of *Prunus persica* recorded using different concentrations of H_2SO_4.

MATERIALS AND METHODS

All chemicals were analytical grade and used without purification. The nuts of *P. persica*, *P. davidiana,* and *P. armeniaca* were purchased from a local pharmacy and grounded into a powder. The chemical oscillating reaction is carried out in a continuously stirred jacketed reactor. The experimental temperature is controlled at 310 K. A certain amount of herbal machines was added into the discussed reactor with different concentrations of H_2SO_4 (10 ml), CH_3COCH_3 (5 ml), and $MnSO_4$ (5 ml). The mentioned solution was stirred 10 min before injection of 5-ml $KBrO_3$. The E-t curve was monitored all the time until potential oscillation disappears. All electrochemical experiments were recorded using a CHI760E working station.

RESULTS AND DISCUSSION

Prunus persica has been used for optimizing the concentrations of all reagents used in the B-Z reaction. **Figure 1** shows the effect of the H_2SO_4 concentration on the electrochemical oscillation of *P. persica*. It can be seen that the oscillation profiles recorded after injection of 10 ml of H_2SO_4 with different concentrations were different. When the sulfuric acid concentration was 1.0 M, the oscillation life is the longest, and the amplitude was the largest. When the sulfuric acid concentration exceeded 2.0 M, the oscillations decayed faster. When the sulfuric acid concentration was 0.5 M, the induction period of the oscillating reaction was too long. Therefore, we selected 1.0 M of sulfuric acid for an oscillating reaction.

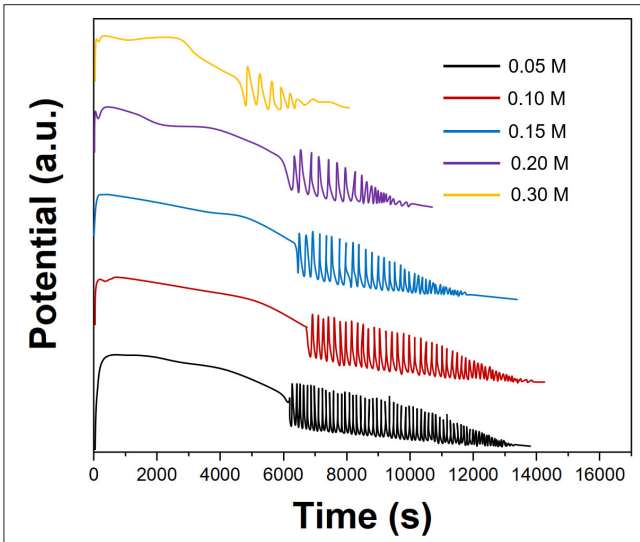

FIGURE 2 | Oscillating profiles of *Prunus persica* recorded using different concentrations of $MnSO_4$.

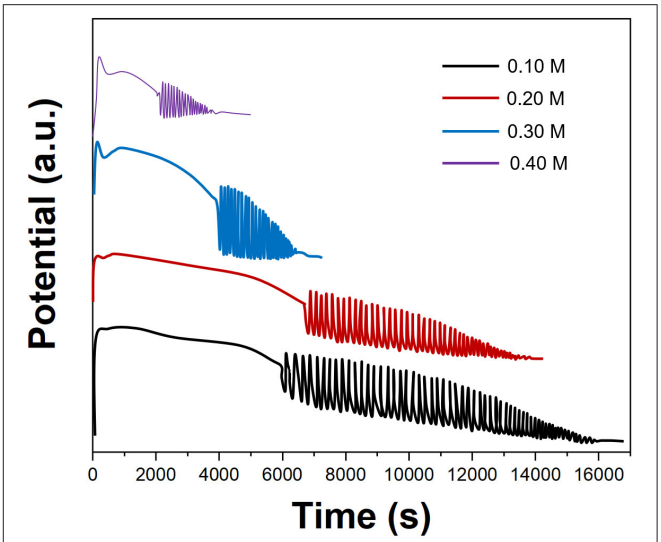

FIGURE 4 | Oscillating profiles of *Prunus persica* recorded using different concentrations of $KBrO_3$.

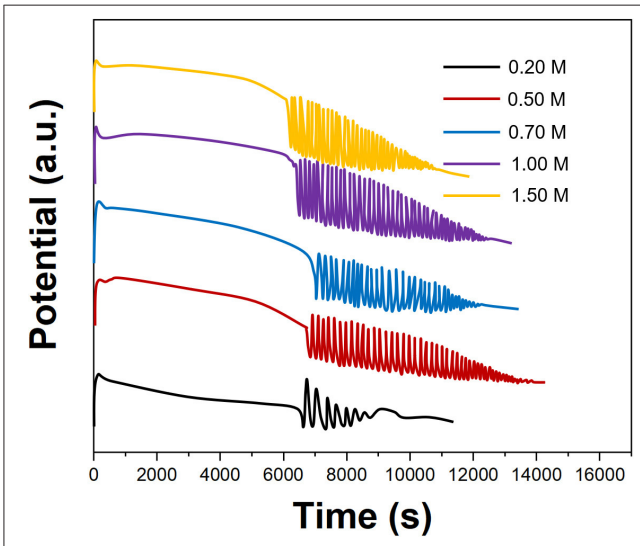

FIGURE 3 | Oscillating profiles of *Prunus persica* recorded using different concentrations of CH_3COCH_3.

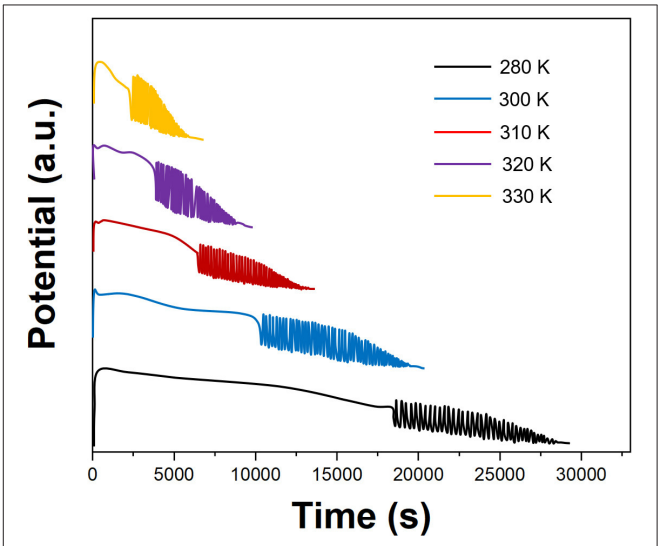

FIGURE 5 | Oscillating profiles of *Prunus persica* recorded using different temperature.

Figure 2 shows the effect of the $MnSO_4$ concentration on the electrochemical oscillation of *P. persica*. In this case, manganese ions were catalysts for oscillating reactions and had little effect on amplitude and induction time. Therefore, we selected 0.1 M of $MnSO_4$ for an oscillating reaction.

Figure 3 shows the effect of the CH_3COCH_3 concentration on the electrochemical oscillation of *P. persica*. When the concentration of CH_3COCH_3 was 0.2 M, the oscillation reaction is irregular; when the concentration of CH_3COCH_3 reaches 0.5 M, a regular oscillation reaction can be produced. CH_3COCH_3 can also produce normal oscillation response at higher concentrations. The role of CH_3COCH_3 was to react with Br_2 to form CH_3COCH_2Br to remove excess Br_2. CH_3COCH_2Br is a toxic preparation, which is irritating to the eyes, so we selected 0.5 M of CH_3COCH_3 for an oscillating reaction.

Figure 4 shows the effect of the $KBrO_3$ concentration on the electrochemical oscillation of *P. persica*. It can be seen from **Figure 4** that as the $KBrO_3$ concentration increases, the maximum amplitude, induction time, and oscillation life increase. However, the solubility of $KBrO_3$ at room temperature is small, so we selected 0.3 M of $KBrO_3$ for an oscillating reaction.

Figure 5 shows the effect of the temperature on the electrochemical oscillation of *P. persica*. The results show that as

the temperature increases, the fingerprint data change in different patterns. Generally speaking, the higher the temperature, the longer the induction time, the shorter the oscillation period, the shorter the oscillation lifetime, and the larger the amplitude. Therefore, the selection of appropriate temperature conditions is of great significance for the control of reaction time, the stability of the fingerprint, and the reproducibility. Therefore, we selected 310 K for oscillating reactions.

Figure 6 shows the effect of the amount of *P. persica* on the electrochemical oscillation. When *P. persica* was 0.1 g, the substrate that can be used as the B-Z oscillation reaction was the least, so the induction period was the longest, and the oscillation period was also the longest. When its oscillating substrate was consumed, its oscillation suddenly stops. With the increase in the dosage of herbal medicine, the number of chemical components in the herbal medicine participating in the oscillation reaction also increased. The oscillation reaction was more likely to occur, so the reaction rate was accelerated, the induction period was reduced, and the oscillation period and oscillation life were also reduced. When the dosage of herbal medicine exceeds 0.5 g, the front part of the curve becomes irregular, which was not conducive to the acquisition of characteristic information. When the dosage was small, the reaction time will become too long, requiring a longer analysis time. To obtain better information, the amount of herbal medicinal materials used in the fingerprints recording was 0.3 g.

The reproducibility of electrochemical oscillation patterns for *P. persica* has been studied. The results indicated that under

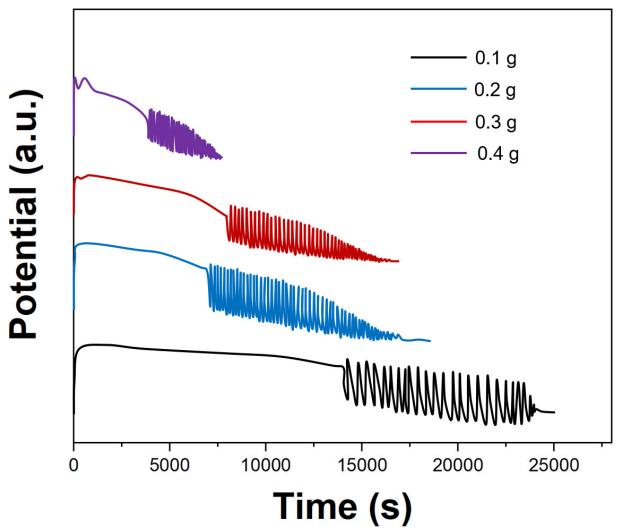

FIGURE 6 | Oscillating profiles recorded using different amount of *Prunus persica*.

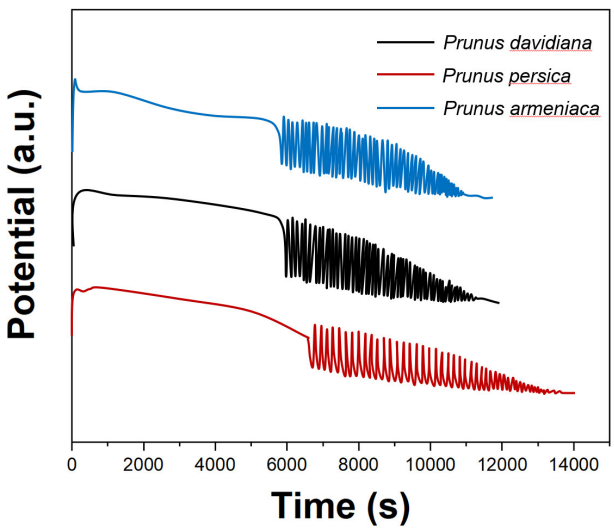

FIGURE 7 | Oscillating profiles recorded for *Prunus persica*, *Prunus davidiana*, and *Prunus armeniaca*.

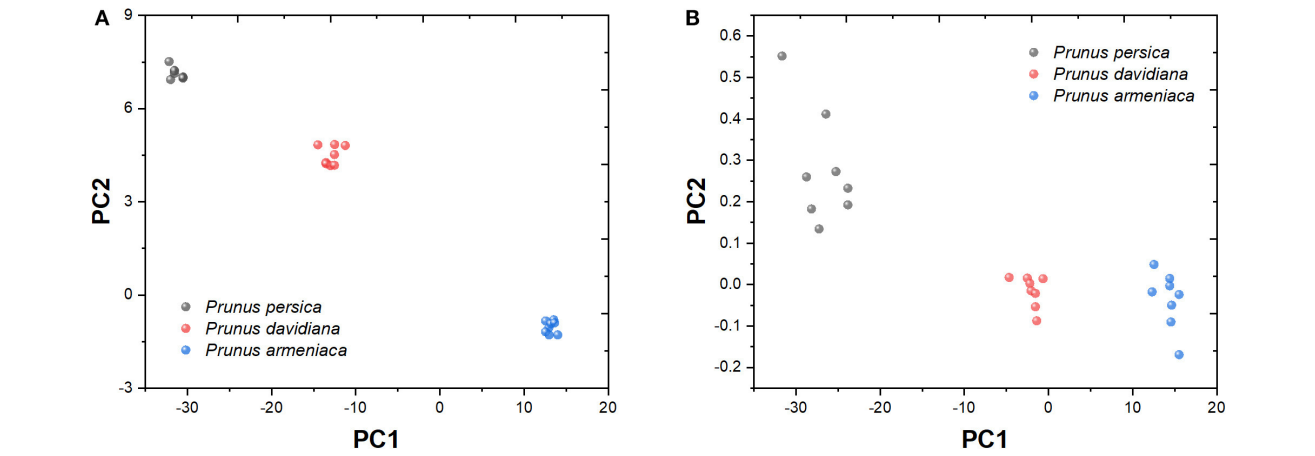

FIGURE 8 | Principal component analysis of *Prunus persica*, *Prunus davidiana*, and *Prunus armeniaca*. **(A)** PC1 vs. PC2. **(B)** PC1 vs. PC3.

TABLE 1 | Eigenvalues and contributions of principle component.

PCA	Eigenvalue	Contribution rate (%)	Accumulating contribution rate (%)
PC1	0.588	89.44	89.44
PC2	0.624	7.25	96.69
PC3	0.007	3.31	100

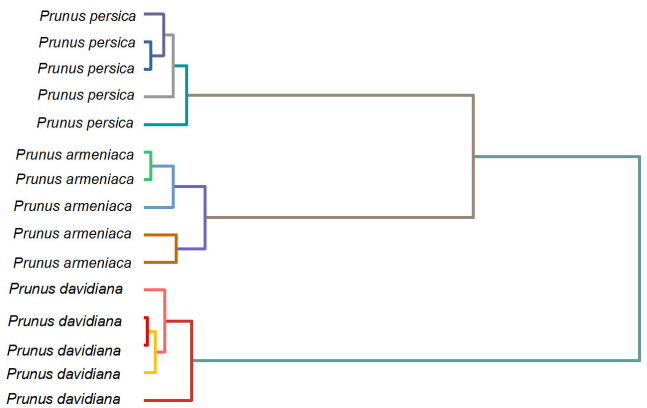

FIGURE 9 | Do9oendrogram of *Prunus persica*, *Prunus davidiana*, and *Prunus armeniaca* deduced from the fingerprint recorded using B-Z reaction.

the same experimental conditions, the various indexes of the electrochemical oscillation measured are basically the same, RSD $\leq$ 2%, indicating good reproducibility.

Figure 7 is the electrochemical fingerprint of *P. persica*, *P. davidiana,* and *P. armeniaca*. It can be seen that due to the different chemical components contained in different species, their participation in the oscillating reaction process is different, so the E-t curve induction time, oscillation life, maximum potential, start-up potential, and other data are different. At the same time, the shape of the induction curve and the oscillation curve are also different. These features help identify species.

Figure 8 shows the principal component analysis of *P. persica*, *P. davidiana,* and *P. armeniaca* recorded from different samples. **Table 1** shows the characteristic value and contribution value of data after the principal component analysis. The contribution rates of the first three principal components were 89.44, 7.25, and 3.31%, respectively. From the analysis in **Figure 8A**, it can be seen that the three samples can be distinguished obviously, whereas part of the data in **Figure 8B** is mutually charged.

As the oscillating fingerprint of species is positively correlated with the distribution and amount of chemical compounds, we attempted to use the fingerprint, as mentioned earlier, for dendrogram analysis. **Figure 9** shows the dendrogram of *P. persica*, *P. davidiana*, and *P. armeniaca* deduced from the fingerprint recorded using B-Z reaction. The dendrogram was divided into three main principal infrageneric clades. Each cluster only contains one species, suggesting that no outlier was observed in this study. Based on the discussed results, we proposed a simple method for herbal medicines identification.

CONCLUSION

In this work, we proposed an authentication method based on the electrochemical oscillation system. B-Z reaction has been selected due to its high stability. The electrochemical oscillation profiles of *P. persica*, *P. davidiana*, and *P. armeniaca* were recorded. The recorded profile varies between the species due to the presence of different contents of chemical compounds. Based on the recorded oscillation fingerprint, these species can be effectively identified. Also, the dendrogram results suggest no outlier was observed in this study. Therefore, the proposed electrochemical oscillation can be used for herbal medicines identification.

DATA AVAILABILITY STATEMENT

The original contributions presented in the study are included in the article/supplementary material, further inquiries can be directed to the corresponding author/s.

AUTHOR CONTRIBUTIONS

SY, YY, and XW contributed conception and design of the study. LS and MH conducted electrochemical experiments. SY, XW, and TZ performed the statistical analysis. XW and SY wrote the manuscript. All authors contributed to manuscript revision, read, and approved the submitted version.

FUNDING

This work was funded by Natural Science Foundation of Jiangsu Province (BK20180219), National Natural Science Foundation of China (81804098), Jiangsu Youth Medical Talents Project (QNRC2016255), and Macao Young Scholars Program (AM2020020).

REFERENCES

Afshar, S., Zamani, H. A., and Karimi-Maleh, H. (2020). NiO/SWCNTs coupled with an ionic liquid composite for amplified carbon paste electrode; A feasible approach for improving sensing ability of adrenalone and folic acid in dosage form. *J. Pharm. Biomed. Anal.* 188:113393. doi: 10.1016/j.jpba.2020.113393

Alfifi, H. Y., Marchant, T. R., and Nelson, M. I. (2016). Non-smooth feedback control for Belousov–Zhabotinskii reaction–diffusion equations: semi-analytical solutions. *J. Math. Chem.* 54, 1632–1657. doi: 10.1007/s10910-016-0641-8

Aliakbarzadeh, G., Sereshti, H., and Parastar, H. (2016). Pattern recognition analysis of chromatographic fingerprints of Crocus sativus L. secondary metabolites towards source identification and quality control. *Anal. Bioanal. Chem.* 408, 3295–3307. doi: 10.1007/s00216-016-9400-8

Bai, H., Qing, S., Yang, D., Zhang, Y., Fan, X., and Tao, C. (2017). Periodic potential oscillation during oxygen evolution catalyzed by manganese oxide at constant current. *J. Electrochem. Soc.* 164:E78. doi: 10.1149/2.1241704jes

Chan, P.-F., and Dow, W.-P. (2019). Spontaneous potential oscillation resulting in copper deposit with ultra-large grains. *J. Electrochem. Soc.* 166:D891.

Chen, D.-D., Xie, X.-F., Ao, H., Liu, J.-L., and Peng, C. (2017). Raman spectroscopy in quality control of Chinese herbal medicine. *J. Chin. Med. Assoc.* 80, 288–296. doi: 10.1016/j.jcma.2016.11.009

Cui, Y., Zhao, J., Zhou, J., Tan, G., Zhao, Q., Zhang, Y., et al. (2019). Development of a sensitive monoclonal antibody-based indirect competitive enzyme-linked immunosorbent assay for analysing nobiletin in citrus and herb samples. *Food Chem.* 293, 144–150. doi: 10.1016/j.foodchem.2019.04.101

Custers, D., Van Praag, N., Courselle, P., Apers, S., and Deconinck, E. (2017). Chromatographic fingerprinting as a strategy to identify regulated plants in illegal herbal supplements. *Talanta* 164, 490–502. doi: 10.1016/j.talanta.2016.12.008

Dai, T., Yang, F., Liu, J., and Sun, G. (2019). Evaluation of the quality consistency of Zhenju Jiangya Tablets by systematic quantified fingerprint method in combination with antioxidant activity and three compounds analyses. *Microchem. J.* 150:104175. doi: 10.1016/j.microc.2019.104175

Deconinck, E., Djiogo, C. A. S., Kamugisha, A., and Courselle, P. (2017). The use of Stationary Phase Optimized Selectivity Liquid Chromatography for the development of herbal fingerprints to detect targeted plants in plant food supplements. *Talanta* 170, 441–450. doi: 10.1016/j.talanta.2017.04.028

Devi, G. K., Kumar, K. S., Parthiban, R., and Kalishwaralal, K. (2017). An insight study on HPTLC fingerprinting of Mukia maderaspatna: Mechanism of bioactive constituents in metal nanoparticle synthesis and its activity against human pathogens. *Microb. Pathog.* 102, 120–132. doi: 10.1016/j.micpath.2016.11.026

Ding, L., Song, Z., Wu, P., Cheng, J., Chen, C., Niu, Y., et al. (2019). Electrochemical oscillations during copper electrodissolution in hydrochloric acid solution. *Int. J. Electrochem. Sci.* 14, 585–597. doi: 10.20964/2019.01.63

Donno, D., Boggia, R., Zunin, P., Cerutti, A. K., Guido, M., Mellano, M. G., et al. (2016). Phytochemical fingerprint and chemometrics for natural food preparation pattern recognition: an innovative technique in food supplement quality control. *J. Food Sci. Technol.* 53, 1071–1083. doi: 10.1007/s13197-015-2115-6

Esteki, M., Shahsavari, Z., and Simal-Gandara, J. (2019). Food identification by high performance liquid chromatography fingerprinting and mathematical processing. *Food Res. Int.* 122, 303–317. doi: 10.1016/j.foodres.2019.04.025

Flores, I. S., Martinelli, B. C. B., and Lião, L. M. (2020). High-resolution magic angle spinning nuclear magnetic resonance (HR-MAS NMR) as a tool in the determination of biomarkers of Passiflora-based herbal medicines. *Fitoterapia* 142:104500. doi: 10.1016/j.fitote.2020.104500

Fouladgar, M., Karimi-Maleh, H., Opoku, F., and Govender, P. P. (2020). Electrochemical anticancer drug sensor for determination of raloxifene in the presence of tamoxifen using graphene-CuO-polypyrrole nanocomposite structure modified pencil graphite electrode: theoretical and experimental investigation. *J. Mol. Liq.* 311:113314. doi: 10.1016/j.molliq.2020.113314

Fu, L., Wu, M., Zheng, Y., Zhang, P., Ye, C., Zhang, H., et al. (2019). Lycoris species identification and infrageneric relationship investigation via graphene enhanced electrochemical fingerprinting of pollen. *Sens. Actuators B Chem.* 298:126836. doi: 10.1016/j.snb.2019.126836

Fu, L., Zheng, Y., Zhang, P., Zhang, H., Xu, Y., Zhou, J., et al. (2020). Development of an electrochemical biosensor for phylogenetic analysis of Amaryllidaceae based on the enhanced electrochemical fingerprint recorded from plant tissue. *Biosens. Bioelectron.* 159:112212. doi: 10.1016/j.bios.2020.112212

Gan, Z., Liang, Z., Chen, X., Wen, X., Wang, Y., Li, M., et al. (2016). Separation and preparation of 6-gingerol from molecular distillation residue of Yunnan ginger rhizomes by high-speed counter-current chromatography and the antioxidant activity of ginger oils *in vitro*. *J. Chromatogr. B* 1011, 99–107. doi: 10.1016/j.jchromb.2015.12.051

Hou, Z., Sun, G., Guo, Y., Yang, F., and Gong, D. (2019). Capillary electrophoresis fingerprints combined with Linear Quantitative Profiling Method to monitor the quality consistency and predict the antioxidant activity of Alkaloids of Sophora flavescens. *J. Chromatogr. B* 1133:121827. doi: 10.1016/j.jchromb.2019.121827

Huang, Y., Huang, Z., Watanabe, C., and Wang, L. (2019). Authentication of Schisandra chinensis and Schisandra sphenantherae in Chinese patent medicines by pyrolysis-gas chromatography/mass spectrometry and fingerprint analysis. *J. Anal. Appl. Pyrolysis* 137, 70–76. doi: 10.1016/j.jaap.2018.11.011

Jin, J. Z., and Shen, C. (2017). Study on electrochemical fingerprints of radix paeoniae alba. *J. Chem. Soc. Pak.* 39:947.

Karimi-Maleh, H., Cellat, K., Arikan, K., Savk, A., Karimi, F., and Sen, F. (2020a). Palladium–Nickel nanoparticles decorated on Functionalized-MWCNT for high precision non-enzymatic glucose sensing. *Mater. Chem. Phys.* 250:123042. doi: 10.1016/j.matchemphys.2020.123042

Karimi-Maleh, H., Karimi, F., Malekmohammadi, S., Zakariae, N., Esmaeili, R., Rostamnia, S., et al. (2020b). An amplified voltammetric sensor based on platinum nanoparticle/polyoxometalate/two-dimensional hexagonal boron nitride nanosheets composite and ionic liquid for determination of N-hydroxysuccinimide in water samples. *J. Mol. Liq.* 310:113185. doi: 10.1016/j.molliq.2020.113185

Karimi-Maleh, H., Kumar, B. G., Rajendran, S., Qin, J., Vadivel, S., Durgalakshmi, D., et al. (2020c). Tuning of metal oxides photocatalytic performance using Ag nanoparticles integration. *J. Mol. Liq.* 314:113588. doi: 10.1016/j.molliq.2020.113588

Kharbach, M., Marmouzi, I., El Jemli, M., Bouklouze, A., and Vander Heyden, Y. (2020). Recent advances in untargeted and targeted approaches applied in herbal-extracts and essential-oils fingerprinting - a review. *J. Pharm. Biomed. Anal.* 177:112849. doi: 10.1016/j.jpba.2019.112849

Li, T., Zhuang, S., Wang, Y., Wang, Y., Wang, W., Zhang, H., et al. (2016). Flavonoid profiling of a traditional Chinese medicine formula of Huangqin Tang using high performance liquid chromatography. *Acta Pharm. Sin. B* 6, 148–157. doi: 10.1016/j.apsb.2016.01.001

Li, Y., Shen, Y., Yao, C., and Guo, D. (2020). Quality assessment of herbal medicines based on chemical fingerprints combined with chemometrics approach: a review. *J. Pharm. Biomed. Anal.* 185:113215. doi: 10.1016/j.jpba.2020.113215

Luiz Fernando Oliveira Maia, R. E. L., Reis, C., Gonçalves Reis, C. D., de Carvalho Damasceno, O. I., and Teixeira dos Reis, L. G. (2019). Potentiometric determination of paracetamol in pharmaceutical formulations by the analyte pulse perturbation technique using Belousov–Zhabotinskii oscillating chemical reaction. *J. Anal. Chem.* 74, 1232–1238. doi: 10.1134/S1061934819120074

Miyazaki, K., Nakata, A., Lee, Y.-S., Fukutsuka, T., and Abe, T. (2016). Influence of surfactants as additives to electrolyte solutions on zinc electrodeposition and potential oscillation behavior. *J. Appl. Electrochem.* 46, 1067–1073. doi: 10.1007/s10800-016-0987-4

Mohanraj, J., Durgalakshmi, D., Rakkesh, R. A., Balakumar, S., Rajendran, S., and Karimi-Maleh, H. (2020). Facile synthesis of paper based graphene electrodes for point of care devices: a double stranded DNA (dsDNA) biosensor. *J. Colloid Interface Sci.* 566, 463–472. doi: 10.1016/j.jcis.2020.01.089

Mohtashami, S., Rowshan, V., Tabrizi, L., Babalar, M., and Ghani, A. (2018). Summer savory (*Satureja hortensis* L.) essential oil constituent oscillation at different storage conditions. *Ind. Crops Prod.* 111, 226–231. doi: 10.1016/j.indcrop.2017.09.055

Mukouyama, Y., Kawasaki, H., Hara, D., Yamada, Y., and Nakanishi, S. (2016). Appearance of new oscillation (Named Oscillation H) induced by Na2SO4 and K2SO4 in electroreduction of H_2O_2 on platinum. *J. Electrochem. Soc.* 164:H1. doi: 10.1149/2.0011702jes

Nawabi, M. Y., Waqar Uddin, G., Ullah, S., Fang, Z., and Sardar, S. (2019). Identification of two hetero-substituent-aromatic isomers of-4-and 7-hydroxy coumarin with the belousov-zhabotinsky oscillator. *Int. J. Electrochem. Sci.* 14, 8676–8685. doi: 10.20964/2019.09.08

Pawar, R. S., Handy, S. M., Cheng, R., Shyong, N., and Grundel, E. (2017). Assessment of the authenticity of herbal dietary supplements: comparison of chemical and DNA barcoding methods. *Planta Med.* 83, 921–936. doi: 10.1055/s-0043-107881

Peng, H., Liu, Z., and Tao, C. (2017). Electrochemical oscillation of vanadium ions in anolyte. *J. Electrochem. Sci. Eng.* 7, 139–144. doi: 10.5599/jese.406

Selvakumari, E., Jenifer, J., Priyadharshini, S., and Vinodhini, R. (2017). Application of DNA fingerprinting for plant identification. *JAIR* 5, 149–151.

Shekari, N., Vosough, M., and Tabar Heidar, K. (2018). Chromatographic fingerprinting through chemometric techniques for herbal slimming pills: a way of adulterant identification. *Forensic Sci. Int.* 286, 213–222. doi: 10.1016/j.forsciint.2018.03.022

Sibug-Torres, S. M., Padolina, I. D., Cruz, P., Garcia, F. C., Garrovillas, M. J., Yabillo, M. R., et al. (2019a). Smartphone-based image analysis and chemometric pattern recognition of the thin-layer

chromatographic fingerprints of herbal materials. *Anal. Methods* 11, 721–732. doi: 10.1039/C8AY02698J

Sibug-Torres, S. M., Padolina, I. D., and Enriquez, E. P. (2019b). Radial multi-stationary phase thin-layer chromatography for the field-ready fingerprinting of herbal materials. *Anal. Methods* 11, 5511–5520. doi: 10.1039/C9AY01714C

Sun, L., Wang, M., Ren, X., Jiang, M., and Deng, Y. (2018). Rapid authentication and differentiation of herbal medicine using 1H NMR fingerprints coupled with chemometrics. *J. Pharm. Biomed. Anal.* 160, 323–329. doi: 10.1016/j.jpba.2018.08.003

Sun, Y., Qian, M., Yuan, G., Yang, H., Cui, X., and Li, Y. (2019). High performance capillary electrophoresis characteristic fingerprint of schisandra chinensis. *Curr. Pharm. Anal.* 15, 456–464. doi: 10.2174/1573412914666180716143939

Szeremeta, D., Knaś, M., Długosz, E., Kowalska, T., and Sajewicz, M. (2017). Thin-layer chromatographic fingerprinting of the nonvolatile fraction extracted from the medicinal herb Cistus incanus L. *J. Liq. Chromatogr. Relat. Technol.* 40, 304–310. doi: 10.1080/10826076.2017.1298033

Tavana, T., Rezvani, A. R., and Karimi-Maleh, H. (2020). Pt-Pd-doped NiO nanoparticle decorated at single-wall carbon nanotubes: an excellent, powerful electrocatalyst for the fabrication of An electrochemical sensor to determine nalbuphine in the presence of tramadol as two opioid analgesic drugs. *J. Pharm. Biomed. Anal.* 189:113397. doi: 10.1016/j.jpba.2020.113397

Ullah, S., Uddin, W., Hu, G., Nawabi, M. Y., Ullah, R., Sardar, S., et al. (2019). Determination of ascorbic acid by using a Belousov-Zhabotinsky oscillating system catalyzed by a macrocylic complex. *Int. J. Electrochem. Sci.* 14, 5563–5572. doi: 10.20964/2019.06.07

Wang, C., Wang, L., Li, C., Hu, C., and Zhao, S. (2020). Anti-proliferation activities of three bioactive components purified by high-speed counter-current chromatography in essential oil from ginger. *Eur. Food Res. Technol.* 246, 795–805. doi: 10.1007/s00217-020-03446-7

Wang, Y., Liu, W., Yang, D., Qing, Y., Du, P., and Jin, Y. et al. (2017). UPLC-MS/MS fingerprint of coptidis rhizoma-scutellariae radix herbal pair. *Chin. J. Exp. Tradit. Med. Formulae* 2017:14. doi: 10.1186/s13020-018-0171-3

Xie, P., Chen, S., Liang, Y., Wang, X., Tian, R., and Upton, R. (2006). Chromatographic fingerprint analysis—a rational approach for quality assessment of traditional Chinese herbal medicine. *Plant Anal.* 1112, 171–180. doi: 10.1016/j.chroma.2005.12.091

Xu, Y., Lu, Y., Zhang, P., Wang, Y., Zheng, Y., Fu, L., et al. (2020). Infrageneric phylogenetics investigation of Chimonanthus based on electroactive compound profiles. *Bioelectrochemistry* 133:107455. doi: 10.1016/j.bioelechem.2020.107455

Xue, Y., Zhu, L., and Yi, T. (2017). Fingerprint analysis of Resina Draconis by ultra-performance liquid chromatography. *Chem. Cent. J.* 11:67. doi: 10.1186/s13065-017-0299-8

Yang, Y., and Deng, J. (2016). Analysis of pharmaceutical products and herbal medicines using ambient mass spectrometry. *TrAC Trends Anal. Chem.* 82, 68–88. doi: 10.1016/j.trac.2016.04.011

Ying, J., Zheng, Y., Zhang, H., and Fu, L. (2020). Room temperature biosynthesis of gold nanoparticles with Lycoris aurea leaf extract for the electrochemical determination of aspirin. *Rev. Mex. Ing. Quím.* 19, 585–592. doi: 10.24275/rmiq/Mat741

Zabihpour, T., Shahidi, S.-A., Karimi-Maleh, H., and Ghorbani-HasanSaraei, A. (2020). An ultrasensitive electroanalytical sensor based on MgO/SWCNTs-1-Butyl-3-methylimidazolium bis(trifluoromethylsulfonyl)imide paste electrode for the determination of ferulic acid in the presence sulfite in food samples. *Microchem. J.* 154:104572. doi: 10.1016/j.microc.2019.104572

Zhou, H., Zhang, N., Bai, H., Ming, H., Zhang, Q., Du, J., et al. (2020). A pulse modulatable self-oscillation kinetics for water oxidation at large current on manganese catalyst. *Electrochimica Acta* 337:135798. doi: 10.1016/j.electacta.2020.135798

Zhu, C.-S., Lin, Z.-J., Xiao, M.-L., Niu, H.-J., and Zhang, B. (2016). The spectrum-effect relationship—a rational approach to screening effective compounds, reflecting the internal quality of Chinese herbal medicine. *Chin. J. Nat. Med.* 14, 177–184. doi: 10.1016/S1875-5364(16)30014-0

Conflict of Interest: The authors declare that the research was conducted in the absence of any commercial or financial relationships that could be construed as a potential conflict of interest.

frontiers in Chemistry

ORIGINAL RESEARCH
published: 16 September 2020
doi: 10.3389/fchem.2020.589560

An Electrochemical Sandwich Immunosensor Based on Signal Amplification Technique for the Determination of Alpha-Fetoprotein

Changming Shen[1,2], *Lin Wang*[3], *Hongyan Zhang*[1,2], *Shaojuan Liu*[4] *and Jianwei Jiang*[1,2*]

[1] Cancer Hospital of the University of Chinese Academy of Sciences (Zhejiang Cancer Hospital), Hangzhou, China, [2] Institute of Cancer and Basic Medicine (IBMC), Chinese Academy of Sciences, Hangzhou, China, [3] The Third Affiliated Hospital of Zhejiang Chinese Medical University, Hangzhou, China, [4] The Third People's Hospital of Hangzhou, Hangzhou, China

The synthesis of Au nanocubes is used to label alpha-fetoprotein antibody (anti-AFP) and horseradish peroxidase (HRP) to form an immune complex for antibody detection. Graphene oxide-methylene blue-gold nanoparticles (GO-MB-AuNPs) nanocomposites were used as the immunosensing platform. This proposed sandwich-type immunoassay shows good performance. This method establishes a feasible amperometric immunoassay method for sensitive analysis of AFP in serum samples. Under the optimal experimental conditions, the DPV current response of the immunosensor is proportional to the logarithmic value of the AFP concentration. The linear detection range can achieve to 0.005–20 ng/mL with a detection limit of 1.5 pg/mL. The proposed immunosensor has good precision, selectivity and stability, and can be used for AFP determination in clinical tests.

Keywords: sandwich immunosensor, alpha-fetoprotein, electrochemical analysis, cancer biomarker, glassy carbon electrode

OPEN ACCESS

Edited by:
Hassan Karimi-maleh, University of Electronic Science and Technology of China, China

Reviewed by:
Li Fu, Hangzhou Dianzi University, China
Sadegh Salmanpour, Islamic Azad University Sari Branch, Iran

***Correspondence:**
Jianwei Jiang
swpru5v2@21cn.com

Specialty section:
This article was submitted to Electrochemistry, a section of the journal Frontiers in Chemistry

Received: *31 July 2020*
Accepted: *17 August 2020*
Published: *16 September 2020*

Citation:
Shen C, Wang L, Zhang H, Liu S and Jiang J (2020) An Electrochemical Sandwich Immunosensor Based on Signal Amplification Technique for the Determination of Alpha-Fetoprotein. Front. Chem. 8:589560. doi: 10.3389/fchem.2020.589560

INTRODUCTION

Alpha-fetoprotein (AFP) is a glycoprotein, mainly produced by embryonic liver cells. About 2 weeks after birth, AFP disappears from the blood. Under normal circumstances, the content of AFP in adult serum is <25 ng/mL. However, it is elevated in the blood of about 80% of liver cancer patients. When liver cells become cancerous, they restore their ability to produce AFP. When the condition gradually worsens, the content will increase substantially (Li et al., 2017, 2020; Yang et al., 2018; Ma L. et al., 2019). Therefore, AFP can be used as a specific clinical detection index for the diagnosis of primary liver cancer. AFP can be detected in multiple channels, generally including fluorescence analysis, enzyme-linked immunoassay, chemiluminescence analysis, chromatography, radioimmunoassay, enzyme-labeled electrophoresis, and electrochemical analysis. From the analysis of markers, it can be divided into labeled AFP sensors and label-free AFP sensors (Fang et al., 2017; Wang et al., 2017; Liu et al., 2018; Fu et al., 2019a; Shamsadin-Azad et al., 2019).

Immunosensor is a combination of sensing technology and specific immune response to detect the reaction between antigen and antibody. A healthy body can defend against the invasion of microorganisms, viruses, and other harmful substances through a variety of mechanisms, including natural immunity and acquired immunity. Antigens are exogenous substances that can induce specific immunity, which can stimulate the immune system of animals and plants and produce

an immune response dominated by antibodies and lymphocytes (Alizadeh et al., 2018; Karimi-Maleh et al., 2020a,b). Immunosensor is a detection device designed using the principle of specific recognition and binding of antigen and antibody. Antigen and antibody molecules are fixed on the surface of the electrode in some form, and form a stable complex with the corresponding antibody or antigen to be detected (Wang et al., 2018; Fu et al., 2020a,b; Karimi-Maleh and Arotiba, 2020). These compounds can cause changes in sensor electrical signals, such as electrode potential or current and capacitance.

Immunolabeling mainly refers to labeling antibodies or antigens in specific reactions to catalyze reactions and improve sensor sensitivity. Common markers include luciferin, enzymes, radioisotopes, nanomaterials, and electronic dense substances. The label sensor is highly sensitive and specific, which has been widely used (Peng et al., 2018; Fu et al., 2019b; Ge et al., 2019; Ma N. et al., 2019; Hu et al., 2020; Ying et al., 2020). When technology enters the nano-era, a large number of nanomaterials were used in biosensors (Baghayeri et al., 2018; Feng et al., 2020; Hojjati-Najafabadi et al., 2020; Hou et al., 2020; Karimi-Maleh et al., 2020c). Therefore, in addition to the above immunolabels, many researchers use nanomaterials as labels to expand the antigen and antibody immune response signals.

In this work, we synthesized Au nanocubes, which are used to effectively label biomacromolecules in electrochemical immunosensors and immunoassays. At the same time, they can also have a significant catalytic effect on the response of the sensor, thereby significantly improving the electrochemical response of the sensor. We then use Au nanocubes to immobilize both AFP antibody and horseradish peroxidase (HRP) as the detection antibody labeling material. In the presence of AFP antigen, a sandwich immunosensor analysis mode is used to perform sensitive and quantitative detection of AFP. The immunosensor has few consumables, high sensitivity and high selectivity, and can be applied to clinical detection.

MATERIALS AND METHODS

Graphene oxide (GO) was purchased from Xianfeng Nano Co., Ltd. $HAuCl_4 \cdot 4H_2O$ was purchased from Shanghai Yuanye Biological Co., Ltd. Methylene blue (MB), cetyltrimethylammonium bromide (CTAB), $NaBH_4$, and trisodium citrate were purchased from Sinopharm Chemical Co., Ltd. The AFP standard solution and mouse monoclonal antibody (anti-AFP) were purchased from Zhengzhou Bosai Biotechnology Co., Ltd. All reagents were analytical grade.

The electrochemical experiment was carried out on the CHI 760C electrochemical analyzer (Shanghai Chenhua Instrument Co., Ltd., China). Three electrode system was adopted: modified electrode as working electrode, platinum wire electrode as counter electrode, saturated calomel electrode as reference electrode (SCE). The solution used in the electrochemical impedance analysis was 0.1 M KCl containing 10 mM $K_4[Fe(CN)_6]$ and 10 mm $K_3[Fe(CN)_6]$. Both cyclic voltammetry (CV) and differential pulse voltammetry (DPV) experiments use 0.1 M PBS as the test solution (containing 0.1 M KCl, pH 6.4).

The preparation of Au cubes was according to the literature. The formed Au cubes were then dispersed into 0.1 M PBS with the addition of HRP and anti-AFP. The mixed solution was stirred under 4°C overnight to form AuC-HRP-anti-AFP.

GO-MB-AuNPs were prepared by mixing of three substances into a 0.1 M PBS overnight. The composite was obtained using a centrifugation process. Then, a certain amount of GO-MB-AuNPs was dip coated on the GCE surface and dried naturally. Ten microliter of anti-AFP was dip coated on the modified electrode and incubated overnight. Then, the electrode was immersed into a BSA solution for removing the excess of anti-AFP. During the AFP sensing, the standard AFP solution was dip-coated on the above-mentioned electrode and incubated for 30 min. Then, the AuC-HRP-anti-AFP was dip-coated on the electrode to forming the sandwich sensor. The DPV scan was recorded in a 0.1 M PBS (containing 4 mM H_2O_2).

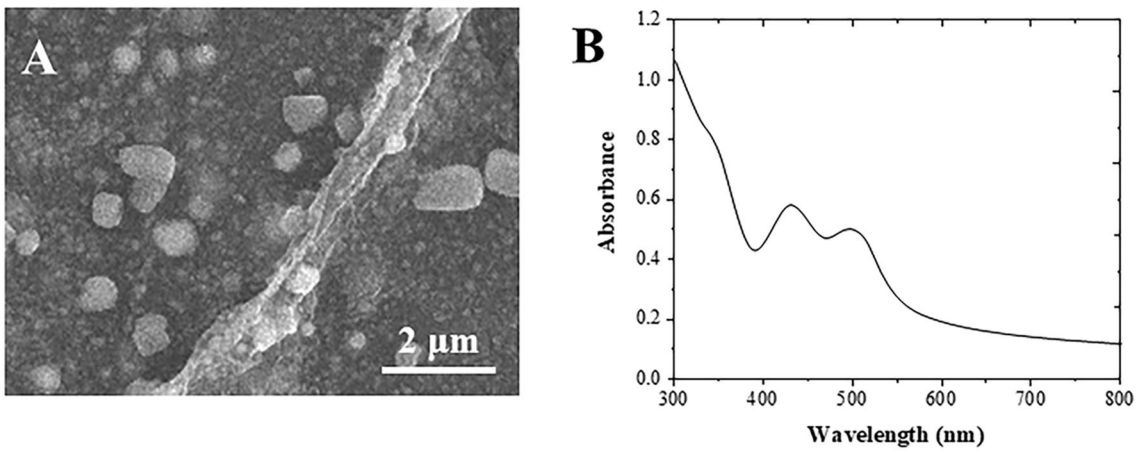

FIGURE 1 | (A) SEM and **(B)** UV-vis spectrum of Au cubes.

RESULTS AND DISCUSSION

Figure 1A shows the SEM image of the formed Au cubes. The diameter of the Au cubes was at an average of 80 nm, in which the structure facilitates the immobilization of anti-AFP antibody and HRP enzyme (Yu et al., 2017). Different substances can produce different UV-visible absorption peaks due to their different structures. It can be seen from **Figure 1B** that there are two obvious absorption peaks at 460 nm and 532 nm in the UV absorption peak of Au cubes (Zhang et al., 2020).

As shown in **Figure 2**, GO has an adsorption peak around 230 nm, while MB has two absorption peaks at around 290 and 650 nm. AuNPs have specific ultraviolet absorption peaks between 500 and 600 nm due to their different particle sizes. The preparation of GO-MB-AuNPs nanocomposites was investigated by UV-vis spectrometer as well (Yang et al., 2017). There are four absorption peaks of GO-MB-AuNPs nanocomposites, which are located at 232, 290,527, and 644 nm respectively, indicating the formation of GO-MB-AuNPs nanocomposites.

Cyclic voltammetry (CV) was used to investigate the electrochemical behavior of modified electrodes at different preparation stages in pH 7.0 PBS (containing 4 mM H_2O_2). As shown in **Figure 3**, the bare GCE has no redox peak in the PBS solution. When the GO-MB-AuNPs nanocomposite material was modified on the electrode surface, a pair of stable redox peaks appeared on the electrode (Zhang et al., 2019). This is the redox of MB immobilized on graphene oxide. After GO-MB-AuNPs capture the anti-AFP antibody and AFP antigen, the redox peak current on the electrode decreases successively, which proves that the antibody and the generated antigen-antibody immune complex have poor conductivity and hinder the electrons transfer on the electrode surface.

EIS can give information about the impedance change on the interface of the electrode during the modification process (Naderi Asrami et al., 2020). The semicircle diameter of EIS is equal to the electron transfer resistance (R_{et}), which controls the electron transfer kinetics of the redox probe on the electrode surface (Campuzano et al., 2017; Ganbat et al., 2020). The EIS results were consistent with the CV results, as shown in **Figure 4**. These results fully indicate that the electrode preparation was successful and the sandwich-type immunosensor can be formed in turn. The synthesized Au nanocubes have high conductivity and electron transfer efficiency, which facilitates the exchange of electrons between the solution and the substrate electrode.

We used the CV method to optimize the amount of modifier, incubation time, pH, and H_2O_2 concentration of the GO-MB-AuNPs nanocomposite. The experimental results show that as the amount of GO-MBAuNPs nanocomposite gradually increases, the peak current gradually increases and the peak current reaches the maximum at 5 μL. When it continues to increase, the peak current decreases instead. Therefore, 5 μL is the best amount of modifier in this work. The incubation time is the time for the antigen-antibody immune reaction on the electrode surface. The results show that the maximum current can be reached when the antigen and antibody reacted for 30 min. There is almost no change in peak current over 30 min. Therefore, we selected 30 min as the incubation time.

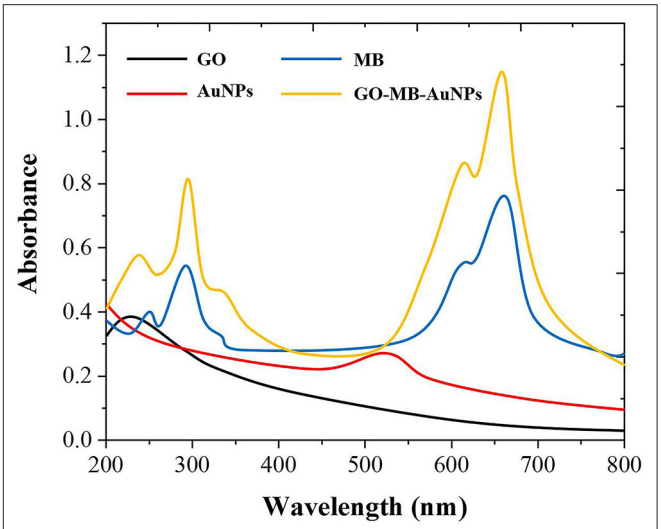

FIGURE 2 | UV-vis spectra of GO, MB AuNPs, and GO-MB-AuNPs nanocomposite.

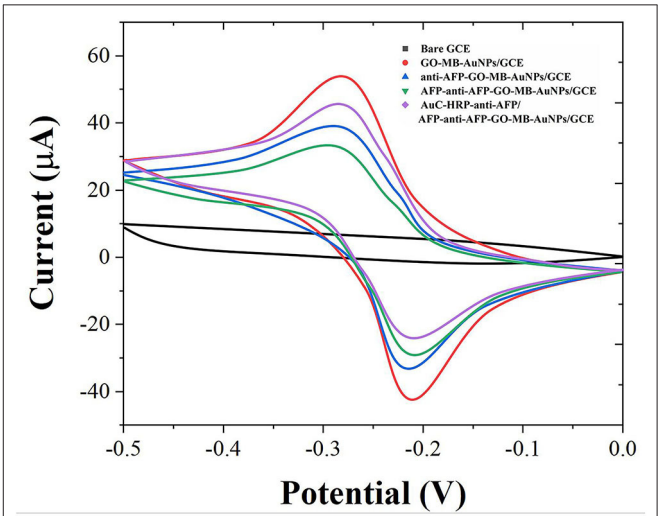

FIGURE 3 | CVs of bare GCE, GO-MB-AuNPs/GCE, anti-AFP-GO-MB-AuNPs/GCE, AFP-anti-AFP-O-MB-AuNPs/GCE, and AuC-HRP-anti-AFP/AFP-anti-AFP-O-MB-AuNPs/GCE.

At the same time, we tested the peak current response of the electrolyte immunosensor at different pH. At pH 5.5–7.0, the peak current of the sensor gradually increases and then gradually decreases. The results prove that pH 7.0 is the optimal pH for the antigen-antibody reaction in this environment, which can ensure the good activity of antigen and antibody. HRP catalyzes H_2O_2 as an important part of signal amplification. The peak current of the sensor increases as the concentration of H_2O_2 increases, and reaches the maximum value at 4 mM. Therefore, 4 mM is used as the optimal concentration of H_2O_2 in subsequent experiments.

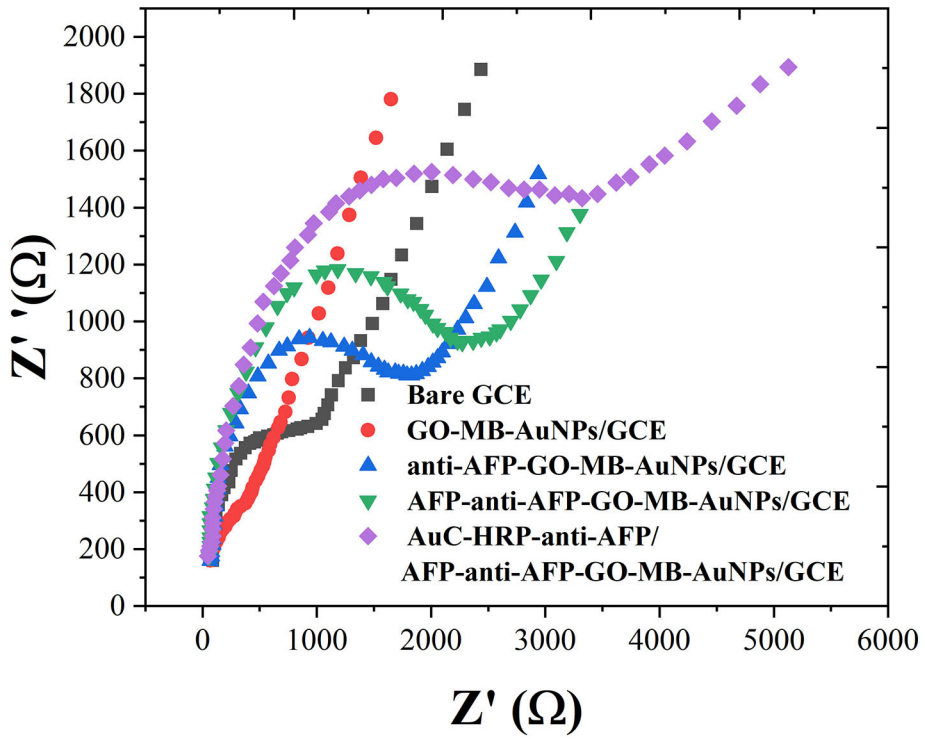

FIGURE 4 | EIS of bare GCE, GO-MB-AuNPs/GCE, anti-AFP-O-MB-AuNPs/GCE, AFP-anti-AFP-O-MB-AuNPs/GCE, and AuC-HRP-anti-AFP/AFP-anti-AFP-O-MB-AuNPs/GCE.

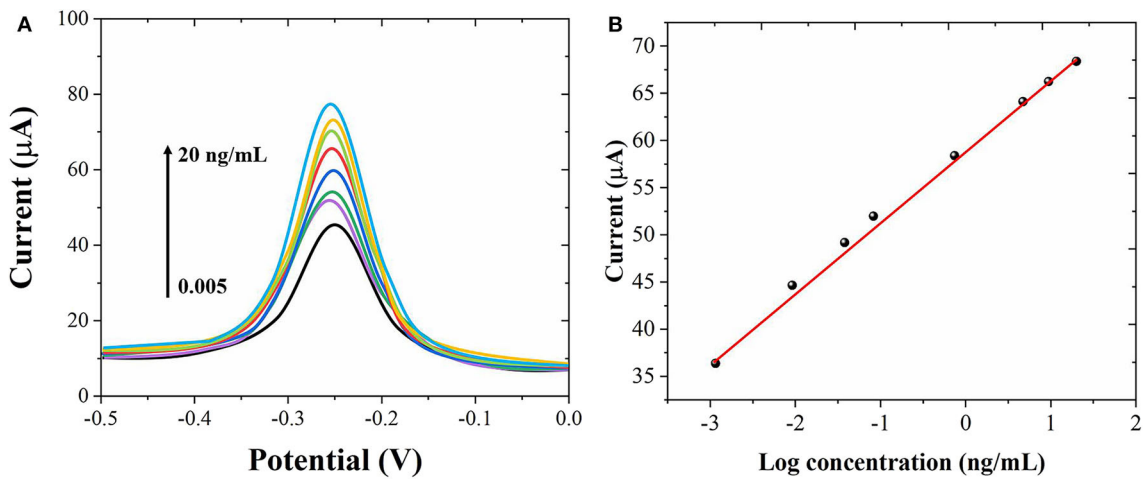

FIGURE 5 | (A) DPV curves of the proposed immunosensor for different concentrations of AFP detection from 0.005 to 20 ng/mL. **(B)** Corresponding linear relationship between the AFP concentrations and peak currents.

Under the optimum conditions, we used the proposed immunosensor to detect AFP standard solutions of different concentrations. **Figure 5A** shows the DPV graph of the sensor to different concentrations of AFP. When the concentration of AFP is between 0.005 and 20 ng/mL, the peak current of DPV increases with the increase of AFP concentration with a good linear relationship. **Figure 5B** shows the linear relationship between the AFP concentrations and the peak current. The limit of detection was calculated to be 1.5 pg/mL. Compared with other related reports (Jiao et al., 2016; Wei et al., 2016; Yuan et al., 2017; Li et al., 2018), this experimental result has a wider linear range and lower detection. The results show that Au nanostructures can be used as a labeling material to immobilize more antibodies and enzymes, which greatly

TABLE 1 | Detection of AFP in serum samples with recovery rate.

Concentration (ng/mL)	Add (ng/mL)	Found (ng/mL)	Recover (%)	RSD (%)
2	2	4.07	101.75	3.37
5	2	6.87	98.14	5.20
10	2	11.74	97.83	2.66

improves the sensitivity and signal response of the electrode, so that the electrode has a wider linear range and lower detection limit.

The proposed electrochemical immunosensor was used to detect the AFP in the serum samples by the standard addition method. The results were shown in **Table 1**. The recovery rate obtained from the experimental results was 97.83–101.75%, indicating that the immunosensor has the potential for clinic AFP determination.

The reproducibility is a key issue of the electrochemical sensor. For this purpose, the current response of the four sensors prepared at the same conditions was measured. The results displayed that the relative standard deviation (RSD) of electrochemical response for four sensors was about 3.31%, indicating that the immunosensor had a good reproducibility. Meanwhile, the RSD obtained from six successive measurements for each electrode was ∼2.61%, suggesting acceptable repeatability.

CONCLUSION

Experimental results show that Au cubes were ideal material for immobilizing antigen-antibody, which can greatly improve the response signal of the electrode. The proposed sandwich-type immunosensor has higher sensitivity. The detection of AFP also has a wide linear range and a low detection limit, and a good recovery rate is obtained when the actual sample is detected.

DATA AVAILABILITY STATEMENT

The original contributions presented in the study are included in the article/supplementary material, further inquiries can be directed to the corresponding author/s.

AUTHOR CONTRIBUTIONS

JJ contributed the conception and design of the study. CS and LW conducted the electrochemical experiments. CS and HZ performed the statistical analysis. SL and JJ wrote the manuscript. All authors contributed to manuscript revision, read, and approved the submitted version.

REFERENCES

Alizadeh, N., Salimi, A., and Hallaj, R. (2018). Magnetoimmunosensor for simultaneous electrochemical detection of carcinoembryonic antigen and α-fetoprotein using multifunctionalized Au nanotags. *J. Electroanal. Chem.* 811, 8–15. doi: 10.1016/j.jelechem.2017.12.080

Baghayeri, M., Mahdavi, B., Hosseinpor-Mohsen Abadi, Z., and Farhadi, S. (2018). Green synthesis of silver nanoparticles using water extract of Salvia leriifolia: antibacterial studies and applications as catalysts in the electrochemical detection of nitrite. *Appl. Organomet. Chem.* 32:e4057. doi: 10.1002/aoc.4057

Campuzano, S., Pedrero, M., Nikoleli, G.-P., Pingarrón, J., and Nikolelis, D. (2017). Hybrid 2D-nanomaterials-based electrochemical immunosensing strategies for clinical biomarkers determination. *Biosens. Bioelectron.* 89, 269–279. doi: 10.1016/j.bios.2016.01.042

Fang, X., Liu, J., Wang, J., Zhao, H., Ren, H., and Li, Z. (2017). Dual signal amplification strategy of Au nanopaticles/ZnO nanorods hybridized reduced graphene nanosheet and multienzyme functionalized Au@ ZnO composites for ultrasensitive electrochemical detection of tumor biomarker. *Biosens. Bioelectron.* 97, 218–225. doi: 10.1016/j.bios.2017.05.055

Feng, Y., Wei, Z., and Zhang, J. (2020). Determination of ursolic acid in extracts from ligustri lucidum fruit using an electrochemical method. *Front. Chem.* 8:444. doi: 10.3389/fchem.2020.00444

Fu, L., Liu, Z., Ge, J., Guo, M., Zhang, H., Chen, F., et al. (2019a). (001) plan manipulation of α-Fe_2O_3 nanostructures for enhanced electrochemical Cr(VI) sensing. *J. Electroanal. Chem.* 841, 142–147. doi: 10.1016/j.jelechem.2019.04.046

Fu, L., Wu, M., Zheng, Y., Zhang, P., Ye, C., Zhang, H., et al. (2019b). Lycoris species identification and infrageneric relationship investigation via graphene enhanced electrochemical fingerprinting of pollen. *Sens. Actuators B Chem.* 298:126836. doi: 10.1016/j.snb.2019.126836

Fu, L., Zhang, H., Zheng, Y., Zhang, H., and Liu, Q. (2020a). An electroanalytical method for brewing vinegar authentic identification. *Rev. Mex. Ing. Quím.* 19, 803–812. doi: 10.24275/rmiq/Alim869

Fu, L., Zheng, Y., Zhang, P., Zhang, H., Xu, Y., Zhou, J., et al. (2020b). Development of an electrochemical biosensor for phylogenetic analysis of Amaryllidaceae based on the enhanced electrochemical fingerprint recorded from plant tissue. *Biosens. Bioelectron.* 159:112212. doi: 10.1016/j.bios.2020.112212

Ganbat, K., Pan, D., Chen, K., Ning, Z., Xing, L., Zhang, Y., et al. (2020). One-pot electrografting preparation of bifunctionalized carbon nanotubes for sensitive electrochemical immunosensing. *J. Electroanal. Chem.* 860:113906. doi: 10.1016/j.jelechem.2020.113906

Ge, L., Li, B., Xu, H., Pu, W., and Kwok, H. F. (2019). Backfilling rolling cycle amplification with enzyme-DNA conjugates on antibody for portable electrochemical immunoassay with glucometer readout. *Biosens. Bioelectron.* 132, 210–216. doi: 10.1016/j.bios.2019.02.051

Hojjati-Najafabadi, A., Rahmanpour, M. S., Karimi, F., Zabihi-Feyzaba, H., Malekmohammad, S., Agarwal, S., et al. (2020). Determination of tert-butylhydroquinone using a nanostructured sensor based on CdO/SWCNTs and ionic liquid. *Int. J. Electrochem. Sci.* 15, 6969–6980. doi: 10.20964/2020.07.85

Hou, K., Zhao, P., Chen, Y., Li, G., Lin, Y., Chen, D., et al. (2020). Rapid detection of bifidobacterium bifidum in feces sample by highly sensitive quartz crystal microbalance immunosensor. *Front. Chem.* 8:548. doi: 10.3389/fchem.2020.00548

Hu, T., Zhang, M., Wang, Z., Chen, K., Li, X., and Ni, Z. (2020). Layer-by-layer self-assembly of MoS_2/PDDA hybrid film in microfluidic chips for ultrasensitive electrochemical immunosensing of alpha-fetoprotein. *Microchem. J.* 158:105209. doi: 10.1016/j.microc.2020.105209

Jiao, L., Mu, Z., Zhu, C., Wei, Q., Li, H., Du, D., et al. (2016). Graphene loaded bimetallic Au@ Pt nanodendrites enhancing ultrasensitive electrochemical immunoassay of AFP. *Sens. Actuators B Chem.* 231, 513–519. doi: 10.1016/j.snb.2016.03.034

Karimi-Maleh, H., and Arotiba, O. A. (2020). Simultaneous determination of cholesterol, ascorbic acid and uric acid as three essential biological compounds at a carbon paste electrode modified with copper oxide decorated reduced graphene oxide nanocomposite and ionic liquid. *J. Colloid Interface Sci.* 560, 208–212. doi: 10.1016/j.jcis.2019.10.007

Karimi-Maleh, H., Cellat, K., Arikan, K., Savk, A., Karimi, F., and Sen, F. (2020a). Palladium–nickel nanoparticles decorated on functionalized-MWCNT for high precision non-enzymatic glucose sensing. *Mater. Chem. Phys.* 250:123042. doi: 10.1016/j.matchemphys.2020.123042

Karimi-Maleh, H., Karimi, F., Malekmohammadi, S., Zakariae, N., Esmaeili, R., Rostamnia, S., et al. (2020b). An amplified voltammetric sensor based on platinum nanoparticle/polyoxometalate/two-dimensional hexagonal boron nitride nanosheets composite and ionic liquid for determination of N-hydroxysuccinimide in water samples. *J. Mol. Liq.* 310:113185. doi: 10.1016/j.molliq.2020.113185

Karimi-Maleh, H., Karimi, F., Orooji, Y., Mansouri, G., Razmjou, A., Aygun, A., et al. (2020c). A new nickel-based co-crystal complex electrocatalyst amplified by NiO dope Pt nanostructure hybrid; a highly sensitive approach for determination of cysteamine in the presence of serotonin. *Sci. Rep.* 10, 11699. doi: 10.1038/s41598-020-68663-2

Li, G., Li, S., Wang, Z., Xue, Y., Dong, C., Zeng, J., et al. (2018). Label-free electrochemical aptasensor for detection of alpha-fetoprotein based on AFP-aptamer and thionin/reduced graphene oxide/gold nanoparticles. *Anal. Biochem.* 547, 37–44. doi: 10.1016/j.ab.2018.02.012

Li, J., Gao, T., Gu, S., Zhi, J., Yang, J., and Li, G. (2017). An electrochemical biosensor for the assay of alpha-fetoprotein-L3 with practical applications. *Biosens. Bioelectron.* 87, 352–357. doi: 10.1016/j.bios.2016.08.071

Li, W., Ma, C., Song, Y., Qiao, X., and Hong, C. (2020). A sandwich-type electrochemical immunosensor for ultrasensitive detection of multiple tumor markers using an electrical signal difference strategy. *Talanta* 219:121322. doi: 10.1016/j.talanta.2020.121322

Liu, S., Ma, Y., Cui, M., and Luo, X. (2018). Enhanced electrochemical biosensing of alpha-fetoprotein based on three-dimensional macroporous conducting polymer polyaniline. *Sens. Actuators B Chem.* 255, 2568–2574. doi: 10.1016/j.snb.2017.09.062

Ma, L., Jayachandran, S., Li, Z., Song, Z., Wang, W., and Luo, X. (2019). Antifouling and conducting PEDOT derivative grafted with polyglycerol for highly sensitive electrochemical protein detection in complex biological media. *J. Electroanal. Chem.* 840, 272–278. doi: 10.1016/j.jelechem.2019.04.002

Ma, N., Zhang, T., Fan, D., Kuang, X., Ali, A., Wu, D., et al. (2019). Triple amplified ultrasensitive electrochemical immunosensor for alpha fetoprotein detection based on MoS_2@ Cu_2O-Au nanoparticles. *Sens. Actuators B Chem.* 297:126821. doi: 10.1016/j.snb.2019.126821

Naderi Asrami, P., Aberoomand Azar, P., Saber Tehrani, M., and Mozaffari, S. A. (2020). Glucose oxidase/nano-ZnO/thin film deposit FTO as an innovative clinical transducer: a sensitive glucose biosensor. *Front. Chem.* 8:503. doi: 10.3389/fchem.2020.00503

Peng, F., Chu, M., Sun, J., Liu, Y., Zhang, Q., Chen, Y., et al. (2018). Preparation of Fe3O4@ PS/PDA-Au nanotubes for sensitive electrochemical detection of alpha-fetoprotein. *J. Electroanal. Chem.* 814, 52–58. doi: 10.1016/j.jelechem.2017.12.076

Shamsadin-Azad, Z., Taher, M. A., Cheraghi, S., and Karimi-Maleh, H. (2019). A nanostructure voltammetric platform amplified with ionic liquid for determination of tert-butylhydroxyanisole in the presence kojic acid. *J. Food Meas. Charact.* 13, 1781–1787. doi: 10.1007/s11694-019-00096-6

Wang, H., Zhang, Y., Wang, Y., Ma, H., Du, B., and Wei, Q. (2017). Facile synthesis of cuprous oxide nanowires decorated graphene oxide nanosheets nanocomposites and its application in label-free electrochemical immunosensor. *Biosens. Bioelectron.* 87, 745–751. doi: 10.1016/j.bios.2016.09.014

Wang, Y., Zhao, G., Wang, H., Cao, W., Du, B., and Wei, Q. (2018). Sandwich-type electrochemical immunoassay based on Co_3O_4@ MnO_2-thionine and pseudo-ELISA method toward sensitive detection of alpha fetoprotein. *Biosens. Bioelectron.* 106, 179–185. doi: 10.1016/j.bios.2018.02.002

Wei, Y., Li, Y., Li, N., Zhang, Y., Yan, T., Ma, H., et al. (2016). Sandwich-type electrochemical immunosensor for the detection of AFP based on Pd octahedral and APTES-M-CeO_2-GS as signal labels. *Biosens. Bioelectron.* 79, 482–487. doi: 10.1016/j.bios.2015.12.082

Yang, S., Zhang, F., Wang, Z., and Liang, Q. (2018). A graphene oxide-based label-free electrochemical aptasensor for the detection of alpha-fetoprotein. *Biosens. Bioelectron.* 112, 186–192. doi: 10.1016/j.bios.2018.04.026

Yang, T., Jia, H., Liu, Z., Qiu, X., Gao, Y., Xu, J., et al. (2017). Label-free electrochemical immunoassay for α-fetoprotein based on a redox matrix of Prussian blue-reduced graphene oxide/gold nanoparticles-poly (3, 4-ethylenedioxythiophene) composite. *J. Electroanal. Chem.* 799, 625–633. doi: 10.1016/j.jelechem.2017.06.031

Ying, J., Zheng, Y., Zhang, H., and Fu, L. (2020). Room temperature biosynthesis of gold nanoparticles with Lycoris aurea leaf extract for the electrochemical determination of aspirin. *Rev. Mex. Ing. Quím.* 19, 585–592. doi: 10.24275/rmiq/Mat741

Yu, S., Wu, X., Sun, B., Wu, W., and Wang, H. (2017). Fabrication of an electrochemical immunosensor containing Au–Ag alloy for the detection of alpha fetoprotein. *Int. J. Electrochem. Sci.* 12, 10381–10389. doi: 10.20964/2017.11.02

Yuan, Y., Li, S., Xue, Y., Liang, J., Cui, L., Li, Q., et al. (2017). A Fe_3O_4@ Au-basedpseudo-homogeneous electrochemical immunosensor for AFP measurement using AFP antibody-GNPs-HRP as detection probe. *Anal. Biochem.* 534, 56–63. doi: 10.1016/j.ab.2017.07.015

Zhang, K., Cao, Z., Wang, S., Chen, J., Wei, Y., and Feng, D. (2020). A novel sandwich-type electrochemical immunosensor based on the signal amplification strategy of core-shell Pd@ Pt nanoparticles for α-fetoprotein detection. *Int. J. Electrochem. Sci.* 15, 2604–2613. doi: 10.20964/2020.03.32

Zhang, S., Zhang, C., Jia, Y., Zhang, X., Dong, Y., Li, X., et al. (2019). Sandwich-type electrochemical immunosensor based on Au@ Pt DNRs/NH_2–$MoSe_2$ NSs nanocomposite as signal amplifiers for the sensitive detection of alpha-fetoprotein. *Bioelectrochemistry* 128, 140–147. doi: 10.1016/j.bioelechem.2019.03.012

Conflict of Interest: The authors declare that the research was conducted in the absence of any commercial or financial relationships that could be construed as a potential conflict of interest.

frontiers in Chemistry

ORIGINAL RESEARCH
published: 20 October 2020
doi: 10.3389/fchem.2020.593070

Electrochemical Determination of Nicotine in Tobacco Products Based on Biosynthesized Gold Nanoparticles

Yanqiu Jing[1†], Shanghui Ning[2†], Yu Guan[3†], Mingfeng Cao[2], Junju Li[3], Li Zhu[2], Qili Zhang[3], Chuance Cheng[1*] and Yong Deng[2*]*

[1] College of Tobacco Science, Henan Agricultural University, Zhengzhou, China, [2] Changde Branch of Hunan Tobacco Corporation, Changde, China, [3] Sichuan of China National Tobacco Corporation, Chengdu, China

OPEN ACCESS

Edited by:
Hassan Karimi-Maleh, University of Electronic Science and Technology of China, China

Reviewed by:
Yuhong Zheng, Jiangsu Province and Chinese Academy of Sciences, China
Sadegh Salmanpour, Islamic Azad University Sari Branch, Iran

***Correspondence:**
Yanqiu Jing
jingyanqiu72t@henau.edu.cn
Chuance Cheng
chuancecheng_hau@163.com
Yong Deng
mu94237937@163.com

[†] These authors have contributed equally to this work

Specialty section:
This article was submitted to Electrochemistry, a section of the journal Frontiers in Chemistry

Received: 09 August 2020
Accepted: 04 September 2020
Published: 20 October 2020

Citation:
Jing Y, Ning S, Guan Y, Cao M, Li J, Zhu L, Zhang Q, Cheng C and Deng Y (2020) Electrochemical Determination of Nicotine in Tobacco Products Based on Biosynthesized Gold Nanoparticles. Front. Chem. 8:593070. doi: 10.3389/fchem.2020.593070

In this work, gold nanoparticles were biosynthesized via *Plectranthus amboinicus* leaf extract as the reducing agent. A series of techniques were used for sample analysis. The biosynthesized gold nanoparticles (bAuNPs) are a uniform size with a spherical shape. The FTIR analysis reveals the presence of many oxygen-containing functional groups on the bAuNP surface. The cyclic voltammetry and electrochemical impedance spectroscopic characterizations reveal that while the bAuNPs have a slightly lower conductivity than chemically synthesized AuNPs (cAuNPs). However, the bAuNPs have a superior electrocatalytic performance toward nicotine reduction. After optimization, the bAuNP-modified SPE could detect nicotine linearly from 10 to 2,000 μM with a low detection limit of 2.33 μM. In addition, the bAuNPs/SPE have been successfully used for nicotine-containing-product analysis.

Keywords: biosynthesis, nicotine, gold nanoparticle, electrochemical sensor, *Plectranthus amboinicus*

INTRODUCTION

Nicotine is an alkaloid found in the Solanaceae family and is an important ingredient in tobacco. Currently, the fact that smoking is harmful to health has become common sense. The main active ingredient of cigarettes is nicotine. When nicotine enters the alveoli, it is quickly absorbed and causes serious respiratory diseases and cancer. The data show that the number of deaths caused by smoking each year is up to several million. Therefore, analysis of the quantity of nicotine that is present in tobacco products is very important to the tobacco and pharmaceutical industries. In recent years, methods for the analysis of nicotine have been continuously developed. In addition to traditional chemical methods and titration methods, electrochemical methods, atomic absorption spectrometry, gas chromatography, spectrophotometry, and high-performance liquid chromatography have all been used for the analytical determination of nicotine. Among these techniques, electrochemical-based methods have been found to be more portable with a quick detection procedure and low cost (Fu et al., 2019a; Feng et al., 2020; Hojjati-Najafabadi et al., 2020; Hou et al., 2020; Karimi-Maleh et al., 2020a,b; Naderi Asrami et al., 2020; Xu et al., 2020). However, the common commercial electrode is not sensitive enough for determination of nicotine at low concentrations. Therefore, electrode surface modification has been used for improving the sensitivity of electrochemical methods. For example, Shehata and coworkers demonstrated the use of a nano-TiO_2-modified carbon paste

sensor for nicotine detection (Shehata et al., 2016). Wang and coworkers demonstrated a sensitive nicotine electrochemical sensor based on multiwalled carbon nanotube–alumina-coated silica (Wang et al., 2009). Yu and coworkers reported an electrochemical nicotine sensor based on a multiwalled carbon nanotube/graphene composite (Yu et al., 2016).

Although these prior works demonstrated excellent performance toward electrochemical detection, the chemical synthesis of the electrode modifiers utilized strong reducing agents or toxic reagents (Fu et al., 2019b). Currently, the green synthesis of metal nanoparticles is an interesting issue in the field of nanoscience. There is also growing attention to the biosynthesis of metal nanoparticles using organisms (Hulkoti and Taranath, 2014; Ahmed et al., 2017; Fu et al., 2020a). Nobel metal nanoparticles have been synthesized using various plant extracts. For example, Zheng et al. reported a facile biosynthetic approach for Ag NP preparation using *Plectranthus amboinicus* leaf extract (Zheng et al., 2017). Medda and coworkers reported a biosynthesis of Ag NPs using *Aloe vera* leaf extract (Medda et al., 2015). Most of the biosynthesized noble metal nanoparticles were applied for antibacterial and catalytic applications (El-Seedi et al., 2019; Otari et al., 2019; Spagnoletti et al., 2019; Fu et al., 2020b; Ramteke et al., 2020). In this work, we attempted to extend the application to biosynthesized Au NPs for electrochemical sensing. Gold nanoparticles have attracted increasing attention due to their unique properties in multidisciplinary research fields (Zhang and Hu, 2019; Li et al., 2020). It's nanostructures have been used for fabrication of optical devices (Noguez and Garzón, 2009), catalysis (Corma and Garcia, 2008), surface-enhanced Raman scattering (SERS) (Wang et al., 2016), biological labeling (Dalal et al., 2016), bioimaging (Sun et al., 2018), and drug delivery and antimicrobial agents (Manzano and Vallet-Regí, 2020). Recently, syntheses of Au and Ag nanoparticles using extracts of cinnamomum camphora leaf (Huang et al., 2007), phyllanthin (Kasthuri et al., 2009), or edible mushroom (Philip, 2009) as reducing and capping agents have been reported. In this article, we further investigate the electrochemical properties of the *Plectranthus amboinicus* leaf extract-synthesized Ag NPs toward nicotine.

EXPERIMENTS

Plectranthus amboinicus plants were purchased from a local nursery of Zhengzhou, China. $HAuCl_4$ and nicotine

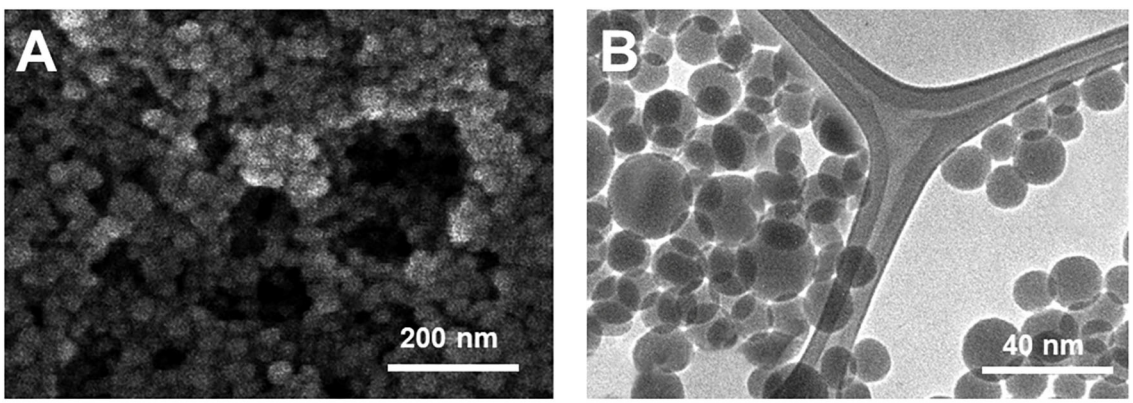

FIGURE 1 | (A) SEM and **(B)** TEM image of bAuNPs.

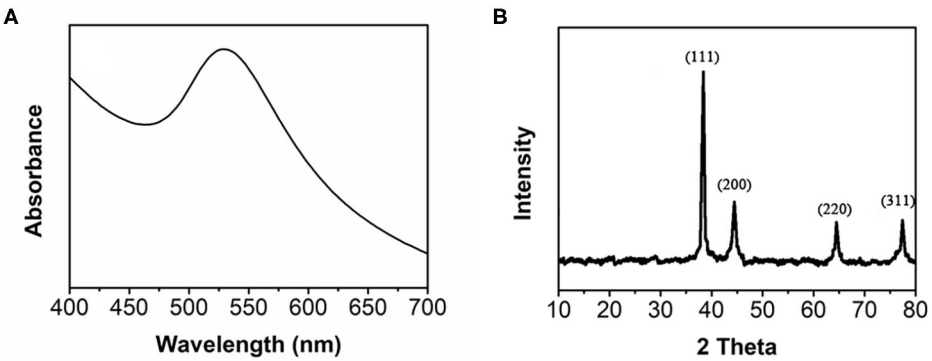

FIGURE 2 | (A) UV-vis spectrum and **(B)** XRD pattern of bAuNPs.

were purchased from Sigma-Aldrich. All other chemicals were analytical grade reagents and were used without further purification.

Ten milliliter of *Plectranthus amboinicus* leaf extract was added into a 0.1 M $HAuCl_4$ solution and stirred continuously at 70°C for 5 h. The gray precipitate was collected using centrifugation. Chemically synthesized Au NPs were prepared using the same quantity of gold precursor and 1 mL of sodium borohydride (0.5 mM) as the reducing agent.

For the electrochemical study, a GCE (3 mm in diameter) was polished with an alumina-water slurry and then rinsed with water. Then, 5 μL of dispersion catalyst (0.5 mg/mL) was dropped onto the GCE surface and dried naturally. Electrochemical measurements were performed on a CHI660A electrochemical Workstation using a three-electrode system. A platinum wire was used as the auxiliary electrode and Ag/AgCl (3M KCl) was used as the reference electrode.

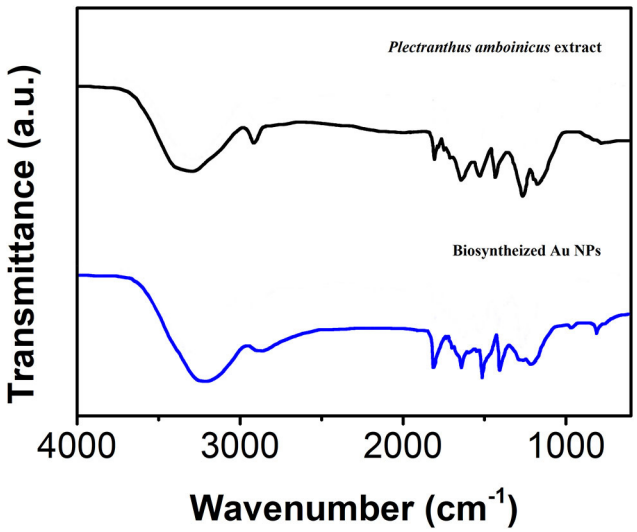

FIGURE 3 | FTIR spectrum of the bAuNPs.

RESULTS AND DISCUSSION

The morphology of the biosynthesized AuNPs (bAuNPs) was characterized using SEM and TEM. **Figure 1A** shows the SEM image of the bAuNPs. It can be observed that the bAuNPs were spherical in shape with a diameter of <20 nm (**Figure 1A**). The boundary between the particles can be clearly observed, suggesting the possibility that biomolecule functional groups are on the bAuNP surfaces, preventing aggregation. TEM characterization provides more detailed morphology information. As shown in **Figure 1B**, the average diameter of the bAuNPs is 14 nm, based on the calculation of 50 individual particles. With the exception of some larger particles, most bAuNPs are a uniform size.

The formation of bAuNPs was then confirmed using UV-Vis spectroscopy and XRD. As shown in **Figure 2A**, the UV-Vis spectrum of the bAuNPs shows a peak located at ∼525 nm, indicating excitations from the surface plasmon vibration of the AuNPs (Vilas et al., 2016). The sharp shape of the UV-Vis peak also suggests the uniform size of the bAuNPs. **Figure 2B** shows the XRD pattern of the bAuNPs. As shown in the figure, the pattern exhibits several peaks located at the scan angles 38.29°, 44.42°, 64.74°, and 77.67°, corresponding to the (111), (200), (220), and (311) planes, respectively, of standard gold metal (Au^0) (Yang et al., 2014). No extra peaks were found in the XRD pattern, suggesting no impurity crystals were formed during the biosynthesis process.

The presence of the surface functional groups on the bAuNPs was confirmed using FTIR spectroscopy. **Figure 3** shows the FTIR spectrum of the bAuNPs with the *Plectranthus amboinicus* leaf extract. The spectrum of the leaf extract displays a series of absorbance bands ranging from 700 to 2,000 cm^{-1}. The absorbance bands at 1,334 and 1,220 cm^{-1} can be ascribed to the C-O stretching frequencies corresponding to polysaccharides and polyols. The polysaccharides and polyols commonly exhibit

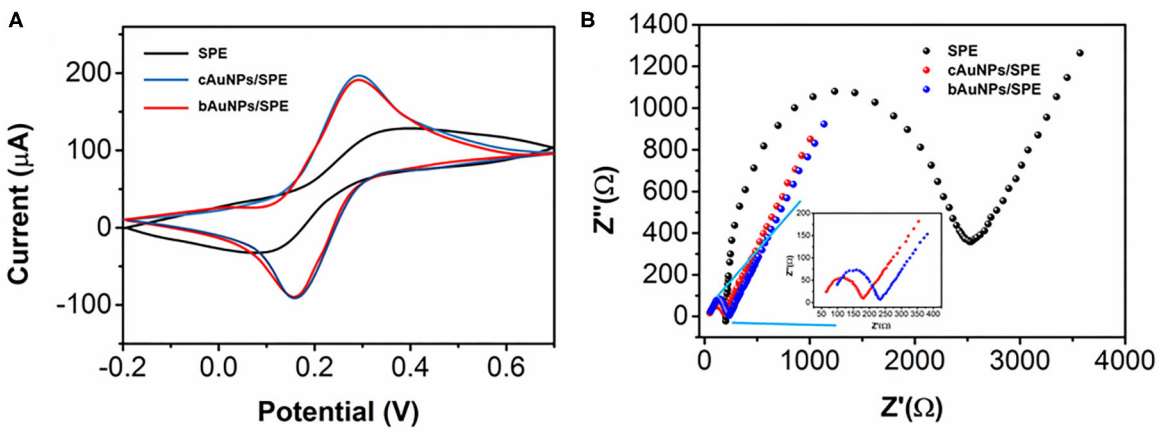

FIGURE 4 | (A) Cyclic voltammograms and **(B)** EIS curves of SPE, bAuNPs/SPE and cAuNPs/SPE toward 5 mM $[Fe(CN)_6]^{3-/4-}$ containing 0.1 M KCl.

weak reducibility, which can be used for Au precursor reduction (Begum et al., 2009). In addition, an absorbance band located at 879 cm^{-1} corresponds to the C-N vibrations of the nitroso groups, which are typically present when nanomaterial surfaces are capped by biomolecules (Slocik and Naik, 2017; Wang et al., 2018; Shamsadin-Azad et al., 2019; Karimi-Maleh et al., 2020c; Karthikeyan et al., 2020).

The electrochemical properties of the bAuNPs were compared with chemically synthesized AuNPs (cAuNPs) by cyclic voltammetry using a $[Fe(CN)_6]^{3-/4-}$ probe. As shown in **Figure 4A**, the bare SPE has well-defined redox peaks at 0.32 and 0.11 V, while both the cAuNPs/SPE and the bAuNPs/SPE exhibit smaller peak-peak separation. Specifically, the cAuNPs/SPE has redox peaks at 0.26 and 0.18 V, while the bAuNPs/SPE has redox peaks at 0.25 and 0.18 V. The results indicate that modification by either of the synthesized AuNPs significantly enhances the electroconductivity of the SPE. It can be observed that the bAuNPs/SPE has a slight lower oxidation peak response compared with that of the cAuNPs/SPE, suggesting that AuNPs biosynthesized using *Plectranthus amboinicus* leaf extract as the reducing agent could be of a competitive quality when compared to common chemically synthesized AuNPs. Electrochemical impedance spectroscopy (EIS) was used for further analysis. As shown in **Figure 4B**, the bare SPE shows a larger capacitive loop than both of the AuNP modified SPEs. As shown in the inset of the **Figure 4B**, the cAuNPs/SPE exhibits a slightly smaller capacitive loop than that of the bAuNPs/SPE, suggesting that the cAuNPs/SPE has a superior electroconductivity. This observation is in good agreement with the results deduced from CV characterization.

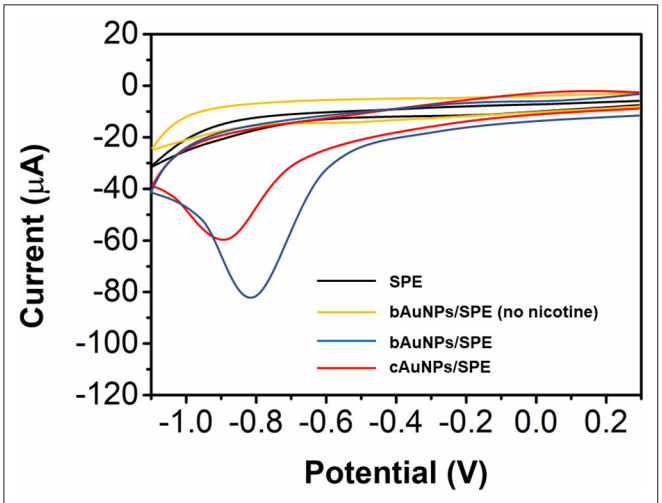

FIGURE 5 | Cyclic voltammograms of the bare SPE, cAuNPs/SPE and bAuNPs/SPE toward 0.5 mM nicotine.

Although the electroconductivity of the bAuNPs/SPE is not as good as the cAuNPs/SPE, the bAuNPs/SPE has a superior electrocatalytic response toward nicotine. As shown in **Figure 5**, bare SPE shows negligible reduction toward 0.5 mM nicotine. In contrast, both bAuNPs/SPE and cAuNPs/SPE exhibit a well-defined reduction peak toward 0.5 mM nicotine, suggesting that the AuNPs could effectively trigger the electrocatalytic reduction of nicotine. More specifically, the cAuNPs/SPE exhibits a reduction peak at −0.86 V with a current response of 60.77 μA, while the bAuNPs/SPE exhibits a reduction peak at −0.80 V with a current response of 87.62 μA. The lower reduction potential with a higher current response indicates the bAuNPs/SPE exhibits a superior electrocatalytic response toward nicotine compared with that of the cAuNPs/SPE. The superior electrocatalytic performance could be ascribed to the presence of the biomolecules of the bAuNPs/SPE surface. As indicated in the FTIR characterization, these molecules offer many oxygen-containing functional groups to the bAuNPs, which could be used for binding nicotine and result in a higher current response. Moreover, as reported in the literature (Huang et al., 2018; Liang et al., 2018; Zhu et al., 2019), oxygen-containing groups could trigger the electrocatalytic reaction during the scan. We also conducted cyclic voltammetry of the bAuNPs/SPE in the absence of nicotine. No noticeable peak can be found in the CV profile, suggesting that the peak located at −0.80 V does indeed belong to the nicotine reduction.

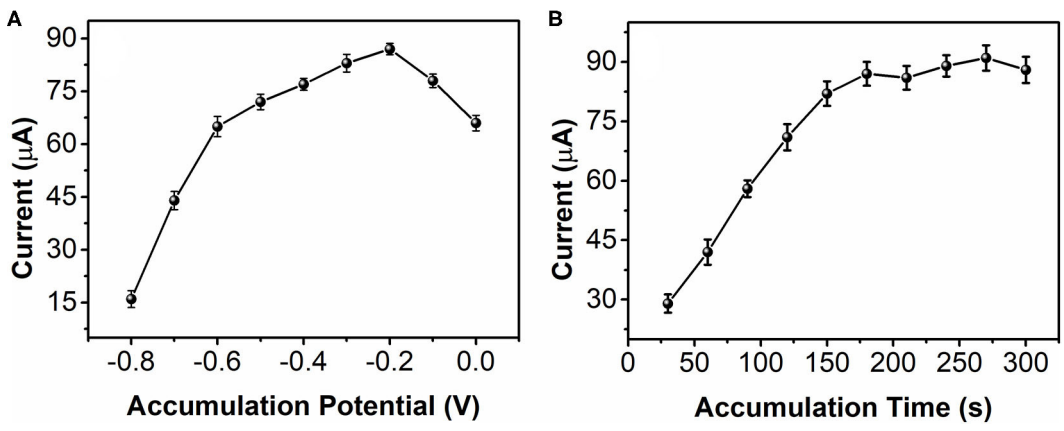

FIGURE 6 | Effect of **(A)** accumulation potential and **(B)** accumulation time of the bAuNPs/SPE toward 0.5 mM nicotine reduction.

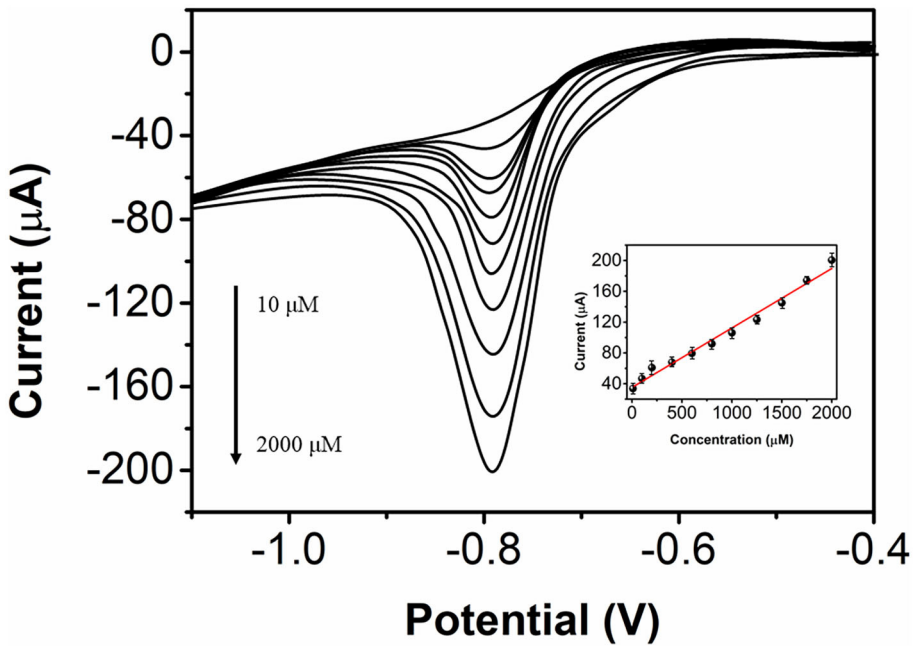

FIGURE 7 | Differential pulse voltammograms of the bAuNPs/SPE toward nicotine from 10 μM to 2 mM.

TABLE 1 | Electrochemical nicotine sensor performance comparison.

Electrode	Linear detection range	Detection limit	References
Nitrogen-doped graphene/GCE	0–200 μM	0.27 μM	Li et al., 2017
PoPD/GCE	0.000183–1.01 μM	55.00 pM	Liang et al., 2012
Boron-doped diamond electrode	0.5–200 μM	0.30 μM	Švorc et al., 2014
RGO/DPA/PGE	131–1,900 μM	7.60 μM	Jing et al., 2017
bAuNPs/SPE	10–2,000 μM	2.33 μM	This work

Accumulation is a important process for enhancing electrochemical sensing. **Figure 6A** shows the effect of 0.5 mM nicotine reduction at bAuNPs/SPE with different accumulation potentials. The results suggest that accumulation at a more negative potential does not improve the sensing performance. The reduction increases along with the accumulation potential decreases from −0.8 to −0.2 V. The maximum current can be noticed at −0.2 V. In addition, further decreasing the accumulation potential can reverse the sensing performance. Therefore, −0.2 V was selected for nicotine reduction. Accumulation time is another important factor. As shown in **Figure 6B**, the current response of the nicotine reduction increases as the accumulation time increases. A significant current increase can be observed as the accumulation time increases from 30 to 150 s. The enhancement speed of the current response was decreased after 150 s, and especially after 180 s accumulation time. Therefore, 180 s was used for the accumulation time.

The determination performance of bAuNPs/SPE toward nicotine was also studied using differential pulse voltammetry (DPV). **Figure 7** shows the DPV profiles of the bAuNPs/SPE toward nicotine at nicotine concentrations of 10 μM to 2 mM, while the inset shows the plot of current response against nicotine concentration. A linear regression was found, and the equation can be expressed as $I(\mu A) = 0.07722$ (concentration) $+35.25039$ ($R = 0.99$). The limit of detection was calculated to be 2.33 μM based on a signal-to-noise ratio of 3. **Table 1** shows the comparison of the performance of the proposed electrochemical nicotine sensor with performances in previous reports. As shown in the table, the bAuNPs/SPE exhibits a wider electrochemical sensing performance compared with other reported performances, which is favorable for nicotine analysis in tobacco products.

The anti-interference property of the bAuNPs/SPE was also studied. **Figure 8** shows the successive addition of 0.5 mM nicotine, glucose, uric acid, ascorbic acid, dopamine, norepinephrine, and tyrosine. It can be seen that all interference molecules showed negligible effects on the nicotine sensing (current changes of <5%). The results suggest that the proposed bAuNPs/SPE has a good anti-interference property to nicotine sensing.

The reproducibility of the bAuNPs/SPE was tested with seven individually prepared electrodes. **Figure 9A** shows the current responses of the seven electrodes toward 0.5 mM nicotine. The RSD is calculated to be 4.41%, suggesting that the proposed bAuNPs/SPE has a stable

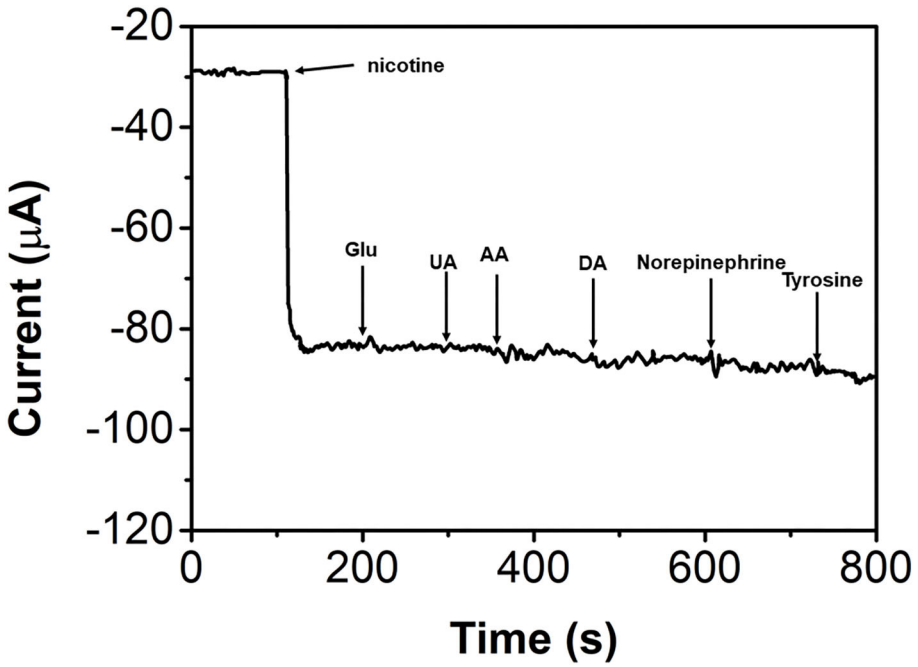

FIGURE 8 | I-T response of the bAuNPs/SPE with successive addition of 0.5 mM nicotine, glucose, uric acid, ascorbic acid, dopamine, norepinephrine and tyrosine.

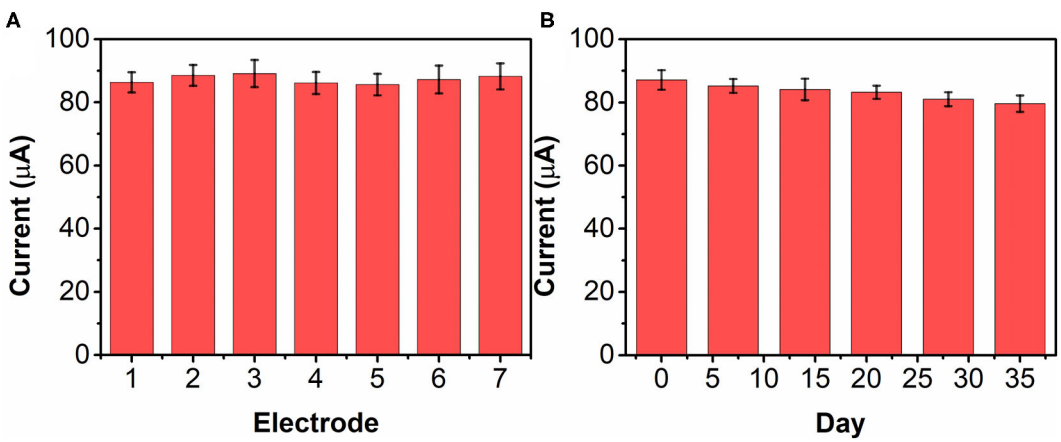

FIGURE 9 | (A) Reproducibility of seven individual bAuNPs/SPE toward 0.2 mM nicotine detection. **(B)** Long-term stability test of bAuNPs/SPE.

performance. The long-term stability of the bAuNPs/SPE was also tested. As shown in **Figure 9B**, the bAuNPs/SPE retain more than 85% of original performance after 35 days of storage at room temperature, suggesting acceptable long-term stability.

Two brands of cigarette and an E-cigarette liquid refill were used as real test samples. Nicotine was extracted from the cigarette samples using ethanol. The detection results are summarized in **Table 2**. A standard addition method was adopted for determining the recovery rate for the proposed electrochemical-sensing strategy. As shown in Table 2, the bAuNPs/SPE show a well-resolved performance and recovery rate, suggesting the potential of the bAuNPs/SPE to be used for commercial nicotine containing product analysis.

CONCLUSIONS

In conclusion, bAuNPs haves been successfully biosynthesized using *Plectranthus amboinicus* leaf extract as the reducing agent. The formed bAuNPs have a uniform size with a spherical shape. Characterizations indicate the proposed biosynthesis method could be used to prepare AuNPs with a high purity. The FTIR spectrum confirms the functional

TABLE 2 | Electrochemical determination of nicotine concentrations in two brands of cigarette and an E-cigarette liquid refill using bAuNPs/SPE.

Sample	Addition (μM)	Found (μM)	RSD (%)	Recovery (%)
Cigarette 1	0	22.4	3.4	–
	50	73.2	5.5	101.1
	100	123.2	2.6	100.7
Cigarette 2	0	14.4	3.3	–
	50	66.3	3.6	103.0
	100	111.4	7.1	97.4
E-cigarette	0	29.7	4.3	–
	50	77.4	2.9	97.1
	100	132.2	4.2	101.9

groups that are present on the bAuNPs surface. Although the conductivity of the bAuNPs is slightly lower than that of the cAuNPs, the electrocatalytic performance of the bAuNPs is superior. The bAuNP-modified SPE performed an effective electrocatalytic reduction of nicotine. Under optimum conditions, the bAuNPs/SPE could detect nicotine over a linear range from 10 to 2,000 μM with a low detection limit of 2.33 μM. In addition, the bAuNPs/SPE have been successfully used for nicotine-containing-product analysis.

DATA AVAILABILITY STATEMENT

The original contributions presented in the study are included in the article/supplementary material, further inquiries can be directed to the corresponding authors.

AUTHOR CONTRIBUTIONS

YJ, SN, and YG conceived of the study. YJ, CC, and YD supervised the development program and collected materials characterization. QZ, MC, and JL received and curated samples and analytical records. SN, LZ, and YJ wrote the manuscript. All authors read and approved of the manuscript.

REFERENCES

Ahmed, S., Chaudhry, S. A., and Ikram, S. (2017). A review on biogenic synthesis of ZnO nanoparticles using plant extracts and microbes: a prospect towards green chemistry. *J. Photochem. Photobiol. B* 166, 272–284. doi: 10.1016/j.jphotobiol.2016.12.011

Begum, N. A., Mondal, S., Basu, S., Laskar, R. A., and Mandal, D. (2009). Biogenic synthesis of Au and Ag nanoparticles using aqueous solutions of Black Tea leaf extracts. *Colloids Surf. B Biointerfaces* 71, 113–118. doi: 10.1016/j.colsurfb.2009.01.012

Corma, A., and Garcia, H. (2008). Supported gold nanoparticles as catalysts for organic reactions. *Chem. Soc. Rev.* 37, 2096–2126. doi: 10.1039/b707314n

Dalal, C., Saha, A., and Jana, N. R. (2016). Nanoparticle multivalency directed shifting of cellular uptake mechanism. *J. Phys. Chem. C* 120, 6778–6786. doi: 10.1021/acs.jpcc.5b11059

El-Seedi, H. R., El-Shabasy, R. M., Khalifa, S. A., Saeed, A., Shah, A., Shah, R., et al. (2019). Metal nanoparticles fabricated by green chemistry using natural extracts: biosynthesis, mechanisms, and applications. *RSC Adv.* 9, 24539–24559. doi: 10.1039/C9RA02225B

Feng, Y., Wei, Z., and Zhang, J. (2020). Determination of ursolic acid in extracts from ligustri lucidum fruit using an electrochemical method. *Front. Chem.* 8:444. doi: 10.3389/fchem.2020.00444

Fu, L., Wang, A., Xie, K., Zhu, J., Chen, F., Wang, H., et al. (2020a). Electrochemical detection of silver ions by using sulfur quantum dots modified gold electrode. *Sens. Actuators B Chem.* 304:127390. doi: 10.1016/j.snb.2019.127390

Fu, L., Wu, M., Zheng, Y., Zhang, P., Ye, C., Zhang, H., et al. (2019a). Lycoris species identification and infrageneric relationship investigation via graphene enhanced electrochemical fingerprinting of pollen. *Sens. Actuators B Chem.* 298:126836. doi: 10.1016/j.snb.2019.126836

Fu, L., Xie, K., Wang, A., Lyu, F., Ge, J., Zhang, L., et al. (2019b). High selective detection of mercury (II) ions by thioether side groups on metal-organic frameworks. *Anal. Chim. Acta* 1081, 51–58. doi: 10.1016/j.aca.2019.06.055

Fu, L., Zheng, Y., Zhang, P., Zhang, H., Xu, Y., Zhou, J., et al. (2020b). Development of an electrochemical biosensor for phylogenetic analysis of Amaryllidaceae based on the enhanced electrochemical fingerprint recorded from plant tissue. *Biosens. Bioelectron.* 159:112212. doi: 10.1016/j.bios.2020.112212

Hojjati-Najafabadi, A., Rahmanpour, M. S., Karimi, F., Zabihi-Feyzaba, H., Malekmohammad, S., Agarwal, S., et al. (2020). Determination of tert-butylhydroquinone using a nanostructured sensor based on CdO/SWCNTs and ionic liquid. *Int. J. Electrochem. Sci.* 15, 6969–6980. doi: 10.20964/2020.07.85

Hou, K., Zhao, P., Chen, Y., Li, G., Lin, Y., Chen, D., et al. (2020). Rapid detection of bifidobacterium bifidum in feces sample by highly sensitive quartz crystal microbalance immunosensor. *Front. Chem.* 8:548. doi: 10.3389/fchem.2020.00548

Huang, D., Li, S., Zhang, X., Luo, Y., Xiao, J., and Chen, H. (2018). A novel method to significantly boost the electrocatalytic activity of carbon cloth for oxygen evolution reaction. *Carbon* 129, 468–475. doi: 10.1016/j.carbon.2017.12.046

Huang, J., Li, Q., Sun, D., Lu, Y., Su, Y., Yang, X., et al. (2007). Biosynthesis of silver and gold nanoparticles by novel sundried *Cinnamomum camphoraleaf*. *Nanotechnology* 18:105104. doi: 10.1088/0957-4484/18/10/105104

Hulkoti, N. I., and Taranath, T. C. (2014). Biosynthesis of nanoparticles using microbes—A review. *Colloids Surf. B Biointerfaces* 121, 474–483. doi: 10.1016/j.colsurfb.2014.05.027

Jing, Y., Yu, B., Li, P., Xiong, B., Cheng, Y., Li, Y., et al. (2017). Synthesis of graphene/DPA composite for determination of nicotine in tobacco products. *Sci. Rep.* 7:14332. doi: 10.1038/s41598-017-13716-2

Karimi-Maleh, H., Karimi, F., Alizadeh, M., and Sanati, A. L. (2020a). Electrochemical sensors, a bright future in the fabrication of portable kits in analytical systems. *Chem. Rec.* 20, 682–692. doi: 10.1002/tcr.201900092

Karimi-Maleh, H., Karimi, F., Malekmohammadi, S., Zakariae, N., Esmaeili, R., Rostamnia, S., et al. (2020b). An amplified voltammetric sensor based on platinum nanoparticle/polyoxometalate/two-dimensional hexagonal boron nitride nanosheets composite and ionic liquid for determination of N-hydroxysuccinimide in water samples. *J. Mol. Liq.* 310:113185. doi: 10.1016/j.molliq.2020.113185

Karimi-Maleh, H., Karimi, F., Orooji, Y., Mansouri, G., Razmjou, A., Aygun, A., et al. (2020c). A new nickel-based co-crystal complex electrocatalyst amplified by NiO dope Pt nanostructure hybrid; a highly sensitive approach for determination of cysteamine in the presence of serotonin. *Sci. Rep.* 10:11699. doi: 10.1038/s41598-020-68663-2

Karthikeyan, C., Varaprasad, K., Akbari-Fakhrabadi, A., Hameed, A. S. H., and Sadiku, R. (2020). Biomolecule chitosan, curcumin and ZnO-based antibacterial nanomaterial, via a one-pot process. *Carbohydr. Polym.* 249:116825. doi: 10.1016/j.carbpol.2020.116825

Kasthuri, J., Kathiravan, K., and Rajendiran, N. (2009). Phyllanthin-assisted biosynthesis of silver and gold nanoparticles: a novel biological approach. *J. Nanoparticle Res.* 11, 1075–1085. doi: 10.1007/s11051-008-9494-9

Li, C., Huang, R., and Shi, X. (2020). Biosynthesis of Cu nanoparticles supported on carbon nanotubes and its catalytic performance under different test conditions. *J. Chem. Technol. Biotechnol.* 95, 1511–1518. doi: 10.1002/jctb.6344

Li, X., Zhao, H., Shi, L., Zhu, X., Lan, M., Zhang, Q., et al. (2017). Electrochemical sensing of nicotine using screen-printed carbon electrodes modified with nitrogen-doped graphene sheets. *J. Electroanal. Chem.* 784, 77–84. doi: 10.1016/j.jelechem.2016.12.009

Liang, J., Han, F., and Chen, Y. (2012). An electrochemical method for high sensitive detection of nicotine and its interaction with bovine serum albumin. *Electrochem. Commun.* 24, 93–96. doi: 10.1016/j.elecom.2012.08.024

Liang, J., Li, C., Li, W., Qi, J., and Liang, C. (2018). Microwave-assisted polyol preparation of reduced graphene oxide nanoribbons supported platinum as a highly active electrocatalyst for oxygen reduction reaction. *J. Appl. Electrochem.* 48, 1069–1080. doi: 10.1007/s10800-018-1235-x

Manzano, M., and Vallet-Regí, M. (2020). Mesoporous silica nanoparticles for drug delivery. *Adv. Funct. Mater.* 30:1902634. doi: 10.1002/adfm.201902634

Medda, S., Hajra, A., Dey, U., Bose, P., and Mondal, N. K. (2015). Biosynthesis of silver nanoparticles from Aloe vera leaf extract and antifungal activity against Rhizopus sp. and Aspergillus sp. *Appl. Nanosci.* 5, 875–880. doi: 10.1007/s13204-014-0387-1

Naderi Asrami, P., Aberoomand Azar, P., Saber Tehrani, M., and Mozaffari, S. A. (2020). Glucose oxidase/nano-ZnO/thin film deposit FTO as an innovative clinical transducer: a sensitive glucose biosensor. *Front. Chem.* 8:503. doi: 10.3389/fchem.2020.00503

Noguez, C., and Garzón, I. L. (2009). Optically active metal nanoparticles. *Chem. Soc. Rev.* 38, 757–771. doi: 10.1039/b800404h

Otari, S. V., Patel, S. K., Kalia, V. C., Kim, I.-W., and Lee, J.-K. (2019). Antimicrobial activity of biosynthesized silver nanoparticles decorated silica nanoparticles. *Indian J. Microbiol.* 59, 379–382. doi: 10.1007/s12088-019-00812-2

Philip, D. (2009). Biosynthesis of Au, Ag and Au–Ag nanoparticles using edible mushroom extract. *Spectrochim. Acta. A. Mol. Biomol. Spectrosc.* 73, 374–381. doi: 10.1016/j.saa.2009.02.037

Ramteke, L., Gawali, P., Jadhav, B., and Chopade, B. (2020). Comparative study on antibacterial activity of metal ions, monometallic and alloy noble metal nanoparticles against nosocomial pathogens. *BioNanoScience.* 3, 1–19. doi: 10.1007/s12668-020-00771-9

Shamsadin-Azad, Z., Taher, M. A., Cheraghi, S., and Karimi-Maleh, H. (2019). A nanostructure voltammetric platform amplified with ionic liquid for determination of tert-butylhydroxyanisole in the presence kojic acid. *J. Food Meas. Charact.* 13, 1781–1787. doi: 10.1007/s11694-019-00096-6

Shehata, M., Azab, S., Fekry, A., and Ameer, M. (2016). Nano-TiO_2 modified carbon paste sensor for electrochemical nicotine detection using anionic surfactant. *Biosens. Bioelectron.* 79, 589–592. doi: 10.1016/j.bios.2015.12.090

Slocik, J. M., and Naik, R. R. (2017). Sequenced defined biomolecules for nanomaterial synthesis, functionalization, and assembly. *Syst. Biol. Nanobiotech.* 46, 7–13. doi: 10.1016/j.copbio.2016.11.025

Spagnoletti, F. N., Spedalieri, C., Kronberg, F., and Giacometti, R. (2019). Extracellular biosynthesis of bactericidal Ag/AgCl nanoparticles for crop protection using the fungus *Macrophomina phaseolina*. *J. Environ. Manage.* 231, 457–466. doi: 10.1016/j.jenvman.2018.10.081

Sun, S.-K., Wang, H.-F., and Yan, X.-P. (2018). Engineering persistent luminescence nanoparticles for biological applications: from biosensing/bioimaging to theranostics. *Acc. Chem. Res.* 51, 1131–1143. doi: 10.1021/acs.accounts.7b00619

Švorc, Ľ., Stanković, D. M., and Kalcher, K. (2014). Boron-doped diamond electrochemical sensor for sensitive determination of nicotine in tobacco products and anti-smoking pharmaceuticals. *Diam. Relat. Mater.* 42, 1–7. doi: 10.1016/j.diamond.2013.11.012

Vilas, V., Philip, D., and Mathew, J. (2016). Biosynthesis of Au and Au/Ag alloy nanoparticles using *Coleus aromaticus* essential oil and evaluation of their catalytic, antibacterial and antiradical activities. *J. Mol. Liq.* 221, 179–189. doi: 10.1016/j.molliq.2016.05.066

Wang, S.-J., Liaw, H.-W., and Tsai, Y.-C. (2009). Low potential detection of nicotine at multiwalled carbon nanotube–alumina-coated silica nanocomposite. *Electrochem. Commun.* 11, 733–735. doi: 10.1016/j.elecom.2009.01.026

Wang, Y., Kang, S., Khan, A., Ruttner, G., Leigh, S. Y., Murray, M., et al. (2016). Quantitative molecular phenotyping with topically applied SERS nanoparticles for intraoperative guidance of breast cancer lumpectomy. *Sci. Rep.* 6:21242. doi: 10.1038/srep21242

Wang, Y., Reddy Satyavolu, N. S., and Lu, Y. (2018). Sequence-specific control of inorganic nanomaterials morphologies by biomolecules. *Biol. Colloids Interfaces* 38, 158–169. doi: 10.1016/j.cocis.2018.10.009

Xu, Y., Lu, Y., Zhang, P., Wang, Y., Zheng, Y., Fu, L., et al. (2020). Infrageneric phylogenetics investigation of Chimonanthus based on electroactive compound profiles. *Bioelectrochemistry* 133:107455. doi: 10.1016/j.bioelechem.2020.107455

Yang, N., WeiHong, L., and Hao, L. (2014). Biosynthesis of Au nanoparticles using agricultural waste mango peel extract and its in vitro cytotoxic effect on two normal cells. *Mater. Lett.* 134, 67–70. doi: 10.1016/j.matlet.2014.07.025

Yu, B., Liu, Y., Zhang, J., Hai, T., Li, B., Lu, P., et al. (2016). Electrochemical analysis of nicotine based on multi-walled carbon nanotube/graphene composite. *Int. J. Electrochem. Sci.* 11, 4979–4987. doi: 10.20964/2016.06.68

Zhang, H., and Hu, X. (2019). Biosynthesis of au nanoparticles by a marine bacterium and enhancing their catalytic activity through metal ions and metal oxides. *Biotechnol. Prog.* 35:e2727. doi: 10.1002/btpr.2727

Zheng, Y., Wang, Z., Peng, F., and Fu, L. (2017). Biosynthesis of silver nanoparticles by *Plectranthus amboinicus* leaf extract and their catalytic activity towards methylene blue degradation. *Rev. Mex. Ing. Quím.* 16, 41–45.

Zhu, A., Qiao, L., Tan, P., Zeng, W., Ma, Y., Dong, R., et al. (2019). Boosted electrocatalytic activity of nitrogen-doped porous carbon triggered by oxygen functional groups. *J. Colloid Interface Sci.* 541, 133–142. doi: 10.1016/j.jcis.2019.01.077

Conflict of Interest: SN, MC, YD, and LZ were employed by the company Changde Branch of Hunan Tobacco Corporation. JL and QZ were employed by the company Sichuan of China National Tobacco Corporation.

The remaining authors declare that the research was conducted in the absence of any commercial or financial relationships that could be construed as a potential conflict of interest.

frontiers in Chemistry

ORIGINAL RESEARCH
published: 03 November 2020
doi: 10.3389/fchem.2020.574986

Facial Fabrication and Characterization of Novel Ag/AgCl Chloride Ion Sensor Based on Gel-Type Electrolyte

Seil Kim[1†], Gwangryeol Park[1,2†], Hong-Ju Ahn[1,2], Bung Uk Yoo[1], In-Hyuck Song[3], Kyu-Hwan Lee[1,4], Kwang Ho Kim[2], Jae-Hong Lim[5*] and Joo-Yul Lee[1*]*

[1] Department of Electrochemistry, Korea Institute of Materials Science, Changwon, South Korea, [2] School of Materials Science and Engineering, Pusan National University, Busan, South Korea, [3] Department of Engineering Ceramic, Korea Institute of Materials Science, Changwon, South Korea, [4] Advanced Materials Engineering, Korea University of Science and Technology, Daejeon, South Korea, [5] Department of Materials Science and Engineering, Gachon University, Seongnam, South Korea

OPEN ACCESS

Edited by:
Fatih Sen,
Dumlupinar University, Turkey

Reviewed by:
Pankaj Madhukar Koinkar,
Tokushima University, Japan
Pramod K. Kalambate,
Huazhong University of Science and Technology, China
Vahid Arabali,
Islamic Azad University Sari Branch, Iran

***Correspondence:**
Kwang Ho Kim
kwhokim@pusan.ac.kr
Jae-Hong Lim
limjh@gachon.ac.kr
Joo-Yul Lee
leeact@kims.re.kr

[†] These authors share first authorship

Specialty section:
This article was submitted to Electrochemistry, a section of the journal Frontiers in Chemistry

Received: 22 June 2020
Accepted: 02 October 2020
Published: 03 November 2020

Citation:
Kim S, Park G, Ahn H-J, Yoo BU, Song I-H, Lee K-H, Kim KH, Lim J-H and Lee J-Y (2020) Facial Fabrication and Characterization of Novel Ag/AgCl Chloride Ion Sensor Based on Gel-Type Electrolyte. Front. Chem. 8:574986. doi: 10.3389/fchem.2020.574986

In this study, a novel chloride ion (Cl^-) sensor based on Ag wire coated with an AgCl layer was fabricated using a gel-type internal electrolyte and a diatomite ceramic membrane, which played an important role in preventing electrolyte leakage from the ion-selective electrode. The sensing performance, including reversibility, response, recovery time, low detection limit, and the long-term stability, was systemically investigated in electrolytes with different Cl^- contents. The as-fabricated Cl^- sensor could detect Cl^- from 1 to 500 mM KCl solution with good linearity. The best response and recovery time obtained for the optimized sensor were 0.5 and 0.1 s, respectively, for 10 mM KCl solution. An exposure period of over 60 days was used to evaluate the stability of the Cl^- sensor in KCl solution. A relative error of 2% was observed between the initial and final response potentials. Further, a wireless sensing system based on Arduino was also investigated to measure the response potential of Cl^- in an electrolyte. The sensor exhibited high reliability with a low standard error of measurement. This type of sensor is crucial for fabricating wireless Cl^- sensors for applications in reinforced concrete structures along with favorable performances.

Keywords: chloride ion sensor, Ag/AgCl electrode, diatomite ceramic membrane, gel-type internal electrolyte, reinforced concrete structure, chronopotentiometry

INTRODUCTION

Reinforced concrete (RC) plays a critical role in the construction industry, especially in the construction of buildings, bridges, and port facilities, because it has higher tensile and compressive strengths than other building materials (Javadian et al., 2020). Steel is the most commonly used reinforcement material for RC structures because it has high tensile strength. However, steel reinforcements undergo corrosion because of chloride ions (Cl^-), which is a main cause of the failure of RC structures (Imounga et al., 2020). These ions promote the breakdown of the protective passive layer by decreasing the pH of the pore water, leading to the formation of corrosion pits in metals (Li et al., 2017). Therefore, Cl^- monitoring in RC structures is a key strategy to prevent the corrosion of reinforced steel. The current techniques for determining the local Cl^- content in

RC structures require destructive sampling methods such as drilling, grinding, and cutting. These methods are time-consuming and costly, and it is difficult to continuously obtain information at the same location over time (RILEM TC 178-TMC, 2002; Femenias et al., 2016). Furthermore, it results in additional indirect costs due to road closures and traffic delays (Torres-Luque et al., 2014). Therefore, several research groups are investigating the development of nondestructive *in situ* monitoring techniques to measure Cl^- ingress in RC structures, which can afford fast measurements with high reliability and real-time ingress profiles without destroying the structures (Abbas et al., 2013). Some existing nondestructive *in situ* monitoring methods include electrical resistivity measurement (Corva et al., 2020), fiber optic sensing (Bassil et al., 2020), potentiometry (Gandía-Romero et al., 2016), and chronopotentiometry (Abbas et al., 2013; Abbas, 2015). Among these, the chronopotentiometry technique based on an electrochemical method is employed for the indicative determination of Cl^- content in infrastructures, the principle of which is described as follows. In a three-electrode system comprising a counter electrode (CE), reference electrode (RE), and working electrode (WE), a constant current is applied to the WE and the potential response is measured with respect to the RE (Abbas, 2015; Dobbelaere et al., 2017; Raccichini et al., 2019). The as-fabricated Ag/AgCl ion-selective electrode (Ag/AgCl ISE) used in this method acts as the WE, which when embedded in the sensor device can be used to determine free Cl^- concentration near the rebar without changing the surrounding environment (Angst and Polder, 2014). This is because the electrode shows a Nernstian response to the variation in Cl^- or Ag^+ activity and displays excellent sensitivity (Karthick et al., 2017). Here, the concrete has a strong alkalinity (pH 12.5–13.5). Therefore, the materials that are used as the electrolytes for RE should have alkali resistance, long-term chemical stability, and leak resistance characteristics. Conventional Ag/AgCl REs comprising a chamber and membrane based on glass are not suitable for the *in situ* measurements at the steel/concreate interface owing to their high alkalinities at the interface as well as fragility (Jin et al., 2014). Furthermore, traditional Ag/AgCl REs employ liquid-type solution as an internal electrolyte, which shows the drawback of continuous exudation of KCl internal solution. KCl exudation is one of the most important parameters for the reliable performance of traditional Ag/AgCl REs (Femenias et al., 2016). Solid-type electrolytes can decrease the rates of electrolyte loss and contamination and prolong the life span of REs. However, these suffer from low ionic conductivities, and the moisture content of the electrolyte varies with the change in concrete moisture, which causes the potential fluctuation of the RE, thus affecting the accuracy of corrosion monitoring in RC structures (Tang et al., 2015). To address this issue, a gel-type internal electrolyte and diatomite ceramic membrane (DCM) were employed in this study to fabricate the Ag/AgCl ISE, which allowed the application of the electrode in

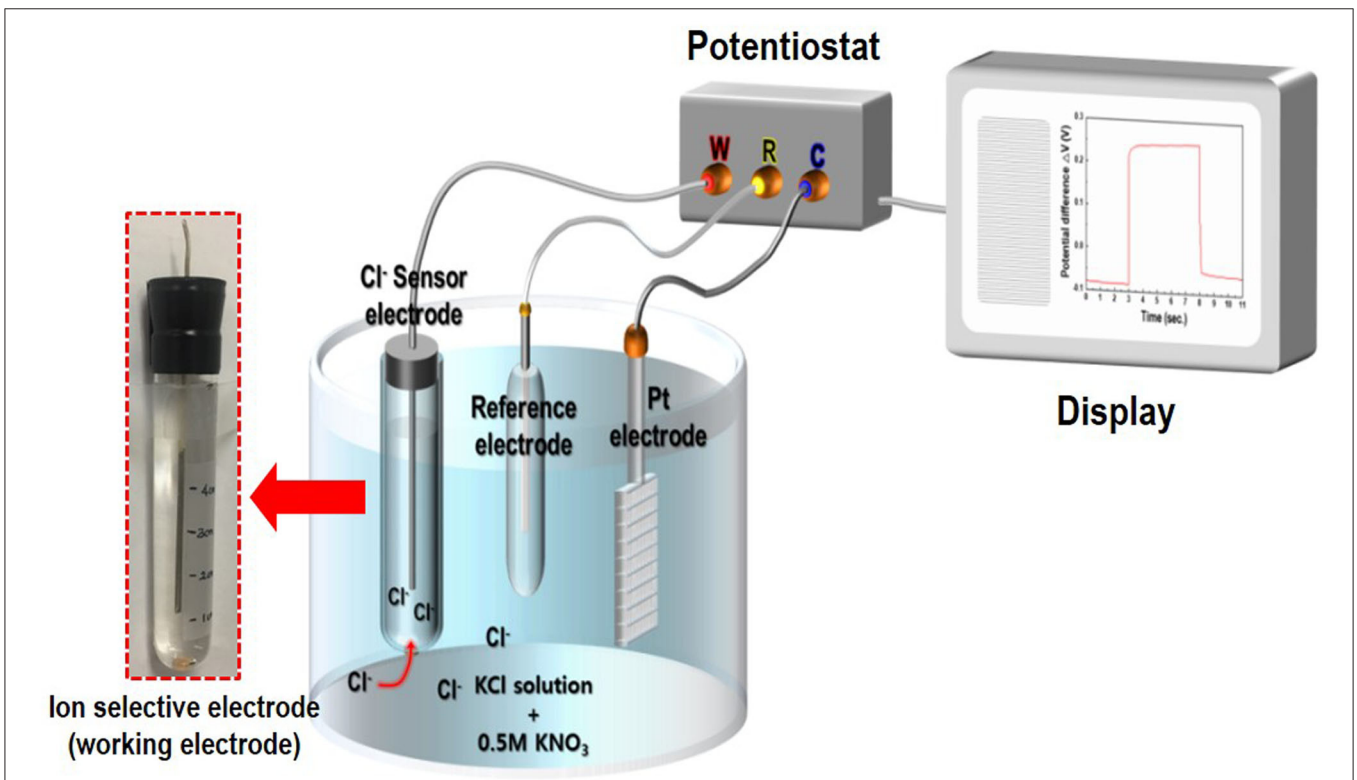

FIGURE 1 | Schematic of the chloride ion sensor comprising an Ag/AgCl reference electrode, Pt-counter electrode, and Ag/AgCl ion-selective electrode (Ag/AgCl ISE) based on a gel-type internal electrolyte and diatomite ceramic membrane.

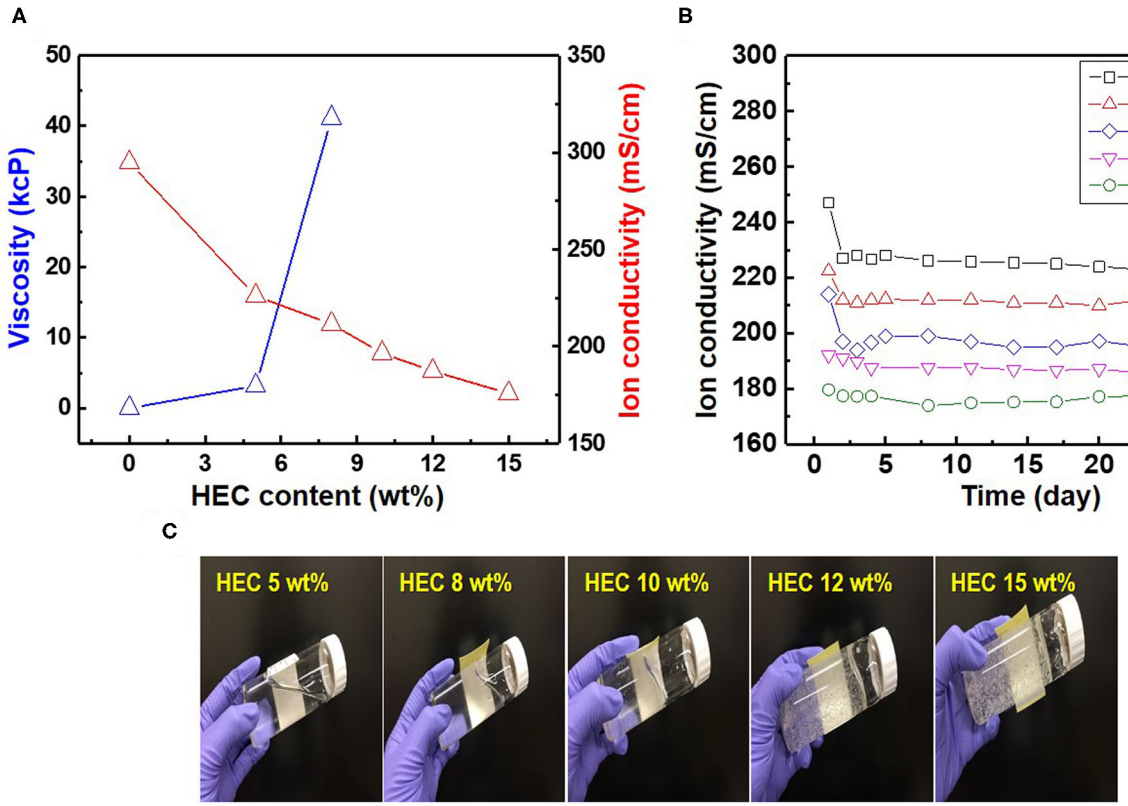

FIGURE 2 | Relationship between **(A)** hydroxyethyl cellulose (HEC; wt.%), viscosity, and ion conductivity, **(B)** time-dependent ion conductivity, and **(C)** optical images of gel-type electrolyte with different HEC contents.

highly alkaline environments, such as RC structures, without the exudation of the internal electrolyte. In particular, the DCM could effectively prevent the leakage of the inner solution, which involved the dissolution of the AgCl coating layer. The aim of the present study was to fabricate a novel Ag/AgCl-based ISE comprising an Ag wire coated with AgCl with a gel-type internal electrolyte and DCM. Cl^- sensing characteristics included the response potential, reliability testing, response time, and recovery time of the sensor device, which were systemically determined in the electrolytes with different Cl^- contents. Finally, wireless sensing based on Arduino Uno was performed using the as-fabricated Cl^- sensor in KCl solution. This type of sensor is a key component for fabricating gel-type internal electrolyte-based Cl^- sensors with favorable sensing performances.

EXPERIMENTAL

Synthesis of Diatomite Ceramic Membrane

Diatomite (Celite 499, Celite Korea Co. Ltd., South Korea) and kaolin (Sigma-Aldrich, USA), as a strength enhancer material, were used to fabricate diatomite–kaolin composite membrane for sensor applications. The average particle sizes of the as-received diatomite and kaolin were 12.7 and 1.5 μm, respectively. To increase the sinterability, the size of the diatomite particles was decreased to a powder-to-volume ratio of 2:1 by ball-milling for 24 h using alumina balls. Diatomite and kaolin (weight ratio of 9:1) were subjected to ball-milling for 3 h to afford a power-to-volume ratio of 0.5:1. Finally, the diatomite–kaolin composite was dry-pressed at 18.7 MPa with polyethylene glycol as a binder, followed by sintering at 1,200°C for 1 h. The as-fabricated diatomite–kaolin composites were cut into cylinder-shaped samples of 1-mm diameter and 1-mm height.

Synthesis of AgCl-Coated Ag Wire

An Ag wire with a diameter of 1 mm and purity of 99.99% was used to synthesize the AgCl-coated Ag wire. The experimental procedure for synthesizing the Ag/AgCl wire in this study is described as follows. First, prior to galvanostatic polarization (GP), the Ag wire was immersed in acetone (ACS reagent, >99.5%, Sigma-Aldrich, USA) with sonication for 10 min to remove the surface oil, followed by rinsing with distilled water. Next, the Ag wire was ground in one direction using a silicon-carbide abrasive paper (#2000 grit) to remove the native oxide layer and then dipped in acetone and 5% nitric acid (HNO_3; 60%, Sigma-Aldrich, USA) solution for 10 min to remove the impurities. Thereafter, the Ag wire was cleaned in ethanol

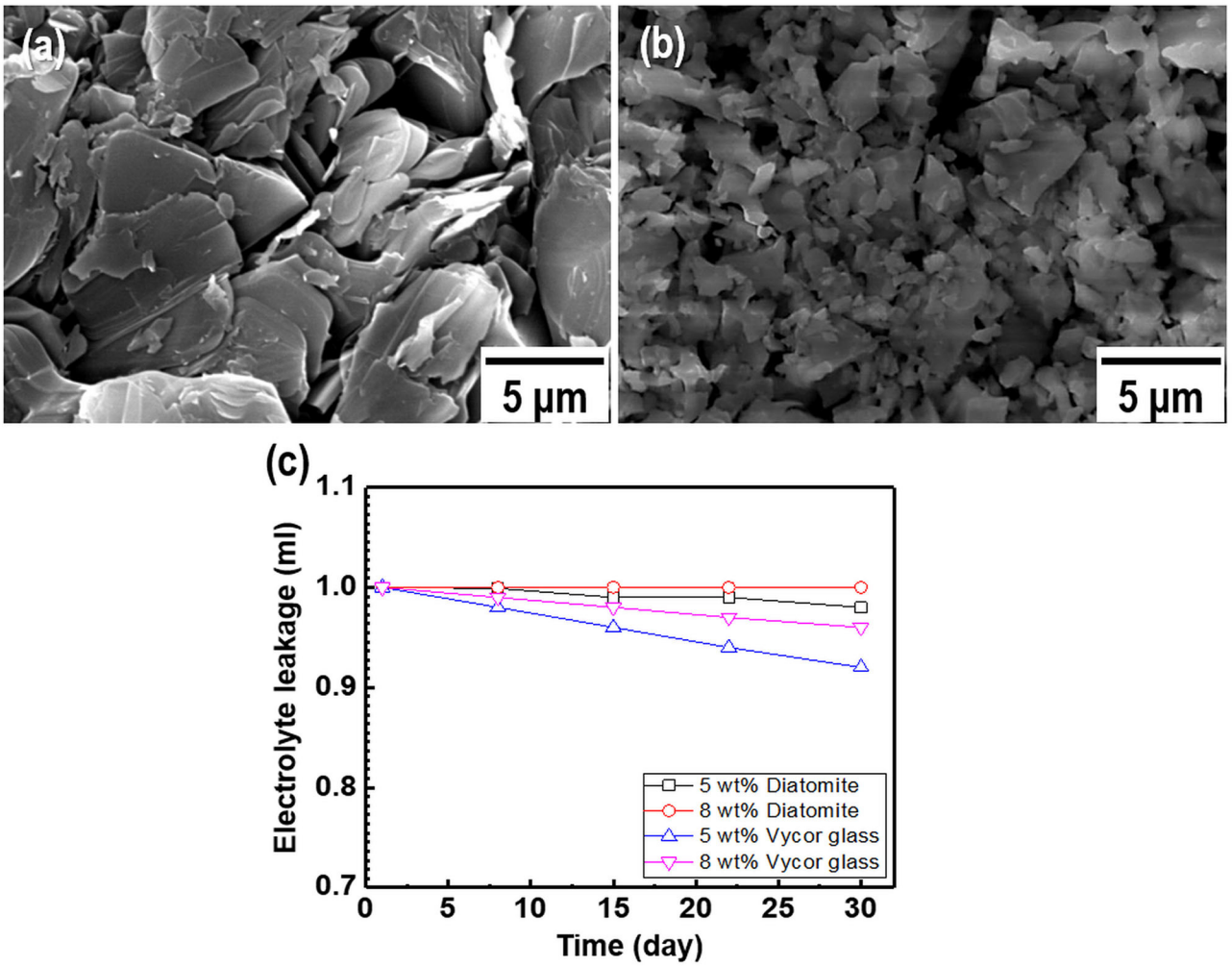

FIGURE 3 | Field-emission scanning electron microscopy (FE-SEM) images of two types of membranes: **(a)** Vycor glass membrane and **(b)** as-synthesized diatomite ceramic membrane. **(c)** Internal electrolyte leakage data for the membranes as a function of time.

ultrasonically and dried in air. For GP, the WE terminal of the potentiostat was connected to the Pt-mesh and the CE terminal was connected to a pretreated Ag wire. After GP, an immersion process was employed to synthesize the AgCl layer on the surface of an Ag segment. The entire process was performed in 1 M hydrochloric acid (HCl; ACS reagent, 37%, Sigma-Aldrich, USA) at room temperature.

Gel-Type Internal Electrolyte

The synthesis of the gel-type internal electrolyte is described as follows. First, 3.5 mol/L potassium chloride (KCl; 99.0%, Sigma-Aldrich, USA) solution was prepared and heated at 60°C. Then, 8 ml of glycerol (>99.5%, Sigma-Aldrich, USA) was poured into the KCl solution, which played an important role in preventing the high-density gelation of internal electrolyte. Finally, 5 wt.% of hydroxyethyl cellulose (HEC, 200–400 mPa·s, DaeJung Co., Ltd., South Korea) was slowly added into the heated KCl solution (100 ml KCl solution with 5 g HEC) with constant stirring at 150 rpm, affording the HEC-gelled electrolyte. The conductivity of the gel-type electrolyte was 226 mS/cm at 5 wt.% HEC and that of 3.5 M KCl solution was 294.8 mS/cm (Kim et al., 2017). This indicated that the gel-type electrolyte could decrease the migrating rate of ions, which further decreased the rates of electrolyte loss and exterior ions entering into the internal electrolyte. Furthermore, HEC showed good water absorptivity. Using the HEC-based gel-type electrolyte decreased the rate of moisture loss, thus prolonging the life time of RE in the RC structure.

Fabrication of Ag/AgCl Ion-Selective Electrode

In this study, polyvinyl chloride (PVC) was used as the housing material because PVC is abrasion resistant and chemically resistant to many acids, bases, and corrosives, with good mechanical strength and toughness. First, a hole with a dimeter of 1 mm was melted at one end of each PVC chamber using a hot

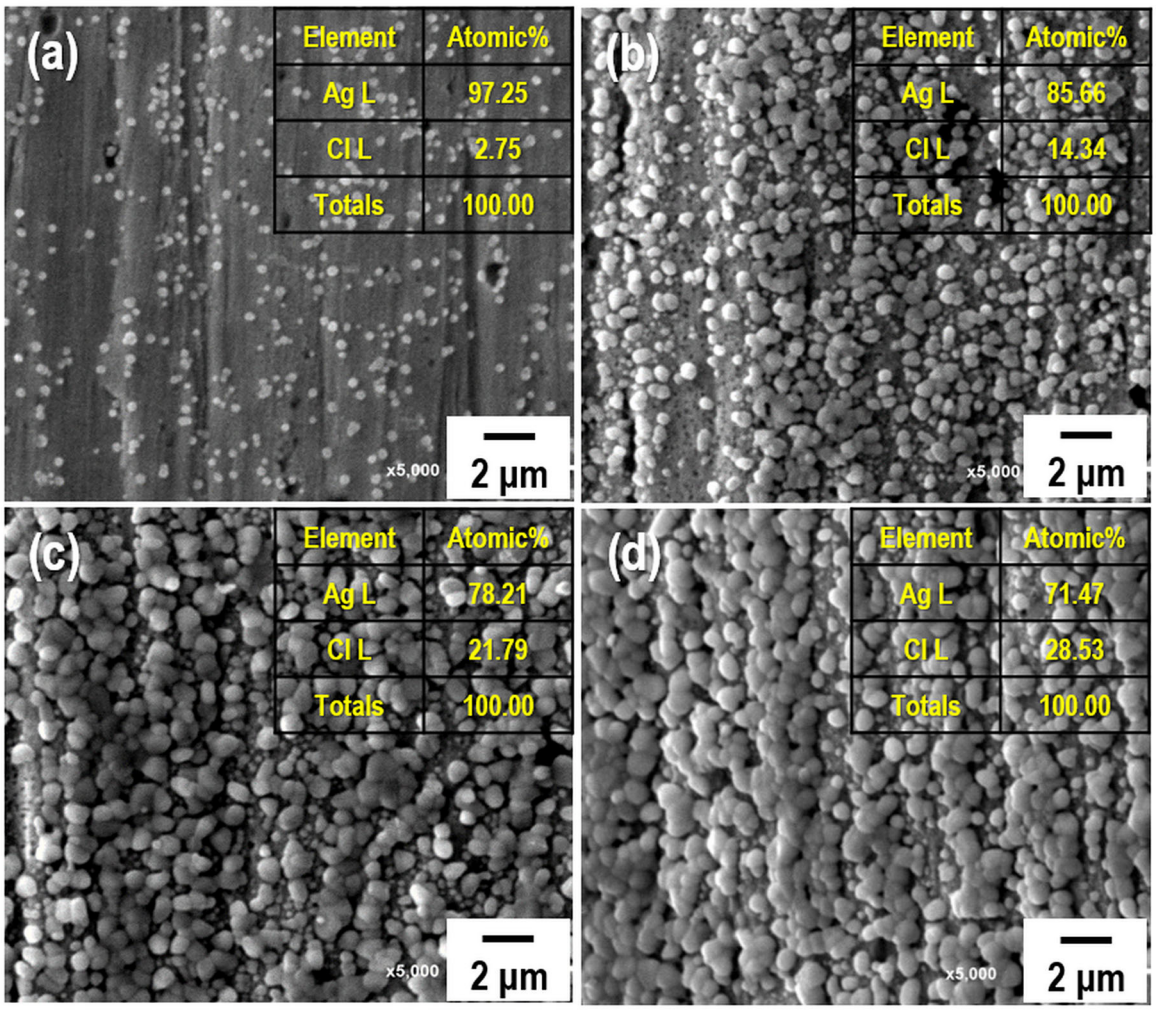

FIGURE 4 | Field-emission scanning electron microscopy (FE-SEM) images and elemental compositions of the AgCl-coated Ag wire with different immersion times: **(a)** 1 s, **(b)** 60 s, **(c)** 90 s, and **(d)** 120 s. The current density and treatment time for the galvanostatic polarization of all samples are fixed at 30 mA/cm^2 and 2 h, respectively.

iron. Cylinder-shaped DCMs were then inserted into the holes. Next, the as-synthesized Ag/AgCl wire was inserted into each PVC chamber, leaving a space between the wire and membrane. Thereafter, 8 ml of the gel-type internal electrolyte was slowly poured into each PVC chamber, in which the Ag/AgCl wires were inserted. Finally, the top of each PVC chamber was sealed using a rubber cap and insulating tape. The as-fabricated Ag/AgCl ISE was stored in 1 M KCl solution.

Characterization

The crystal structure and crystallinity of the as-synthesized Ag/AgCl wire obtained by GP and immersion were determined using X-ray diffraction (XRD; Ultima IV CuK, Rigaku Corporation, Tokyo, Japan). X-ray photoelectron spectroscopy (XPS; Kratos Analytical Ltd., Manchester, UK) was employed to measure the changes in the surface composition of the Ag/AgCl wire. The morphology and composition were analyzed using field-emission scanning electron microscopy (FE-SEM; Hitachi S-4800, Hitachi Ltd., Tokyo, Japan) coupled with energy-dispersive X-ray spectroscopy (EDS; Oxford INKA X-Act, Oxford Instruments, Abingdon, UK). Cl^- measurement with the as-fabricated Ag/AgCl electrode was performed using a potentiostat (BioLogic, EC-Lab instrument, Seyssinet-Pariset, France) in electrolytes containing 0.5 M KNO_3 and 10–600 mM KCl. The WE terminal of the potentiostat was connected to the as-fabricated Ag/AgCl ISE. The CE terminal was connected to the Pt-mesh, and the RE terminal was connected to the commercial Ag/AgCl RE. When a current pulse was applied between the WE and CE, Cl^- species near the WE were consumed, locally depleting the Cl^- near the surface of the WE, leading to a concentration gradient that resulted in a potential difference at the WE with respect to the RE (Bard and Faulkner, 2001). A schematic of the sensing measurement setup is shown in **Figure 1**.

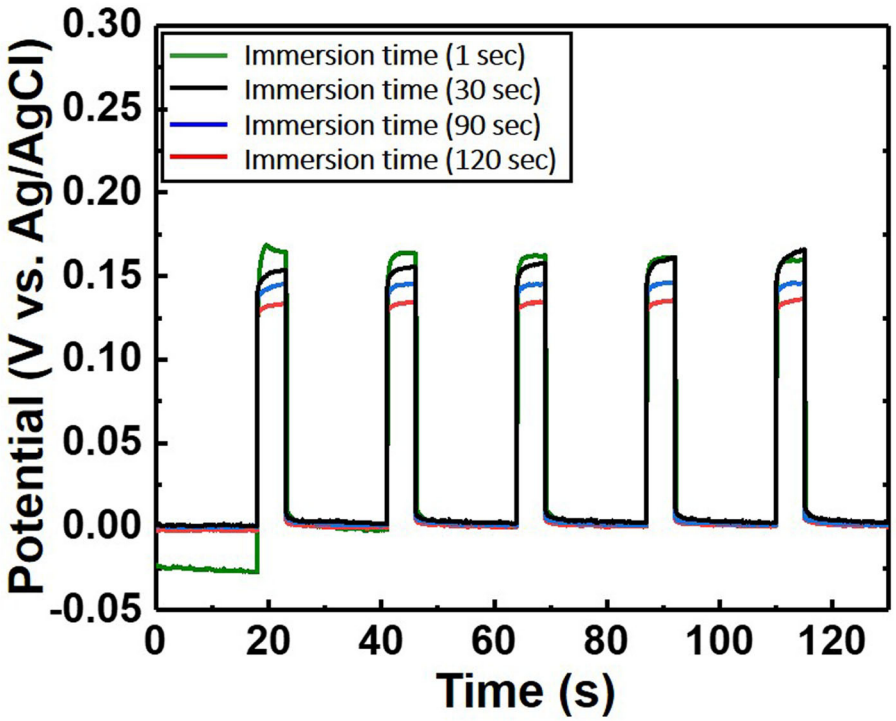

FIGURE 5 | Potential difference of the chloride ion sensor as a function of immersion time. The electrolyte comprises 300 mM KCl and 0.5 M KNO_3. The length of the Ag/AgCl wire and the distance between the Ag/AgCl wire and diatomite ceramic membrane are fixed at 3 and 1 cm, respectively.

RESULTS AND DISCUSSION

As most commercial REs use a liquid-type solution as an internal electrolyte, which can leak under various pressures and salinity conditions, periodic replacement and maintenance are necessary to retain the electrode performance (Kim et al., 2017). Compared to the liquid-filled electrodes, gel-type internal electrolytes have numerous advantages. It is possible to take measurements with various pressure changes using gel-type electrolytes, and these are heat resistant up to 121°C (Guth et al., 2009; Inzelt et al., 2013). Various water-soluble polymers such as polyvinyl alcohol, methylcellulose, and HEC can be used as gel-type internal electrolytes owing to their viscous characteristics. These play a key role in preventing electrolyte leakage from the internal to external electrodes. Among these polymers, HEC is a nonionic cellulose, the aqueous solutions of which are stable at pH 2–12 with the suitable solution viscosities and gelling states at normal temperatures. HEC also exhibits a high salt tolerance and long-term stability over a wide pH range (3.5–11). For this reason, HEC can be applied to gel-type internal electrolytes for application in coastal structures. **Figure 2A** shows the relationship between the HEC content, viscosity, and ion conductivity. The results reveal that the viscosity of each electrolyte increases upon the addition of HEC, and a maximum value is obtained at 8 wt.% HEC. The viscosity of the electrolyte with >10 wt.% HEC cannot be measured with the viscometer owing to its limited detection range (1.5–4,800 cP). In contrast, the ion conductivity of the electrolyte decreases with an increase in the HEC content because of the limitation of ion mobilities. The time dependency of ion conductivity for the as-synthesized gel-type electrolytes is shown in **Figure 2B**. The ion conductivities of all internal electrolytes with different HEC contents stabilize after initial measurements (1–3 days), except with high HEC contents (12 and 15 wt.%) owing to ion transfer limitations. The gel-type electrolyte with 5 wt.% HEC shows higher ion conductivity and appropriate viscosity compared with those of other samples. Based on these results, the electrolyte with 5 wt.% HEC was selected as the optimal internal electrolyte for fabricating the Ag/AgCl ISE. **Figure 2C** shows the images of the gel-type internal electrolyte, acquired 3 s after electrolyte synthesis. The data show that gelling progresses with an increase in the HEC content. In particular, ideal gelling characteristics are observed with 12 and 15 wt.% HEC. The membrane is a critical part of the electrode. It not only ensures the transmission of electrolyte but also decreases it and determines the lifetime of the electrode. The FE-SEM images of two types of membranes employed are shown in **Figures 3a,b**. The particle size of the DCM is smaller than that of the Vycor glass membrane (VGM); the average particle sizes are 1.5 and 5.4 μm, respectively. The small particle size of DCM with a dense structure can minimize the leakage of internal electrolyte from the electrode, which can lead to the stability of the electrode in RC structures.

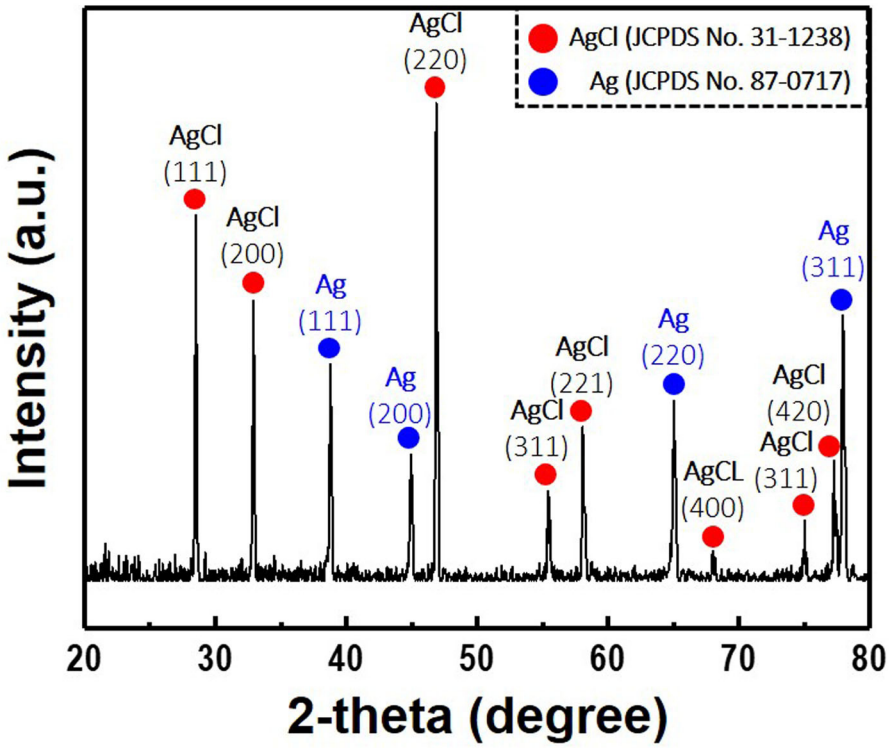

FIGURE 6 | X-ray diffraction patterns of the Ag/AgCl wire synthesized via galvanostatic polarization and immersion (120 s) in 1 M hydrochloric acid. Current density and treatment time for the galvanostatic polarization are fixed at 30 mA/cm^2 and 2 h, respectively.

Additionally, the morphology of VGM shows a randomly stacked plate-type structure with large pore sizes, which leads to the leakage of the internal electrolyte. **Figure 3c** shows the time-dependent leakage of the internal electrolyte from the PVC housing with four types of membranes. After 1 month, electrolyte leakage is observed in all membranes, which decreases with an increase in the ceramic content. However, the two types of DCMs show lower leakages compared to those of VGMs. These results are in good agreement with the corresponding FE-SEM data. In this study, GP and immersion were used to synthesize AgCl-coated Ag wire to remove undesired impurities from the Ag wire surface and increase the active sites using small AgCl particles for enhancing the interaction between Cl^- and the as-synthesized Ag/AgCl wire by introducing fine roughness. For this process, the WE terminal of the potentiostat was connected to the Pt-mesh and the CE terminal was connected to the Ag wire. In this case, the immersion process after GP is important for the formation of the AgCl layer on the Ag wire surface. The suggested formation mechanism of the AgCl layer on the Ag wire during GP and immersion is described by reactions (1) and (2).

$$Cl_{2(g)} + H_2O_{(aq)} \rightarrow HOCl_{(aq)} + HCl_{(aq)} \quad (1)$$

$$2Ag_{(s)} + HOCl_{(aq)} \rightarrow AgCl_{(s)} + AgOH_{(aq)} \Delta G = -153.69 KJ/mol \quad (2)$$

TABLE 1 | Atomic percentage of Ag/AgCl wire determined from X-ray photoelectron spectroscopy (XPS) survey spectra after galvanostatic polarization and immersion in 1 M hydrochloric acid.

	Ag3d	O1s	Cl2p	C1s
Atomic percentage (at.%)	6.85	6.8	2.88	30.28

When a current pulse is applied, chlorine (Cl_2) is generated on the Pt-mesh (anode) and it reacts with water, resulting in the formation of a mixture of hypochlorous acid (HOCl) and HCl. In other words, the HOCl content in the electrolyte increases with an increase in the GP time. In this reaction, Cl_2 is oxidized as well as reduced ($Cl_2^0 + H_2O \rightarrow \ H^+Cl^- + H^+O^{2-}Cl^+$); such reactions are called auto oxidation–reduction (redox) reactions (disproportionation reaction) (Gu and Bennion, 1977; Guo et al., 2014) and involve the reduction and oxidation reactions of the same substance (reactant). In HOCl, the oxidation state of chlorine is +1, showing that it has a high affinity for electrons. Therefore, HOCl oxidizes Ag to AgCl. After GP, the immersion process is immediately carried out in the same electrolyte without applying a current pulse. When the applied current pulse is removed, the as-generated HOCl reacts with the Ag wire (cathode), resulting in the generation of AgCl and AgOH on the Ag wire surface. **Figure 4** shows the FE-SEM images and

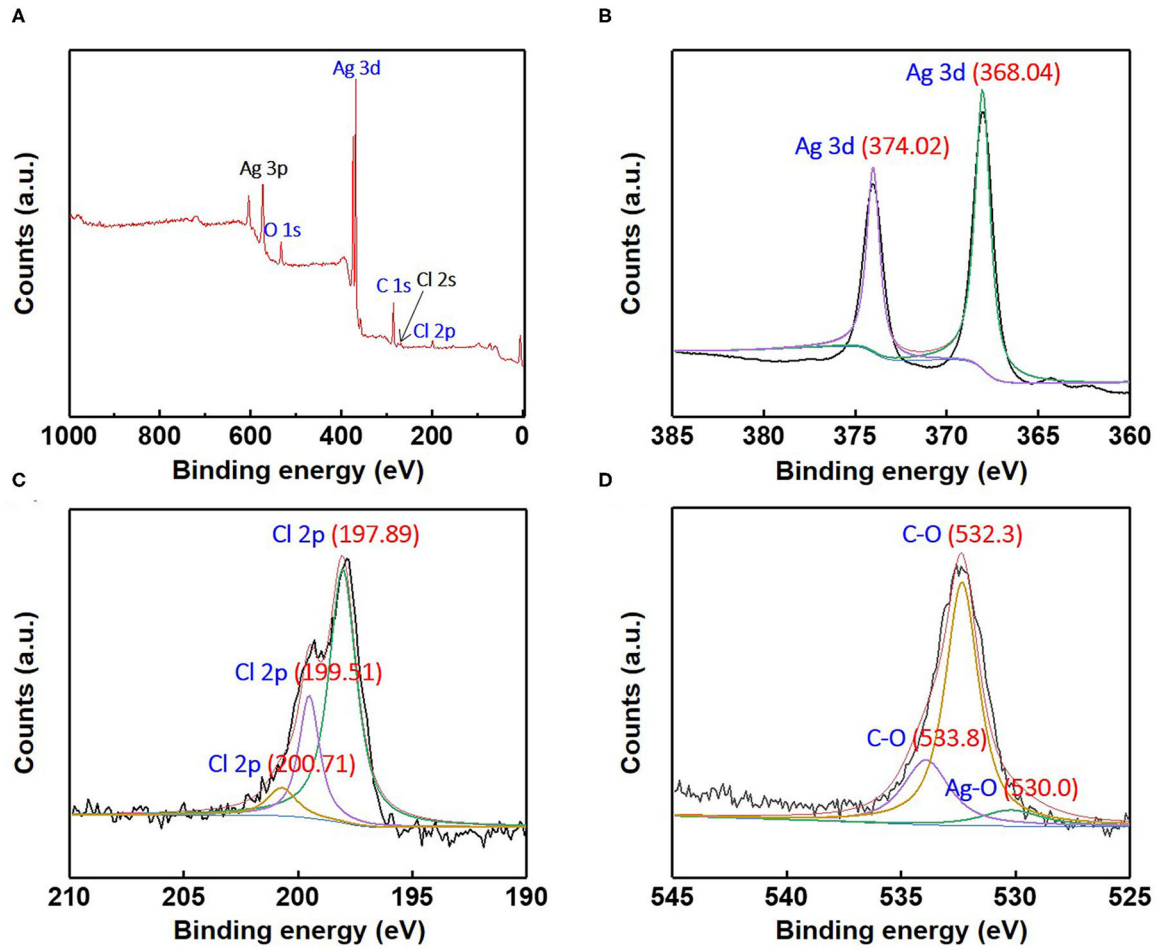

FIGURE 7 | (A) X-ray photoelectron survey spectra and high-resolution X-ray photoelectron; **(B)** Ag3d, **(C)** Cl2p, and **(D)** O1s spectra for the as-synthesized Ag/AgCl wire.

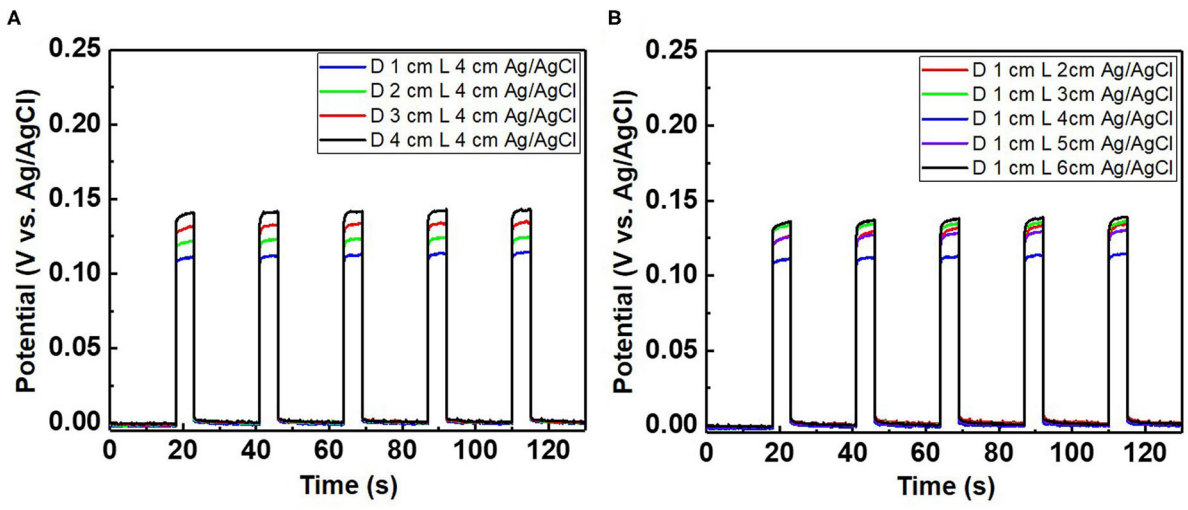

FIGURE 8 | Potential difference of the chloride ion sensor as a function of **(A)** the distance (D) between the Ag/AgCl wire and diatomite ceramic membrane with a fixed wire length (L) of 4 cm and **(B)** various wire lengths with a fixed distance between the Ag/AgCl wire and diatomite membrane. The applied current pulse for chloride sensing is fixed at 1 mA, and the electrolyte comprises 300 mM KCl and 0.5 M KNO_3.

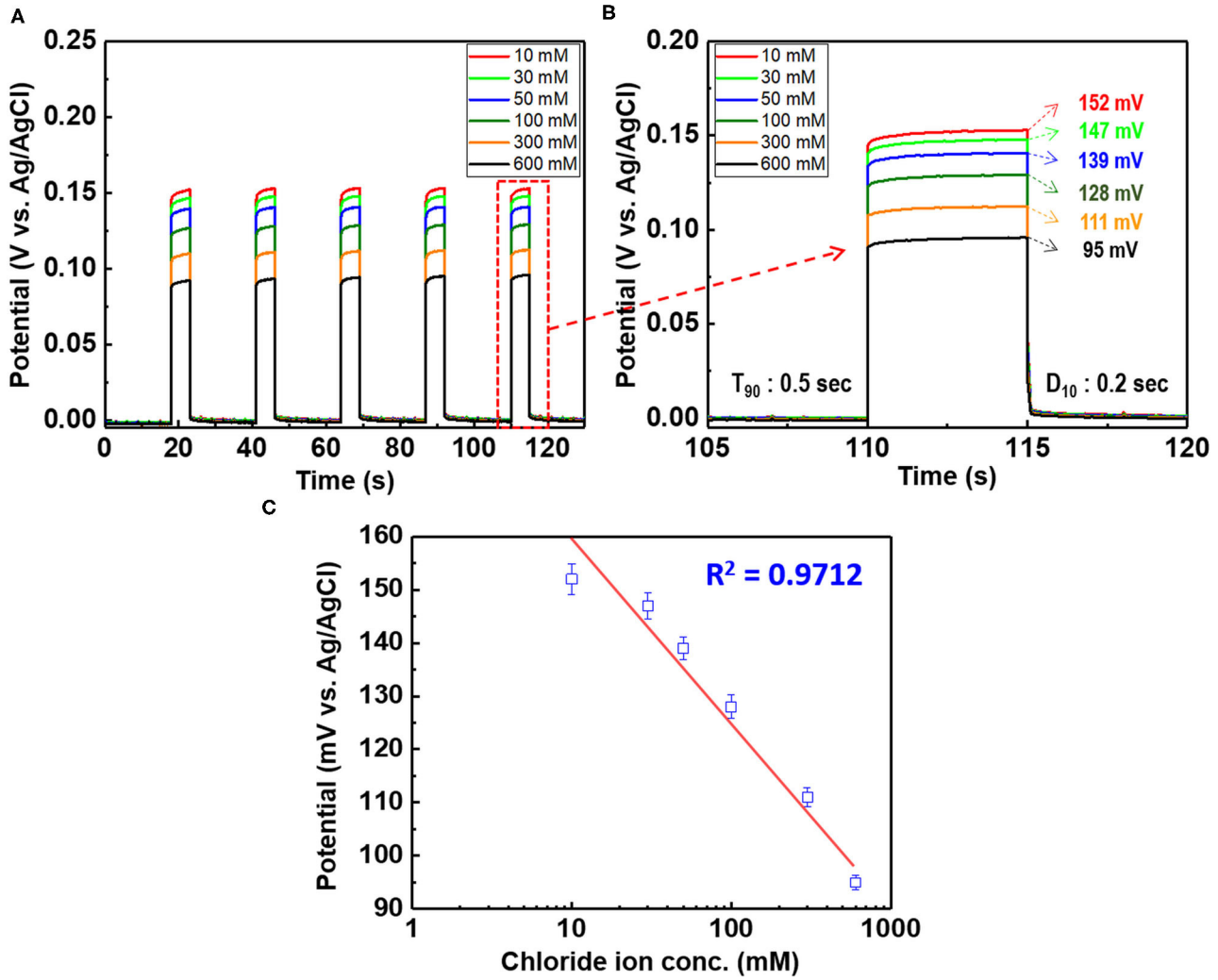

FIGURE 9 | (A) Potential difference of the chloride ion sensor (D: 1 cm, L: 4 cm Ag/AgCl) as a function of the chloride ion content of 10–600 mM KCl and **(B)** magnified image of the fifth bar (enclosed in red rectangle) in **(A)**. **(C)** Linear fitting of the chloride ion sensor potential with the experimental data. The applied current pulse is fixed at 1 mA.

elemental compositions of Ag coated with AgCl with different immersion times. The applied current density and GP time for all samples were fixed at 30 mA/cm^2 and 2 h, respectively. As a result, the number and sizes of the as-synthesized AgCl particles, as well as the chloride content on the surface of the Ag wire, increase with an increase in immersion time. The AgCl particles appear to be relatively uniform with round shapes of $<$1-μm sizes and a distinct boundary between these particles in all conditions. The boundaries between AgCl particles and pore channels through the layer, known as micro-channels, are the main pathways for the transport of ions within the AgCl layer. As the AgCl layer thickness increases, the ion transport becomes limited due to micro-channel confinement (Pemberton and Girand, 1987; Neary and Parkin, 2015; Pargar et al., 2018). For this reason, it is important to optimize the applied current density and treatment time during anodization. Additionally, the immersion time is a more important parameter in the synthesis of AgCl layer on Ag wire in comparison to the current density and GP time. Cl^- sensing with the as-fabricated Ag/AgCl ISE was performed to confirm the effect of immersion time and determine the optimal conditions for Cl^- sensing by the sensor. The length of the Ag/AgCl wire and distance to the diatomite membrane were fixed at 3 and 1 cm, respectively. The Cl^- response was measured using a three-electrode system with the as-fabricated Ag/AgCl ISE, Pt-mesh, and a commercially available Ag/AgCl RE at ambient atmosphere (24°C) and humidity of 50%. The time periods for each applied current pulse and no-pulse were fixed at 5 and 20 s, respectively. The data for Cl^- sensing by the sensor in an electrolyte containing 300 mM KCl and 0.5 mM KNO_3 as a function of immersion time using an applied current pulse of 1 mA are shown in **Figure 5**. For an immersion time of 1 s, the initial potential difference before applying the current pulse is

ca. −0.018 V, which is ideally not zero. This result is attributed to an insufficient AgCl layer on the surface of the Ag wire, which results in different half-cell potentials with respect to the Ag/AgCl RE. Furthermore, when the current pulse is applied, the initial potential difference for an immersion time of 1 s is higher and shows a non-stable sensing signal as compared to those observed with other conditions. This is due to the formation of AgCl salt on the surface of the Ag wire during the current pulse application, resulting in the depletion of Cl^- near the WE and generation of a large potential difference. An immersion time of 120 s shows a lower potential difference than those obtained with 1, 60, and 90 s. As the immersion time increases, the AgCl content on Ag wire increases, while the exposed Ag surface decreases. This results in a lower depletion of Cl^- near the WE during Cl^- sensing, resulting in a low potential difference between the Ag/AgCl ISE and Ag/AgCl RE. In other words, the concentration gradient of Cl^- at an immersion time of 120 s is small owing to the large amount of AgCl on the Ag wire. This is in good agreement with the FE-SEM data shown in **Figure 4**. Therefore, an immersion time of 120 s was selected in this study as the optimal condition for synthesizing the Ag/AgCl ISE. **Figure 6** shows the XRD data of the Ag/AgCl wire synthesized employing an immersion time of 120 s. It clearly confirms that the wire is composed of cubic AgCl (JCPDS No. 31-1238) and metallic Ag (JCPDS No. 04-0783). The diffraction peaks at 27.86°, 32.23°, 46.24°, 54.83°, 57.48°, 67.46°, and 76.59° correspond to the (111), (200), (220), (311), (221), (400), and (420) planes, respectively,

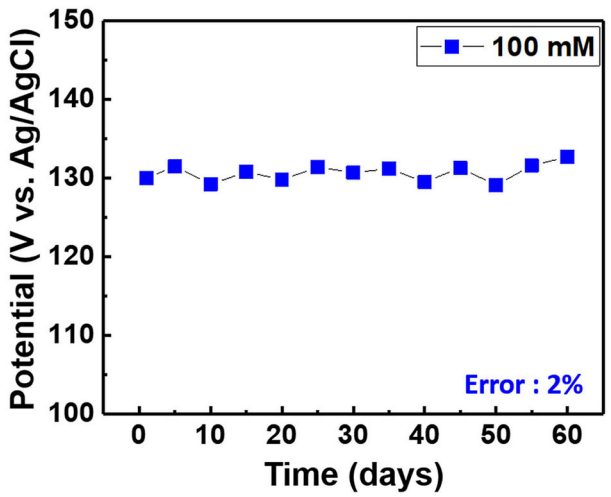

FIGURE 10 | Long-term stability of the chloride ion sensor in the electrolyte comprising 100 mM KCl and 0.5 M KNO_3.

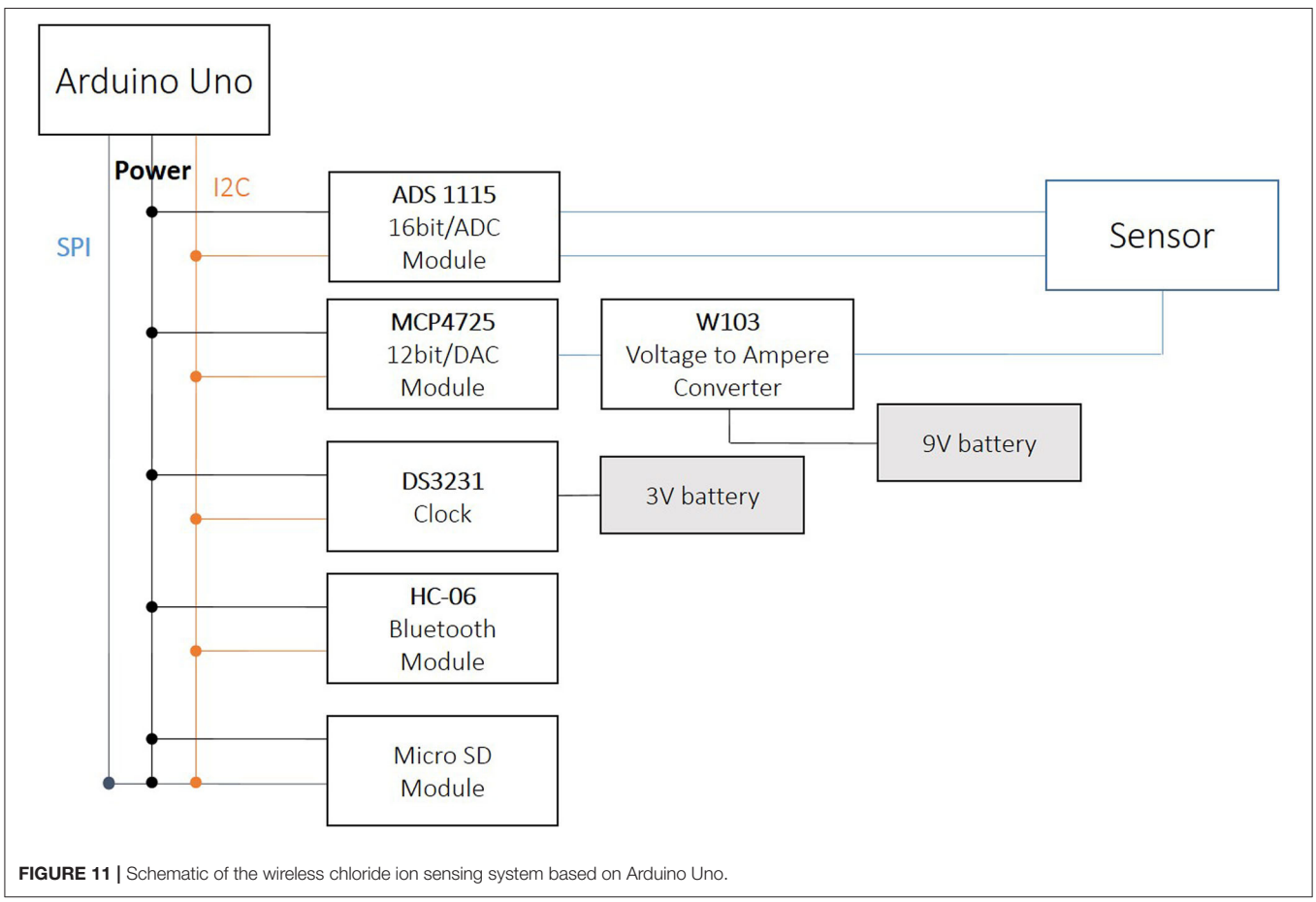

FIGURE 11 | Schematic of the wireless chloride ion sensing system based on Arduino Uno.

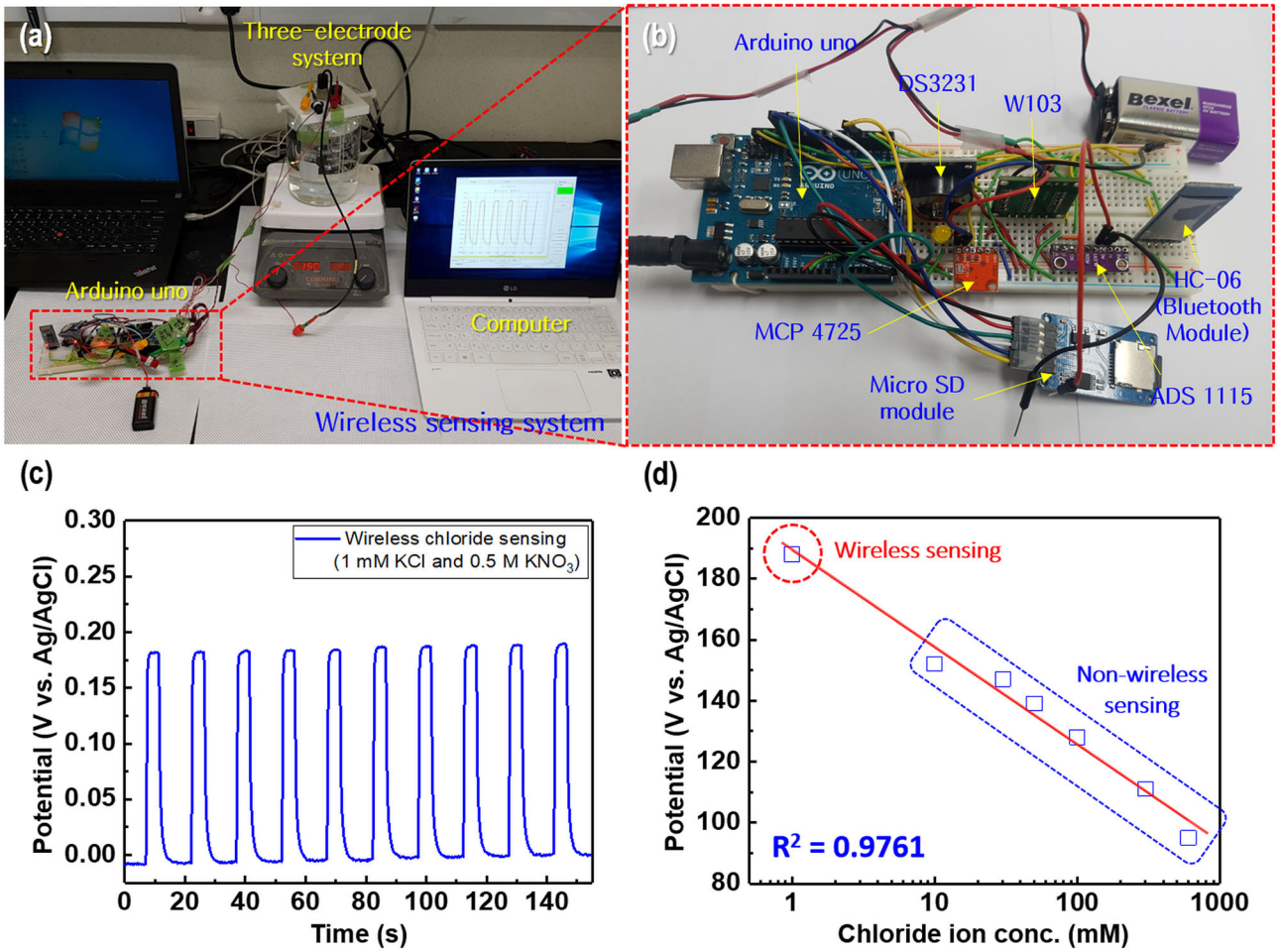

FIGURE 12 | (a) Wireless chloride ion sensing system based on Arduino Uno and **(b)** magnified image of the wireless sensor module. **(c)** Potential difference for the wireless chloride ion sensor with a regular current pulse of 1 mA in the electrolyte comprising 1 mM KCl and 0.5 M KNO_3. **(d)** Linear fitting of the chloride ion sensor potential response to the merged experimental data of wireless and non-wireless sensing.

of the Ag/AgCl layer. The peaks at 38.08°, 44.29°, 64.50°, and 77.89° are attributed to the diffraction of the (111), (200), (220), and (311) planes, respectively, of metallic Ag (Liu et al., 2019). The elemental compositions and surface chemical states of the as-synthesized Ag/AgCl wire were analyzed using XPS (**Figure 7**). **Figure 7A** shows the XPS survey spectra, indicating that Ag and Cl are the main components, and trace amounts of C and O are attributed to the adventitious hydrocarbons from the XPS instrument. The peaks at 368.04 and 374.02 eV correspond to the binding energies of $Ag3d_{5/2}$ and $Ag3d_{3/2}$, respectively, of Ag^+ in AgCl (**Figure 7B**) (Liu et al., 2019). The two peaks at 197.89 and 199.51 eV with a doublet separation of 1.7 eV in the Cl2p spectrum correspond to the binding energies of $Cl2p_{3/2}$ and $Cl2p_{1/2}$, respectively (**Figure 7C**) (Wang et al., 2012). The results obtained from the XPS data confirm the presence of Ag and AgCl in the wire, which are in complete agreement with the XRD data. High-resolution O1s spectra of the Ag/AgCl wire include three peaks centered at 530.0, 532.3, and 533.8 eV. The latter two peaks are attributed to the organic contamination absorbed on the surface of the Ag wire, whereas the first peak located at a low binding energy is associated with Ag-O (**Figure 7D**) (Wang et al., 2012). The elemental atomic percentages derived from the XPS survey spectra are also shown in **Table 1**. These data are in good agreement with the EDS data shown in **Figure 4d**. To optimize the length of the Ag/AgCl wire and distance between the Ag/AgCl wire and diatomite membrane, Cl^- sensing by the as-fabricated Ag/AgCl ISE was investigated as a function of the distance at a fixed Ag/AgCl wire length of 4 cm (**Figure 8A**). As shown, the potential difference decreases with an increase in the distance between the Ag/AgCl wire and DCM. This is probably due to the low reaction speed with an increase in the distance between the Ag/AgCl wire and Cl^- in the electrolyte upon the application of a current pulse. Next, Cl^- sensing was analyzed as a function of the Ag/AgCl wire length at a fixed distance of 1 cm (**Figure 8B**). As observed, the Ag/AgCl wire with a length of 4 cm and distance of 1 cm shows the lowest potential difference. Based on the above experimental results, an Ag/AgCl length of 4 cm and distance of 1 cm to the membrane were selected to fabricate the Cl^- sensor. The potential difference of the Cl^- sensor as a function of Cl^- concentration with an identical current pulse

of 1 mA is shown in **Figure 9A**. Prior to the application of the current pulse, the potential difference is nearly zero for all Cl^- concentrations because of the nearly identical half-cell potential between the as-fabricated Ag/AgCl ISE (WE) and commercially available Ag/AgCl RE. **Figure 9B** shows the magnification of the fifth data set (enclosed in red rectangle) in **Figure 9A**. With an increase in the amount of Cl^- in the electrolyte, the potential difference between the Ag/AgCl ISE and Ag/AgCl RE decreases. This is due to ion depletion near the WE in the electrolyte with a high Cl^- concentration compared to the low-concentration electrolyte. The response and recovery times were calculated using the time required for 90% change in the potential difference upon the supply and removal of Cl^-, respectively (Kwon et al., 2016). The average response and recovery times of the Cl^- sensor were 0.5 and 0.1 s, respectively. When no kinetic restrictions are applied, the dynamic equilibrium between metallic silver (Ag^0) and Ag^+ can be established in a short duration. This feature makes the noble Ag metal prone to "corrosion" in environments with aggressive ions such as Cl^- (Pargar et al., 2017). As shown in **Figure 9C**, a good linear fit curve is obtained, and the correlation coefficient (R^2) of the Cl^- sensor is 0.9712. As R^2 value approaches 1, a strong relationship between the sensing signal and Cl^- concentration is observed (Kim et al., 2019). The long-term stability of the Cl^- sensor is important for ensuring excellent and reliable sensing performance. The potential difference of the sensor was measured as a function of time over a period of 60 days at 5-day intervals using 100 mM KCl solution (**Figure 10**). The relative error between the initial and final signals was 2%, indicating that the potential response was quite stable during the test period. A wireless Cl^- monitoring system based on Arduino Uno was developed in this study for the real-time monitoring of Cl^- in the electrolyte comprising 1 mM KCl and 0.5 M KNO_3. Schematic and real images of the wireless sensing system are shown in **Figures 11**, **12a,b**, respectively. The wireless Cl^- sensing system is composed of individual electronic components including the micro controller unit, voltage to ampere converter (W103), clock (DS 3231), micro SD module, as-fabricated Cl^- sensor, circuit device for the wireless sensing measurement of the contained single channel readout, Arduino Uno, and analysis software (visual basic). Wireless Cl^- sensing characterization of the sensor was performed to measure the repeated potential responses in Cl^--containing solution. The potential difference for the Cl^- sensor with a regular current pulse of 1 mA is shown in **Figure 12c**. The 10 reversible cycles of the response curve indicate the stable and repeatable response characteristics with a small relative error (<4%) between the average initial and final signals. Linear fit curves of the Cl^- sensor potential response to the merged experimental data of wireless and non-wireless sensing are shown in **Figure 12d**, the R^2 of the Cl^- sensor is 0.9761. It was found that the wireless sensing of Cl^- sensor is reliable data. A movie for the real-time wireless Cl^- sensing with an applied current pulse of 1 mA in 1 mM KCl and 0.5 M KNO_3 is shown in **Supplementary Figure 1**.

CONCLUSION

A novel Cl^- sensor based on Ag wire coated with an AgCl layer composed of a gel-type internal electrolyte and DCM was manufactured *via* GP and immersion in 1 M HCl solution. Both the DCM and the gel-type electrolyte played essential roles in preventing electrolyte leakage from the ion-selective electrode. The AgCl layer was dense and uniformly coated on the surface of the Ag wire; the AgCl particles were relatively uniform with round shapes and a size of <1 μm. The size and content of AgCl increased with an increase in the immersion time at a fixed current density of 30 mA/cm^2 and GP time of 2 h. The length of the Ag/AgCl wire and its distance to the membrane were optimized to minimize the potential difference. Consequently, the sensor could detect Cl^- in 10–500 mM Cl^- concentration with good linearity; moreover, the sensor exhibits good long-term stability (about 2 months). A wireless sensing system based on Arduino was investigated to measure the Cl^- response in an electrolyte containing 1 mM KCl and 0.5 M KNO_3. A small relative error of <4% was obtained between the initial and final signals. A linearity of 0.9712 was obtained from the experimental data of non-wireless Cl^- sensing. In conclusion, this study presented a practical method for inexpensive and scalable fabrication of wireless Ag/AgCl-based Cl^- sensors for applications in RC structures with good reliability.

DATA AVAILABILITY STATEMENT

The original contributions presented in the study are included in the article/**Supplementary Material**, further inquiries can be directed to the corresponding author/s.

AUTHOR CONTRIBUTIONS

SK and GP conducted the most experiment and wrote the paper. H-JA, BY, and I-HS made some parts and did analysis. K-HL made Arduino set-up. J-HL and J-YL organized the experiment and revised the manuscript. All authors contributed to the article and approved the submitted version.

FUNDING

This work was supported by the Global Frontier Program through the Global Frontier Hybrid Interface Materials (GFHIM) project (Grant 2013M3A6B1078870) of the National Research Foundation of Korea (NRF), which was funded by the Ministry of Science, ICT, and the Future Planning and Technology Innovation Program (20002694) funded by the Ministry of Trade, Industry & Energy (MOTIE, Korea), and the Fundamental Research Program of the Korea Institute of Materials Science (PNK6740).

SUPPLEMENTARY MATERIAL

The Supplementary Material for this article can be found online at: https://www.frontiersin.org/articles/10.3389/fchem.2020.574986/full#supplementary-material

Video S1 | The movie of wireless chloride ion sensing based on Arduino Uno.

REFERENCES

Abbas, Y. (2015). *In-Situ Measurement of Chloride Ion Concentration in Concrete* (Ph.D. thesis). University of Twente, Enschede, Netherlands.

Abbas, Y., Olthuis, W., and Berg, A. V. D. (2013). A chronopotentiometric approach for measuring chloride ion concentration. *Sen. Actuat. B* 188, 433–439. doi: 10.1016/j.snb.2013.07.046

Angst, U. M., and Polder, R. (2014). Spatial variability of chloride in concrete within homogeneously exposed areas. *Cem. Concr. Compos.* 56, 40–51. doi: 10.1016/j.cemconres.2013.10.010

Bard, A. J., and Faulkner, L. R. (2001). Electrochemical methods: fundamentals and applications, New York: Willey, 2nd ed. *Russ. J. Electrochem.* 38, 1364–1365. doi: 10.1023/A:1021637209564

Bassil, A., Chapeleau, X., Leduc, D., and Abraham, O. (2020). Concrete crack monitoring using a novel strain transfer model for distributed fiber optics sensors. *Sensors* 20:2220. doi: 10.3390/s20082220

Corva, D. M., Hosseini, S. S., Collins, F., Adams, S. D., Gates, W. P., and Kouzani, A. Z. (2020). Miniature resistance measurement device for structural health monitoring of reinforced concrete infrastructure. *Sensors* 20:4313. doi: 10.3390/s20154313

Dobbelaere, T., Vereecken, P. M., and Detavernier, C. (2017). A usb-controlled potentiostat/galvanostat for thin-film battery characterization. *HardwareX* 2, 34–49. doi: 10.1016/j.ohx.2017.08.001

Femenias, Y. S., Angst, U., Caruso, F., and Elsener, B. (2016). Ag/AgCl ion-selective electrodes in neutral and alkaline environments containing interfering ions. *Mater. Struct.* 49, 2637–2651. doi: 10.1617/s11527-015-0673-8

Gandía-Romero, J. M., Bataller, R., Monzón, P., Campos, I., García-Breijo, E., Valcuende, M., et al. (2016). Characterization of embeddable potentiometric thick-film sensors for monitoring chloride penetration in concrete. *Sens. Actuators B Chem.* 222, 407–418. doi: 10.1016/j.snb.2015.07.056

Gu, H., and Bennion, D. N. (1977). Diffusion and charge transfer parameters for the Ag/AgCl electrode. *J. Electrochem. Soc.* 124, 1364–1370. doi: 10.1149/1.2133655

Guo, H., Chen, Y., Cortie, M. B., Liu, X., Xie, Q., Wang, X., et al. (2014). Shape-selective formation of monodisperse copper nanospheres and nanocubes via disproportionation reaction route and their optical properties. *J. Phy. Chem. C* 118, 9801–9808. doi: 10.1021/jp5014187

Guth, U., Gerlach, F., Decker, M., Oelßner, W., and Vonau, W. (2009). Solid-state reference electrodes for potentiometric sensors. *J. Solid State Electrochem.* 13, 27–39. doi: 10.1007/s10008-008-0574-7

Imounga, H. M., Bastidas-Arteaga, E., Moutou Pitti, R., Ekomy Ango, S., and Wang, X.-H. (2020). Bayesian assessment of the effects of cyclic loads on the chloride ingress process into reinforced concrete. *Appl. Sci.* 10:2040. doi: 10.3390/app10062040

Inzelt, G., Lewenstam, A., and Scholz, F. (2013). *Handbook of Reference Electrodes*. Berlin: Springer.

Javadian, A., Smith, I. F. C., and Hebel, D. E. (2020). Application of sustainable bamboo-based composite reinforcement in structural-concrete beams: design and evaluation. *Materials* 13:696. doi: 10.3390/ma13030696

Jin, M., Xu, J., Jiang, L., Gao, G., Chu, H., Xiong, C., et al. (2014). Electrochemical characterization of a solid embeddable Ag/AgCl reference electrode for corrosion monitoring in reinforced concrete. *Electrochemistry* 82, 1040–1046. doi: 10.5796/electrochemistry.82.1040

Karthick, S., Kwon, S.-J., Lee, H. S., Muralidharan, S., Saraswathy, V., and Natarajan, R. (2017). Fabrication and evaluation of a highly durable and reliable chloride monitoring sensor for civil infrastructure. *RSC Adv.* 7, 31252–31263. doi: 10.1039/C7RA05532C

Kim, S., Song, Y., Hwang, T.-Y., Lim, J.-H., and Choa, Y.-H. (2019). Facial fabrication of an inorganic/organic thermoelectric nanocomposite based gas sensor for hydrogen detection with wide range and reliability. *Int. J. Hydrogen Energy* 44, 11266–11274. doi: 10.1016/j.ijhydene.2019.03.004

Kim, Y.-J., Lee, H.-D., and Kim, D.-W. (2017). Fabrication of gel-type electrolyte for the development of reference electrode for sea water and application to measuring equipment for total residual oxidants. *App. Chem. Eng.* 28, 153–157. doi: 10.14478/ace.2016.1086

Kwon, Y. J., Na, H. G., Kang, S. Y., Choi, S.-W., Kim, S. S., and Kim, H. W. (2016). Selective detection of low concentration toluene gas using Pt-decorated carbon nanotubes sensors. *Sens. Actuator B Chem.* 277, 157–168. doi: 10.1016/j.snb.2015.12.024

Li, B., Huan, Y., and Zhang, W. (2017). Passivation and corrosion behavior of P355 carbon steel in simulated concrete pore solution at pH 12.5 to 14. *Int. J. Electrochem. Sci.* 12, 10402–10420. doi: 10.20964/2017.11.51

Liu, J., Wu, Z., He, Q., Tian, Q., Wu, W., Xiao, X., et al. (2019). Catalytic application and mechanism studies of argentic chloride coupled Ag/Au hollow heterostructures: considering the interface between Ag/Au bimetals. *Nanoscale Res. Lett.* 14, 1–13. doi: 10.1186/s11671-019-2862-9

Neary, M. C., and Parkin, G. (2015). Dehydrogenation, disproportionation and transfer hydrogenation reactions of formic acid catalyzed by molybdenum hydride compounds. *Chem. Sci.* 6, 1859–1865. doi: 10.1039/C4SC03128H

Pargar, F., Kolev, H., Koleva, D. A., and Breugel, K. V. (2018). Microstructure, surface chemistry and electrochemical response of Ag/AgCl sensors in alkaline media. *J. Mater. Sci.* 53, 7527–7550. doi: 10.1007/s10853-018-2083-0

Pargar, F., Koleva, D. A., and Breugel, K. V. (2017). Determination of chloride content in cementitious materials: from fundamental aspects to application of Ag/AgCl chloride sensors. *Sensors* 17, 1–22. doi: 10.3390/s17112482

Pemberton, J. E., and Girand, M. M. (1987). Electrochemical and sem characterization of Ag electrodes roughened by potential sweep potential step processes in aqueous chloride + pyridine media. *J. Electroanal. Chem. Interfacial Electrochem.* 217, 79–92. doi: 10.1016/0022-0728(87)85065-9

Raccichini, R., Amores, M., and Hinds, G. (2019). Critical review of the use of reference electrodes in Li-ion batteries: a diagnostic perspective. *Batteries* 5:12. doi: 10.3390/batteries5010012

RILEM TC 178-TMC (2002). Analysis of total chloride content in concrete. *Mater. Struct.* 35, 583–585. doi: 10.1617/13840

Tang, Y.-B., Wang, S.-N., Chen, L., and Fan, Z.-H. (2015). Preparation and properties of embeddable Ag/AgCl gelling reference electrode for rebars corrosion monitoring in concrete. *China Ocean Eng.* 29, 925–932. doi: 10.1007/s13344-015-0065-4

Torres-Luque, M., Bastidas-Arteaga, E., Schoefs, F., Sánchez-Silva, M., and Osma, J. F. (2014). Non-destructive methods for measuring chloride ingress into concrete: state-of-the-art and future challenges. *Constr. Build. Mater.* 68, 68–81. doi: 10.1016/j.conbuildmat.2014.06.009

Wang, J., An, C., Zhang, M., Qin, C., Ming, X., and Zhang, Q. (2012). Photochemical conversion of AgCl nanocubes to hybrid AgCl-Ag nanoparticles with high activity and long-term stability towards photocatalytic degradation of organic dyes. *Can. J. Chem.* 90, 858–864. doi: 10.1139/v2012-079

Conflict of Interest: The authors declare that the research was conducted in the absence of any commercial or financial relationships that could be construed as a potential conflict of interest.

frontiers in Chemistry

ORIGINAL RESEARCH
published: 25 November 2020
doi: 10.3389/fchem.2020.592538

Preparation of Electrochemical Sensor Based on Zinc Oxide Nanoparticles for Simultaneous Determination of AA, DA, and UA

Yuanzhi Pan[1,2,3]*, *Junli Zuo*[4], *Zhongyu Hou*[1]*, *Yizhong Huang*[5]* and *Cancan Huang*[6]

[1] National Key Laboratory of Science and Technology on Micro/Nano Fabrication, Key Laboratory for Thin Film and Microfabrication of Ministry of Education, Department of Micro/Nano Electronics, School of Electronic Information and Electrical Engineering, Shanghai Jiao Tong University, Shanghai, China, [2] Central Academe, Shanghai Electric Group Co., Ltd., Shanghai, China, [3] Zhenjiang Hongxiang Automation Technology Co., Ltd., Zhenjiang, China, [4] Department of Geriatrics, Ruijin Hospital, Shanghai Jiao Tong School of Medicine, Shanghai, China, [5] School of Materials Science and Engineering, Nanyang Technological University, Singapore, Singapore, [6] Beijing Kanghong Biomedical Co., Ltd., Beijing, China

OPEN ACCESS

Edited by:
Hassan Karimi-Maleh,
University of Electronic Science and Technology of China, China

Reviewed by:
Yuhong Zheng,
Jiangsu Province and Chinese Academy of Sciences, China
Sadegh Salmanpour,
Islamic Azad University Sari Branch, Iran
Afsaneh L. Sanati,
University of Coimbra, Portugal

***Correspondence:**
Yuanzhi Pan
yuanzhi_p@hotmail.com
Zhongyu Hou
zhyhou@sjtu.edu.cn
Yizhong Huang
yzhuang@ntu.edu.sg

Specialty section:
This article was submitted to Electrochemistry, a section of the journal Frontiers in Chemistry

Received: 07 August 2020
Accepted: 27 August 2020
Published: 25 November 2020

Citation:
Pan Y, Zuo J, Hou Z, Huang Y and Huang C (2020) Preparation of Electrochemical Sensor Based on Zinc Oxide Nanoparticles for Simultaneous Determination of AA, DA, and UA. Front. Chem. 8:592538. doi: 10.3389/fchem.2020.592538

ZnO nanoparticles (NPs) were synthesized using a hydrothermal method. Scanning electron microscope (SEM) and X-ray diffraction have been used for characterizing the synthesized ZnO NPs. An electrochemical sensor was fabricated using ZnO NPs–modified glassy carbon electrode for simultaneous determination of ascorbic acid (AA), dopamine (DA), and uric acid (UA). The proposed electrochemical sensor exhibited excellent detection performance toward three analytes, demonstrating that it can potentially be applied in clinical applications. The results indicated the ZnO NPs–modified electrode can detect AA in the concentrations range between 50 and 1,000 μM. The ZnO NPs–modified electrode can detect DA in the concentrations range between 2 and 150 μM. The ZnO NPs–modified electrode can detect UA in the concentrations range between 0.2 and 150 μM. The limits of detections of AA, DA, and UA using ZnO NPs–modified electrode were calculated to be 18.4, 0.75, and 0.11 μM, respectively.

Keywords: electrochemical sensor, zinc oxide, ascorbic acid, dopamine, uric acid

INTRODUCTION

Ascorbic acid (AA), dopamine (DA), and uric acid (UA) are active substances with important biological research value existing in the extracellular fluid of the human central nervous system. Among them, AA plays an important role in promoting the growth of organisms and synthesizing antibodies (Ejaz and Jeon, 2017; Fu et al., 2018). As an important biological small molecule substance in the human central nervous system, the content of DA in the body below or beyond the normal level will directly affect the mental activities of the human body (Atta et al., 2019). When purine metabolism is abnormal in the human body, excessive UA can be produced; UA retained in the body will change the pH value of body fluid and form an acidic internal environment, which has an important impact on the function of somatic cells (Hsu et al., 2017; Nagles et al., 2017). In view of the important medical research value of detecting the contents of these three substances, rapid and accurate detection methods are essential for the diagnosis (Abellán-Llobregat et al., 2018). In recent years, the detection of AA, DA, and UA has attracted considerable attention (Fu et al., 2019, 2020; Shamsadin-Azad et al., 2019; Karimi-Maleh et al., 2020c; Zhou et al., 2020).

At present, the common detection methods of AA are spectrophotometry, chromatography, fluorescence, and electrochemical sensor (Gopalakrishnan et al., 2018; Atta et al., 2020). The principle of spectrophotometry is that AA reacts with reagent to form chromogenic group and deoxyascorbic acid through redox or derivatization reaction with reagent, thus indirectly realizing the detection of AA concentration. This method is simple and has good selectivity, but the dyes involved in the reaction are unstable and easily interfered by sulfhydryl, reducing ketone and sulfite plasma. High-performance thin-layer chromatography (HPLC) uses silica particles with narrow particle size as adsorbent, which has obvious advantages in the separation effect. Gas chromatography has good selectivity in the determination of trace substances (Zhang et al., 2018a,b). However, AA is a polar compound, which requires a series of sample pretreatment and increases the complexity of determination. The fluorescence method is a direct or indirect detection method based on the fluorescence intensity quenching and recovery of the probe after adding AA. Fluorescence detection of AA has strong interference ability and high sensitivity, which is suitable for the rapid detection of trace AA in actual samples (Zhang et al., 2018c; de Faria et al., 2020). The detection methods of DA include chemiluminescence, spectrophotometry, fluorescence, liquid chromatography, and electrochemical sensors. The detection principle of chemiluminescence is that the chemical energy absorbed by the material is converted into light energy when the chemical reaction occurs (Cinti et al., 2018). The content of the material in the sample is reflected by the luminous intensity. In spectrophotometry, the complex is formed by the reaction between DA and chromogenic agent. The absorbance of the complex at a specific absorption wavelength has a certain linear relationship with the concentration of DA. The fluorescence method can detect the content of DA in pharmaceuticals by measuring the fluorescence intensity (Ghanbari and Hajian, 2017; Long and Fu, 2017). Compared with other methods, HPLC has a higher separation rate. Because the DA itself has fluorescence, the combination of fluorescence and HPLC as an effective detection method has been widely concerned in the analysis of DA. At present, phosphotungstic acid reduction (PAR) method, HPLC, enzyme method, and electrochemical sensor have been established in clinical setting to detect UA. The principle of determination of UA by PAR is that under alkaline conditions, phosphotungstic acid reacts with UA to produce tungsten blue and allantoin (Feng et al., 2020; Hou et al., 2020; Karimi-Maleh et al., 2020a). The concentration of UA is indirectly obtained by colorimetry. This method has good accuracy for the detection of UA, but it requires higher purity of phosphotungstic acid. HPLC has the advantages of simple mobile phase and good separation effect, but the complex pretreatment of samples is time-consuming. The enzyme detection of UA is to use enzyme to catalyze the decomposition of UA to get a certain concentration of product and then calculate the content of UA (Karimi-Maleh and Arotiba, 2020; Karimi-Maleh et al., 2020a). The enzyme method for UA detection is relatively simple; however, the high cost of enzyme and the constant temperature of the reaction process limit its application.

The specificity of recognition between enzyme and substrate makes the enzyme sensor have high selectivity and low detection limit. However, the activity of the enzyme is greatly affected by external environmental factors such as pH, temperature, and material toxicity, which makes the enzyme sensor have low stability and short life. At the same time, because of the limited types of enzymes, its application scope is greatly limited. In order to overcome the shortcomings of enzyme sensors, many scientists have developed a series of enzyme-free sensors with good stability, simple preparation, and low cost. Nanomaterials have the advantages of large specific surface area, many surface-active sites, high conductivity, good adsorption performance, and strong catalytic performance, which can greatly improve the sensitivity and stability of the sensor. They can be used to immobilize biomolecules and as biomarkers to label biomolecules. They can be used as catalysts in electrochemical reactions to catalyze reactions and enhance the efficiency of electron transfer. In this work, we report the preparation of ZnO nanoparticles (NPs) using a simple one-pot synthesis method (Yumak et al., 2011; Naderi Asrami et al., 2020). The formed ZnO NPs have been used for glassy carbon electrode (GCE) modification and used as a sensitive electrochemical sensor for simultaneous detection of AA, DA, and UA. As oxidation potentials of AA, DA, and UA severely overlap, their electrochemically simultaneous determination is still a challenge. The modification of ZnO could successfully separate three analyte oxidation peaks.

MATERIALS AND METHODS

Zinc nitrate hexahydrate [$Zn(NO_3)_2{\cdot}6H_2O$], UA, DA, AA, and hydrazine were purchased from Yeyuan Biotech. Co. Ltd. Phosphate-buffered solution was prepared by mixing K_2HPO_4 and KH_2PO_4 to appropriate 0.1 M with an appropriate pH. All reagents were of analytical grade. Millipore Milli-Q water (18 MΩ cm) was used throughout.

The preparation of ZnO NPs has been carried out by previous report (Fu and Fu, 2015). Briefly, 20 mL of zinc nitrate solution (0.05 M) was prepared under stirring. Then 0.5 mL hydrazine solution (1 wt %) was added into the solution. The slurry was sonicated for 0.5 h and transferred into a Teflon-lined stainless-steel autoclave. The autoclave was heated to 120°C for 2 h. The precipitate (denoted as ZnO NPs) was collected after centrifugation and dried in an oven.

All electrochemical measurements were performed using CHI 760 electrochemical workstation with a conventional three-electrode system. A platinum wire, a 3 M Ag/AgCl electrode, and a GCE were as auxiliary electrode, reference, and working electrode, respectively. The GCE was modified by the ZnO NPs dispersion and coated with a layer of Nafion before analysis.

RESULTS AND DISCUSSION

Figure 1A shows the scanning electron microscope image of ZnO NPs after coating with Nafion film. It can be seen that a thin layer of the Nafion was covered above the ZnO NPs, which could

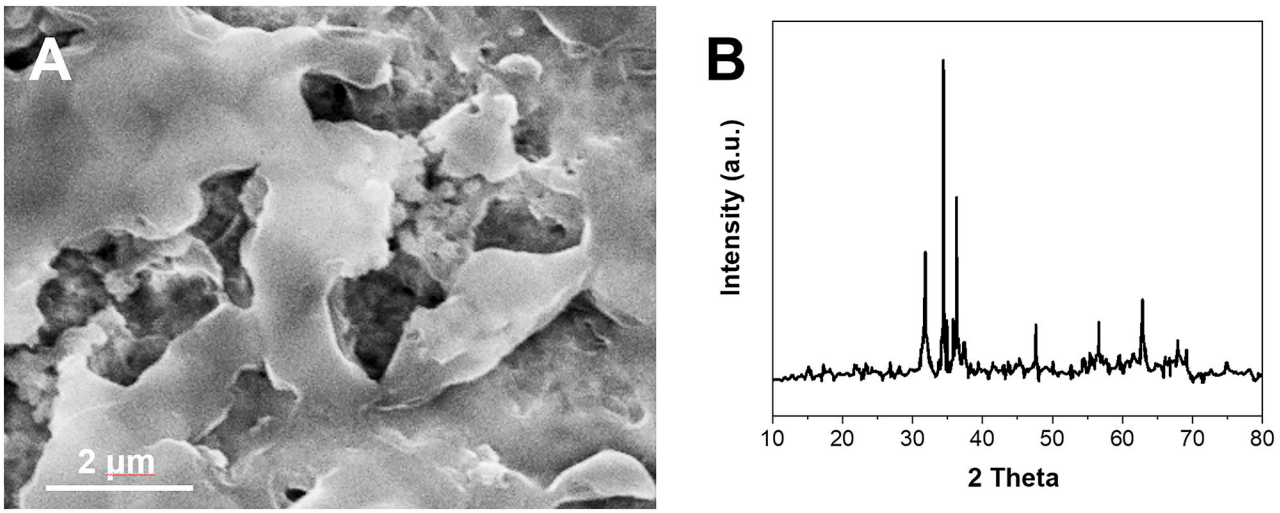

FIGURE 1 | (A) SEM image and **(B)** XRD pattern of synthesized ZnO NPs.

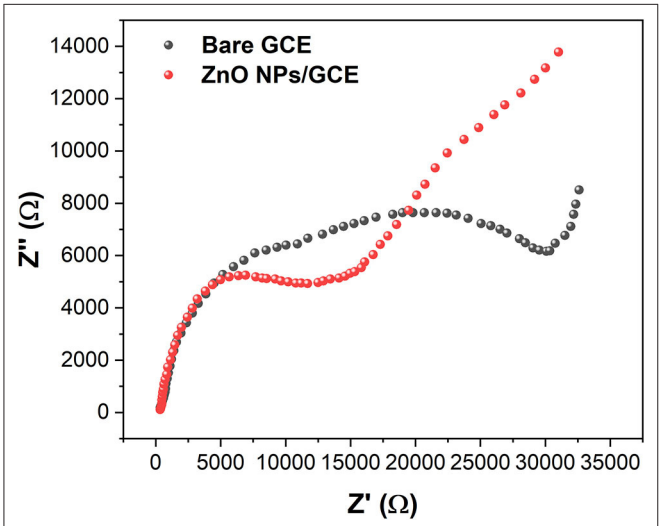

FIGURE 2 | EIS plots of bare GCE and ZnO NPs/GCE.

prevent the detachment of the NPs during the electrochemical reaction. The formation of ZnO NPs was investigated by X-ray diffraction (XRD) (**Figure 1B**). The XRD pattern of the ZnO NPs displays the peaks at 31.5°, 34.4°, 36.4°, 47.2°, 56.1°, 62.8°, and 68.2°. These peaks can be indexed to hexagonal wurtzite ZnO (JCPDS 36-1451). The average size of the ZnO NPs can be calculated to 32.3 nm using the Debye–Scherrer equation.

The electrochemical property of the synthesized ZnO NPs–modified GCE and bare GCE were investigated by electrochemical impedance spectroscopy (EIS). The EIS plot of bare GCE exhibited a larger semicircle compared with that of the ZnO NPs/GCE (**Figure 2**), suggesting the modification of ZnO NPs could lower the electron-transfer resistance of GCE. This result indicates the modification of ZnO NPs can enhance the electrochemical property of the GCE. Therefore, it is expected to have a higher electrochemical response when interacting with analytes (Karimi-Maleh et al., 2020b).

The electrocatalytic activity of the ZnO NPs was studied using AA as an analyte and shown in **Figure 3A**. It can be seen that the CV of bare GCE exhibited no distinct response toward 0.5 mM AA oxidation, whereas the ZnO NPs/GCE showed a clear oxidation peak of AA at 0.07 V. The superior sensing activity can be ascribed to the enhanced conductivity by ZnO NPs with the intrinsic electrocatalytic property. In addition, the ZnO NPs–modified GCE showed a larger background compared with that of the bare GCE, suggesting the ZnO NPs increase the electroactive surface area of the electrode. Then, the electrocatalytic behavior of the ZnO NPs/GCE was further studied using all three analytes. **Figure 3B** shows the CV profiles of ZnO NPs/GCE toward AA, DA, and UA. Three well-separated oxidation peaks were noticed at 0.08, 0.42, and 0.79 V, corresponding to the oxidation of UA, DA, and AA, respectively. This observation indicates the prepared ZnO NPs/GCE can be used as an electrochemical sensor for AA, DA, and UA simultaneous detection.

The effect of pH on the detection of AA, DA, and UA using ZnO NPs/GCE was investigated. **Figures 4A–C** show the CV profiles of ZnO NPs/GCE toward AA, DA, and UA in the range of 4.4–8.4, respectively. The increasing of peak current was observed in all three cases when the pH increases until 7.4. Then, further increasing of pH leads to the decreasing of the current response. Therefore, pH 7.4 was selected to be an optimum condition.

The sensing activity of ZnO NPs/GCE has been tested for individual AA, DA, and UA. During the test, the concentration of one analyte was changed, whereas the other two analytes remained the same. **Figure 5A** shows the SWV profiles of the ZnO NPs/GCE toward AA in the concentrations range between

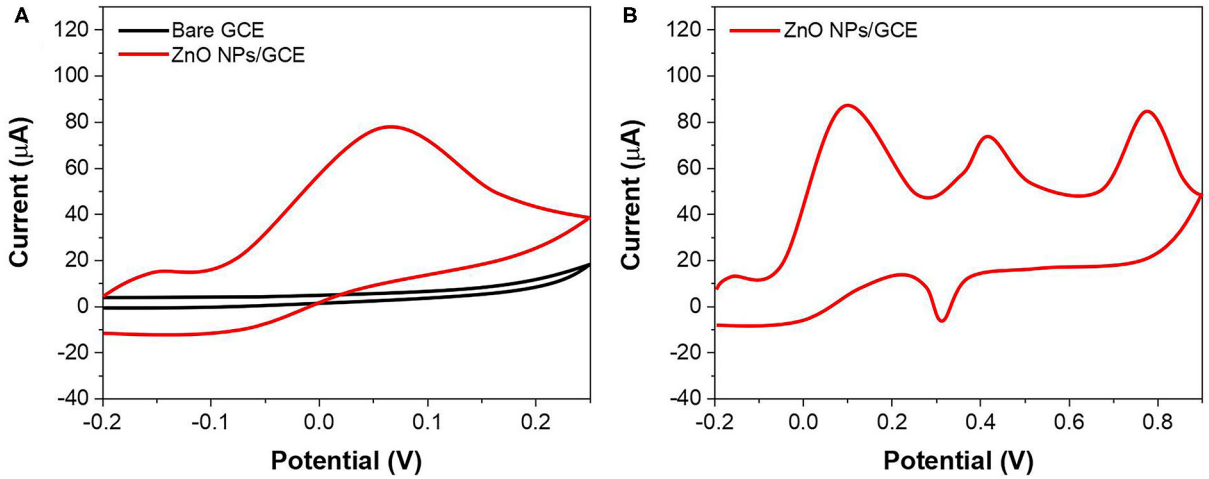

FIGURE 3 | (A) CV of bare GCE and ZnO NPs/GCE toward 500 μM AA. **(B)** CV of ZnO NPs/GCE at mixture of AA, DA, and UA.

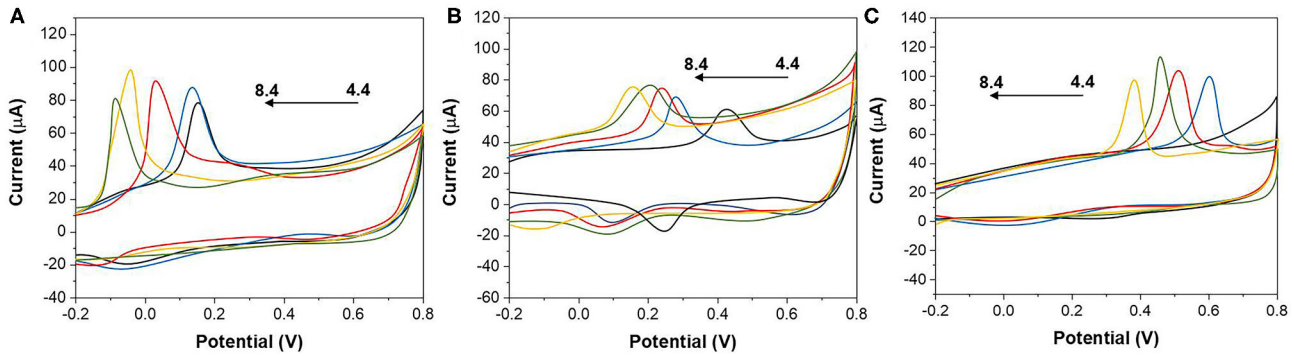

FIGURE 4 | CVs of **(A)** 1,000 μM AA, **(B)** 100 μM DA, and **(C)** 100 μM UA at the ZnO NPs/GCE values of 4.4, 5.4, 6.4, 7.4, and 8.4.

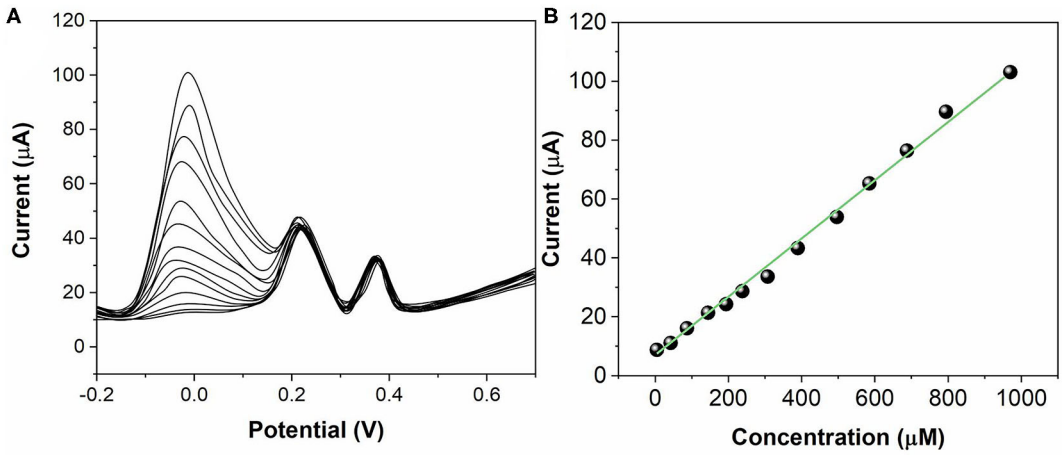

FIGURE 5 | (A) SWVs for AA (50–1,000 μM) at ZnO NPs/GCE. **(B)** Calibration plots of AA concentration vs. current.

50 and 1,000 μM. The peak currents exhibited a linear regression from 50 to 1,000 μM (**Figure 5B**) with an equation of $I_{pa(AA)} = 5.3662 + 0.10771\ C_{AA}$ ($R^2 = 0.9976$). **Figure 6A** shows the SWV profiles of the ZnO NPs/GCE toward DA in the concentrations range between 2 and 150 μM. The peak currents exhibited a linear regression from 2 to 150 μM (**Figure 6B**) with an equation

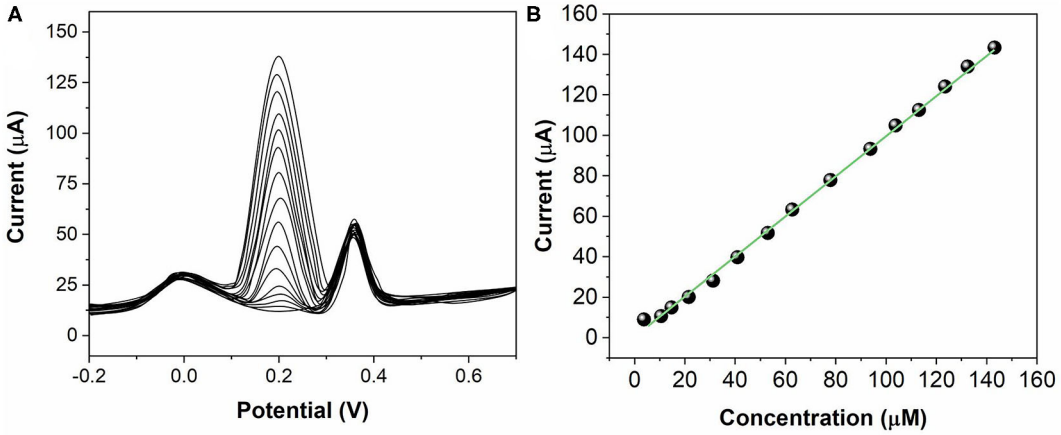

FIGURE 6 | (A) SWVs for DA (2–150 μM) at ZnO NPs/GCE. **(B)** Calibration plots of DA concentration vs. current.

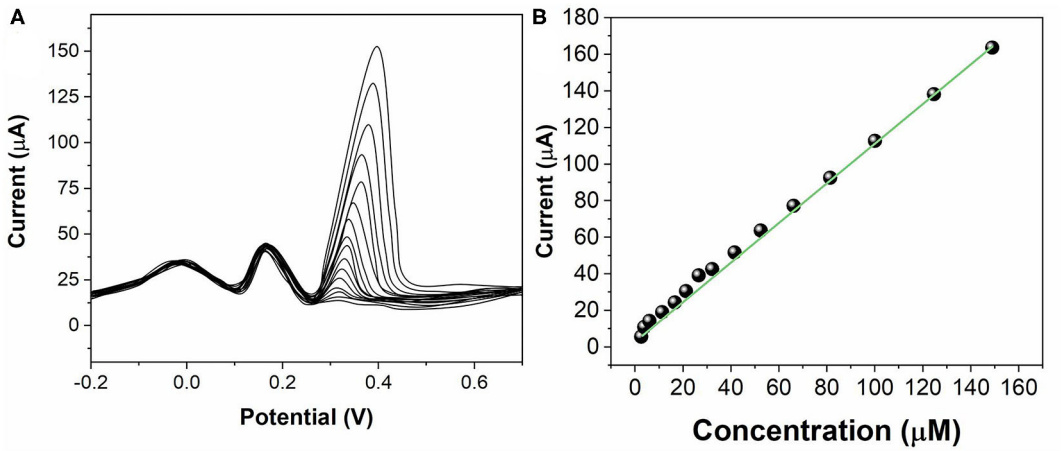

FIGURE 7 | (A) SWVs for UA (0.2–150 μM) at ZnO NPs/GCE. **(B)** Calibration plots of UA concentration vs. current.

of $I_{pa(DA)} = 0.6997 + 1.02465\ C_{AA}$ ($R^2 = 0.9985$). **Figure 7A** shows the SWV profiles of the ZnO NPs/GCE toward UA in the concentration range between 0.2 and 150 μM. The peak currents exhibited a linear regression from 0.2 to 150 μM (**Figure 7B**) with an equation of $I_{pa(DA)} = 7.7951 + 1.07205\ C_{AA}$ ($R^2 = 0.9977$). The limits of detections of AA, DA, and UA using ZnO NPs/GCE were calculated to be 18.4, 0.75, and 0.11 μM, respectively.

The stability of the ZnO NPs/GCE was tested by 10 successive measurements in three analytes. The responses remained almost stable with relative standard deviation (RSD) of 3.2, 3.7, and 4.5% for AA, DA, and UA, respectively. The reproducibility of the ZnO NPs/GCE was investigated by six individual ZnO NPs/GCE toward three analytes. The RSD was calculated to be 2.6, 3.1, and 4.4% for AA, DA, and UA, respectively. The selectivity of the ZnO NPs/GCE was tested by the presence of several potential interferences. As shown in **Figure 8**, 50-folds of common ions such as Na^+, K^+, Mg^{2+}, Ni^{2+}, and Ca^{2+} and 20-folds of glucose, sucrose, vitamin B_6, and acetaminophen exhibited no interference on the sensing.

To illustrate the applicability of the ZnO NPs/GCE for real sample analysis, measurements were carried out in vitamin C (labeled as 50 mg/mL) and DA hydrochloride tablet (labeled as 20 mg/mL) by employing the standard addition method. As shown in **Supplementary Table 1**, the recovery of the spiked samples ranged between 93.49 and 102.01%, indicating the successful application of the ZnO NPs/GCE for the determination of AA, DA, and UA in real samples.

CONCLUSION

We proposed an electrochemical sensor based on ZnO NPs for the simultaneous determination of AA, DA, and UA. The sensor showed a stronger ability to oxidize AA, DA, and UA compared with that of a bare GCE. The ZnO NPs/GCE exhibited a linear regression from 50 to 1,000 μM for AA, a linear regression

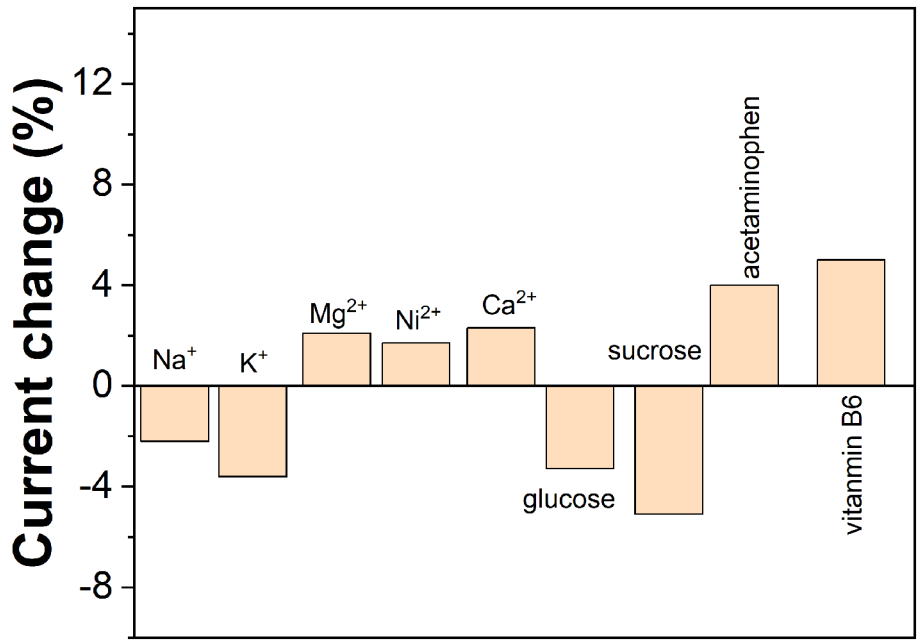

FIGURE 8 | Anti-interference property of the ZnO NPs/GCE.

from 2 to 150 μM for DA and a linear regression from 0.2 to 150 μM for UA. The limit of detections of AA, DA, and UA using ZnO NPs/GCE were calculated to be 18.4, 0.75, and 0.11 μM, respectively. The results suggest that ZnO NPs can be considered as an excellent candidate for electrochemical sensing.

DATA AVAILABILITY STATEMENT

The original contributions presented in the study are included in the article/**Supplementary Material**, further inquiries can be directed to the corresponding author/s.

AUTHOR CONTRIBUTIONS

YP and ZH contributed conception and design of the study. JZ and YP conducted electrochemical experiments. YH and CH performed the statistical analysis. YP and ZH wrote the manuscript. All authors contributed to manuscript revision, read, and approved the submitted version.

FUNDING

This work was supported by Technology Innovation Fund for Small and Medium-sized Enterprises of Science and Technology of Shanghai Science and Technology Commission (1301H195000).

SUPPLEMENTARY MATERIAL

The Supplementary Material for this article can be found online at: https://www.frontiersin.org/articles/10.3389/fchem.2020.592538/full#supplementary-material

REFERENCES

Abellán-Llobregat, A., González-Gaitán, C., Vidal, L., Canals, A., and Morallón, E. (2018). Portable electrochemical sensor based on 4-aminobenzoic acid-functionalized herringbone carbon nanotubes for the determination of ascorbic acid and uric acid in human fluids. *Biosens. Bioelectron.* 109, 123–131. doi: 10.1016/j.bios.2018.02.047

Atta, N. F., Galal, A., Ahmed, Y. M., and El-Ads, E. H. (2019). Design strategy and preparation of a conductive layered electrochemical sensor for simultaneous determination of ascorbic acid, dobutamine, acetaminophen and amlodipine. *Sens. Actuators B Chem.* 297:126648. doi: 10.1016/j.snb.2019.126648

Atta, N. F., Galal, A., and El-Gohary, A. R. (2020). Crown ether modified poly(hydroquinone)/carbon nanotubes based electrochemical sensor for simultaneous determination of levodopa, uric acid, tyrosine and ascorbic acid in biological fluids. *J. Electroanal. Chem.* 863:114032. doi: 10.1016/j.jelechem.2020.114032

Cinti, S., Colozza, N., Cacciotti, I., Moscone, D., Polomoshnov, M., Sowade, E., et al. (2018). Electroanalysis moves towards paper-based printed electronics: carbon black nanomodified inkjet-printed sensor for ascorbic acid detection as a case study. *Sens. Actuators B Chem.* 265, 155–160. doi: 10.1016/j.snb.2018.03.006

de Faria, L. V., Lisboa, T. P., de Farias, D. M., Araujo, F. M., Machado, M. M., de Sousa, R. A., et al. (2020). Direct analysis of ascorbic acid in food beverage samples by flow injection analysis using reduced graphene oxide sensor. *Food Chem.* 319:126509. doi: 10.1016/j.foodchem.2020.126509

Ejaz, A., and Jeon, S. (2017). A highly stable and sensitive GO-XDA-Mn2O3 electrochemical sensor for simultaneous electrooxidation

of paracetamol and ascorbic acid. *Electrochim. Acta* 245, 742–751. doi: 10.1016/j.electacta.2017.05.193

Feng, Y., Wei, Z., and Zhang, J. (2020). Determination of ursolic acid in extracts from ligustri lucidum fruit using an electrochemical method. *Front. Chem.* 8:444. doi: 10.3389/fchem.2020.00444

Fu, L., and Fu, Z. (2015). Plectranthus amboinicus leaf extract-assisted biosynthesis of ZnO nanoparticles and their photocatalytic activity. *Ceram. Int.* 41, 2492–2496. doi: 10.1016/j.ceramint.2014.10.069

Fu, L., Liu, Z., Ge, J., Guo, M., Zhang, H., Chen, F., et al. (2019). (001) plan manipulation of α-Fe2O3 nanostructures for enhanced electrochemical Cr(VI) sensing. *J. Electroanal. Chem.* 841, 142–147. doi: 10.1016/j.jelechem.2019.04.046

Fu, L., Wang, A., Lai, G., Su, W., Malherbe, F., Yu, J., et al. (2018). Defects regulating of graphene ink for electrochemical determination of ascorbic acid, dopamine and uric acid. *Talanta* 180, 248–253. doi: 10.1016/j.talanta.2017.12.058

Fu, L., Zhang, H., Zheng, Y., Zhang, H., and Liu, Q. (2020). An electroanalytical method for brewing vinegar authentic identification. *Rev. Mex. Ing. Quím.* 19, 803–812. doi: 10.24275/rmiq/Alim869

Ghanbari, K. H., and Hajian, A. (2017). Electrochemical characterization of Au/ZnO/PPy/RGO nanocomposite and its application for simultaneous determination of ascorbic acid, epinephrine, and uric acid. *J. Electroanal. Chem.* 801, 466–479. doi: 10.1016/j.jelechem.2017.07.024

Gopalakrishnan, A., Sha, R., Vishnu, N., Kumar, R., and Badhulika, S. (2018). Disposable, efficient and highly selective electrochemical sensor based on Cadmium oxide nanoparticles decorated screen-printed carbon electrode for ascorbic acid determination in fruit juices. *Nano-Struct. Nano-Objects* 16, 96–103. doi: 10.1016/j.nanoso.2018.05.004

Hou, K., Zhao, P., Chen, Y., Li, G., Lin, Y., Chen, D., et al. (2020). Rapid detection of bifidobacterium bifidum in feces sample by highly sensitive quartz crystal microbalance immunosensor. *Front. Chem.* 8:548. doi: 10.3389/fchem.2020.00548

Hsu, S.-C., Cheng, H.-T., Wu, P.-X., Weng, C.-J., Santiago, K. S., and Yeh, J.-M. (2017). Electrochemical sensor constructed using a carbon paste electrode modified with mesoporous silica encapsulating PANI chains decorated with GNPs for detection of ascorbic acid. *Electrochim. Acta* 238, 246–256. doi: 10.1016/j.electacta.2017.04.021

Karimi-Maleh, H., and Arotiba, O. A. (2020). Simultaneous determination of cholesterol, ascorbic acid and uric acid as three essential biological compounds at a carbon paste electrode modified with copper oxide decorated reduced graphene oxide nanocomposite and ionic liquid. *J. Colloid Interface Sci.* 560, 208–212. doi: 10.1016/j.jcis.2019.10.007

Karimi-Maleh, H., Cellat, K., Arikan, K., Savk, A., Karimi, F., and Sen, F. (2020a). Palladium-nickel nanoparticles decorated on functionalized-MWCNT for high precision non-enzymatic glucose sensing. *Mater. Chem. Phys.* 250:123042. doi: 10.1016/j.matchemphys.2020.123042

Karimi-Maleh, H., Karimi, F., Alizadeh, M., and Sanati, A. L. (2020b). Electrochemical sensors, a bright future in the fabrication of portable kits in analytical systems. *Chem. Rec.* 20, 682–692. doi: 10.1002/tcr.201900092

Karimi-Maleh, H., Karimi, F., Orooji, Y., Mansouri, G., Razmjou, A., Aygun, A., et al. (2020c). A new nickel-based co-crystal complex electrocatalyst amplified by NiO dope Pt nanostructure hybrid; a highly sensitive approach for determination of cysteamine in the presence of serotonin. *Sci. Rep.* 10:11699. doi: 10.1038/s41598-020-68663-2

Long, W., and Fu, L. (2017). Hydrothermal synthesis of ZnO flower-reduced graphene oxide composite for electrochemical determination of ascorbic acid. *Fuller. Nanotub. Carbon Nanostructures* 25, 404–409. doi: 10.1080/1536383X.2017.1324952

Naderi Asrami, P., Aberoomand Azar, P., Saber Tehrani, M., and Mozaffari, S. A. (2020). Glucose oxidase/Nano-ZnO/thin film deposit FTO as an innovative clinical transducer: a sensitive glucose biosensor. *Front. Chem.* 8:503. doi: 10.3389/fchem.2020.00503

Nagles, E., Ibarra, L., Llanos, J. P., Hurtado, J., and Garcia-Beltrán, O. (2017). Development of a novel electrochemical sensor based on cobalt(II) complex useful in the detection of dopamine in presence of ascorbic acid and uric acid. *J. Electroanal. Chem.* 788, 38–43. doi: 10.1016/j.jelechem.2017.01.057

Shamsadin-Azad, Z., Taher, M. A., Cheraghi, S., and Karimi-Maleh, H. (2019). A nanostructure voltammetric platform amplified with ionic liquid for determination of tert-butylhydroxyanisole in the presence kojic acid. *J. Food Meas. Charact.* 13, 1781–1787. doi: 10.1007/s11694-019-00096-6

Yumak, T., Kuralay, F., Muti, M., Sinag, A., Erdem, A., and Abaci, S. (2011). Preparation and characterization of zinc oxide nanoparticles and their sensor applications for electrochemical monitoring of nucleic acid hybridization. *Colloids Surf. B Biointerfaces* 86, 397–403. doi: 10.1016/j.colsurfb.2011.04.030

Zhang, L., Wang, G., Wu, D., Xiong, C., Zheng, L., Ding, Y., et al. (2018a). Highly selective and sensitive sensor based on an organic electrochemical transistor for the detection of ascorbic acid. *Biosens. Bioelectron.* 100, 235–241. doi: 10.1016/j.bios.2017.09.006

Zhang, W., Liu, L., Li, Y., Wang, D., Ma, H., Ren, H., et al. (2018b). Electrochemical sensing platform based on the biomass-derived microporous carbons for simultaneous determination of ascorbic acid, dopamine, and uric acid. *Biosens. Bioelectron.* 121, 96–103. doi: 10.1016/j.bios.2018.08.043

Zhang, Y., Liu, P., Xie, S., Chen, M., Zhang, M., Cai, Z., et al. (2018c). A novel electrochemical ascorbic acid sensor based on branch-trunk Ag hierarchical nanostructures. *J. Electroanal. Chem.* 818, 250–256. doi: 10.1016/j.jelechem.2018.04.007

Zhou, J., Wu, M., Xu, Y., Li, Z., Yao, Y., and Fu, L. (2020). 2D pattern recognition of white spirit based on the electrochemical profile recorded by screen-printed electrode. *Int. J. Electrochem. Sci.* 15, 5793–5802. doi: 10.20964/2020.06.27

Conflict of Interest: YP was employed by company Shanghai Electric Group Co., Ltd. and Zhenjiang Hongxiang Automation Technology Co., Ltd. CH was employed by company Beijing Kanghong Biomedical Co., Ltd.

The remaining authors declare that the research was conducted in the absence of any commercial or financial relationships that could be construed as a potential conflict of interest.

Advantages of publishing in Frontiers

OPEN ACCESS
Articles are free to read for greatest visibility and readership

FAST PUBLICATION
Around 90 days from submission to decision

HIGH QUALITY PEER-REVIEW
Rigorous, collaborative, and constructive peer-review

TRANSPARENT PEER-REVIEW
Editors and reviewers acknowledged by name on published articles

Frontiers
Avenue du Tribunal-Fédéral 34
1005 Lausanne | Switzerland

Visit us: www.frontiersin.org
Contact us: frontiersin.org/about/contact

REPRODUCIBILITY OF RESEARCH
Support open data and methods to enhance research reproducibility

DIGITAL PUBLISHING
Articles designed for optimal readership across devices

FOLLOW US
@frontiersin

IMPACT METRICS
Advanced article metrics track visibility across digital media

EXTENSIVE PROMOTION
Marketing and promotion of impactful research

LOOP RESEARCH NETWORK
Our network increases your article's readership